KfK 5363
Oktober 1994

Behavior of a VVER-1000 Fuel Element with Boron Carbide/Steel Absorber Tested under Severe Fuel Damage Conditions in the CORA Facility

(Results of Experiment CORA-W2)

S. Hagen, P. Hofmann, V. Noack, G. Schanz,
G. Schumacher, L. Sepold
Hauptabteilung Ingenieurtechnik
Institut für Materialforschung
Institut für Neutronenphysik und Reaktortechnik
Projekt Nukleare Sicherheitsforschung

Kernforschungszentrum Karlsruhe

Kernforschungszentrum Karlsruhe

Hauptabteilung Ingenieurtechnik
Institut für Materialforschung
Institut für Neutronenphysik und Reaktortechnik
Projekt Nukleare Sicherheitsforschung

KfK 5363

Behavior of a VVER-1000 Fuel Element with Boron Carbide/Steel Absorber Tested under Severe Fuel Damage Conditions in the CORA Facility

(Results of Experiment CORA-W2)

S. Hagen, P. Hofmann, V. Noack, G. Schanz, G. Schumacher, L. Sepold

Kernforschungszentrum Karlsruhe GmbH, Karlsruhe

Als Manuskript gedruckt

Kernforschungszentrum Karlsruhe GmbH
Postfach 3640, 76021 Karlsruhe

ISSN 0303-4003

Abstract

The "Severe Fuel Damage" (SFD) experiments of the Kernforschungszentrum Karlsruhe (KfK), Federal Republic of Germany, were carried out in the out-of-pile facility "CORA" as part of the international Severe Fuel Damage (SFD) research.

The experimental program was set up to provide information on the failure mechanisms of Light Water Reactor (LWR) fuel elements in a temperature range from 1200°C to 2000°C and in a few cases up to 2400°C.

Between 1987 and 1992 a total of 17 CORA experiments with two different bundle configurations, i.e. PWR (Pressurized Water Reactor) and BWR (Boiling Water Reactor) bundles were performed. These assemblies represented "Western-type" fuel elements with the pertinent materials for fuel, cladding, grid spacer, and absorber rod.

At the end of the experimental program two VVER-1000 specific tests were run in the CORA facility with identical objectives but with genuine VVER-type materials. The experiments, designated CORA-W1 and CORA-W2 were conducted on February 18, 1993 and April 21, 1993, respectively. Test bundle CORA-W1 was without absorber material whereas CORA-W2 contained one absorber rod (boron carbide/steel).

As in the earlier CORA tests the test bundles were subjected to temperature transients of a slow heatup rate in a steam environment. The transient phases of the tests were initiated with a temperature ramp rate of 1 K/s. With these conditions a so-called small-break LOCA was simulated. The temperature escalation due to the exothermal zircon/niobium-steam reaction started at about 1200°C, leading the bundles to maximum temperatures of approximately 1900°C. The thermal response of bundle CORA-W2 is comparable to that of CORA-W1. In test CORA-W2, however, the temperature front moved faster from the top to the bottom compared to test CORA-W1. The reason for this behavior may be found in an earlier melt formation and relocation of the absorber rod material in CORA-W2. With the movement of the melt heat is transported to the lower region also. Below 300 mm elevation the test fuel rods remained intact due to the low temperature. An essential portion of the absorber melt has resolidified at about 200 mm, i.e. at the second grid spacer, where a partial flow blockage had formed. The absorber rod and its pertinent guide tube failed at ca. 200 mm, i.e. above this elevation the absorber rod is missing. Bundle CORA-W2 is characterized by a

oxidation above 300 mm elevation. Besides the severe oxidation the test bundle experienced in considerable fuel dissolution by ZrNb1/UO_2 interaction in the upper part, complete spacer destruction at 600 mm due to chemical interactions between steel and the ZrNb1 cladding.

The documentation of the experimental results is planned to be a joint effort of the Russian and the German side. In particular, the posttest investigations will be documented by the participating institutions of Russia and Germany. This report is the contribution of the Karlsruhe Nuclear Research Center providing the test data and some results of the posttest examinations.

Despite some specific features the material behavior of the VVER-1000 bundle is comparable to that observed in the PWR and BWR tests of Western design.

Verhalten eines WWER-Brennelements mit Borkarbid/Stahl-Absorber, das unter Bedingungen von schweren Reaktorunfällen in der CORA-Anlage getestet wurde (Ergebnisse des Experiments CORA-W2)

Kurzfassung

Die Severe-Fuel-Damage-(SFD)-Experimente des Kernforschungszentrums Karlsruhe (KfK) werden in der Out-of-pile-Versuchsanlage "CORA" als Teil des internationalen "Severe-Fuel-Damage"-Forschungsprogramms durchgeführt.

Mit Hilfe der CORA-Versuche sollen die Versagensmechanismen von LWR (Leichtwasser-Reaktor)-Brennelementen im Temperaturbereich von 1200 bis 2000°C und in einigen Fällen bis 2400°C ermittelt werden.

In den Jahren 1987 bis 1992 wurden 17 CORA-Versuche mit zwei unterschiedlichen Typen von Brennstabbündeln, DWR (Druckwasserreaktor)- und SWR (Siedewasserreaktor)-Bündel, durchgeführt. Die Testbündel repräsentierten westliche Brennelemente mit Originalmaterialien bezüglich Brennstoff, Brennstabhüllen, Abstandshalter und Absorberstäben.

Am Ende des SFD-Versuchsprogramms standen zwei Experimente mit WWER-typischen Brennelementen (russische Bauart). Die Experimente CORA-W1 und CORA-W2 wurden am 18. Februar 1993 bzw. am 21. April 1993 durchgeführt. Versuchsbündel CORA-W1 war ohne Absorberelement, CORA-W2 mit einem Absorberstab aus Borkarbid/Stahl ausgestattet.

Wie in den CORA-Versuchen zuvor wurden die Testbündel Temperaturtransienten mit langsamer Aufheizrate und in Dampfatmosphäre ausgesetzt. Die transiente Phase der Versuche wurde mit einer Aufheizrate von 1 K/s begonnen. Damit wird ein Unfallablauf für einen LWR simuliert, der sich aus einem Kühlmittelverluststörfall durch Auftreten eines sogenannten kleinen Lecks entwickeln kann.

Die Temperatureskalation aufgrund der exothermen Zirkon/Niob-Wasserdampfreaktion setzte ab ca. 1200°C ein. Die Höchsttemperaturen betrugen 1900°C. Das Temperaturverhalten des Bündels CORA-W2 ist vergleichbar mit dem des Experiments CORA-W1, jedoch mit dem Unterschied, daß sich die Temperaturfront im Vergleich zu CORA-W1 schneller von oben nach unten ausbreitete. Der Grund da-

für dürfte in der frühen Schmelzbildung und der damit verbundenen Umverlagerung der Absorberschmelze liegen; denn mit dem Schmelzfluß wird auch Wärme in den unteren Bündelbereich transportiert. Die Brennstäbe des unteren Bündelabschnitts (bis 300 mm) blieben aufgrund der axialen Temperaturverteilung unversehrt. Ein wesentlicher Teil der Absorberschmelze ist bei ca. 200 mm, d. h. in der Höhe des zweiten Abstandshalters erstarrt. Hier hat sich eine teilweise Kühlkanalblockade gebildet. In derselben Höhe liegt die Versagensstelle des Absorberstabs und des zugehörigen Führungsrohrs, d. h. oberhalb ca. 200 mm fehlen Absorberstab und Führungsrohr. Das Versuchsbündel weist eine starke Oxidation im oberen Bereich auf. Neben der Oxidation zeigte das Versuchsbündel ausschließlich im oberen Bündelbereich Brennstoffauflösung durch die Wechselwirkung $ZrNb1/UO_2$ und vollständige Zerstörung des Abstandshalters in der Höhe 600 mm aufgrund chemischer Wechselwirkungen zwischen Stahl und dem ZrNb1-Hüllrohrmaterial.

Die Dokumentation der experimentellen Ergebnisse ist als gemeinsame Aufgabe der russischen und der deutschen Seite geplant. Insbesondere werden die Ergebnisse der Nachuntersuchungen von den beteiligten Institutionen in Rußland und Deutschland dokumentiert. In diesem Bericht werden die Versuchsdaten des Experiments CORA-W2 und einige Ergebnisse der Nachuntersuchungen dargelegt. Sie sind der Beitrag des Kernforschungszentrums Karlsruhe.

Von einigen spezifischen Merkmalen abgesehen ist das Materialverhalten des WWER-1000-Bündels vergleichbar mit dem der DWR- und BWR-Versuche westlicher Bauart.

Contents

1. Introduction

Safety studies demonstrated that so-called small break loss-of-coolant accidents in Light-Water Reactors (LWR), in combination with failure of the required safety systems, can lead to overheating of the core and thus result in severe fuel damage (SFD) and fission product release.

In such an accident the nuclear fuel rods may be subjected to temperatures beyond the present design basis accident limit of 1200°C. The temperature transient, however, will not necessarily escalate to an uncontrolled core meltdown accident, as it was learned from the TMI accident in 1979.

The transient of a SFD-type accident is initiated by a slow temperature rise in the order of 0.5-1.0 K/s, followed by a rapid temperature escalation (about 10 - 20 K/s) due to the exothermal heat produced by the zirconium alloy cladding oxidation in steam environment. Besides oxidation and embrittlement of the fuel rod cladding, local melting of the cladding and interactions between solid and molten zircaloy and uranium dioxide pellets occur and lead to destruction of fuel rod elements and other core structures at temperatures far below the melting point of the fuel. The concern with melting of fuel rod materials in a SFD accident is relocation, solidification, and therefore the formation of coolant channel blockages.

To investigate the relevant damage mechanisms in an uncovered core, and to develop models for estimating core damage initiation and propagation, research programs have been defined in various countries. In these programs in-pile and out-of-pile experiments are being performed under severe fuel damage conditions, i.e. temperature escalation to about 2000°C with termination of the transient before complete core meltdown.

At the Kernforschungszentrum Karlsruhe (KfK) a series of out-of-pile experiments on SFD research was performed in the CORA facility. The entire experimental program is provided with Table 1 (CORA test matrix). As can be seen from this list, 17 experiments using bundle configurations of the Western design were conducted. All of these CORA experiments were performed with UO_2 as pellet material and with absorber material (except for CORA-2 and -3). Two different absorber materials were used within the two different bundle configurations, i.e. (Ag,In,Cd) rods represented PWR (Pressurized Water Reactor) conditions whereas boron carbide refers to the experiments simulating BWR (Boiling Water Reactor) fuel elements.

At the end of the experimental program two VVER-1000 specific tests were run in the CORA facility with analogous objectives but with genuine VVER-type materials. The experiments, designated CORA-W1 and CORA-W2 were conducted - under the same conditions as the previous tests - on February 18, 1993 and April 21, 1993, respectively. Test bundle CORA-W1 was without absorber material whereas CORA-W2 contained one absorber rod (boron carbide/ steel).

The documentation of the experimental results is planned to be a joint effort of the Russian and the German side. In particular, the posttest investigations are to be performed at different laboratories in Russia as well as at the Karlsruhe Nuclear Research Center, i.e. polished samples were distributed for the posttest examinations to the different institutions. This report is meant as documentation of the test data of the second CORA-VVER experiment CORA-W2 and includes some results of the post test examinations performed at KfK.

2. Test Description

2.1 Description of the Test Facility

A detailed description of the CORA facility (see Figures 1 and 2) is given in reference /1/. The test bundle is surrounded by a high-temperature shield which is located within the pressure tube. The vertical and the horizontal cross-sections of the high-temperature shield are given in Figures 3 and 4. The high-temperature shield consists mainly of ceramic fibre plates. The inner layer of plates consists of ZrO_2, and the outer one of Al_2O_3. The fibre ceramics are excellent insulators and have a low density which results in a low heat capacity. The thermal shock behaviour of the fibre ceramics is also excellent.

The mechanical strength of the high temperature shield is provided by outer walls of stainless steel (0,9 mm). The fibre ceramic plates are attached to the stainless steel cover by ceramic nails. The inner ZrO_2 layer is 38 mm thick, and the outer Al_2O_3 layer is 76 mm thick, separated by a gap of 23 mm. The distance from the inner insulation surface to the centre of the bundle is 153 mm.

The test bundle is being inspected during the test by several video and still cameras through a number of holes in the shield.

Steam generator and steam superheater are placed inside the CORA containment. A maximum steam temperature of more than 800°C can be attained. The maximum steam flow rate amounts to 33 g/s.

Two different condensers are installed in the CORA facility: A vent condenser and a surge condenser. Under normal operating conditions the steam which is not consumed by oxidation of the bundle, is condensed in two vent condenser units. The surge condenser is physically separated from the high pressure system by four rupture disks. In case of emergency, e.g. due to an extremely high evaporation rate caused by quenching of the bundle, the void volume of the surge condenser serves as a pressure suppression system.

The condensate from the vent condensers and - in the case of emergency - the excess spray water of the surge condenser are collected in the condensate tank. After each test the amount of water in the condensate tank is determined to perform a water mass balance.

To avoid any hazard of hydrogen formed during the zirconium oxidation, the non-condensable gases are expanded and diluted in a mixing chamber (see Fig. 1). The hydrogen is diluted to a concentration below explosion limits by adding air to the gas.

The test facility has a quench capability which is activated by raising a water-filled quench cylinder into the test section at a controlled speed. This option was not used in the VVER-specific experiments. After a test, the high-temperature shield can be lowered into the quench unit without moving the bundle. So, the tested bundle can be inspected and photographed in its original condition that existed at termination of the transient.

2.2 Test Bundle Design

Test bundle CORA-W2 consisted of 19 fuel rod simulators. The test rods were arranged within the bundle as shown in the schematic cross section of Figs. 5 and 5a. 13 of the 19 fuel rods were electrically heated by using tungsten pins as heating elements. Five rods were unheated and one position within the bundle was filled with an absorber rod and its pertinent guide tube. The heated rods (fuel rod simulators) as well as the unheated rods were filled with annular UO_2 pellets of the same outer diameter but with different size of the central holes. The design of the heated and unheated types of rods used in the CORA-VVER test bundle is given with Fig. 6. The rod claddings and the shroud surrounding the rods are made of zirconium-1%niobium (Zr1%Nb). The shroud itself is insulated with a 20 mm-thick layer of ZrO_2 fiber material to guarantee a uniform radial temperature distribution.

Three grid spacers of 20 mm length were mounted below the heated region, in the lower bundle region, and above its axial center. All three grid spacers are made of stainless steel. Details on the location of the spacers and the fuel rod simulator design characteristics are given in Table 2.

The bundle head funnel (at the top of Fig. 3) is made of copper and is water-cooled by the double-walled outer chamber. To make the cooling more effective the space around the rods inside this chamber is filled with water. In consequence, the upper ends of the heated rods (the copper electrode inside the Zry-cladding) and the connectors for the pressure capillaries and thermocouples of the unheated rods are surrounded by water.

At the lower end the heated fuel rod simulators are cooled by the water inside the quench cylinder. The gross volume of water inside the quench cylinder (230 mm ID) amounts to about 70 l. The initial water level is at the -220 mm elevation.

The test train instrumentation comprised thermocouples and two-color pyrometers for the various temperature measurements. Besides the standard NiCr/Ni Al type thermoelements with stainless steel sheath, the test section was instrumented with different types of high-temperature thermocouples listed in Table 3. The Russian TC design is additionally illustrated in Fig. 8. The exact positions of the thermocouples are provided with Table 4 and Table 5 (locations of the high-temperature shield).

Two videoscopes, at 600 mm and 800 mm (120 ° orientation), were used in test CORA-W2 to observe the materials behavior and the relocation of material during transient testing. A schematic of the videoscope system with video camera and 35-mm still camera is given with Fig. 9.

The hydrogen produced during the test by the steam/Zr reaction is measured with means of two mass spectrometer systems at two different positions, i.e. above the test section and in the mixing chamber after the gas had passed the condenser (see Fig. 1). The gas at the test section outlet can contain a high steam partial pressure and has therefore to be diluted by helium before it enters the analyser through the capillary tube. For this purpose a dilution chamber with flow meters is installed.

A schematic of the probes, gas lines, and gas analysis system is provided with Fig. 10. The off-gas mixture which contains hydrogen among other gases is being transported to the spectrometer via capillary tubes. It is analyzed by quadrupole mass spectrometers of the type Leybold PQ 100. The ion currents representing the partial pressures of the respective gases are determined. The hydrogen generation rate is evaluated as follows:

$$R_m = 2\, p_H \cdot F_{Ar} / 22.4 \cdot p_{Ar}$$

with

R_m = Mass production rate of hydrogen [g/s]

p_H = Partial pressure of hydrogen [Pa]

p_{Ar} = Partial pressure of argon [Pa]

F_{Ar} = Volumetric argon flow through mixing chamber [l/s].

The mass production rate of hydrogen as well as of the other gases is calculated with the ratio of the partial pressure of the particular gas and that one of argon (carrier gas) and multiplied by the argon flow rate through the test bundle.

Based on a calibration test with bundle CORA-7 in which a mixture of argon and 30 % hydrogen was radially injected in the test section the delay time of monitoring the gas was estimated to be 80 s. This time was taken into account for the measured hydrogen production of all CORA experiments.

From the same calibration test it was learned that the measured gas concentration showed lower slopes of the hydrogen production rate than it had to be expected from the injected gas flow. For this reason the measured data were corrected based on the real gas concentration, i.e. on the gas input during the calibration test. A transfer function was determined and applied to the measured data. The result is a corrected curve that better represents the H_2 production rate in the test section.

3. Test Conduct and Initial Boundary Conditions

In the CORA experiments one can generally distinguish the following phases for the test sequence:

- Pre-heating	0000 - 3000 s (argon only)
- Heat-up	3000 - 3900 s (argon; argon+steam from 3300 s)
- Escalation	3900 - 4500 s (argon + steam)
- Cool-down	> 4500 s (argon only).

The test sequence of the experiment CORA-W1 can be taken from Table 6. During the preheating phase argon of about 500 °C entered the test bundle with a flow rate of 8 g/s (Figures 11 and 12). Between 3000 s and 4500 s the electric power was increased from 2 kW to 14.5 kW with a ramp rate of approx. 0.01 kW/s to achieve the initial heatup rate of 1 K/s. At 3300 s within the test a constant flow of superheated steam of 4 g/s was added to the argon flow of 6 g/s. At about 4150 s the slow temperature rise was followed by a rapid increase caused by increasing electric power input and additional energy from the exothermal zirconium - steam reaction.

The electric power supply was turned off at 4500 s (termination by slow cooldown) together with the steam supply.

The power input history for test CORA-W2 together with the coolant data as argon flow, steam flow (provided as mass flow of the injected water into the evaporator), and coolant pressure are given in Figs. 11 through 14.

The measured voltage input during the transient phase, the total electric energy input, the total current, and the total electric resistance of the bundle are given in Fig. 15 and Figs. 17 through 19. The variation of currents of the individual rods plotted per rod group can be found in Fig. 20. The resistances of the three rod groups are given in Fig. 21 and the resistances of the individual heaters are given in Figs. 22 through 24.

The water temperature in the quench cylinder at -250 and -350 mm elevation is shown in Fig. 25. During the transient the water temperatures increase to 80 and 60°C, respectively, due to heat conduction from the heated fuel rod simulators that immerse into the water of the quench cylinder and due to the radiation from the bundle.

In Fig. 26 four measured steam tube temperatures at -50 mm elevation are provided. The steam inlet temperature at 0 mm elevation is given with Fig. 27. During the heatup the temperature increases from 520 to about 640°C. The internal pressures of the absorber rod and of unheated rods during test CORA-W2 can be taken from Figs. 32 and 33.

4. Temperature Response, Hydrogen Generation, and Bundle End State

4.1 Temperature Measurements of the Bundle

The initial temperatures of the different components at 0 s and at the onset of the transient, i.e. at 3000 s, are provided with Tables 7 and 8.

The temperature measurements are presented as a function of time in the following way: On one hand, the temperatures of the components (heated rods, unheated rods, spacers, shroud, high-temperature shield) are given, on the other hand - for comparative reasons - the temperature measurements for different components are grouped for the same axial elevations (Figs. 42 through 51). Moreover, so - called best-estimate temperatures at different elevations (Fig. 52) and axial temperature distributions for different time steps (Fig. 53) are presented.

Different types of thermocouples were installed in test bundle CORA-W2 (Table 3):

- In the center and at the outer surface of unheated rods
- At the outer surface of heated rods
- At the outer surface of the shroud and its insulation
- Above the shroud and at the bundle flange (gas temperature)
- Between the cladding of the absorber rod and the guide tube
- At the grid spacer
- At the steam entrance.

The thermocouple locations listed in Tables 4 and 5 are in addition illustrated in Figures 28, 37, and 54.

The course of the rod temperatures during the CORA-W2 transient at different locations and elevations is provided with Figs. 29 through 31. The temperatures of the heated rods show fairly consistent traces from 350 mm to 1150 mm. The data for the lower as well as for the upmost locations of 1250 mm, 1350 mm, and 1450 mm differ significantly. The temperatures of the unheated rods (Figs. 30 and 31) confirm the thermal behavior for as long as they worked, i.e. TC failure occurred earlier for some elements compared to those mounted at the heated rods.

Temperatures at locations from 350 mm upward continued to rise more rapidly (temperature escalation at about 1200 °C) due to the zirconium-steam reaction with the strongest heatup at 650 - 750 mm. At this location the maximum measured temperature amounts to 1900 °C.

The temperature escalation can also be found in Fig. 36 which depicts the temperatures of the three grid spacers and in Figs. 38 and 39 with shroud and shroud insulation temperature. While the temperatures of the grid spacers at the low elevations, i.e. at -15 mm and 200 mm, do not show any escalation the 600 mm level exhibits a sharp temperature rise.

The start of absorber rod failure was indicated by the measured rod internal pressure (Figs. 32 and 33). At the time of the pressure loss (4069 s) the absorber rod temperature was 1230 °C and the maximum bundle temperature at 850 - 950 mm elevation ca. 1250 °C. This leads to the conclusion that the failure location was in the upmost region of the heated zone, may be even above the 1000-mm elevation. The temperature mentioned above is below the melting point of the absorber rod cladding. The early absorber rod failure indicates an interaction between the boron carbide and the SS cladding and/or between the SS guide tube and the fuel rod cladding made of Zr1%Nb.

The gas temperatures at three elevations are given in Fig. 40, those of the high-temperature shield for elevations between 50 mm and 1270 mm in Figs. 56 through 76. The temperatures of the high-temperature (HTS) shield are compared to each other for different axial elevations or for different azimuthal positions. The high-temperature shield has measurement planes at 153 mm (inner surface), 172 mm, 192 mm, 255 mm, 293 mm and 380 mm (outer surface). Temperatures at different radial positions (different components) but at individual elevations are shown in Figs. 42 through 51, axial temperature distributions in Fig. 53. The best-estimate values used for evaluating the axial temperature profiles have the following uncertainties: ± 100 K in maximum up to the time of temperature escalation. Beyond the escalation the uncertainties are often larger.

In the temperature range beyond the escalation the given "best-estimate" temperatures are considered to present lower values because some TC signals used in the evaluation could possibly originate from thermocouples which had formed TC junctions at positions of lower temperatures. As thermocouples usually fail at the time of the maximum temperature an exact number cannot be given. Uncertainties due to eccentricities of the rod arrangements that can form during the course of the transient are included in the error range.

4.2 Hydrogen Generation

The hydrogen production rate during test CORA-W2 and the integral hydrogen production (measured and corrected* data) are given in Fig. 77 as a function of time. The measured data are obtained from the gas probes at the mixing chamber. The total hydrogen amounts to 75 g. This value corresponds to an average of 32 % oxidation based on 5.368 kg zirconium, i.e. 3.184 kg of cladding and 2.184 kg of shroud (1.2 m length). With the total hydrogen of 75 g H_2 and the time at temperatures above 1400 °C - estimated to be 400 s - the fraction of steam consumed is calculated to be 42 % of the total steam flow of 4 g/s injected into the test section.

4.3 Mass Distribution and Blockage Formation

An axial profile of voids and structure material, respectively, can be obtained by using the epoxying process. As can be seen in Fig. 78 the epoxy resin is filled into the mould from the bottom end. By weighing the resin left in the supply container after each step, i.e. when the resin level has raised in the bundle by 1 cm, the difference of mass allows the calculation of the void volume of the bundle as a function of axial height. The filling process is slow enough so that the reading at the scale can be taken per cm providing a specific mass in (g/cm). The error of this method amounts to about 15 % with respect to readings of the epoxy level at 1 cm increments. It is too large to give reliable results. The error, however, is alternating, i.e. epoxy mass not measured at one step is certainly included in the next reading at the scale.

The data of the specific mass of resin as a function of elevation (g/cm) in Fig. 79 demonstrate the scatter (crosses). The smoothed solid-line curve in Fig. 79 was obtained from the data (crosses) by filtering, i.e. by using a Fourier transformation where higher frequencies were cut off by a low-pass filter. This filtering method

---

* Corrected data are based on the CORA-7 calibration test.

has an additional advantage in reducing the uncertainty when dealing with alternating errors. The axial distribution in Fig. 79 is a distribution of voids because a higher amount of resin is equivalent to a larger void volume.

Fig. 80 presents the axial distribution of the structural material. For the evaluation of this profile the cut bundle segments were weighed. These data represent the mass of the structure and the mass of the heater elements:

Specific mass = Mass of weighed samples - Epoxy mass - Mass of shroud remnants referred to the pertinent axial segment.

As the shroud of the axial center (hot region) was removed together with the fiber insulation after the test, the remnants of the shroud which were present during the filling process were excluded in the evaluation,i.e. it was assumed that there had been no shroud.

For practical reasons segments were cut to a length of 5 cm for weighing and evaluating the axial distribution of the specific mass [g/cm]. This length means a compromise with respect to uncertainty and resolution. Concerning the uncertainty, the relative error of the epoxy mass is only one fifth compared to the 1-cm reading of the filling process mentioned above. The error of the specific mass is even lower because the portion of the epoxy mass within the total mass of the segments is small. On the other hand the choice of a 5-cm length for the segments limits the resolution of the axial mass distribution.

In Fig. 81 the axial mass distribution is depicted together with the axial temperature distribution (best-estimate values), for various time steps. The masses of the epoxy resin and of the shroud are eliminated in the evaluation. From this distribution it can be learned that the higher temperatures, i.e. temperatures above 1500 °C/1600 °C existed in the upper half (between 700 to 1100 mm)at approx. 4200 s and in the zone (from 300 to 1100 mm) for the time of 4600 s. At these times the material relocated from the upper regions to lower elevations. The partial blockage - as a result of this material relocation - had formed above the 200-mm elevation, at an axial zone with a steep temperature gradient. This behavior of solidification of melt was found in test bundle CORA-W1 /3/ and in other CORA experiments.

5. Posttest Appearance of the Bundle

Overall views of test bundle CORA-W2 after the test at different orientations are given in Figs. 82 through 114 with the first pictures demonstrating the condition of the bundle prior to the removal of the shroud insulation. Above ca. 700 mm the shroud was completely oxidized and broke away because of its brittleness except for some remnants. In the lower region one finds quite some areas where the shroud insulation is glued to the shroud. More detailed views are presented with the photographs of Figs. 85 through 114.

Prior to the encapsulation of the bundle three loose fragments of the many that had collected at the very bottom of the bundle were taken for chemical analyses (Table 9). It is very likely that that these melt droplets had formed during the early stage of the transient because the analyses indicate components of steel, i.e. material of the absorber rod and its pertinent guide tube (Table 10).

The following description of the posttest appearance with an insight into the interior of the test bundle was made possible with the additional help of cross sections (Figs. 115 through 132) with enlarged views in Figs. 119 through 132. The positions of the cross sections can be taken from Table 11.

To obtain cross sections a mould was set up around the bundle that was filled with epoxy resin (see also Fig. 78). For encapsulation of the bundle the epoxy system Rütapox 0273 with the hardener designated LC (Epoxy resin and hardener manufactured by Bakelite GmbH, Iserlohn) was chosen. The bundle was filled starting from the bottom, through the steam inlet line, to avoid air entrainment in the encapsulant. The epoxy showed some heating during the curing stage but the shrinkage effect was negligible. After epoxying the bundle the resin was allowed to harden for one week. A saw with a 2.3 mm-thick diamond blade (mean diamond size 138 µm) of 500 mm OD was used to cut the slabs at 3200 rpm.

After visual inspection of the horizontal sections some 50-mm slabs were vertically cut according to Figs. 133 and 134. The vertical sections are shown in Figs. 135 through 137.

Some sections were selected for metallographic examination (Table 12) and had therefore to be polished. So, the samples were infiltrated by "Araldit" resin to close up residual pores then ground and polished. The entire procedure of the preparation for the metallographic examination is given with Table 13). The steps described in the list were performed using a semi-automatic machine with a closed water circuit for grinding and an automatic lubricant feeder for the polishing steps.

From the posttest photography and the cross sections one can recognize that

- the test bundle is fairly intact up to an elevation of about 200 mm,
- the severely oxidized part of the bundle lies above 400 mm,
- the central grid spacer is intact (see cross section at 206/208 mm) due to a local temperature of below 1100 °C,
- the upper grid spacer has completely molten away (cannot be detected in the cross section of 605 mm) due to chemical interactions with the ZrNb1 cladding and by reaching the melting point,
- the absorber melt has created a partial flow blockage at about 200 mm, i.e. at the location of the central grid spacer,
- the absorber rod failed at about 210 mm (i.e. above this elevation the absorber rod does not exist any more),
- the radial deformation of the cladding, the so-called "flowering" is evident from about 400 mm upward,
- a strong variation of the oxide layer thickness of the cladding was evaluated.

Moreover, the video observation revealed

- that only a relatively small amount of melt relocated downward,
- that the first droplets of melt could be detected at 4190 s at both inspected elevations, i.e. at 600 and 800 mm (at this time the temperature was in the order of 1500 - 1700 °C, i.e. in the period of temperature escalation),
- that the first lumps of melt were observed at 4210 s and 4328 s at 800 and 600 mm, respectively,
- that the stainless steel grid spacer melted away from 4312 s to 4370 s, i.e within 58 s (at this time the 600-mm elevation had reached the maximum temperature of approx. 1900 °C).

In general, the material behavior of this VVER-1000-type bundle is comparable to that of a PWR of Western design /2/.

6. Microstructural Post-Test Investigation

In this chapter the final status of the bundle is described on the basis of the metallographic investigation at four cross sections, beginning with the lowest elevation. Next, the series of oxide scale thickness measurements, performed on fuel rod cladding across the bundle and at the external and internal surface around the shroud, are presented separately, in order to facilitate the comparison of different elevations. All the information is interpreted with the effort, to reconstruct the bundle degradation mechanisms and sequences. It is mentioned, that the investigation of other bundle cross sections by the Russian partners is expected to provide confirmatory and complementary information.

6.1 Bundle Elevation 206 mm

At this elevation the bundle is characterized by its still retained configuration (Fig. 138). Relative to the spacer grid, the fuel rods and the absorber rod, the shroud is found excentric and slightly tilted. Considerable proportions of the free volume are blocked by melt, mostly of metallic nature. The annulus between absorber cladding and guide tube is completely filled.

Uniform layers of ZrO_2 scale followed by an α-Zr(O) sublayer, the β-Zr cladding matrix, and finally an interaction zone in contact with the fuel, here denoted as uranium-modified α-Zr(O), are observed (Fig. 139, Pos. 1). At other positions, lenticular scale growth and spalling of partial layers have occurred (Pos. 2). Often, a layer of externally adhering melt, which was oxidized and is locally lifted off the scale, cannot be clearly distinguished from the usually formed thin external subscale of Zr1Nb cladding, for which similar morphologies are known from HT oxidation studies (Pos. 3, 4).

Embedded into relocated metallic melt, in this case stainless steel melt with molybdenum content (originating from dissolved TC cladding) the fuel rod cladding got isolated from further steam oxidation (Fig. 140). At Pos. 1 the temperature was sufficiently high to dissolve the scale and to partially melt the cladding. At Pos. 3 a delicate sequence of thin, spalled sublayers have been preserved below the melt, an interesting example of the breakaway oxidation phenomenon /4/.

The oxidation of the shroud has resulted in scales with considerable azimuthal thickness variation and, unexpectedly, the external scales are in general thicker than the internal ones (Fig. 141).

6.2 Bundle Elevation 392 mm

According to Fig. 142 the bundle is characterized by strong degradation of absorber rod, spacer grid, and fuel rod cladding compared to relatively intact fuel, and relatively small fractions of retained melt.

The cladding oxidation is almost complete, even for fuel rods of the second ring, which show complete conversion of the cladding to Zirconia (Fig. 143). The morphologies allow to distinguish the already discussed bulged surface layer (Pos. 2), the bulk scale, which was formed by solid state oxidation, and the inner oxidized part, which was formed after the melting of the cladding (Pos. 4). At Pos. 3 external melt has formed a porous, ceramic structure and modified the substrate scale morphology.

The shroud oxidation is much advanced, but not complete (Fig. 144). The wall thickness is larger than the original 1 mm plus the expected increment related with oxide formation. The thickness increase can only be explained by the assumption, that melt, most probably from the molten shroud matrix above, has accumulated between the stabilizing external and internal scale. The shroud microstructures confirm this interpretation in so far, as shroud melting is indicated by duplex α-Zr(O) + ZrO_2 phase distribution with obviously flat oxygen concentration profiles. In addition, also interference with other melt, originating from steel structures is identified, according to the special microstructures, Fe-modified ZrO_2 in Fig. 7, Pos. 2 and Fe-modified ZrO_2+(Zr,O) at Pos. 4. This contamination might have penetrated from the internal side into the shroud wall. This would also explain the observation, that the internal scale is generally thinner than the external scale: Eutectic formation between the steel-rich melt and the shroud could have protected the internal shroud surface from extensive oxidation.

6.3 Bundle Elevation 605 mm

At this elevation the bundle is characterized by accumulation of melt, resulting mainly from fuel dissolution into molten cladding, which has occurred here and above (Fig. 145). The absorber rod arrangement has completely disappeared, the spacer grid is almost destroyed, ca. one third of the shroud is missing.

The cladding oxidation, as illustrated in Fig. 146 for corner rods of the second ring, was almost complete. Obviously, simultaneous reactions, competing with the external cladding oxidation by steam, have been the internal clad melting and fuel dissolution (Pos. 1), the axial splitting of the cladding, its opening under oxide growth stresses (the so-called flowering), the penetration of melt into the rod (Pos. 3) and the melt relocation downwards and outwards.

The shroud oxidation is not yet complete at all circumferential positions, according to duplex matrix microstructures of some remaining metallic α-Zr(O) together with ZrO_2 (Fig. 147), Pos. 2 to 4). With the increased total wall thickness and the relatively thin or even missing internal scale the shroud oxidation corresponds to that of the already discussed elevation at 392 mm.

6.4 Bundle Elevation 910 mm

At this elevation the bundle is characterized by completely oxidized (and "flowered") cladding residues, oxidized fuel interaction melt, in contrast to a pool of other retained, still metallic melt (Fig. 148). A wide spectrum of pellet conditions and the absence of absorber rod and shroud should be mentioned.

The oxidation status of the cladding, as shown in Fig. 149, is that of a complete conversion of the total wall (Pos. 1) or the residual wall fraction (Pos. 3) to oxide. Melt. in external or internal contact, exists in oxidized form.

6.5 Quantitative Results on Fuel Rod Cladding and Shroud Oxidation

In order to quantify the extent of oxidation of the fuel rod cladding and the shroud, series of ZrO_2 scale thickness measurements have been performed at the already discussed bundle elevations 206, 392, 605 and 910 mm.

The minimum / average / maximum values for the individual fuel rods are based on typical local values obtained at several circumferential positions with free steam exposed scale surface. They include not only the internal partial scale, grown after clad melting, but also the oxidized originally molten reaction zone with the pellet, since these zones cannot be easily distinguished in the oxidized condition. In order to draw oxidation profiles across the bundle, pairs of measurements at opposite sides in the 90°/270° direction were included for the two lowest elevations. The shroud oxidation was determined on both sides every 20° around the circumference.

Cladding oxidation profiles across the bundle in the 90° to 270° direction along the central row of five rods and the parallel rows of four or three rods are drawn for the 206 mm elevation in Fig. 150. The metal consumption in % of the original wall thickness was estimated on the basis of a Pilling-Bedworth ratio of 1.56. The central profile is rather flat and decreases sharply towards the small internal shroud scale values. The parallel profiles, as far as measurable, are comparatively low. The respective values at the 392 mm level are more than an order of magnitude higher (Fig. 150). Compared to the central profile, by chance rather regular, the parallel side profiles are very unsystematic. Low values are the consequence of partial cladding meltdown before complete oxidation. Temporal contact with relocated melt could also have delayed the cladding oxidation locally. The high scale thickness values always include the contribution of agglomerated and subsequently oxidized melt. In total the observed disturbances of the oxidation profiles have been explained.

The plot of the shroud oxidation around its circumference at the 206 mm level is rather complex (Fig. 151): Some high external side values are comparable to the cladding oxidation at this elevation. A certain correlation between the both sides is obvious, the internal oxidation is generally less advanced or even negligible at a few position. The corresponding plot at the 392 mm elevation (Fig. 151) combines the smooth external scale curve with the fluctuating internal scale curve. Similar results are drawn for the 605 mm elevation in Fig. 151. Here the smooth additional curve for total oxidation, the percentage of cladding conversion to oxide, was defined as the fractional thickness of both scales plus the estimated volume fraction of ZrO_2 in the ceramic/metallic matrix. The discrepancy between thin scales, as measured, and the high oxygen content of the wall matrix, as deduced from the microstructure, are the typical result of fast, equilibrating oxygen diffusion in the liquid state, in which a strong dissolution tendency was moderating the scale growth. This interpretation alone does not explain the smaller scale thickness at the inner side. Here the already mentioned interaction with other metallic melt has occurred, deduced from the iron contamination of the shroud.A further, most probable explanation is that spalling of scale has occurred during or in the cooldown phase of the transient. Consequently, the measured thickness values of the internal side of the shroud would not be adequate for a comparison with oxidation calculations.

The axial oxidation profile along the bundle, drawn in Fig. 152, shows unimportant differences between the average values for central rod, first and second ring, but broad scatter bands and a steep axial increase to the plateau of complete oxidation.

6.6 Summary of the Microstructural Post-Test Investigation

- Morphologies of oxidized cladding indicate the formation of regular sublayers or, locally observed, forms of lenticular scale growth or spalling of scale sublayers.
- Towards complete external steam oxidation the fuel rod cladding is also degraded by melting and fuel dissolution together with deformation ("flowering") and embrittlement.
- Lateral cladding oxidation profiles across the bundle are rather flat, but disturbed and therefore irregular, at the lowest elevation due to resolidified metallic melt, at the higher elevations due to partial meltdown before oxidation or melt agglomeration and continuing oxidation.
- According to the axial cladding oxidation profile more than half of the bundle length is completely oxidized.
- The shroud oxidation profiles around the circumference confirm the pronounced axial gradient and indicate considerable azimuthal variations and disturbances in relation with shroud melting and contamination by melt, wall thickening and local scale spalling.
- The lower half of the bundle has retained relatively intact fuel pellets compared to the advanced degradation of other components and the relocation of metallic melt.
- The upper half of the bundle has experienced strong melt formation and relocation due to fuel dissolution as well as strong degradation of all components by chemical interactions and fragmentation.

7. Post-Test SEM/EDX Examination

Four cross sections of the fuel rod bundle CORA-W2 were chemically analyzed by SEM/EDX (scanning electron microscope, energy dispersive X-ray) examinations to

- describe the high-temperature reaction behavior among the bundle components, and to
- provide reference chemical compositions of typical phases (reaction products, solidified melts).

The measurements were performed with a SEM type JEOL 6100. For the EDX examination a newly developed light element (B, C, N, O) detector was used (Quantum 3600 - 19, Kevex).

Altogether 13 cross sections of the bundle CORA-W2 were metallographically prepared and chemically analyzed by MPA or SEM examinations in Germany and Russia. In the following chapter only the examination results of four cross sections are described which were examined in Germany (Figure 1); the other nine cross sections were analyzed in Russia. Therefore, the summary description of the chemical behavior of the bundle CORA-W2 in this report has to be considered as preliminary. An independent joint report will be prepared which will contain a detailed description of all destructive post-test examination results obtained in Germany and Russia.

The objective of the SEM/EDX examinations has been to describe at each examined cross-section elevation

- the fuel/cladding chemical interactions,
- the chemical behavior of th B_4C absorber assembly,
- the chemical behavior of the shroud, and
- the chemical composition and homogeneity of the solidified melts.

At the examined lowest cross-section elevation CORA-W2-d (206 mm) the majority of the reaction products and relocated and solidified melts are metallic in nature. The B_4C absorber assembly is still present. At all the other examined cross-section elevations CORA-W2-g (392 mm), W2-k (605 mm), and W2-p (910 mm) the reaction products and a great part of the once molten material are oxidized. The absorber assembly has dissappeared at these elevations (Figure 153).

7.1 Cross-section Elevation CORA-W2-d (206 mm)

The cross section W2-d is shown in Figure 154. The original arrangement of the heated and unheated rods, the B_4C absorber assembly, the stainless steel spacer grid, and the shroud can still be recognized. Various metallic melts relocated to this elevation and solidified. The heat content of the melts resulted in localized onset of melting of the ZrNb1 shroud and cladding and caused intensified chemical interactions with the UO_2 fuel. The B_4C absorber assembly is still present at this bundle elevation; the gap between the stainless steel guide tube and stainless steel clad B_4C absorber rod is filled with once molten material. The B_4C was chemically attacked by the stainless steel. The cross section also exhibits the great number of thermocouples which were used for temperature measurements. Especially at higher cross-section elevations, which reached higher temperatures, the thermocouples participated in the chemical interactions.

The examined locations of the cross section are indicated by numbers. Melts were analyzed with respect to their homogeneity at different spots indicated by letters.

7.2 Cross-Section Elevation CORA-W2-g (392 mm)

The cross section W2-g is shown in Figure 155. The cladding of the fuel rods has partially melted and relocated to lower bundle elevations; the remaining part has been oxidized. The molten part of the cladding has been oxidized later in the course of the test. The molten cladding dissolved a part of the UO_2 fuel. The B_4C absorber assembly has been destroyed; some of the B_4C absorber material remained at this elevation. The shroud was partially molten and the post-test wall thickness is much thicker than the original one before the test.

7.3 Cross-Section Elevation CORA-W2-k (605 mm)

The cross section is shown in Figure 156. The destruction of the individual fuel rods is stronger and the fuel dissolution is more intensive than at the lower cross-section elevations. A great part of the molten material remained at this elevation. The absorber assembly has completely melted and relocated. The cladding partially dissappeared and the remaining part is fully oxidized. The shroud has a similar appearance as that of the cross-section elevation CORA-W2-g (392 mm); it became thicker due to interactions with relocating melts and failed locally.

7.4 Cross-Section Elevation CORA-W2-p (910 mm)

The cross-section is shown in Figure 157. One can recognize the strong destruction of the bundle arrangement at this elevation. The B_4C absorber assembly disappeared completely. The molten part of the cladding relocated and dissolved some UO_2 fuel; the remaining part of the cladding is completely oxidized. Some once molten material remained at this elevation. The shroud is completely missing (either destroyed during the test or during dismantling of the bundle).

7.5 Chemical Composition of the Melts

The chemical composition of the various melts at different cross-section elevations is listed in Tables 14 and 15 and plotted in Figure 158 as a function of the axial bundle elevation. The results indicate that at the lowest examined cross-section elevation of 206 mm all melts are metallic in nature. The melts consist mainly of stainless steel components with very small amounts of Zr (1 - 2 wt. %) and some Mo (3 - 7 wt. %), which is coming from the thermocouple material; and no U, B, C or O. This is an indication that the melts formed rather early during the high-temperature transient by liquefaction of the absorber assembly and relocation to this bundle elevation. At this early stage of bundle degradation the chemical interactions of the stainless steel melts with other bundle components or the steam environment are very small.

At the higher cross-section elevations, besides the metallic melts, also ceramic $(U, Zr)O_2$ melts of different chemical composition can be recognized. The average Zr content of the mixed oxide decreases from about 55 to 38 wt. % with increasing bundle elevation; the average U concentration increases simultaneously from about 14 to 41 wt. % (Figure 158). The concentration of the stainless steel components in the $(U, Zr)O_2$ mixed oxide varies between 0 and 10 wt %. In some cases also some Mo, W and Nb can be detected (Tables 14, 15). The metallic melts at the higher cross-section elevations 392, 605 and 910 mm are rich in Zr, Mo, U and B and contain various concentrations of stainless steel components and some oxygen. In some metallic melts also W and Nb is present.

It is interesting to note the behavior of C of the B_4C absorber material; it could neither be detected in any once liquid nor in any solid phase. B is concentrated in the metallic melts.

7.6 Summary of the Post-Test SEM/EDX Examination

The post-test examination results show the strong impact of the B_4C absorber assembly and stainless steel grid spacer on the early damage progression of the VVER-1000 fuel rod bundle simulator. The stainless steel of the absorber assembly and/or grid spacer interacts eutectically with the ZrNb1 cladding tubes. This results in liquid phase formation below the melting point of the cladding. In many fuel rods, which showed still an intact cladding tube, a solidified (Zr, Fe, Cr, Ni, O) melt could be detected inbetween the UO_2 pellet and the ZrO_2 layer on the cladding outer surface. This indicates a liquefaction process of the "oxygen-poor" cladding by stainless steel in axial direction over long distances.

During the high-temperature transient the ZrNb1 cladding interacts with UO_2 forming the typical solid state interaction layers [α-Zr(O,U), (U, Zr) alloy, α-Zr(O)]. At temperatures above the melting point of the cladding, extensive fuel dissolution occurred forming larger quantities of α-Zr(O, U) and $(U, Zr)O_2$ reaction products at higher bundle elevations.

The impact of the thermocouple materials and the tungsten heaters on the meltdown behavior of the fuel rod simulator is probably negligible. Damage initiation and damage progression is caused exclusively by the bundle components.

Whereas in other CORA tests with B_4C absorber rods the absorber material relocated completely to the lower bundle elevations in the test CORA-W2 some boron remained within the bundle (fixed in metallic melts). This observation may be important with respect to accident management considerations.

8. References

/1/ S. Hagen, K. Hain, "Out-of-pile Bundle Experiments on Severe Fuel Damage (CORA Program): Objectives, Test Matrix, and Facility Description", KfK 3677 (1986)

/2/ S. Hagen, V. Noack, L. Sepold, P. Hofmann, G. Schanz, G. Schumacher, "Results of SFD Experiment CORA-13 (OECD International Standard Problem 31)", KfK 5054 (1993)

/3/ S. Hagen, P. Hofmann, V. Noack, G. Schanz, G. Schumacher, L. Sepold, "Behavior of a VVER-1000 Fuel Element Tested under Severe Accident Conditions in the CORA Facility (Test and Posttest Results of Experiment CORA-W1)", KfK 5212 (1994)

/4/ G. Schanz, S. Leistikow, "Microstructural Reasons for Mechanical Oxide Degradation (Breakaway Effect) and Resulting Kinetic Anomalies of Zircaloy-4/Steam-HT-Oxidation", Proc. 8th Intern. Congress Metallic Corrosion, Mainz 6. - 11.9.81, Vol. II, p. 1712-1717

9. Acknowledgements

The CORA-VVER program is a joint effort of the Kernforschungszentrum Karlsruhe (KfK) and the Kurchatov Institute Moscow. It is part of a bi-lateral agreement on scientific-technical cooperation between the Russian Federation and the Federal Republic of Germany. For the efforts to realize this cooperation the authors would like to express their thanks to the project managers at the Kurchatov Institute Drs. V. Pavchuk and L. Yegorova.

At the Kernforschungzentrum Karlsruhe a variety of support needed for preparation, conduct, and evaluation of the experiment is gratefully acknowledged:

The fuel elements were designed by Mr. H. Junker. The test rods were assembled by Mr. E. Mackert, the test bundles by Messrs. H. Giesmann and R. Röder. The authors would like to thank Messrs. H. Benz, C. Grehl, and H.J. Röhling for test preparations and conduct.

Mr. K.P. Wallenfels is acknowledged for arrangement of camera and video systems and for the preparation of temperature measurements. Messrs. R. Huber and H. Malauschek prepared and conducted the on-line measurements of the off-gas composition.

The authors would like to thank Mr. L. Anselment for sectioning of the epoxied bundle and for the preparation of the metallographic samples, Mr. H. Metzger for examination of the metallographic samples by optical microscope, and Mr. J. Burbach for the SEM examinations.

10. List of Tables

11. List of Figures

Appendix:

Fig. A23 CORA-W2; Temperatures at fixed elevations, pre-heat phase (-50, -200, -300 mm)

Table 1: CORA Test Matrix

Test No.	Max. Cladding Temperatures	Absorber Material	Other Test Conditions	Date of Test
2	≈ 2000°C	-	UO_2 refer., inconel spacer	Aug. 6, 1987
3	≈ 2400°C	-	UO_2 refer., high temperature	Dec. 3, 1987
5	≈ 2000°C	Ag, In, Cd	PWR-absorber	Febr. 26, 1988
12	≈ 2000°C	Ag, In, Cd	quenching	June 9, 1988
16	≈ 2000°C	B_4C	BWR-absorber	Nov. 24, 1988
15	≈ 2000°C	Ag, In, Cd	rods with internal pressure	March 2, 1989
17	≈ 2000°C	B_4C	quenching	June 29, 1989
9	≈ 2000°C	Ag, In, Cd	10 bar system pressure	Nov. 9, 1989
7	< 2000°C	Ag, In ,Cd	57-rod bundle, slow cooling	Febr. 22, 1990
18	< 2000°C	B_4C	59-rod bundle, slow cooling	June 21, 1990
13	≈ 2200°C	Ag, In, Cd	OECD/ISP; quench initiation at higher temperature	Nov. 15, 1990
29*	≈ 2000°C	Ag, In, Cd	pre-oxidized,	April 11, 1991
31*	≈ 2000°C	B_4C	slow initial heat-up (≈ 0.3 K/s)	July 25, 1991
30*	≈ 2000°C	Ag, In, Cd	slow initial heat-up (≈ 0.2 K/s)	Oct. 30, 1991
28*	≈ 2000°C	B_4C	pre-oxidized	Febr. 25, 1992
10	≈ 2000°C	Ag, In, Cd	cold lower end 2 g/s steam flow rate	July 16, 1992
33	≈ 2000°C	B_4C	dry core conditions, no extra steam input	Oct. 1, 1992
W1	≈ 2000°C	-	VVER-test	Febr. 18, 1993
W2	≈ 2000°C	B_4C	VVER-test with absorber	April 21, 1993

Table 2: Design characteristics of test bundle CORA-W2

Bundle type:		VVER
Bundle size:		19
Number of heated rods:		13
Number of unheated rods:		5
Pitch:		12.75 mm
Cladding outside diameter		9.13 mm
Cladding inside diameter:		7.72 mm
Cladding material:		Zr-1%Nb
Heater:	- material	Tungsten (W)
	- diameter	4 mm
Fuel pellets:	- heated rods	UO_2 annular pellets
	- outer diameter (nominal)	7.57 mm
	- diameter of central void	4.2 mm
	- unheated rods	UO_2 annular pellets
	- diameter of central void	2.4 mm
Pellets stack:	- heated rods	0 to 1000 mm
	- unheated rods	-142/-192 to 1400 mm
U-235 enrichment		0.3 %
Grid spacer	- material	Stainless steel: 1.4541 (06Ch18N10T and 08Ch18N10T)
	- height	20 mm
	- number	3
	- location by elevation of upper edges (from level 0 mm)	-5; 210; 610 mm
Shroud	- material	Zr-1%Nb
	- wall thickness	1.0 mm
	- outer dimension	68 mm
	- length	1195 mm
Absorber rod	- material	B_4C
	- cladding	Stainless steel
	- cladding OD	8.2 mm
	- cladding ID	7.0 mm
Absorber rod guide tube	- material	Stainless steel
	- OD	12.6 mm
	- ID	11.0 mm

Table 3: Thermocouples used in the CORA-VVER TEST CORA-W2 (with absorber rod)

	1. *)	2. *)	3.	4.	5.
Thermo-element wire	WRe 5 % - WRe 20 %	C_r/Al	WRe 5 % - WRe 26 %	WRe 5 % - WRe 26 %	NiCr/Ni Al (Type K)
Insulation	BeO	MgO	HfO_2	HfO_2	Al_2O_3
Cladding	Mo-ZrC-Mo-$MoSi_2$	SS	Niobium + Zry-4	Niobium	Stainless steel
Outer Diameter [mm]	2.3	1.1/0.8	2.3	1.5	1.0
Positions for measurements	In the center and outer surface of unheated rods	Between the cladding of the absorber rod and the guide tube	At the outer surface of heated rods, of the shroud and of the shroud insulation	At the grid spacer	At the lower part of heated rods, of grid spacer, of the shroud and insulation, for gas temperature, temperature of the bundle flange and of the steam entrance

*) Russian design

Table 4: CORA-W2; Positions of thermocouples of test bundle CORA-W2

Positions of thermocouples in unheated rods (CORA -W 2)

Slot Number	Elevation [mm]	Rod Number
105	1150	2.2
104	1050	2.4
102	950	3.o
103	850	2.6
101	750	2.o
222	650	3.o
223	550	2.6
221	450	2.o
225	350	2.2
224	250	2.4

Positions of thermocouples at unheated rods (CORA-W 2)

Slot Number	Elevation [mm]	Rod Number
110	1147	2.2
109	1050	2.4
107	950	3.o
108	821	2.6
106	850	2.o
228	750	3.o
244	750	2.2
242	650	2.4
229	646	3.o
226	550	2.o
230	531	2.6
227	450	2.o
241	421	2.6
245	350	2.2
243	250	2.4

Positions of thermocouples at absorber rod (CORA-W2)

Slot Number	Elevation [mm]	Rod Number
231	800	2.8
232	600	2.8
233	200	2.8

Positions of thermocouples at guide tube of absorber rod

Slot Number	Elevation [mm]	Rod Number
131	1250	2.8
111	1031	2.8
246	791	2.8
247	599	2.8

Positions of thermocouples at guide tube of absorber rod

Slot Number	Elevation [mm]	Rod Number
248	386	2.8
249	181	2.8

Positions of thermocouples at heated rods (CORA-W2)

Slot Number	Elevation [mm]	Rod Number
132	1450	3.1
133	1350	4.3
112	1250	3.3
113	1150	4.5
114	1050	3.7
115	950	1.1
116	950	5.1
117	850	4.1
118	750	5.3
250	650	3.3
251	550	1.1
252	550	4.1
253	450	4.9
254	350	3.1
255	250	4.3
256	150	4.7
234	50	3.7
235	-50	4.5

Positions of thermocouples at grid spacer (CORA-W2)

Slot Number	Elevation [mm]	Direction of TE
257	600	60°
258	600	240°
259	200	60°
260	200	240°
261	-15	60°
262	-15	240°

Positions of thermocouples for gas (CORA-W2)

Slot Number	Elevation [mm]	Direction of TE
119	1350	0°
120	1250	210°
121	1150	150°
134	1491	120°
135	1451	180°

Positions of thermocouples at shroud outer surface (W2)

Slot Number	Elevation [mm]	Direction of TE
122	1150	300°
123	1050	240°
124	950	120°
125	850	180°
126	750	60°
211	650	180°
212	550	0°
213	450	240°
214	350	60°
215	250	0°
216	150	300°
236	50	120°

Positions of thermocouples at shroud insulation(CORA-W 2)

Slot Number	Elevation [mm]	Direction of TE
217	650	240°
218	550	240°
237	450	240°
238	350	300°
239	250	300°
263	150	300°
264	50	300°
265	950	0°
266	850	0°
267	750	0°

Positions of thermocouples steam distribution tube(C-W2)

Slot Number	Elevation [mm]	Direction of TE
268	0	180°
269	0	180°
270	-50	15°
271	-50	195°
272	-50	165°
273	-50	345°
274	50	300°
275	-250	300°
62	-300	180°

Table 5: CORA-W2; Positions of thermocouples in the high-temperature shield

ANGLE ∠		30°	55°	75°	120°	145°	165°	210°	235°	255°	300°	345°				
RADIUS	(mm)	153	153	153	153	153	153	153	153	153	153	153	172	192	255	293
	1250											**174** *33Ni*				
	1150											**175** *56Ni*				
	1050											**176** *55Ni*				
	950		**162** *54Ni*			**166** *53Ni*			**170** *52Ni*			**177** *51Ni*	**188** *29Ni*	**191** *30Ni*	**194** *38Ni*	**197** *39Ni*
	850											**178** *24Ni*				
	750											**179** *23Ni*				
	650											**180** *22Ni*				
	550	**slot161** *19Ni*		**163** *18Ni*	**165** *17Ni*		**167** *16Ni*	**169** *15Ni*		**171** *14Ni*	**173** *13Ni*	**181** *12Ni*	**189** *20Ni*	**192** *21Ni*	**195** *36Ni*	**198** *37Ni*
	450											**182** *11Ni*				
	350											**183** *10Ni*				
	250											**184** *9Ni*				
	150											**185** *8Ni*				
	50			**164** *5Ni*			**168** *4Ni*			**172** *3Ni*		**186** *2Ni*	**190** *6Ni*	**193** *7Ni*	**196** *34Ni*	**199** *35Ni*
	-50											**187** *1Ni*				

Table 6: Sequence of events in test CORA-W2

- 10 500 s	Start of the argon injection of 3 g/s into the bundle (F408)
- 8 400 s	Argon injection increased to 8 g/s
- 8 400 s	Begin ot the argon injection (F402) for videoscopes and bundle head plate with 4 g/s
- 6 300 s	Argon injection into the bundle (F408) increased to 10 g/s
- 1 800 s	Argon injection in the bundle reduced to 8 g/s
- 300 s	Total argon injection (F402) 6 g/s: 0.62 g/s for videoscopes and 5.38 g/s for the bundle head plate
0 s	Start of the bundle heating (0.52 KW)
2 700 s	Argon injection in the bundle reduced to 6 g/s
3 000 s	Start of the transient with a linear electric power input rate (Initial value 1.6 kW, Final value 14.3 KW)
3 300 s	Begin of the steam injection: 4 g/s
4 100 s	Begin of the temperature escalation
4 500 s	Electric power reduced to 0.52 KW
4 700 s	Heating of evaporator and superheater turned off

Table 7: Temperatures [°C] of test CORA-W2 for different components at 0 seconds

	Components						
Elevation [mm]	**Heated rod**	**Unheated rod**		**Guide tube**	**Shroud**	**Shroud insulation**	**HTS 153 mm**
		Central position	**Outer surface**				
1450	41						
1350	58						
1250	176			118			91
1150	289	345			233		101
1147			326				
1050	347	371	362		312		101
1031							
950	370	378	371		325	151	99
850	383	389	380		332	155	95
821			384				
791				390			
750	383	(370)	390		333	146	93
650	394	409	399		349	159	92
646			396				
599				399			
550	405	415	404		345	172	91
531			403				
450	399	422	408		359	166	89
421			406				
386				406			
350	410	433	416		362	132	85
250	410	443	422		363	167	78
181				411			
150	402				368	165	82
50	436				384	240	82
-50	295						75

Table 8: Temperatures [°C] of test CORA-W2 for different components at 3000 seconds

	Components						
Elevation [mm]	Heated rod	Unheated rod		Guide tube	Shroud	Shroud insulation	HTS 153 mm
		Central position	Outer surface				
1450	42						
1350	58						
1250	185			121			93
1150	335	394			263		110
1147			368				
1050	418	439	427		369		110
1031							
950	466	463	456		390	166	107
850	461	469	(727)		395	171	102
821			465				
791				467			
750	467	(341)	467		397	159	101
650	472	483	466		407	170	98
646			467				
599				465			
550	475	476	469		396	186	97
531			462				
450	463	478	468		404	177	93
421			458				
386				460			
350	467	484	466		406	140	89
250	443	473	462		393	176	80
181				445			
150	434				384	170	85
50	445				384	235	86
-50	305						77

Table 9: Samples taken from the tested bundle CORA-W2 prior to encapsulation

Sample No.	Elevation	Remarks
W2-101	Below the bottom of the bundle	1 lump of melt [a]; for chemical analysis
W2-102	Below the bottom of the bundle	Several spheres of melt[a], approx. 2 - 4 mm diameter; for chemical analysis
W2-103	Below the bottom of the bundle	Several spheres of melt[a], approx. 2 - 4 mm diameter; for investigation with the optical microscope

a Melt probably mainly contains boron carbide (B_4C)/steel

Table 10: Chemical analysis of samples taken from the bottom of bundle CORA-W2

Element	W2-101 [%]	W2-102 [%]
Fe	71,3	68,2
Cr	14,2	13,1
Ni	11,4	10,7
B	1,1	2,3
Ag	< 0,1	< 0,1
Cd	< 0,1	< 0,1
In	< 0,1	< 0,1
U	< 0,1	< 0,1
Zr	< 0,1	0,1
Sn	< 0,1	< 0,1
Ca	0,2	< 0,1
Mg	< 0,1	< 0,1
Cu	0,1	< 0,1
Zn	< 0,1	< 0,1
Mo	0,5	2,9
W	< 0,1	< 0,1
pH	-	-
Leitf.	-	-

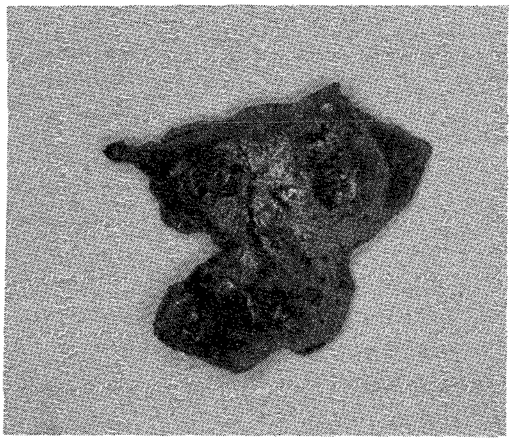

W2-101

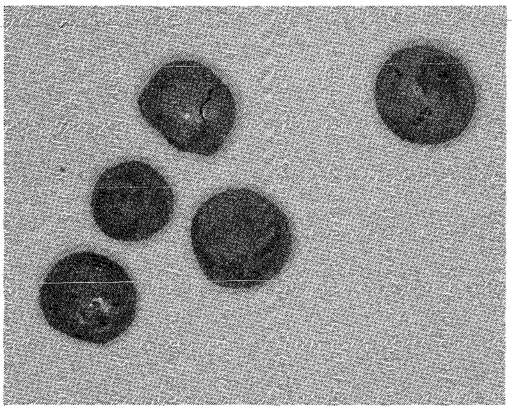

W2-102

Table 11: Cross sections of test bundle CORA-W2

Sample	Sample length	Axial position bottom	Axial position top	Remarks
W2-a	xxx mm	-xxx mm	-15 mm	Remnant
Cut	2 mm			Lower grid spacer
W2-b	100 mm	-13 mm	87 mm	
Cut	2 mm			
W2-c	50 mm	89 mm	139 mm	
Cut	2 mm			
W2-01	13 mm	141 mm	154 mm	Cross section
Cut	2 mm			
W2-d	50 mm	156 mm	206 mm	Additional longitudinal cut
Cut	2 mm			Central grid spacer
W2-02	13 mm	208 mm	221 mm	Cross section
Cut	2 mm			
W2-e	50 mm	223 mm	273 mm	Additional longitudinal cut
Cut	2 mm			
W2-f	50 mm	275 mm	325 mm	Additional longitudinal cut
Cut	2 mm			
W2-03	13 mm	327 mm	340 mm	Cross section
Cut	2 mm			
W2-g	50 mm	342 mm	392 mm	
Cut	2 mm			
W2-h	50 mm	394 mm	444 mm	
Cut	2 mm			
W2-i	50 mm	446 mm	496 mm	
Cut	2 mm			
W2-04	13 mm	498 mm	511 mm	Cross section
Cut	2 mm			

W2-j	50 mm	513 mm	563 mm	
Cut	2 mm			
W2-k	40 mm	565 mm	605 mm	
Cut	2 mm			Upper grid spacer
W2-05	13 mm	607 mm	620 mm	Cross section
Cut	2 mm			
W2-l	50 mm	622 mm	672 mm	
Cut	2 mm			
W2-m	50 mm	674 mm	724 mm	
Cut	2 mm			
W2-06	13 mm	726 mm	739 mm	Cross section
Cut	2 mm			
W2-n	50 mm	741 mm	791 mm	
Cut	2 mm			
W2-o	50 mm	793 mm	843 mm	
Cut	2 mm			
W2-07	13 mm	845 mm	858 mm	Cross section
Cut	2 mm			
W2-p	50 mm	860 mm	910 mm	
Cut	2 mm			
W2-q	50 mm	912 mm	962 mm	
Cut	2 mm			
W2-08	13 mm	964 mm	977 mm	Cross section
Cut	2 mm			
W2-r	50 mm	979 mm	1029 mm	
Cut	2 mm			
W2-s	50 mm	1031 mm	1081 mm	

Cut	2 mm			
W2-09	13 mm	1083 mm	1096 mm	Cross section
Cut	2 mm			
W2-t	50 mm	1098 mm	1148 mm	
Cut	2 mm			
W2-u	xxx mm	1150 mm	xxxx mm	Remnant

Table 12: CORA-W2; Polished samples

- W2-01 bottom 141 mm → Moscow
- W2-02 bottom 208 mm → Moscow
- W2-03 bottom 327 mm → Moscow
- W2-04 bottom 498 mm → Moscow
- W2-05 bottom 607 mm → Moscow
- W2-06 bottom 726 mm → Moscow
- W2-07 bottom 845 mm → Moscow
- W2-08 bottom 964 mm → Moscow
- W2-09 bottom 1083 mm → Moscow

- W2-d top 206 mm (to be compared with W2-02 bottom) → KfK
- W2-g top 392 mm → KfK
- W2-k top 605 mm (to be compared with W2-05 bottom) → KfK
- W2-p top 910 mm → KfK

Table 13: Procedure of the preparation of the samples for the metallographic examination

	Horizontal grinding	Grinding	Lapping	Polishing		
Abrasive	Corrundum disc 120 µm Diamond disc 64 µm	Diamond disc 20 µm	Petrodisc-M or DP Net*)	PAW cloth	PAN-W	NAP cloth
Particle size			Diamond spray 6 µm	6 µm	3 µm	1 µm
Lubricant	Water	Water	W. lubric. **)	W. lub.	W. lub.	W. lub.
Revolutions of disc	300 rpm	300 rpm	150 rpm (Net) or 300 rpm (Petrod.)	150 U/min	150 U/min	150 U/min
Pressure	200-400 N	200-300 N	200 N	100 N	100 N	100 N
Time	to level	25 min	30 min	30 min	60 min	60 min

*) Petrodisc-M and DP Net are registered trade marks of Struers company

**) "White lubricant" of Struers; liquid on an oil/alcohol/glycerin basis

Table 14: Range of chemical composition of various types of melts at different cross-section elevations of the VVER-1000 bundle CORA-W2

Cross-section elevation	Type of melt	Range of chemical composition of the examined melts, wt.%										
		Fe	Cr	Ni	Zr	U	O	B	C	Mo	W	Nb
CORA-W2-d; 206 mm	metallic	67 - 69	14 - 17	11	1 - 2	-	-	-	-	3 - 7	-	-
CORA-W2-g; 392 mm	metallic	6 - 8	2	0 - 2	20 - 69	7 - 29	2 - 5	5 - 11	-	10 - 23	-	-
	ceramic*	1 - 6	0 - 2	-	49 - 60	10 - 21	15 - 29	-	-	0 - 5	-	4 - 13
CORA-W2-k; 605 mm	metallic	10 - 19	6 - 9	2 - 3	9 - 41	2 - 13	0 - 7	-	-	3 - 39	5 - 18	4 - 7
	ceramic*	1 - 10	1 - 4	1 - 2	38 - 62	13 - 39	12 - 24	-	-	0 - 3	5 - 6	-
CORA-W2-p; 910 mm	metallic*	4 - 17	1 - 4	1 - 3	33 - 59	2 - 19	0 - 9	8 - 14	-	2 - 21	0 - 2	-
	ceramic	-	-	-	34 - 42	39 - 44	19 - 22	-	-	-	-	-

*) chemical nature of the majority of examined melts at this cross-section elevation

Table 15a: Average chemical composition of various types of melts at different cross-section elevations of the VVER-1000 bundle CORA-W2

Element; wt . %	Cross-Section Elevation															
	CORA-W2-d; 206 mm			CORA-W2g; 392 mm							CORA-W2-k 605 mm					
Fe	67	69	67	3	6	8	2	3	6	1	19	17	10	13	10	1
Cr	17	16	14	1	2	2	-	1	2	-	9	9	4	6	4	-
Ni	11	11	11	-	-	2	-	-	-	-	3	3	1	2	1	-
Zr	2	1	1	60	69	20	56	58	49	53	41	38	46	34	38	45
U	-	-	-	13	7	29	21	14	10	14	13	10	19	21	26	33
O	-	-	-	19	2	5	21	17	15	29	-	-	12	9	13	20
B	-	-	-	-	5	11	-	-	-	-	-	-	-	-	-	-
C	-	-	-	-	-	-	-	-	-	-	-	-	-	-	-	-
Mo	3	3	7	4	10	23	-	4	5	3	5	14	3	3	2	-
W	-	-	-	-	-	-	-	-	-	-	11	5	5	4	6	-
Nb	-	-	-	-	-	-	-	4	13	-	-	4	-	-	-	

Table 15b: Average chemical composition of various types of melts at different cross-section elevations of the VVER-1000 bundle CORA-W2

Element; wt . %	Cross-Section Elevation																
	CORA-W2-k 605 mm									CORA-W2-p; 910 mm							
Fe	-	11	8	-	10	-	3	10	-	14	11	17	11	15	4	-	-
Cr	-	6	2	-	3	-	1	6	-	3	3	4	3	3	1	-	-
Ni	-	2	2	-	2	-	1	2	-	3	2	3	2	3	1	-	-
Zr	47	10	51	43	53	62	45	9	39	42	50	33	41	46	59	42	34
U	34	2	20	37	15	13	32	2	39	2	19	19	12	8	9	39	44
O	20	7	17	20	18	24	19	6	22	-	-	7	3	-	9	19	22
B	-	-	-	-	-	-	-	-	-	13	14	14	11	14	8	-	-
C	-	-	-	-	-	-	-	-	-	-	-	-	-	-	-	-	-
Mo	-	39	-	-	-	-	-	39	-	21	2	3	15	11	10	-	-
W	-	17	-	-	-	-	-	18	-	2	-	-	2	-	-	-	-
Nb	-	6	-	-	-	-	-	7	-	-	-	-	-	-	-	-	-

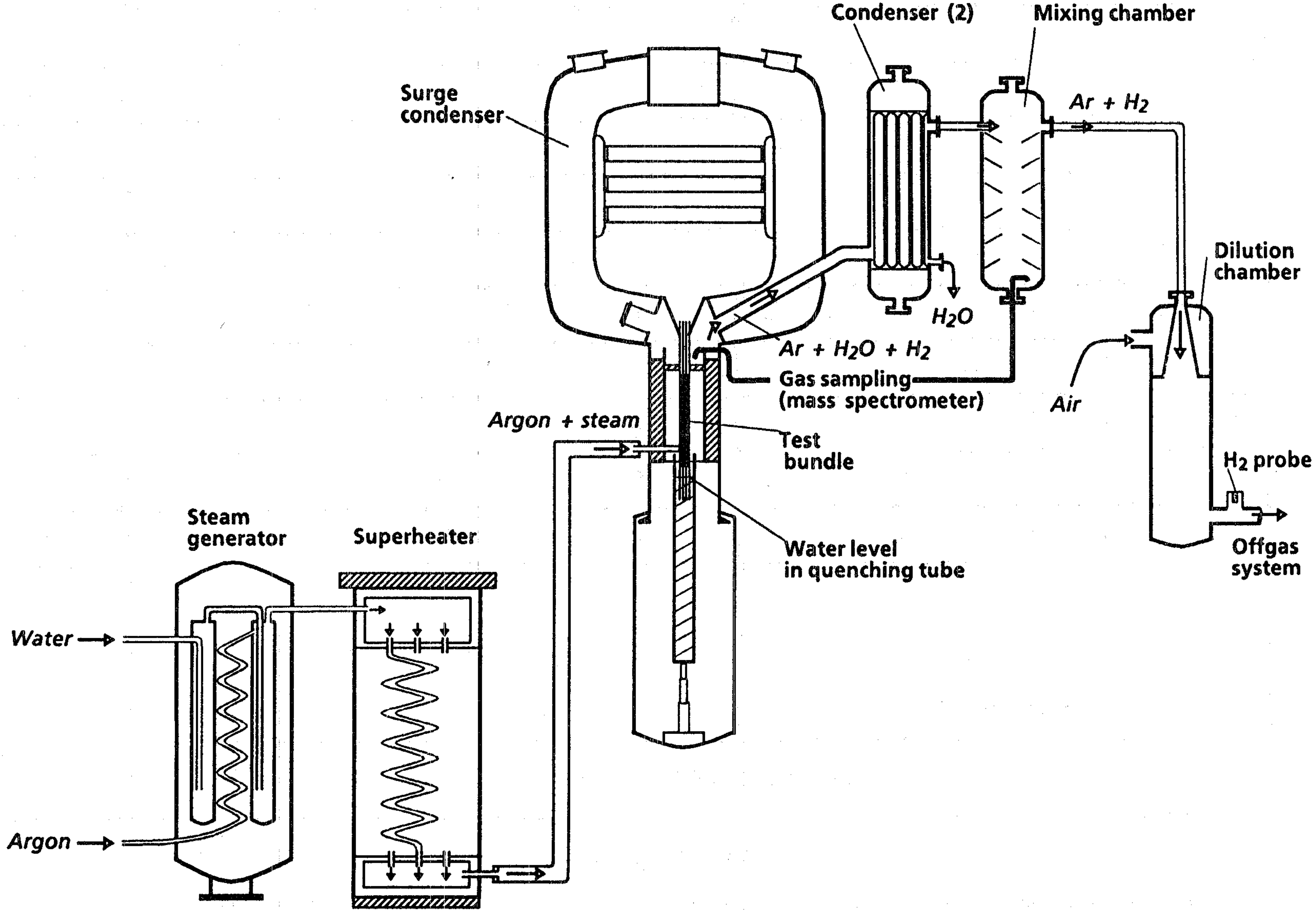

Fig. 1: SFD Test Facility (Simplified flow diagram)

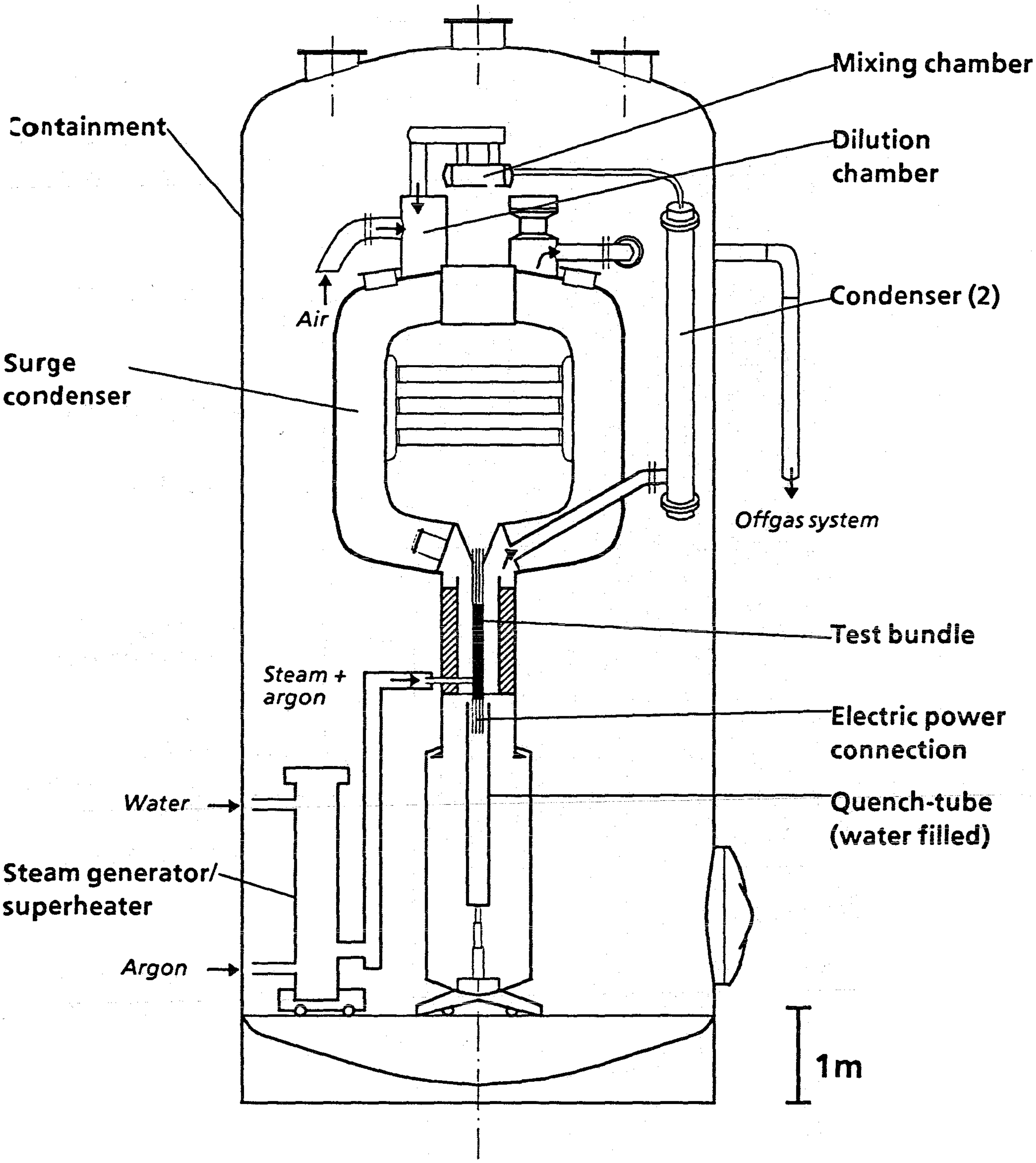

Fig. 2: SFD Test Facility CORA (Main components)

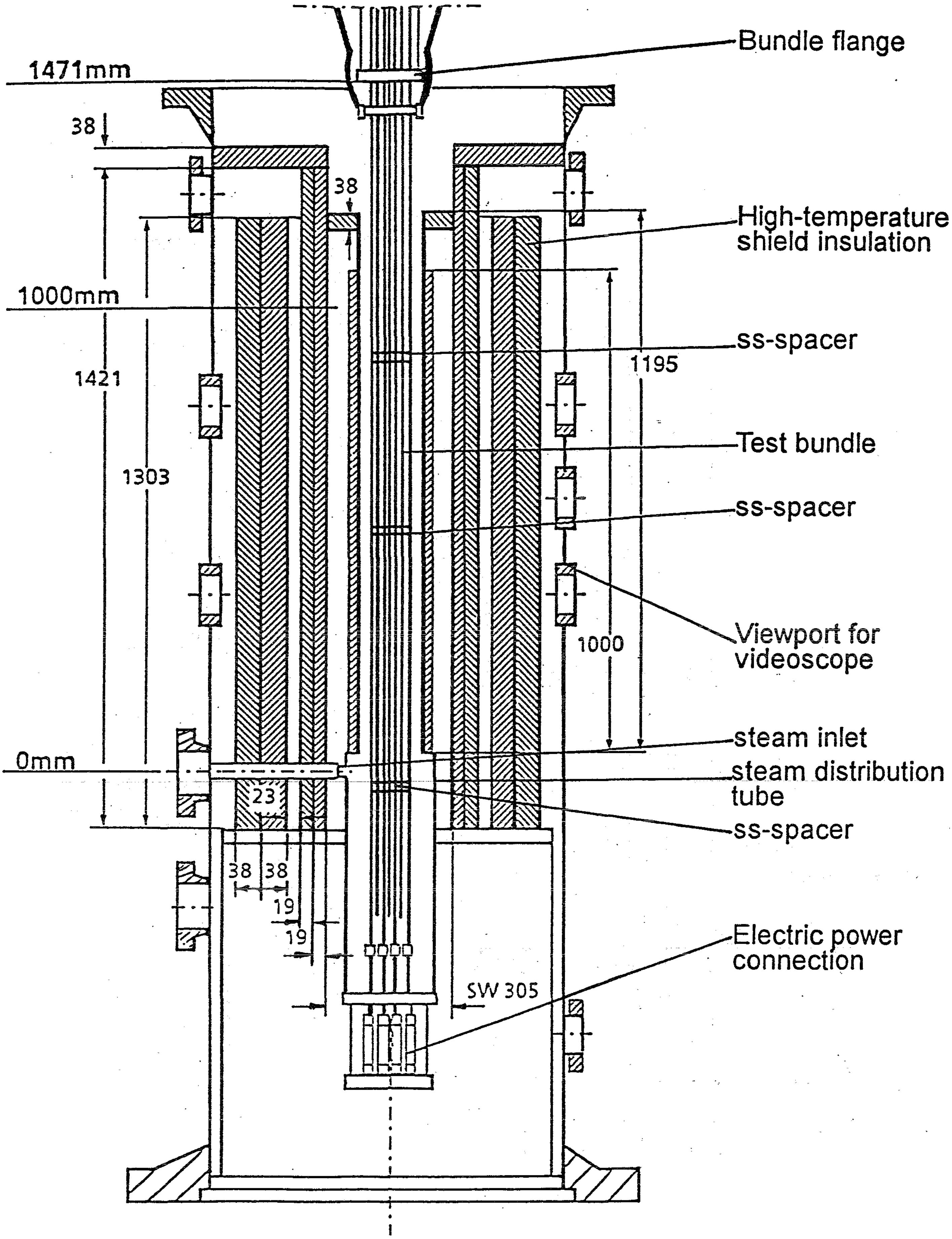

Fig. 3: CORA bundle arrangement

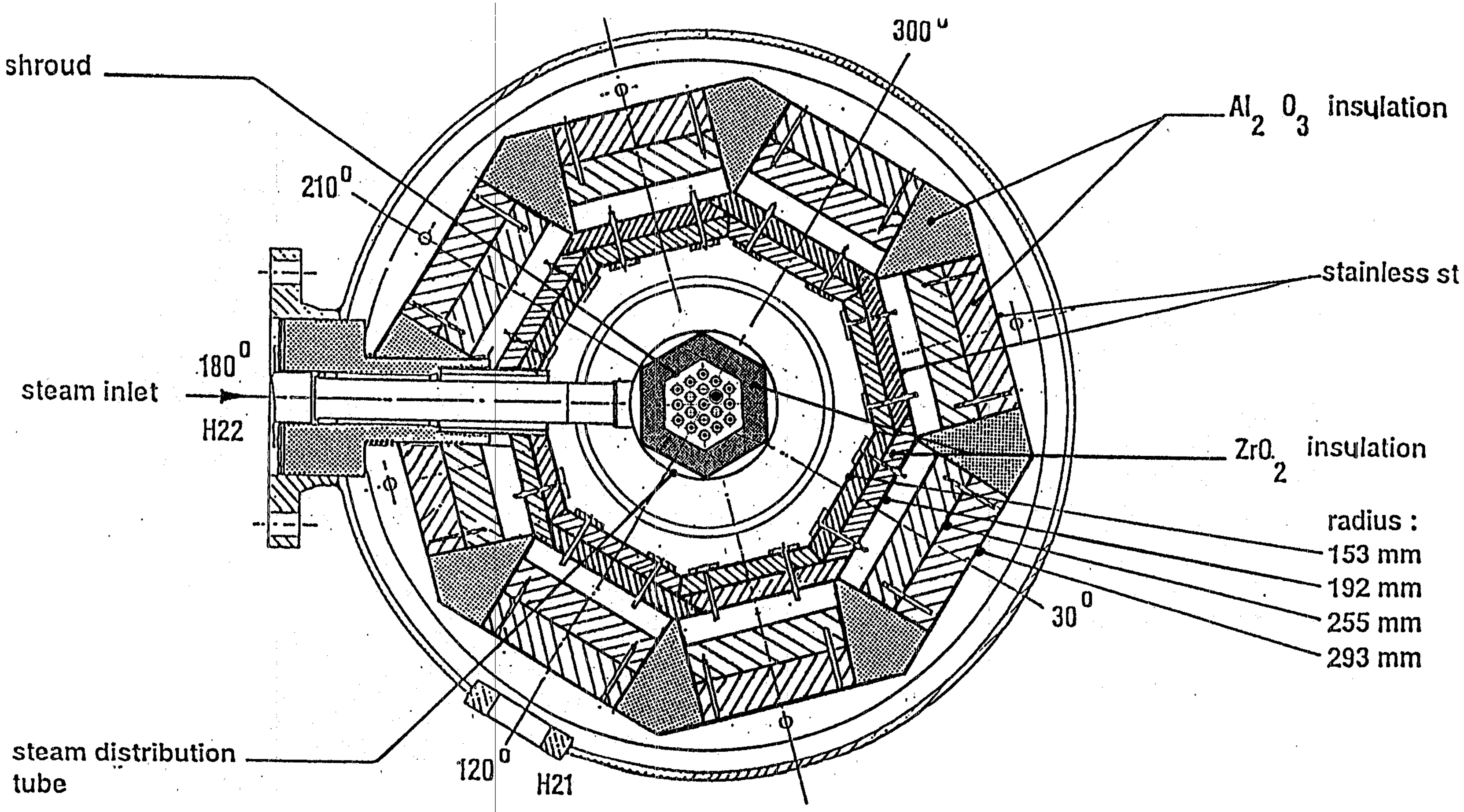

Fig. 4: Horizontal cross section of the high temperature shield

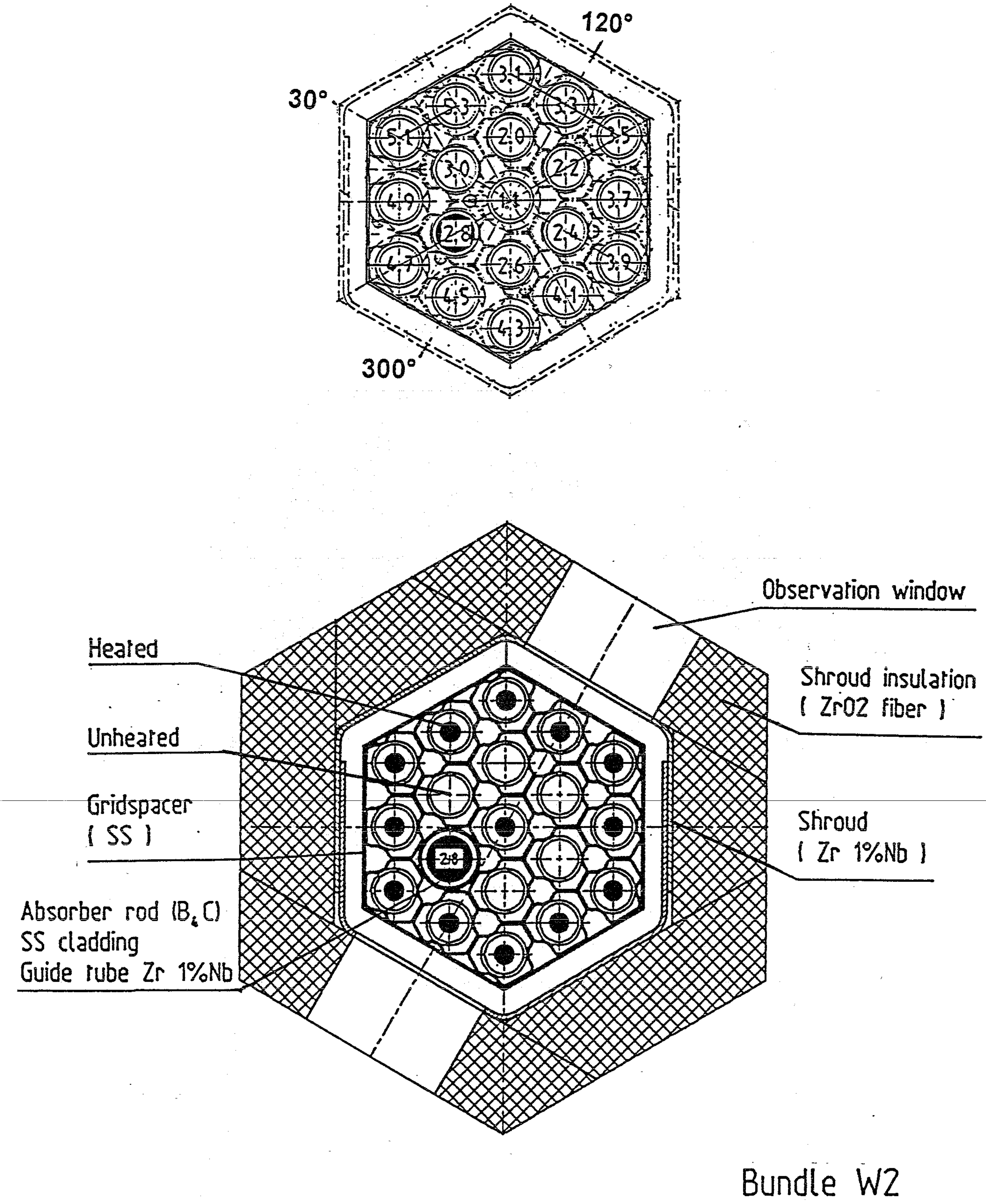

Fig. 5: Rod arrangement and test rod designation of bundle CORA-W2

Shroud

Length = 1195 mm

Thickness = 1 mm

Material = 2 pieces : 140 mm x 1195 mm

2 windows at 120°/800 mm and 900 mm elevation

Window size: 30 mm x 30 mm

Spacer

Length = 20 mm

Thickness = 0.5 mm

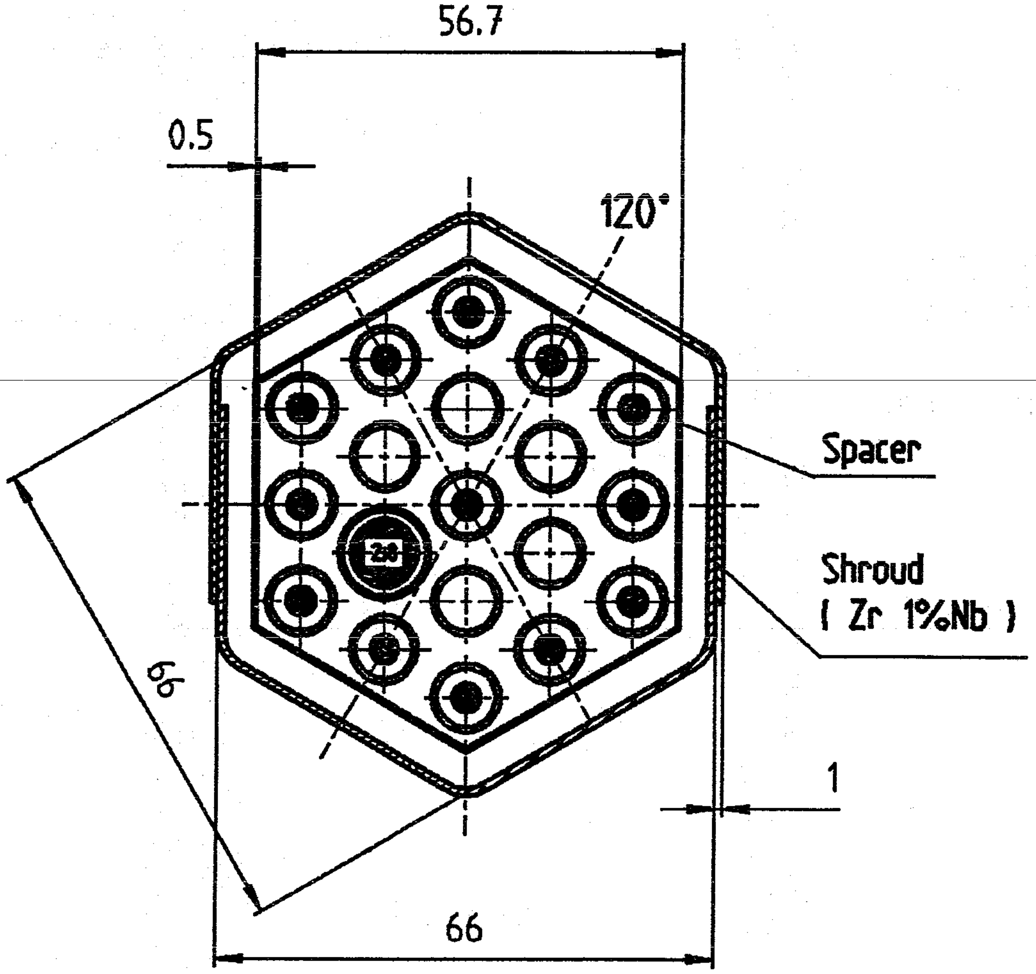

Fig. 5a: Dimensions of test bundle CORA-W2

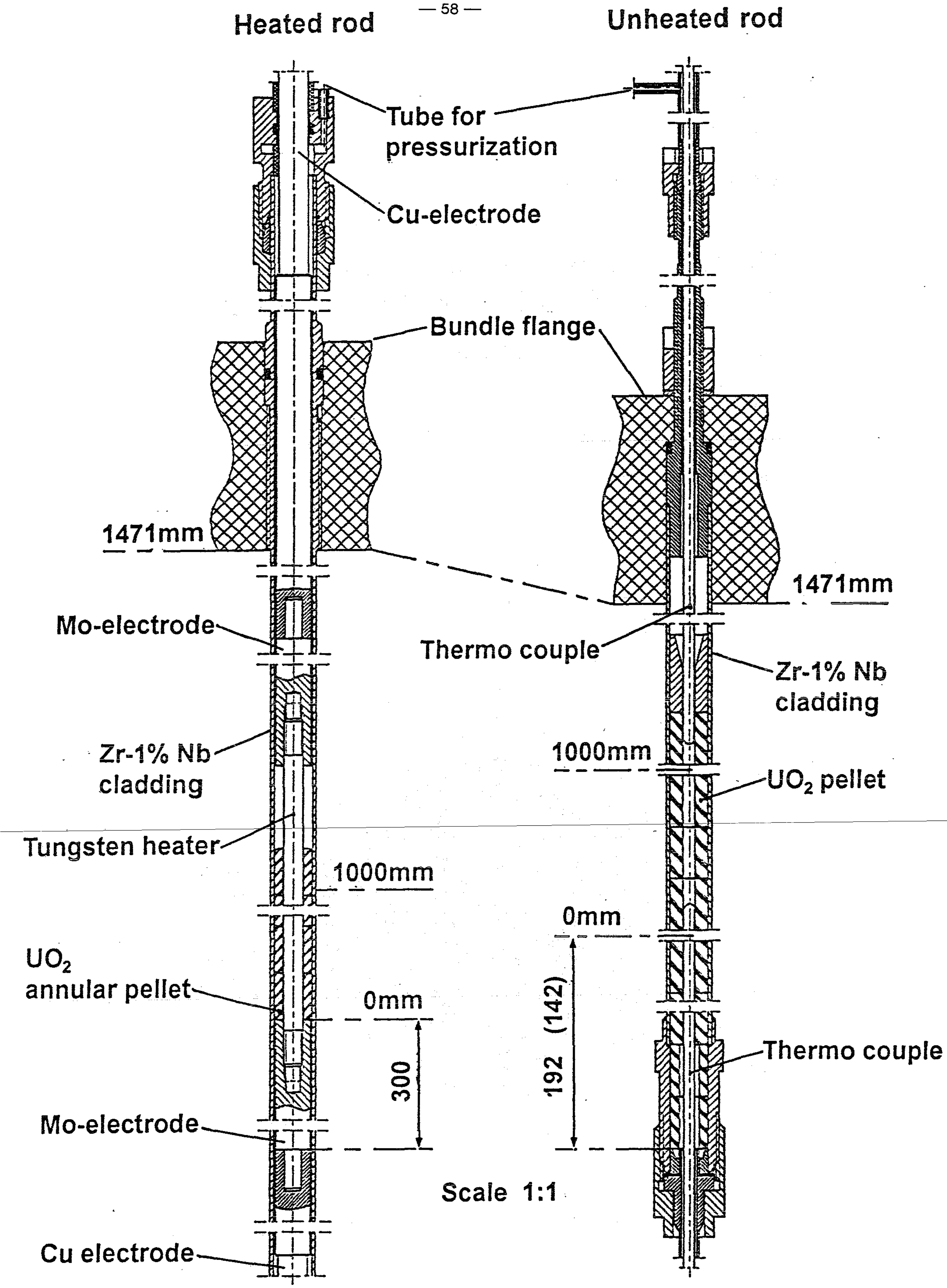

Fig. 6: Rod types used in the CORA / VVER experiments

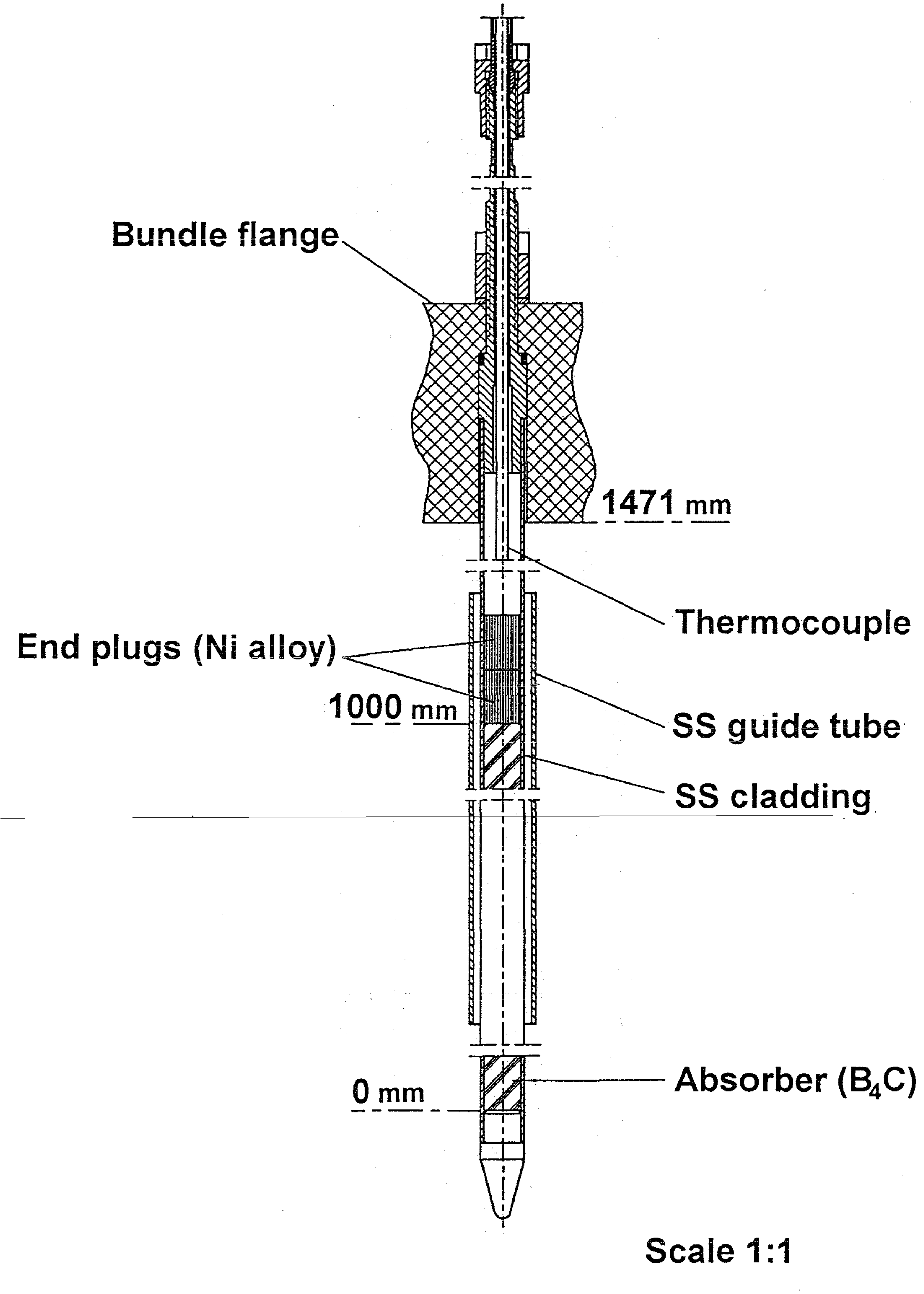

Fig. 7: CORA-W2; Absorber rod design

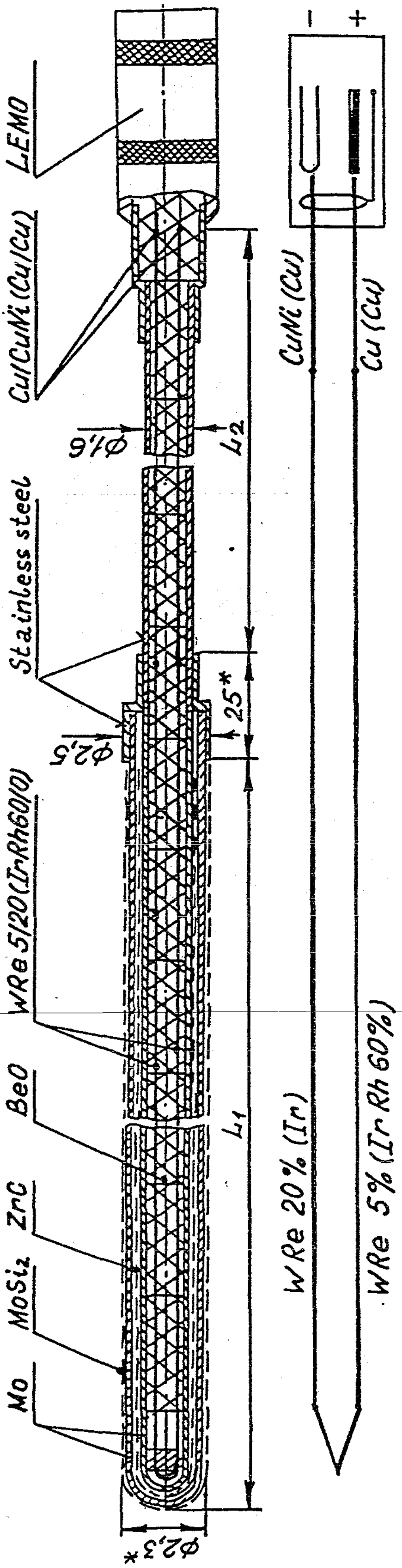

Fig. 8: The high-temperature thermoelectric transducer (HTT) of Russian design

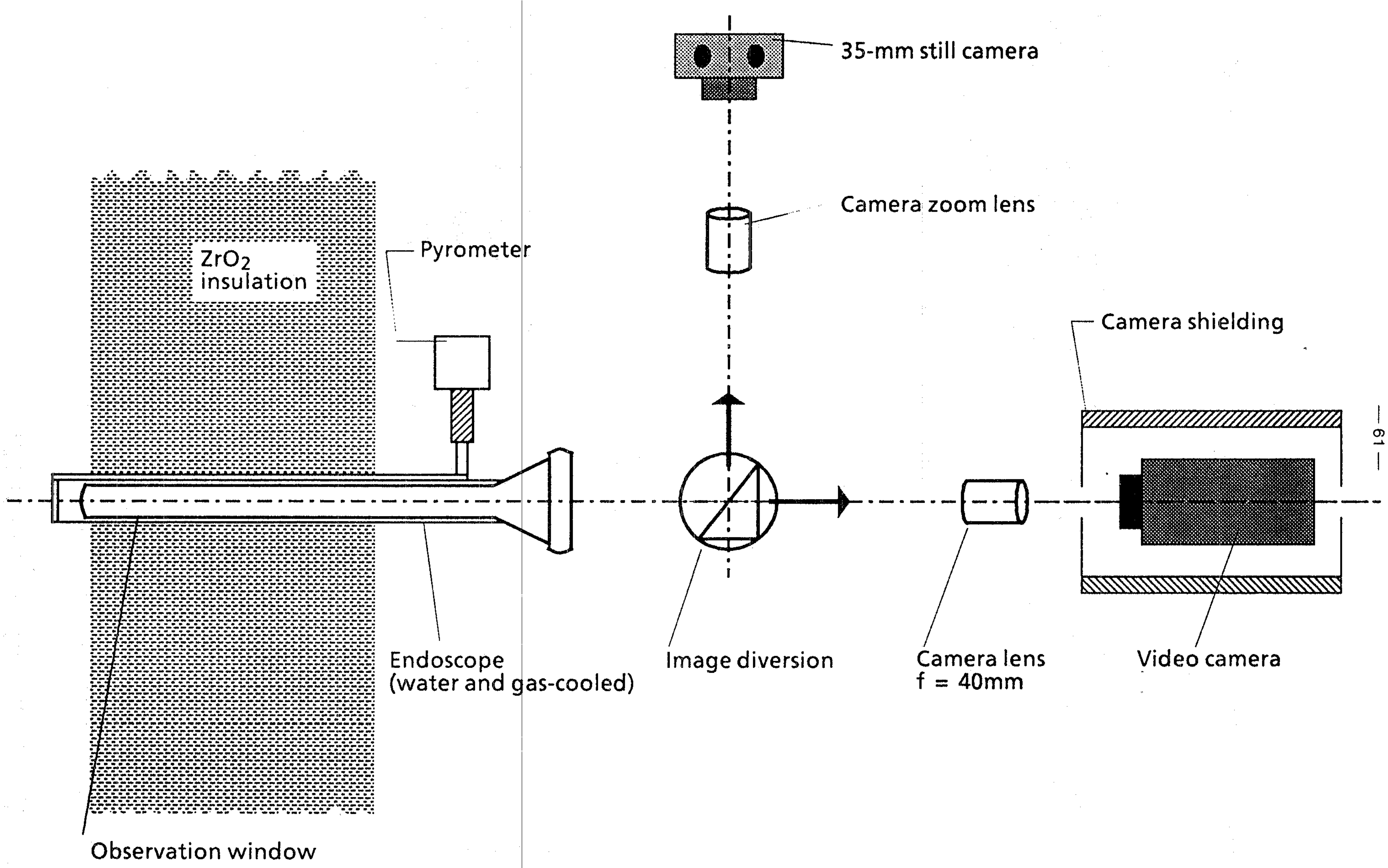

Fig. 9: Videoscope system for the CORA test bundle

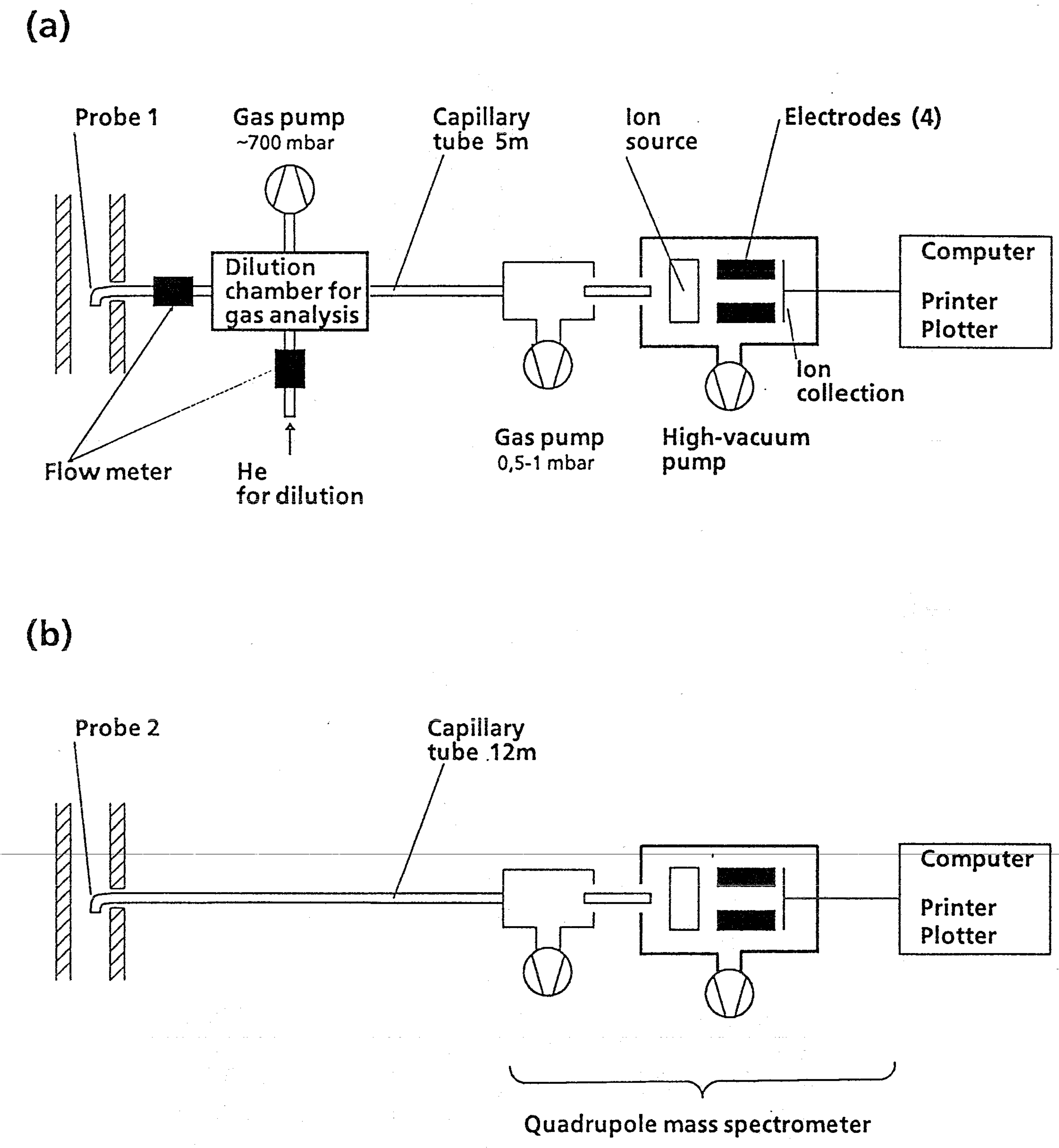

Location (a) : Outlet of test section

Location (b) : Mixing chamber

Fig. 10: Hydrogen measurement

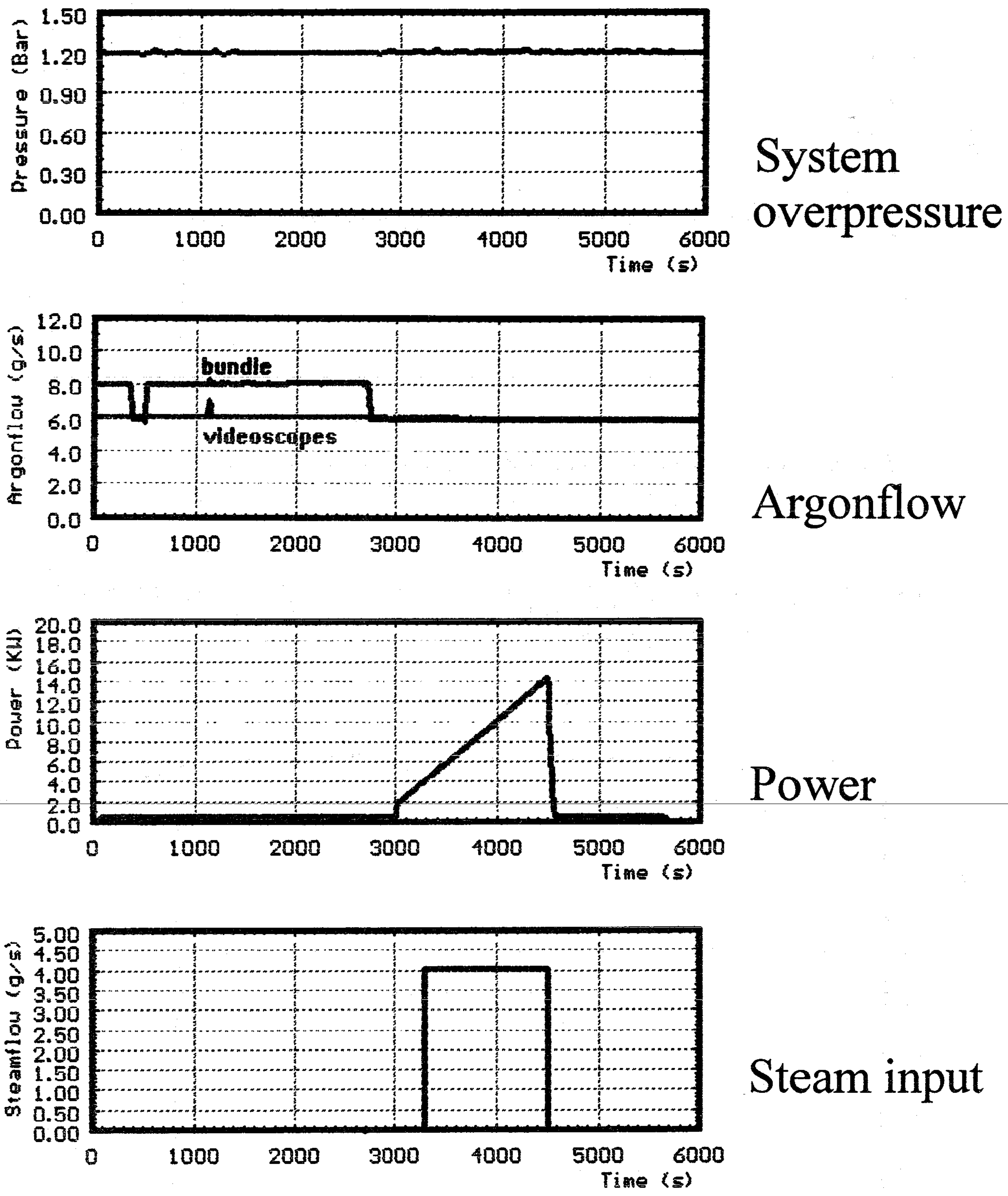

Fig. 11: CORA-W2; System pressure, argon flow, steam input and power

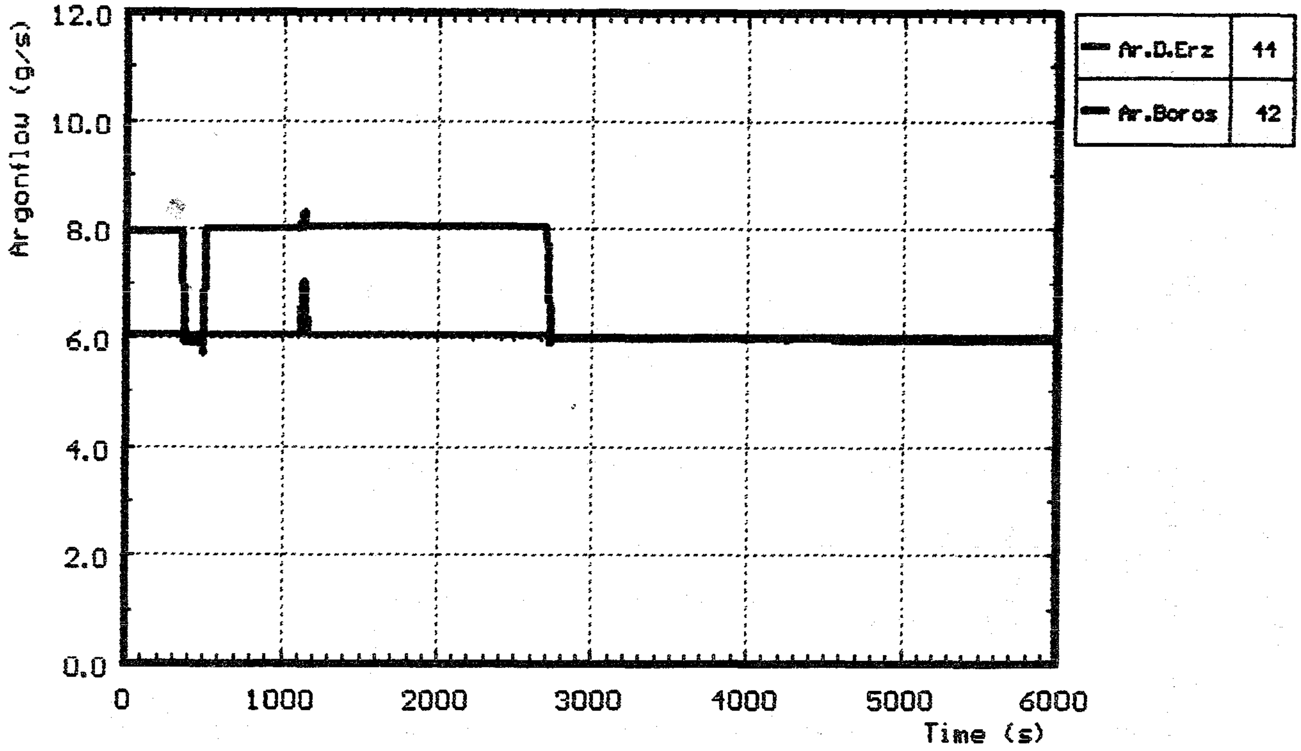

Fig. 12: CORA-W2; Argon flow through bundle and videoscopes

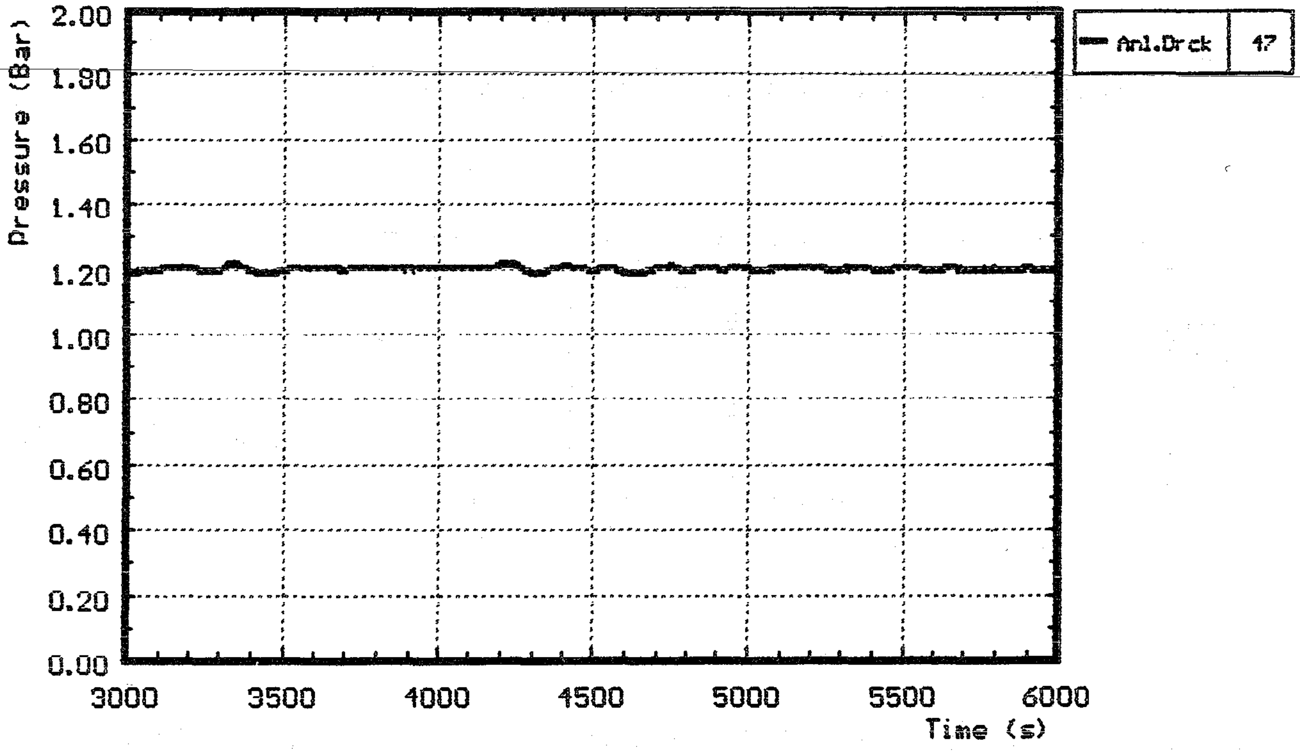

Fig. 13: CORA-W2; System pressure (gauge)

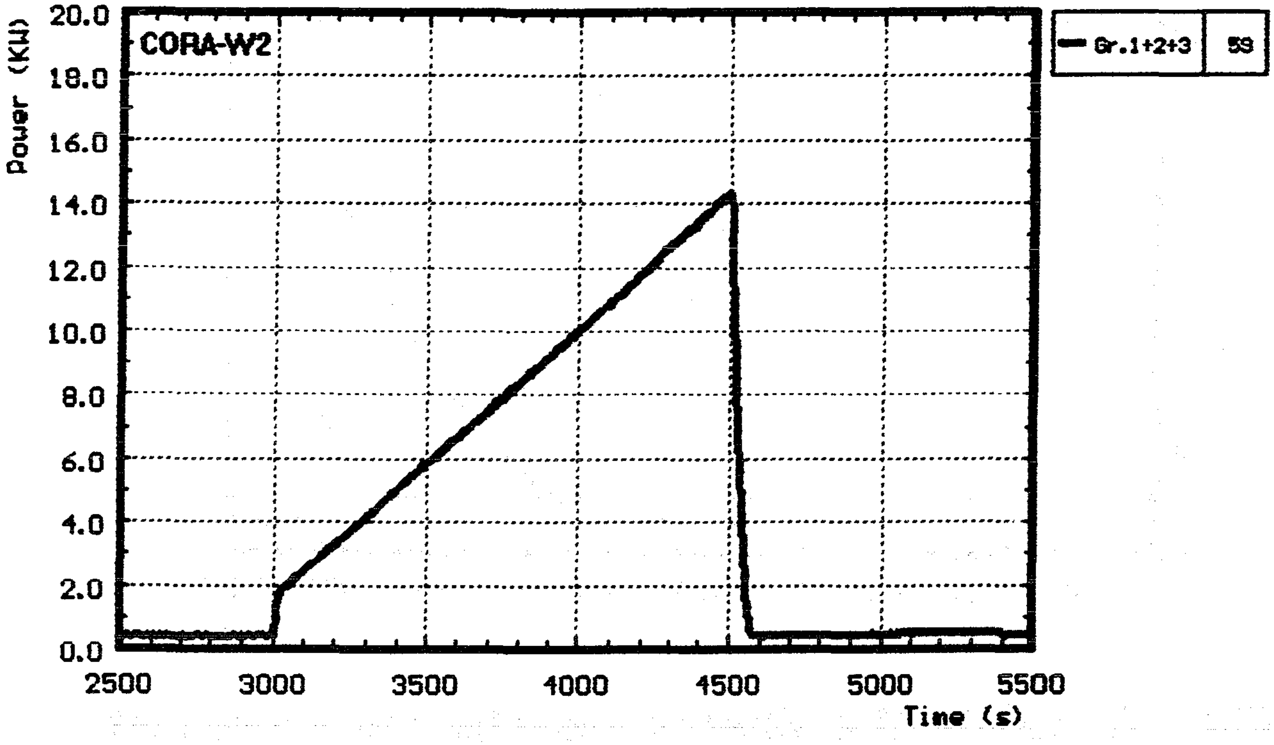

Fig. 14: CORA-W2; Total electric power input

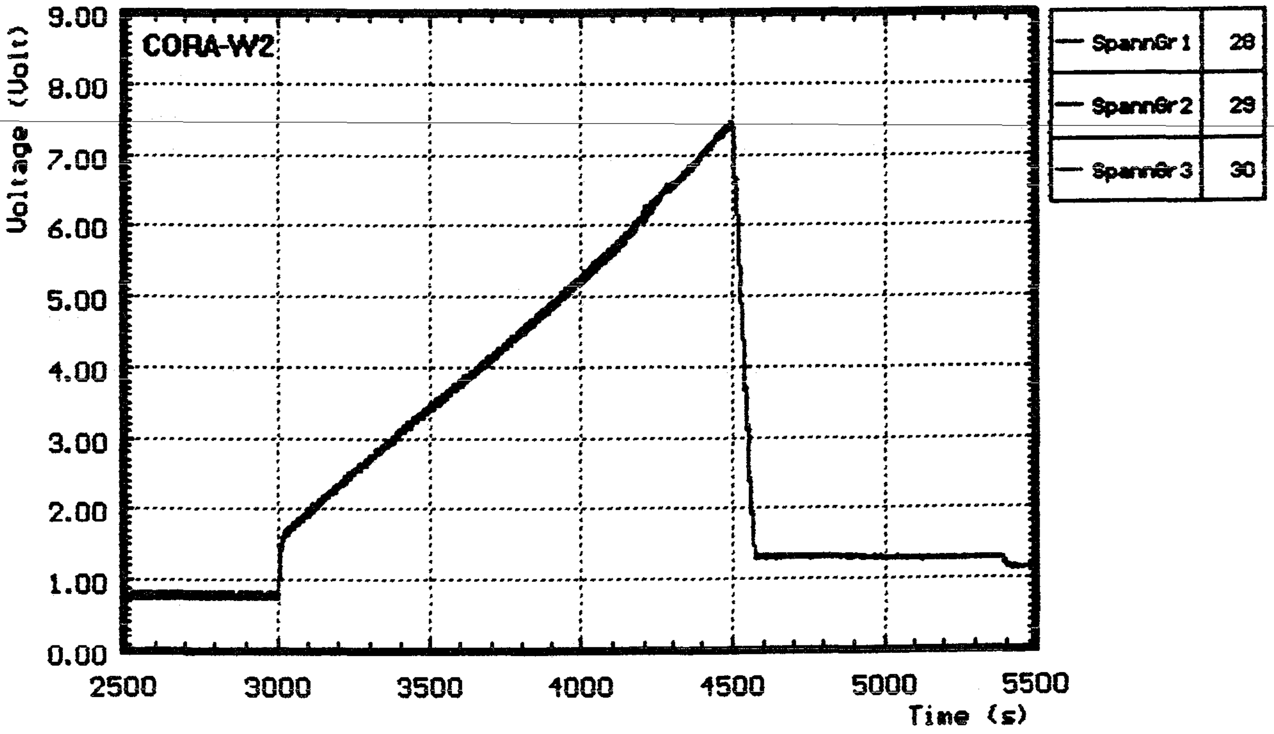

Fig. 15: CORA-W2; Voltage input for the 3 rod groups

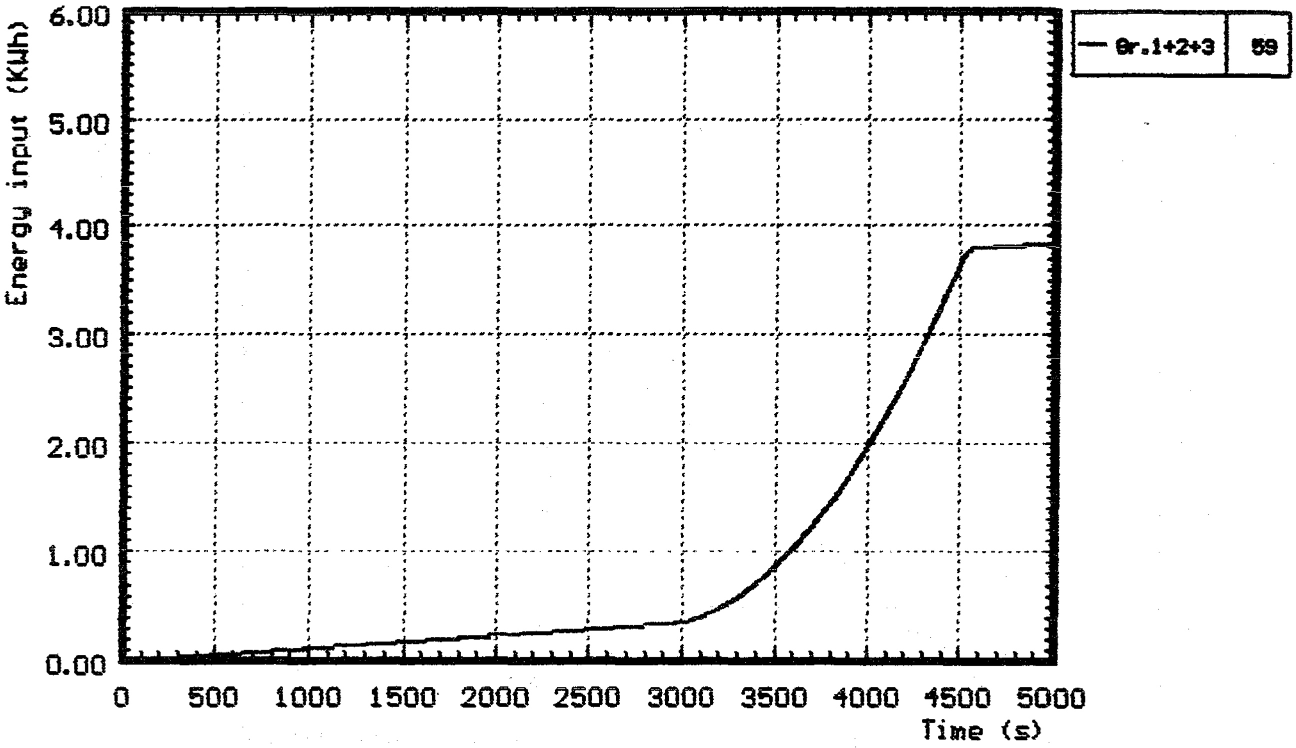

Fig. 17: CORA-W2; Energy input for the entire test time

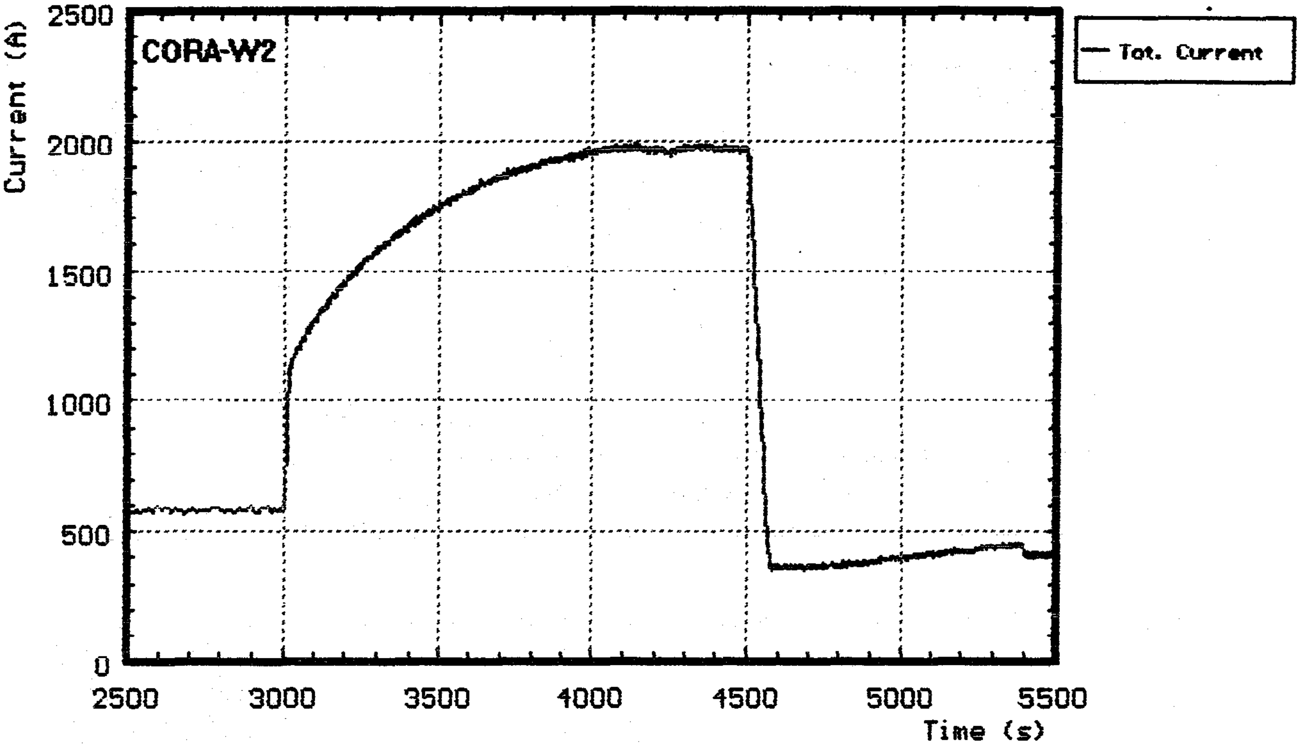

Fig. 18: CORA-W2; Total current

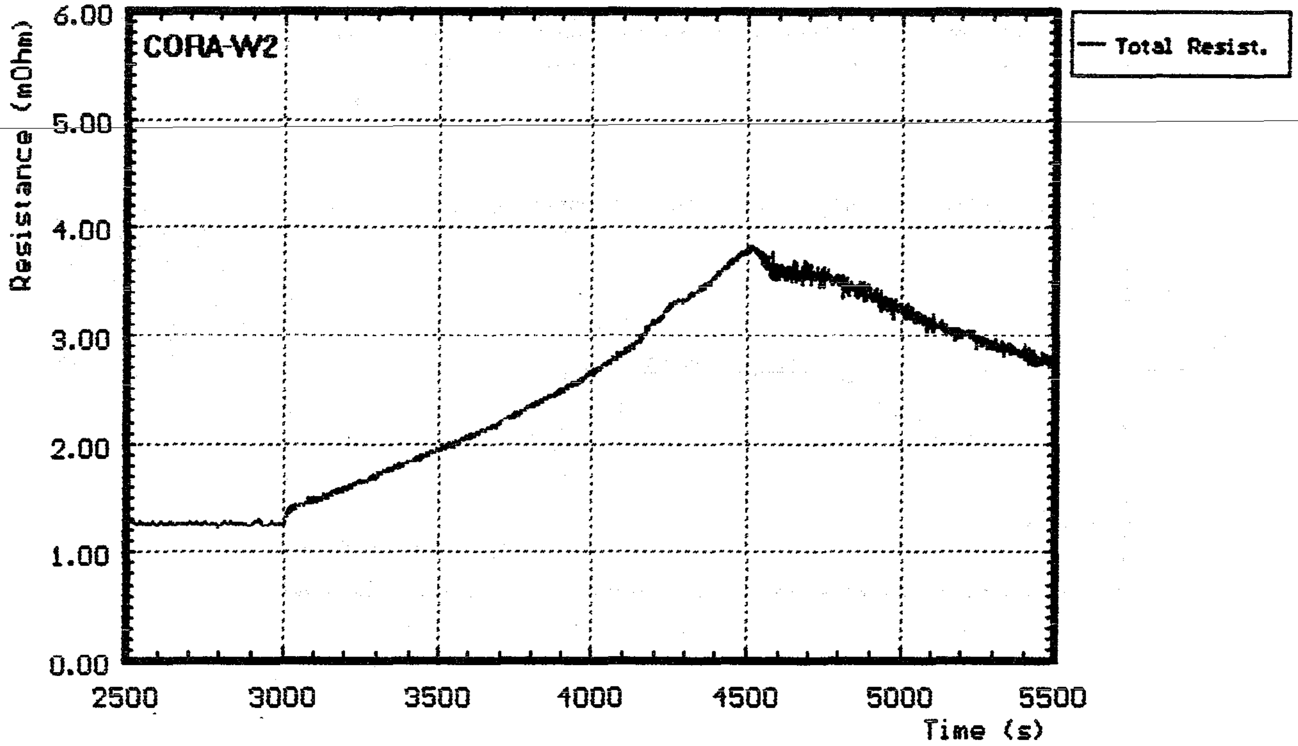

Fig. 19: CORA-W2; Resistance of bundle (voltage group1/total current)

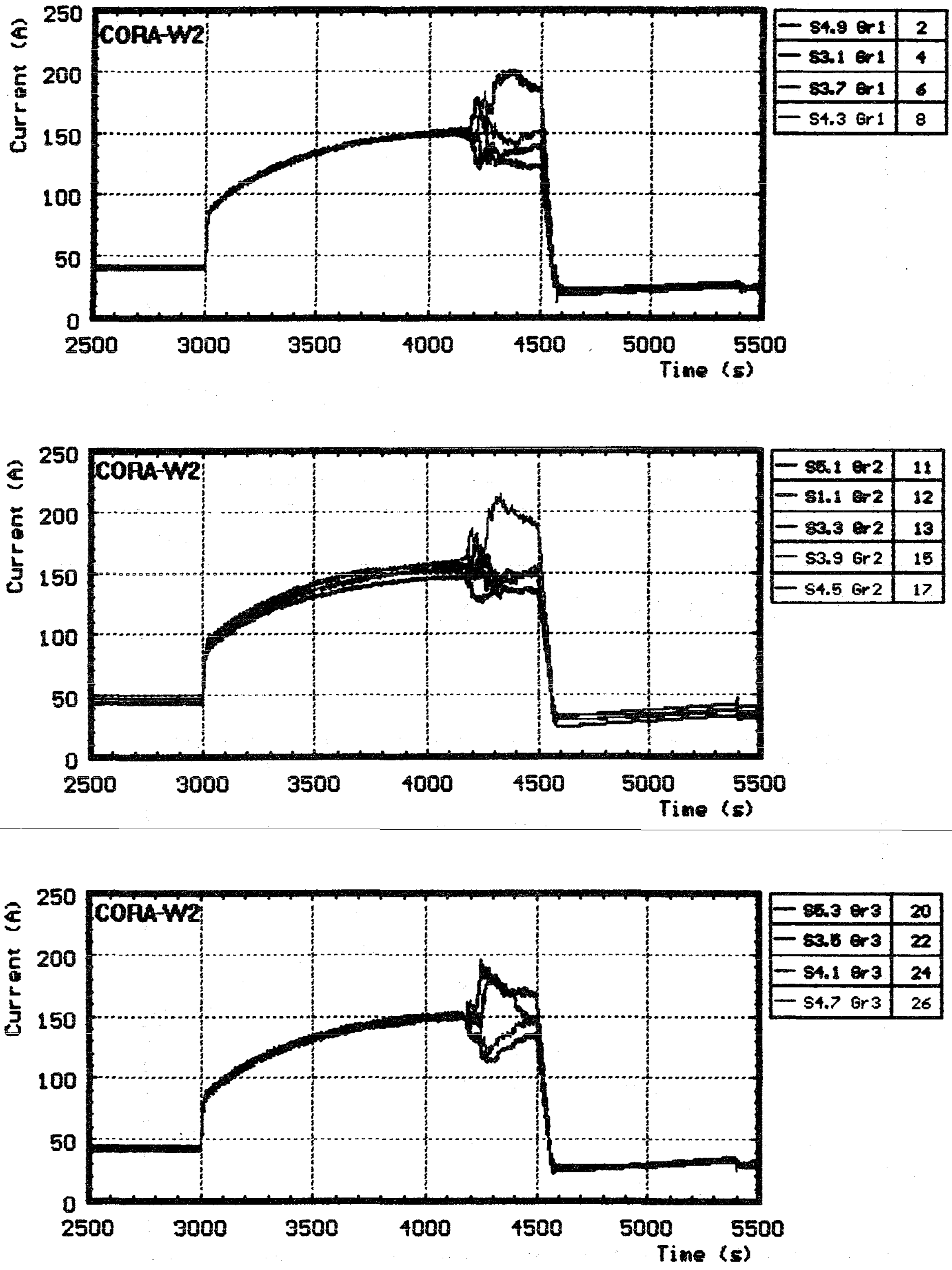

Fig. 20: CORA-W2; Variation of currents within the rod groups

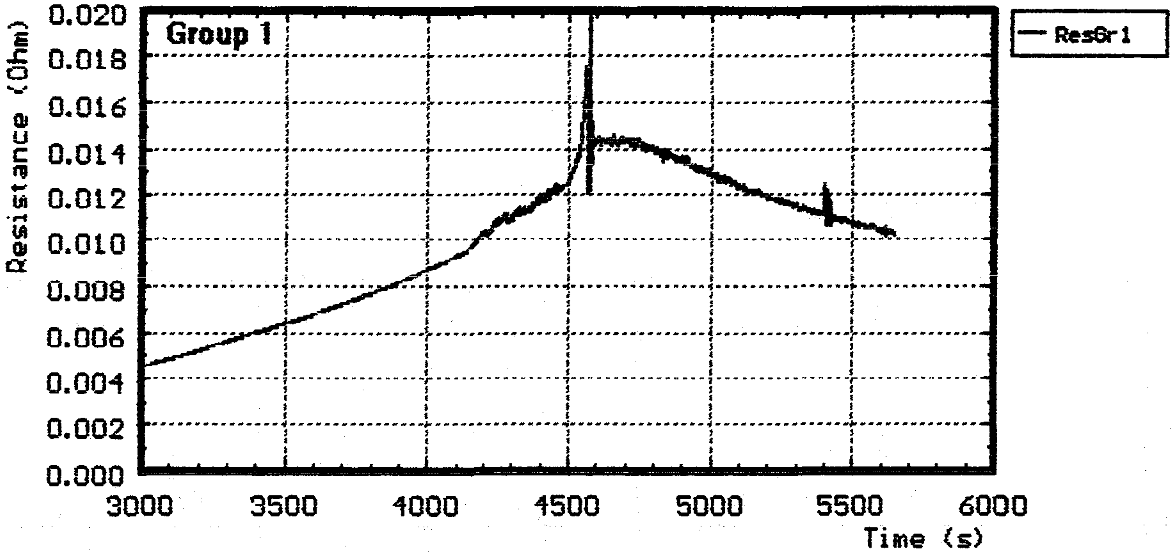

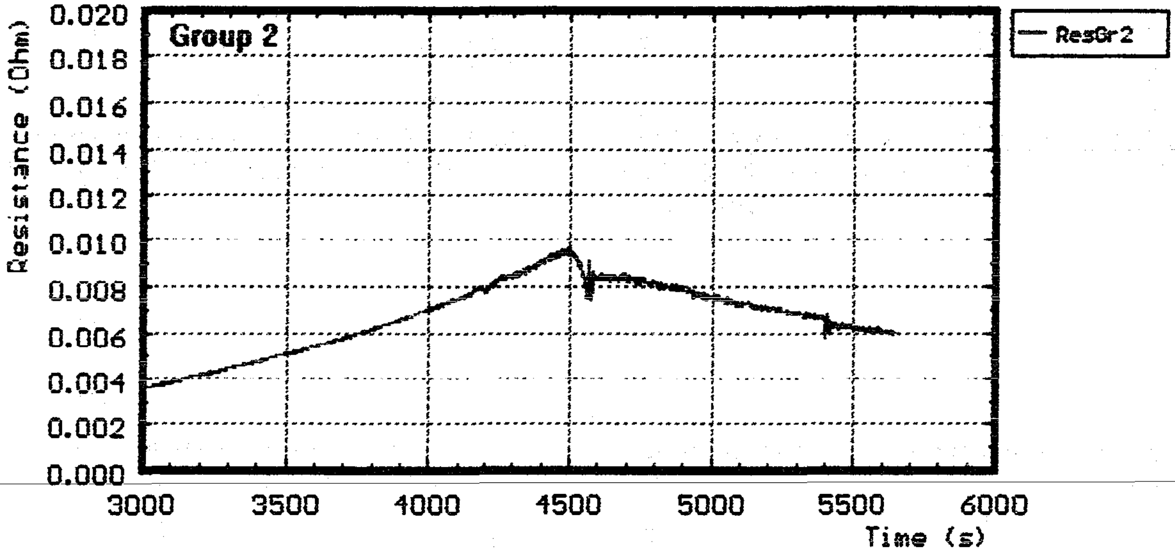

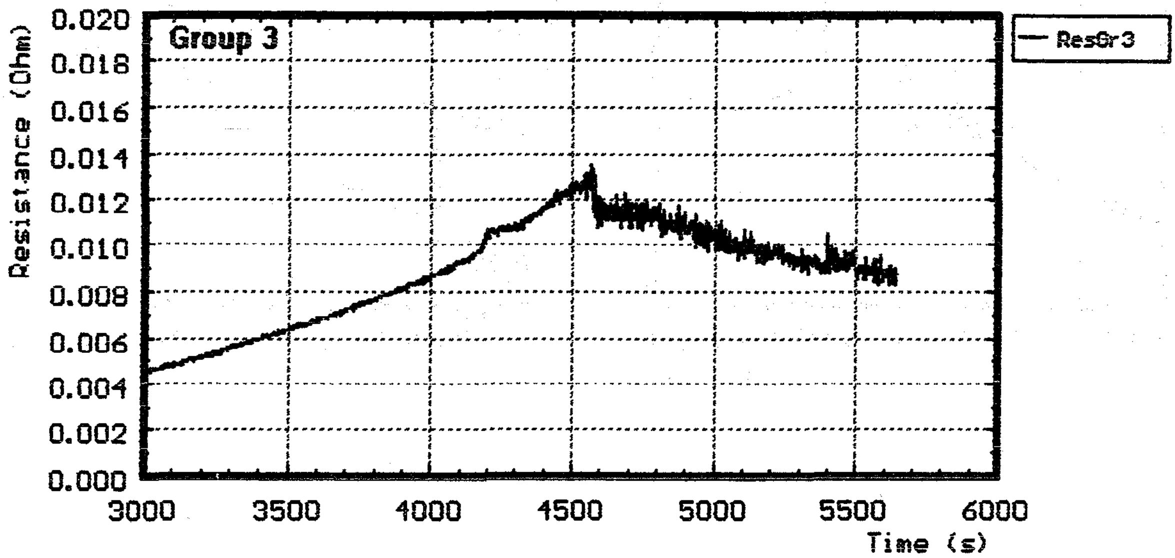

Fig. 21: CORA-W2; Resistance of the rod groups

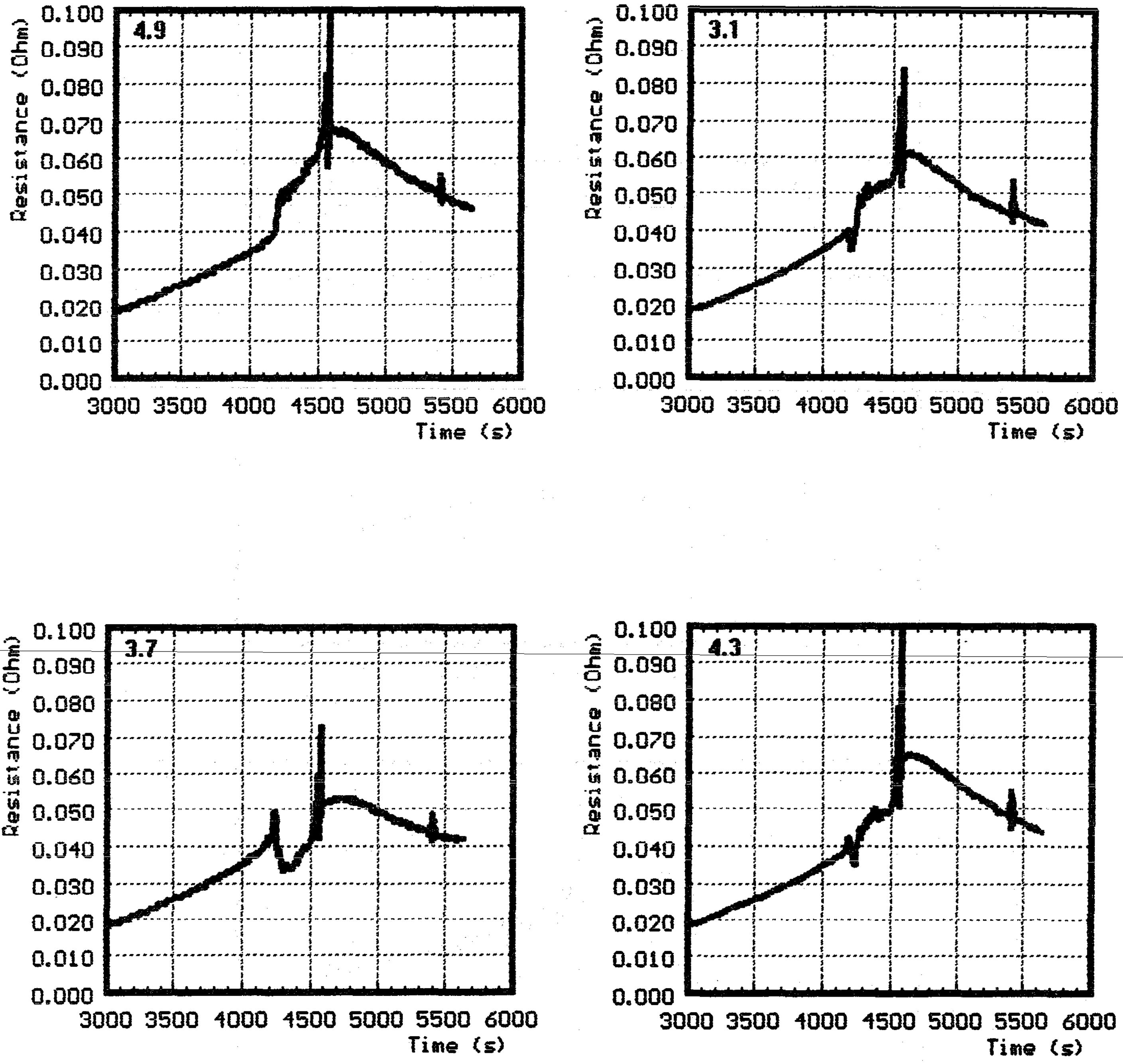

Fig. 22: CORA-W2; Resistance of rods: group 1

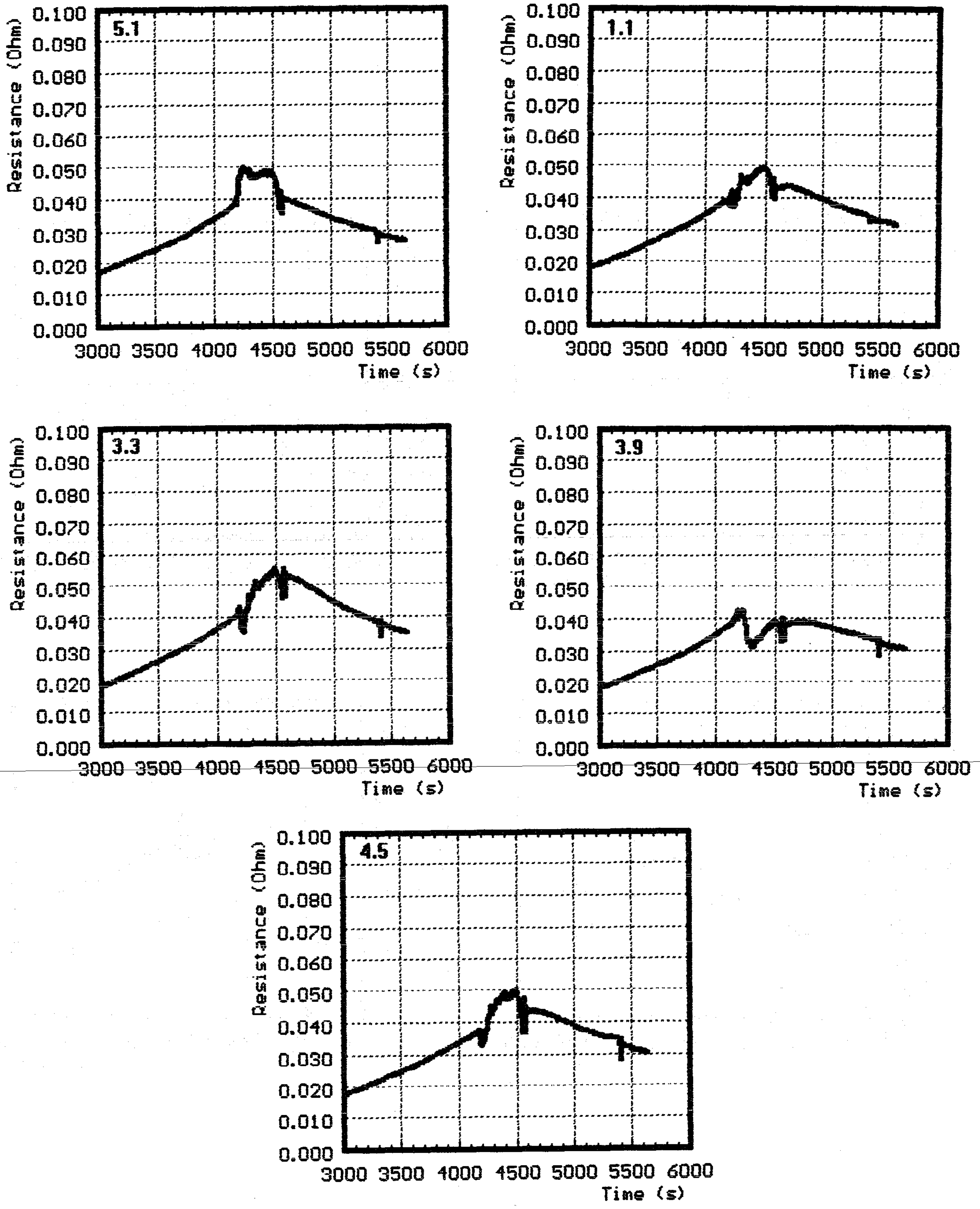

Fig. 23: CORA-W2; Resistance of rods: group 2

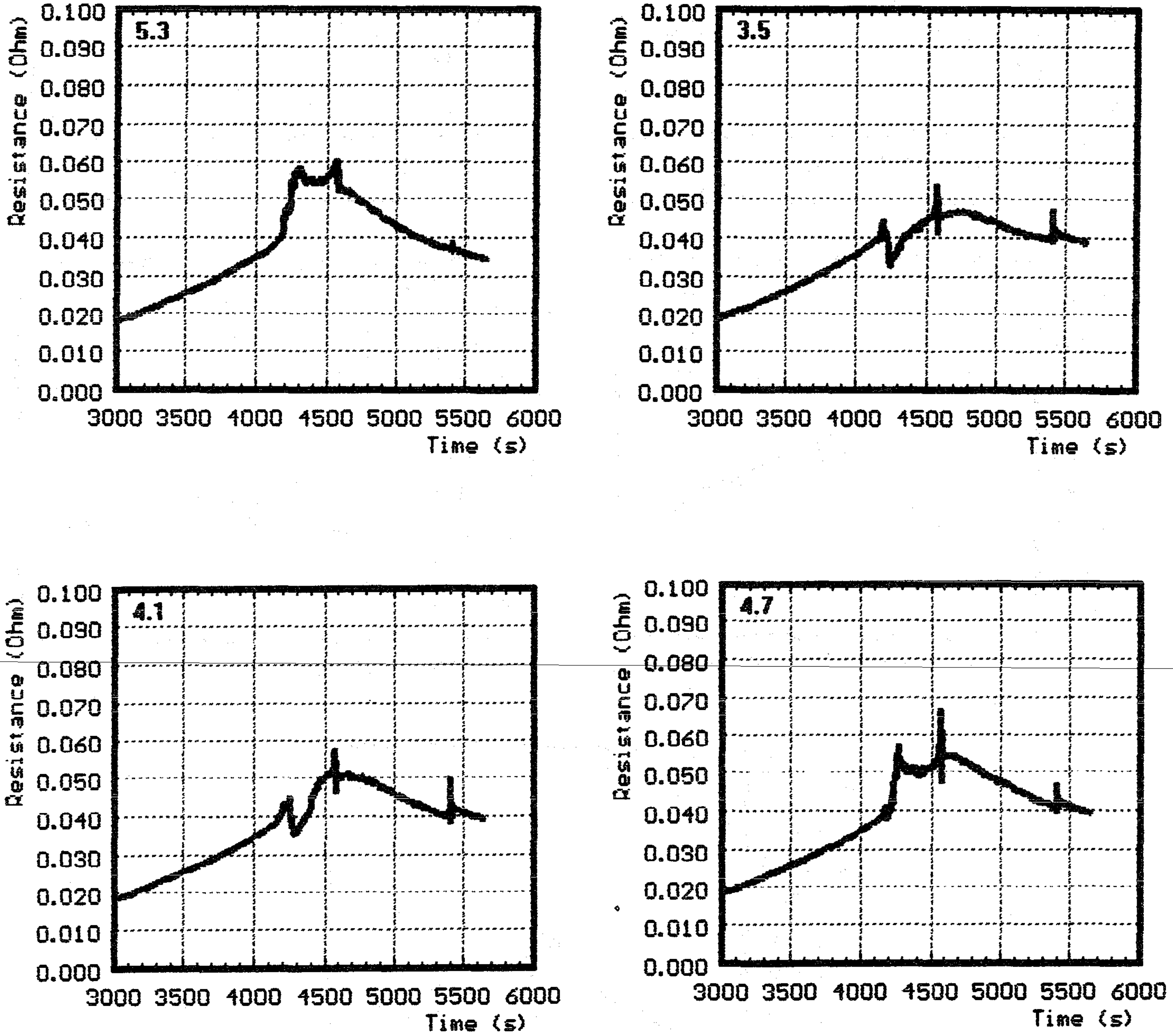

Fig. 24: CORA-W2; Resistance of rods: group 3

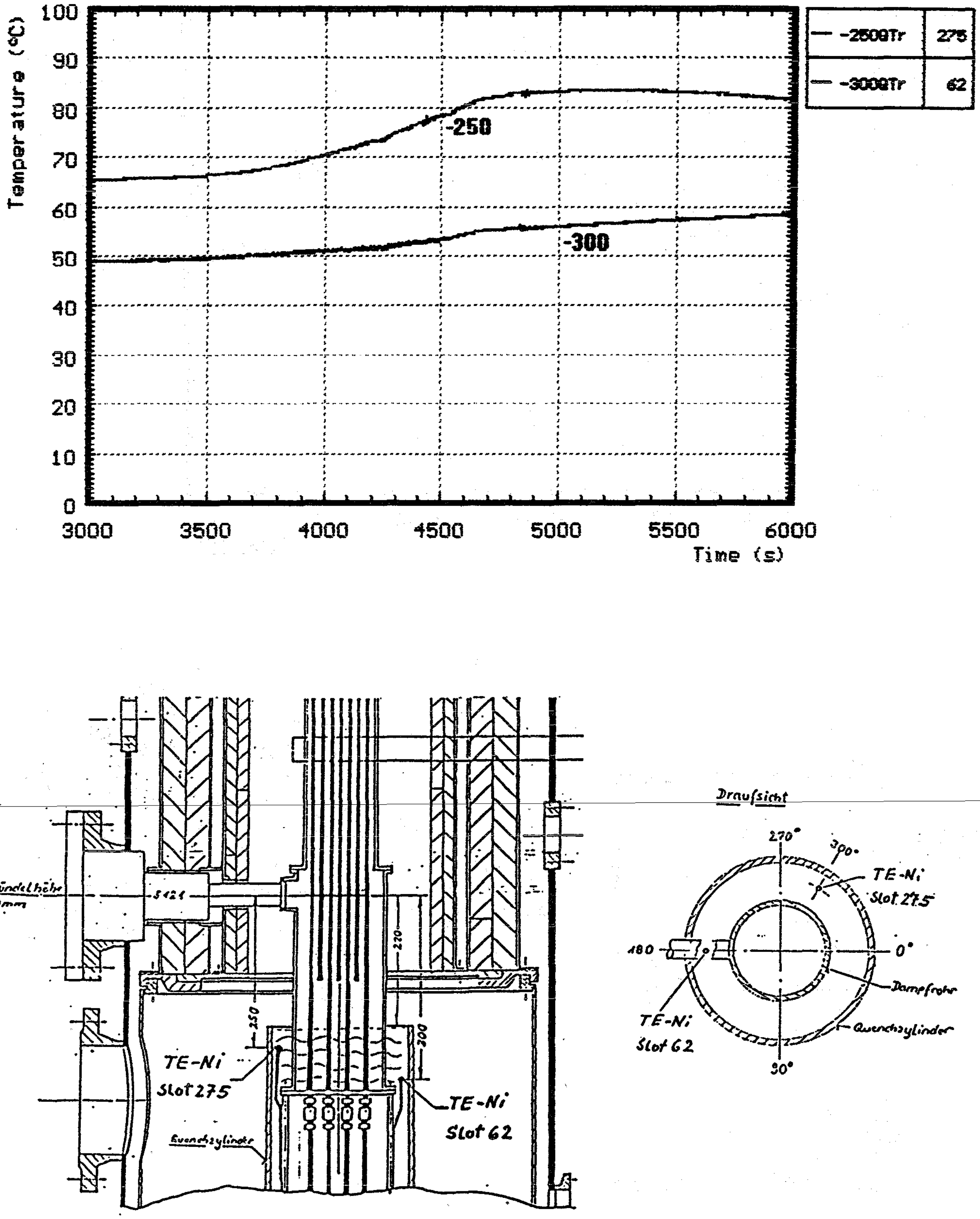

Fig. 25: CORA-W2; Water temperature in the quench cylinder at -250 and -300 mm

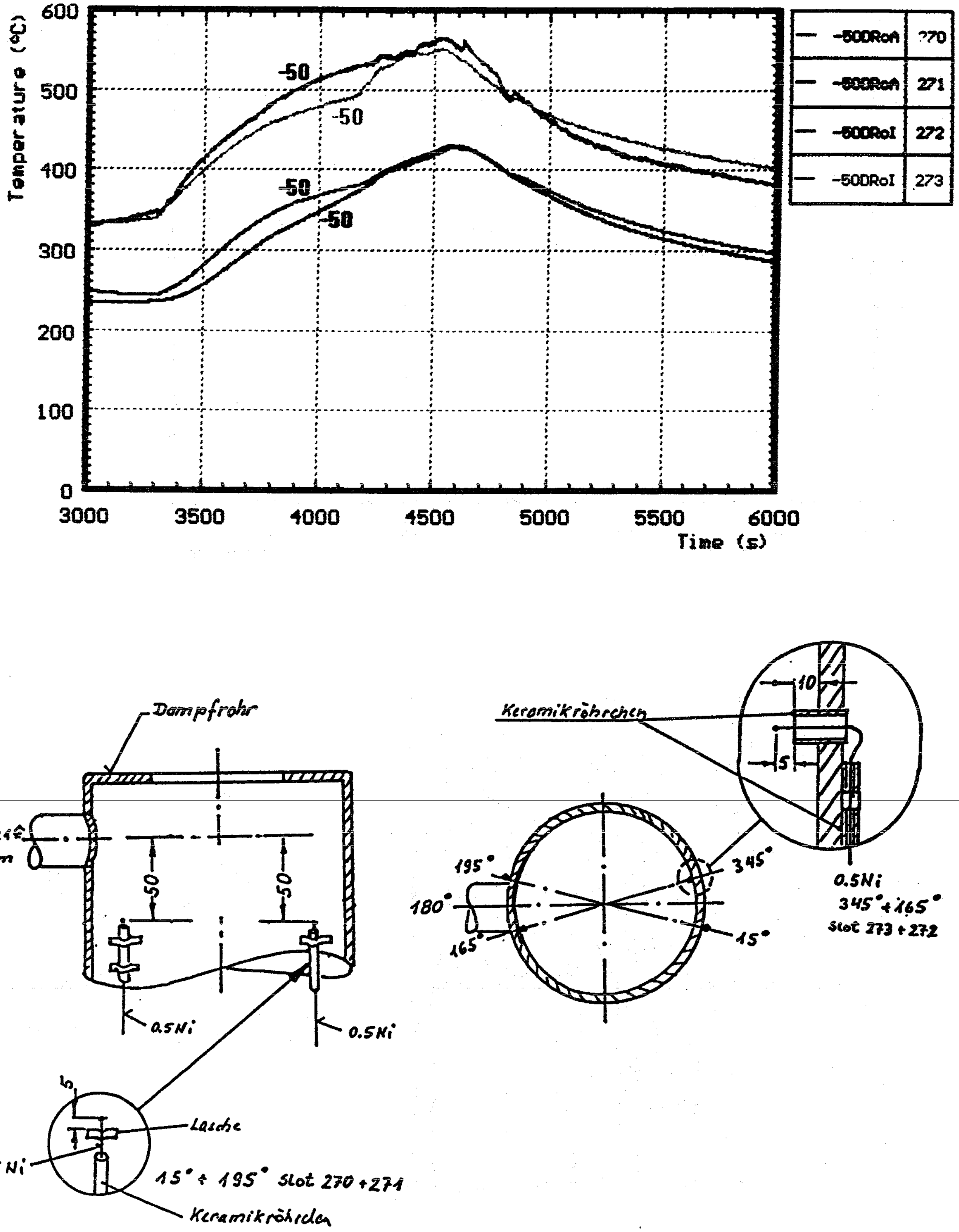

Fig. 26: CORA-W2; Temperature in and on steam tube at -50 mm elevation

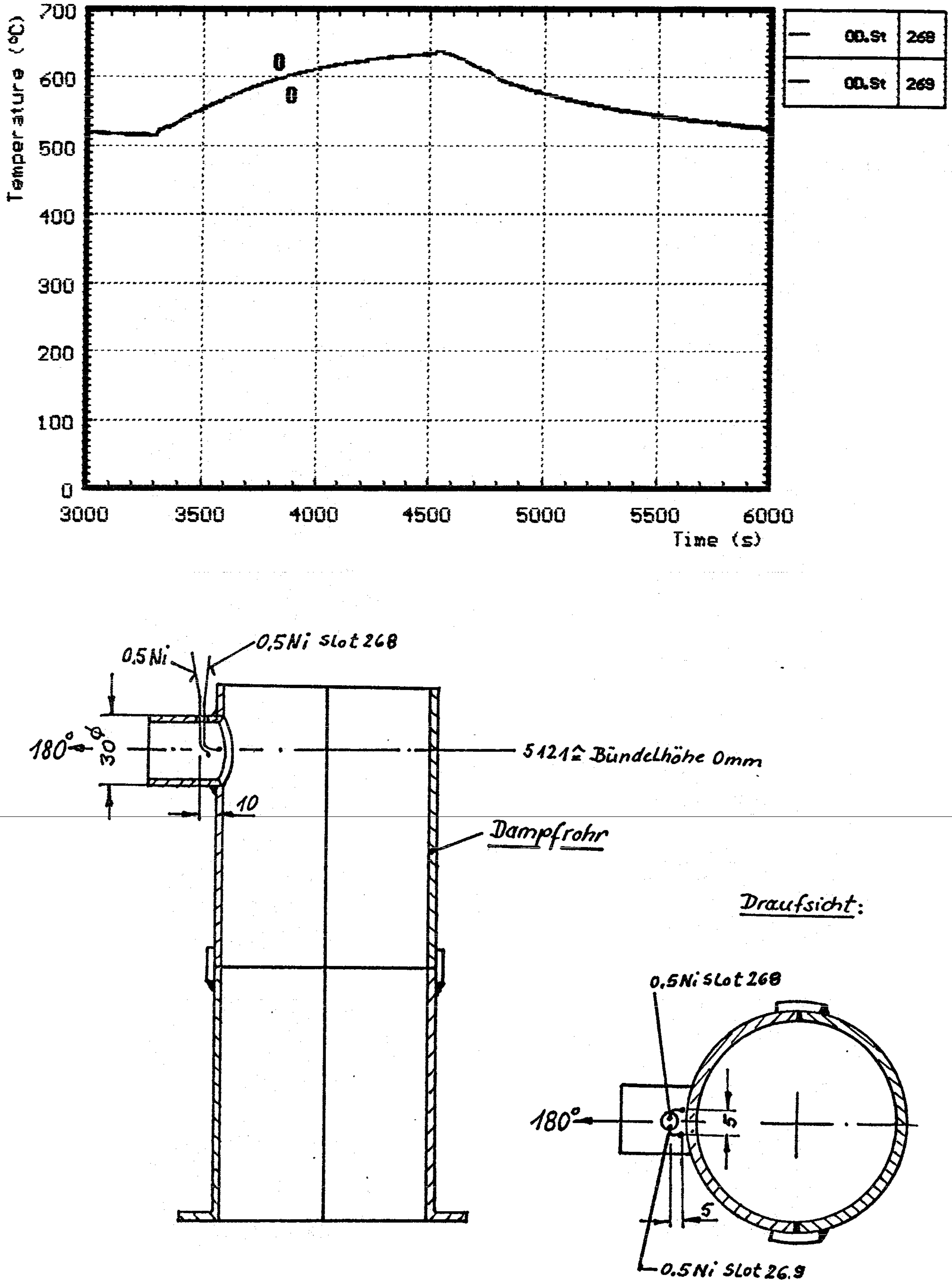

Fig. 27: CORA-W2; Temperatures at steam inlet

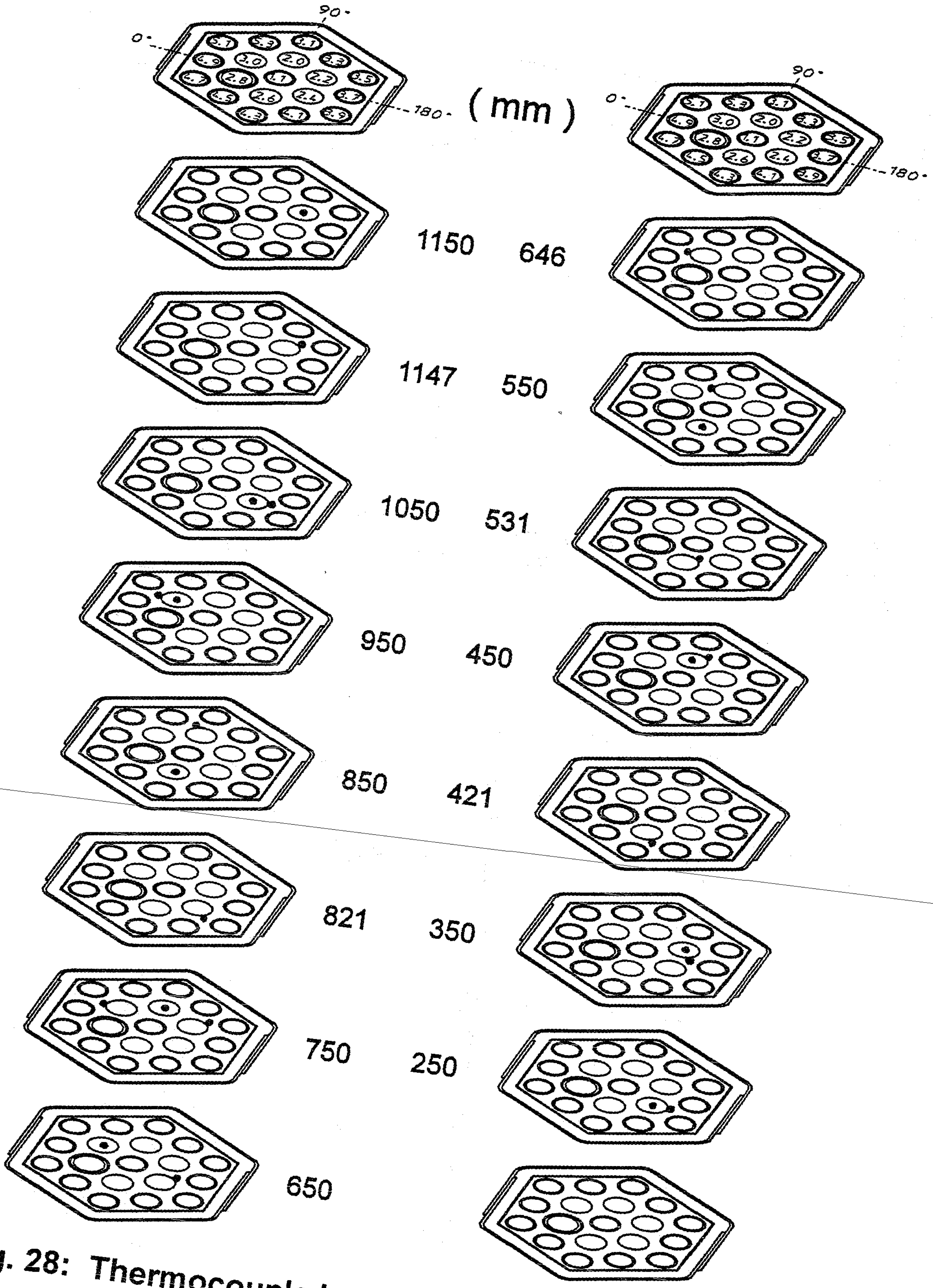

Fig. 28: Thermocouple locations within the bundle (CORA-W2)

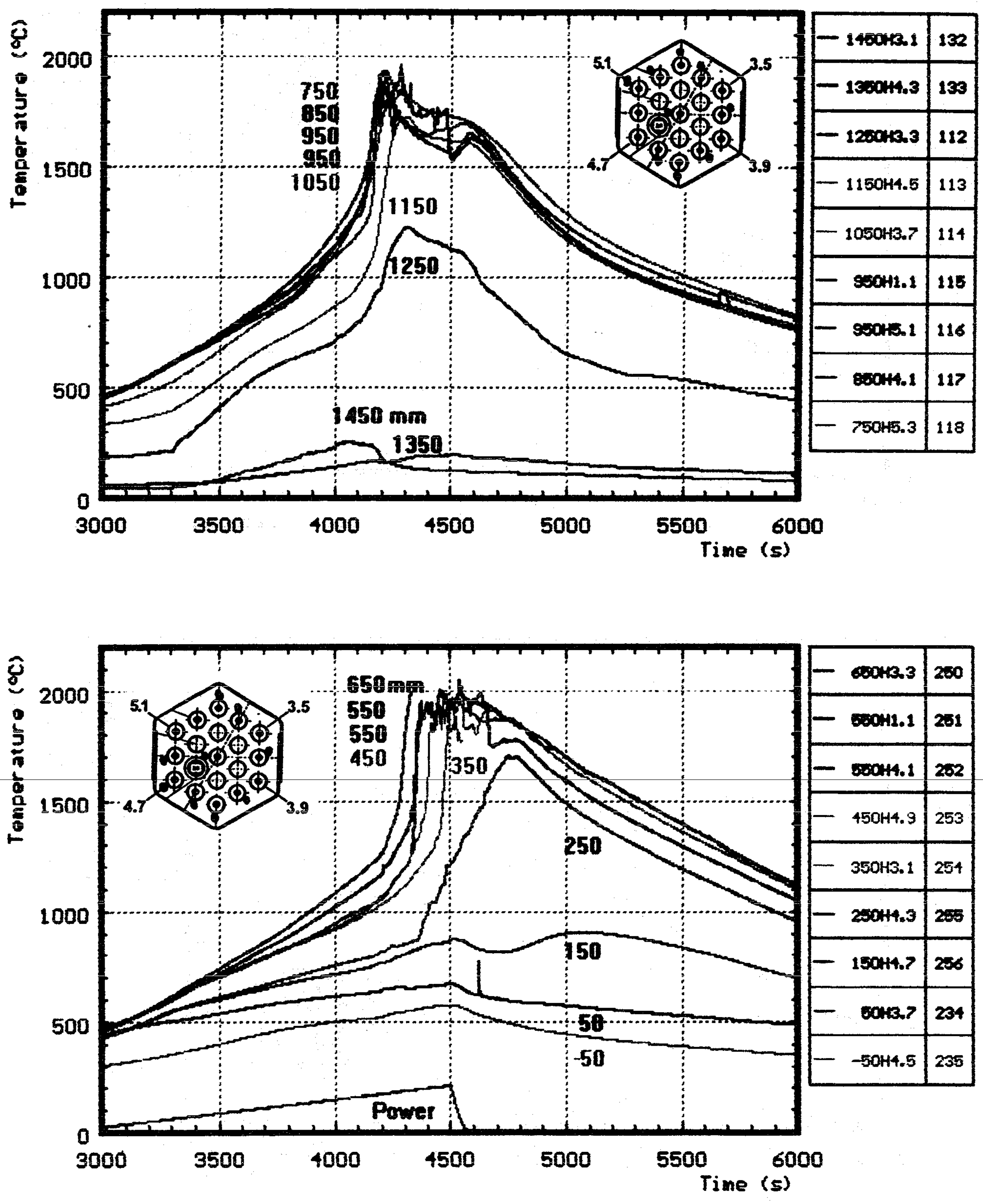

Fig. 29: CORA-W2; Temperatures on heated rods
]

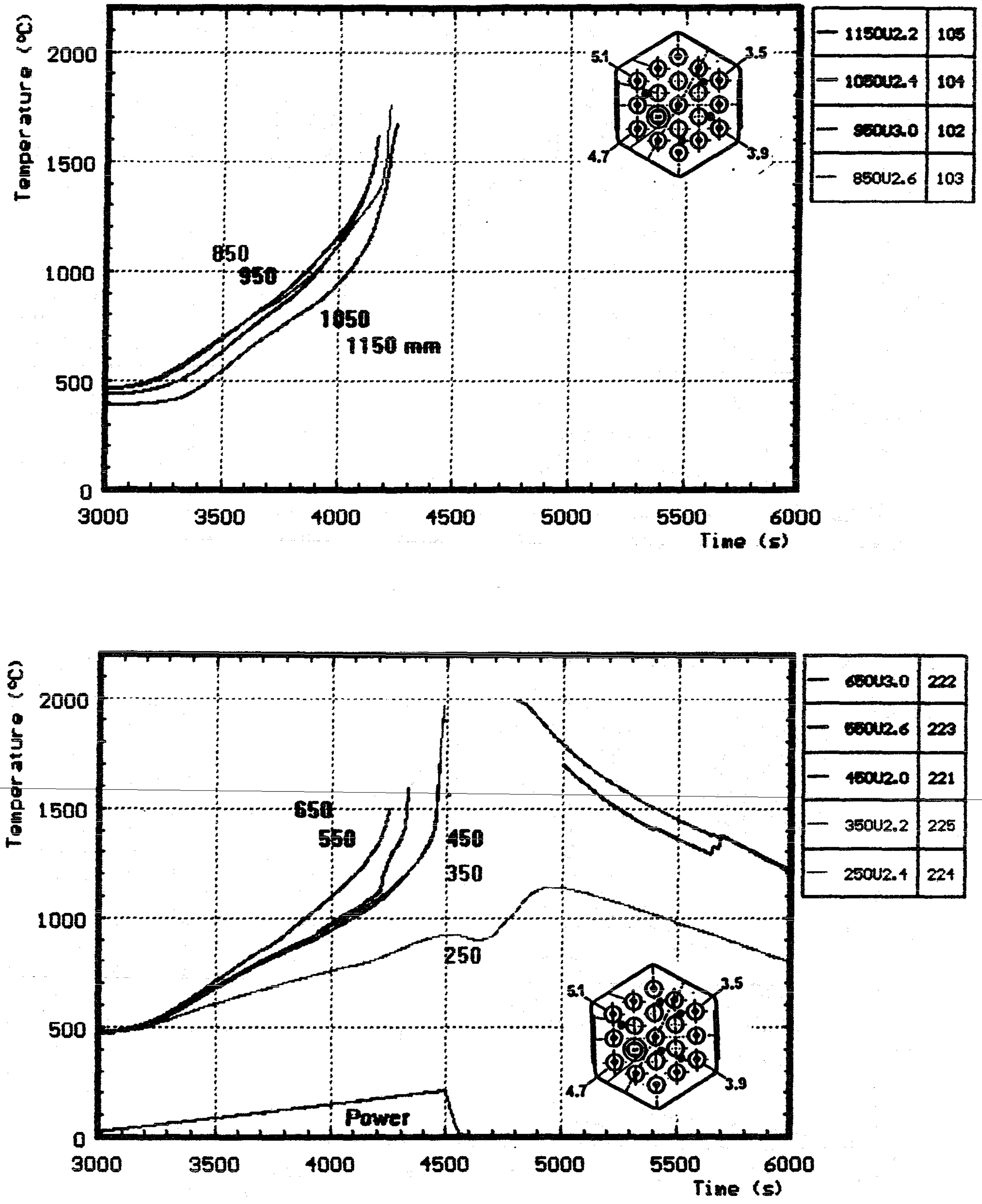

Fig. 30: CORA-W2; Temperatures of unheated rods (TCs in central position)

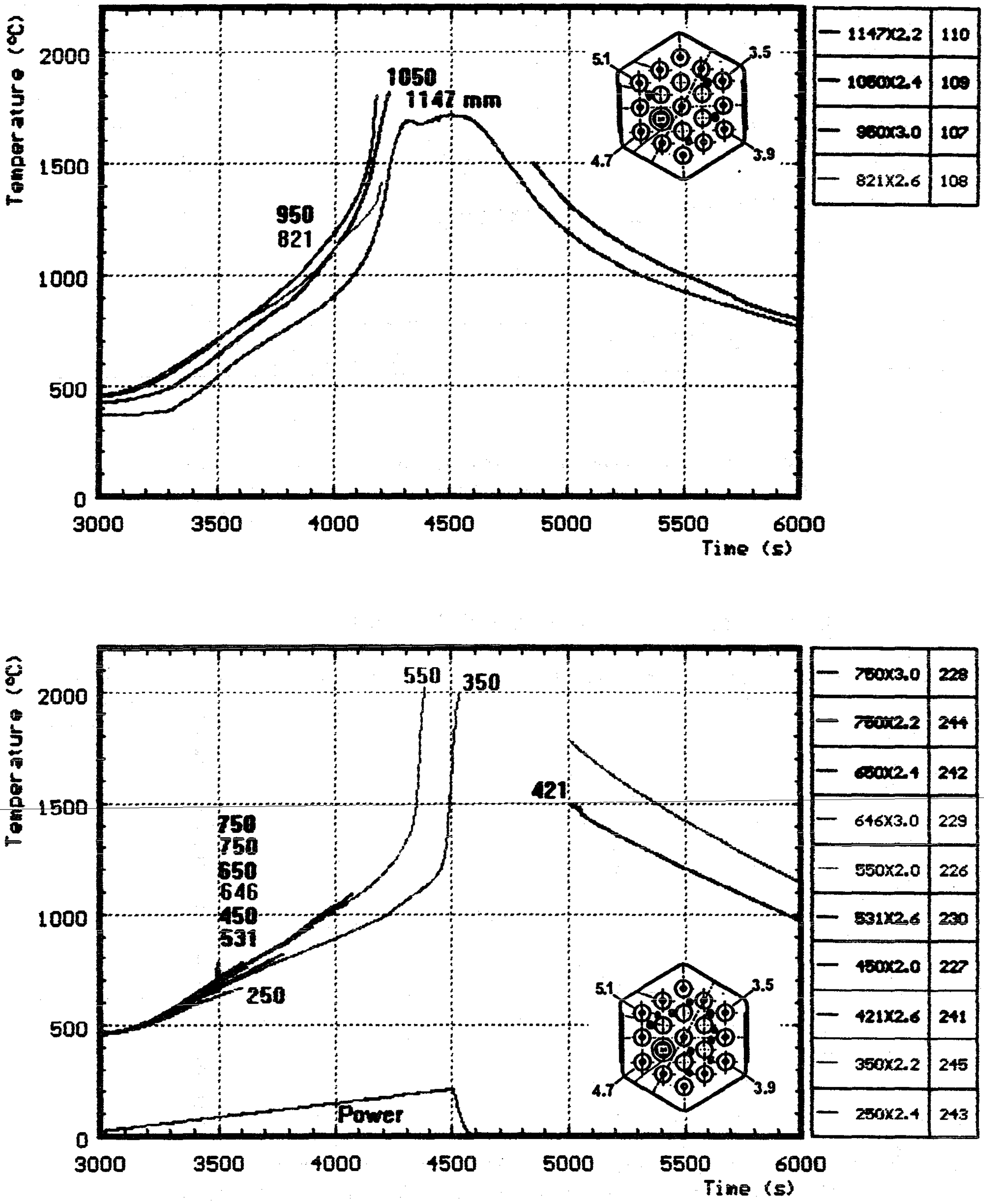

Fig. 31: CORA-W2; Temperatures of unheated rods (TCs on outer surface)

Internal pressure of absorber rod (2.8) and unheated rods

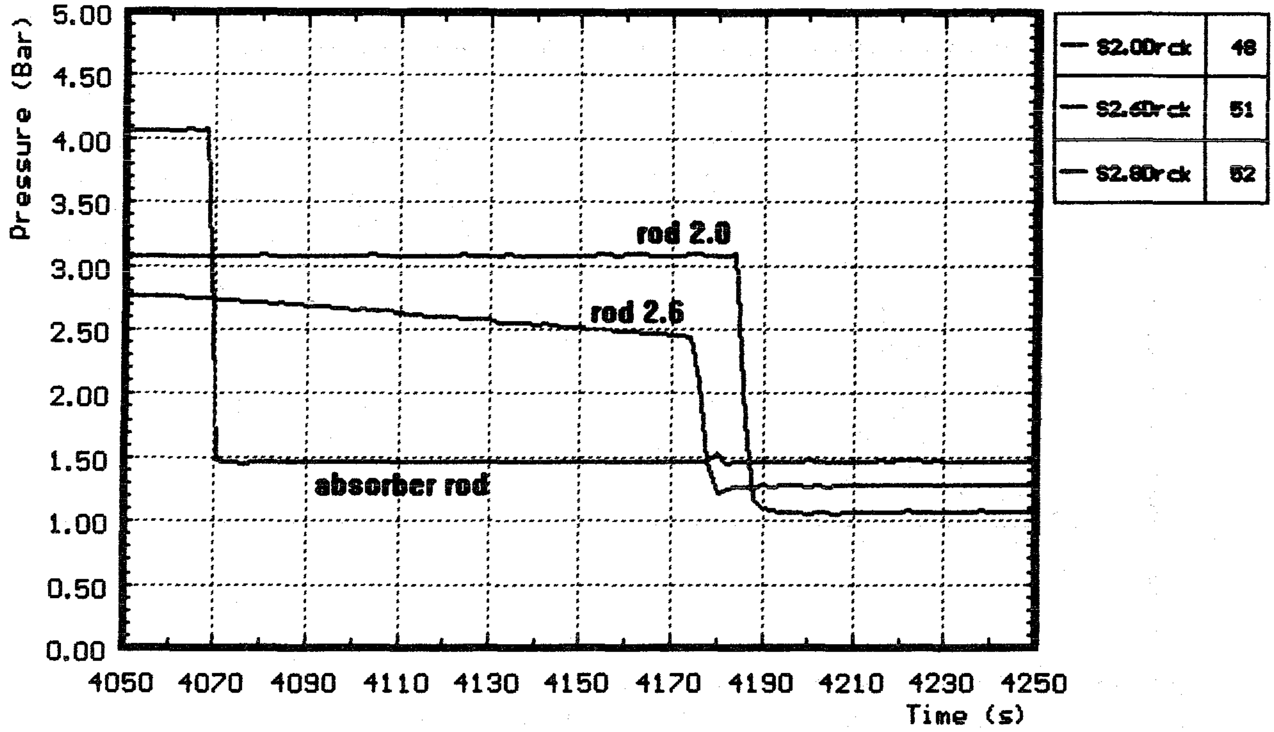

Temperatures of absorber rod at 1001 mm

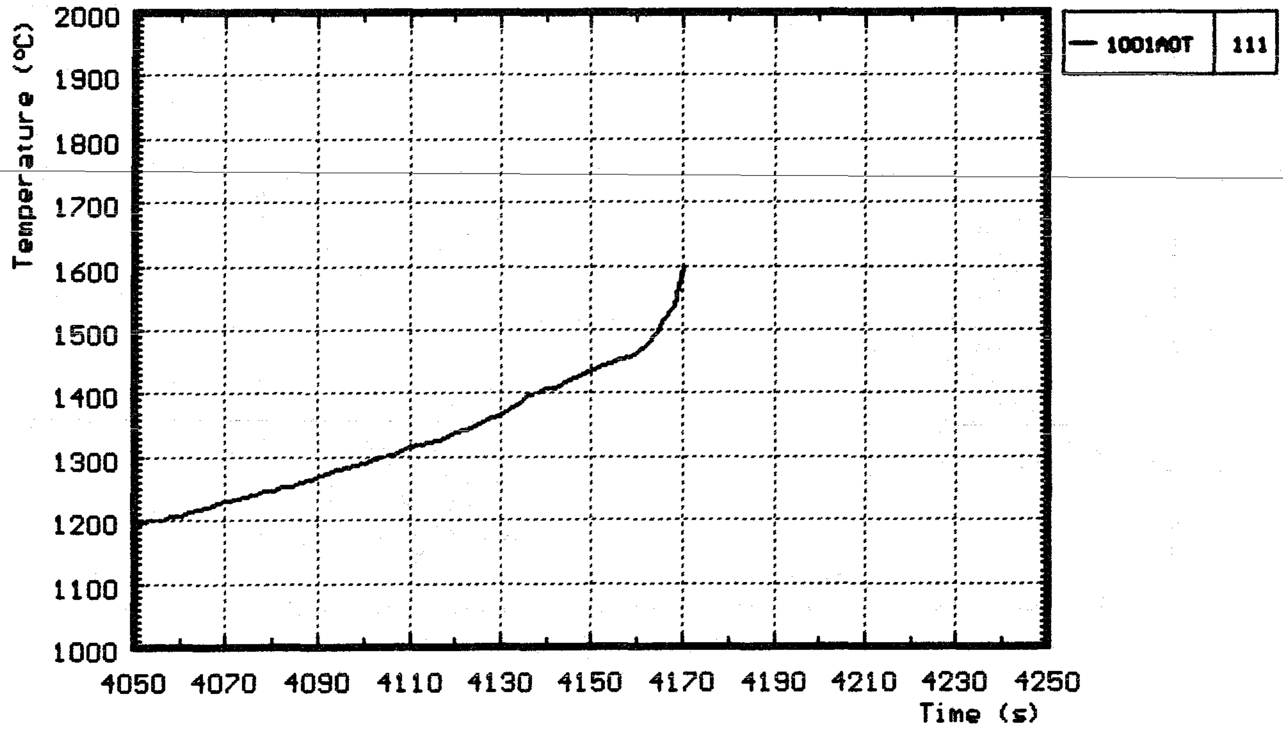

Fig. 32: CORA-W2: Comparsion of internal pressure of absorber rod (2.8) and unheated rods with temperature of absorber rod at 1001 mm

Internal pressure of absorber rod (2.8) and unheated rods

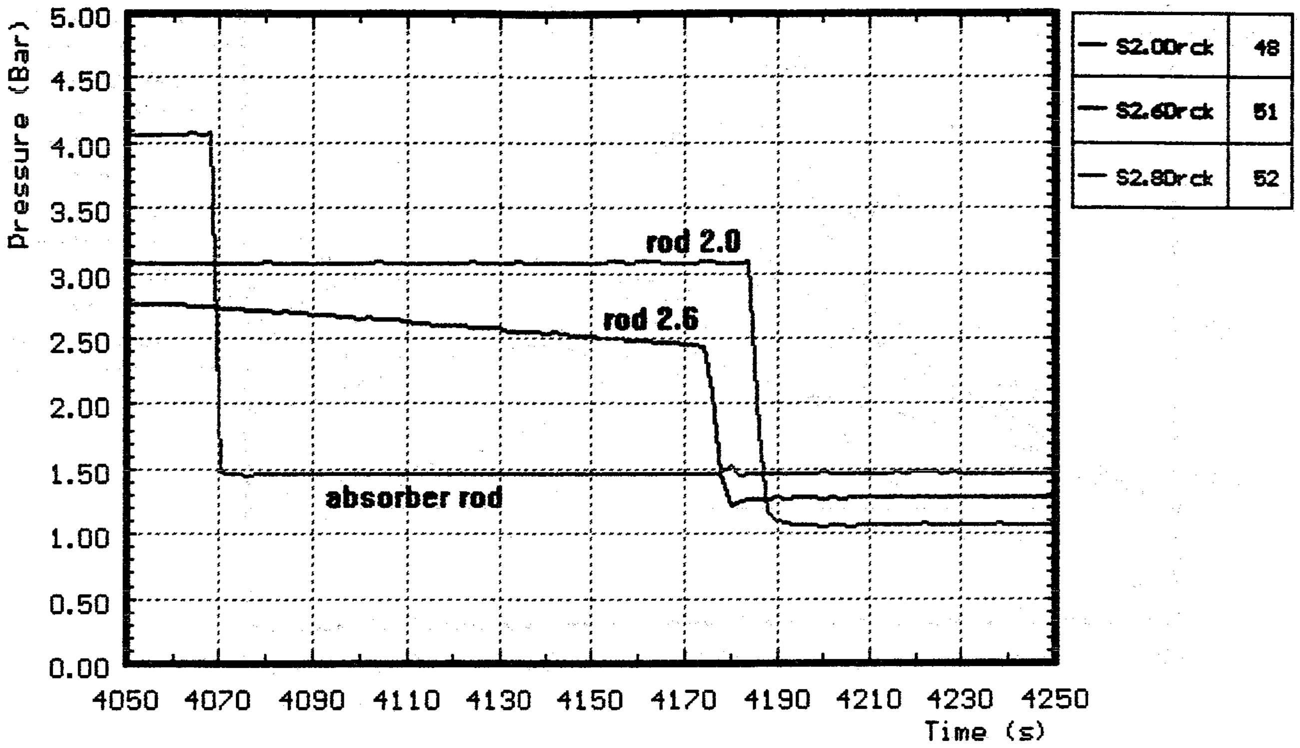

Temperatures of heated rods at 750, 850, and 950 mm

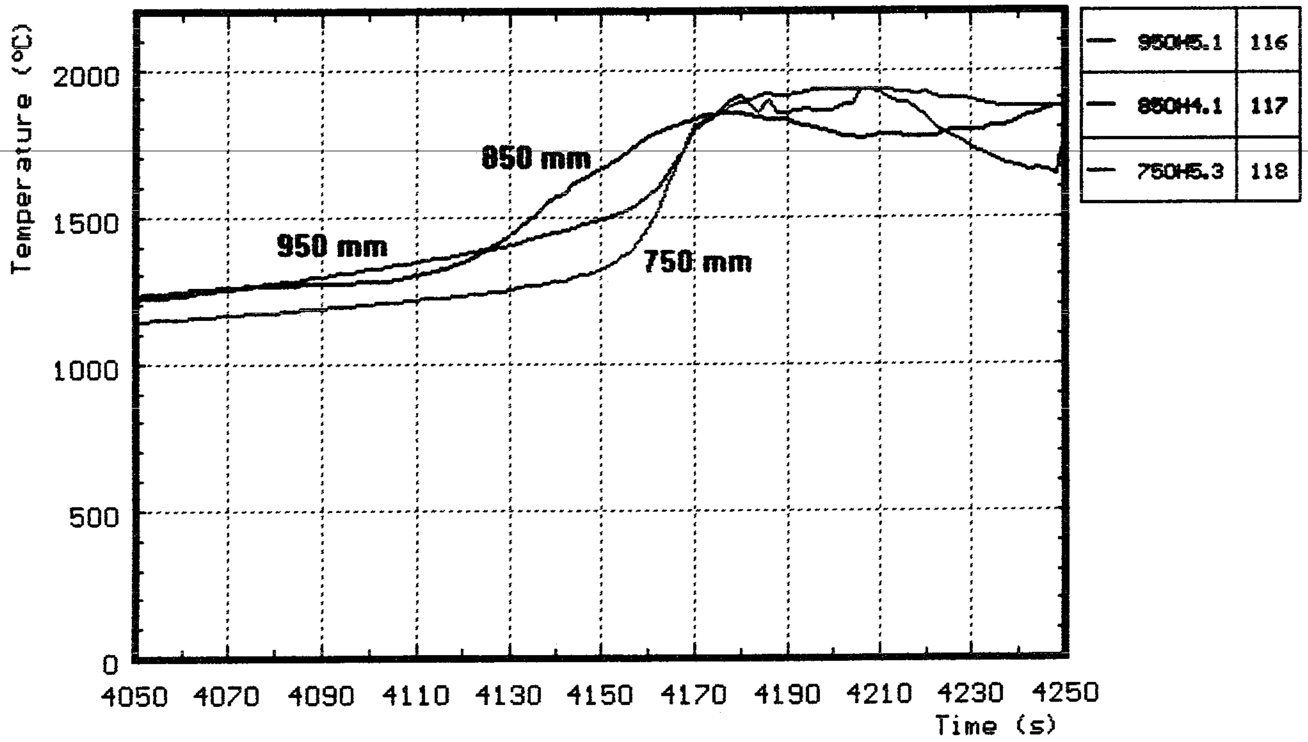

Fig. 33: CORA-W2: Comparsion of internal pressure of absorber rod and unheated rods with temperatures of heated rods at 750, 850, and 950 mm

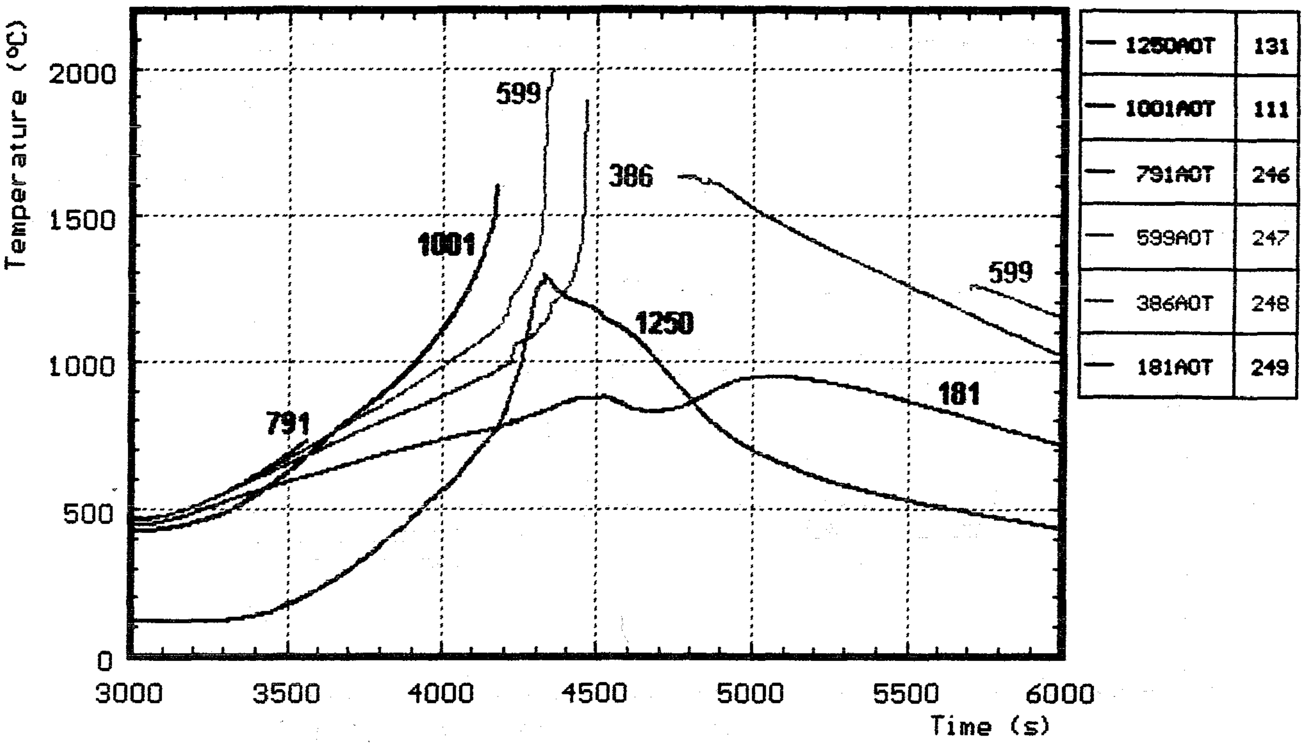

Fig. 34: CORA-W2; Temperatures of the guide tube of the absorber rod (outer surface)

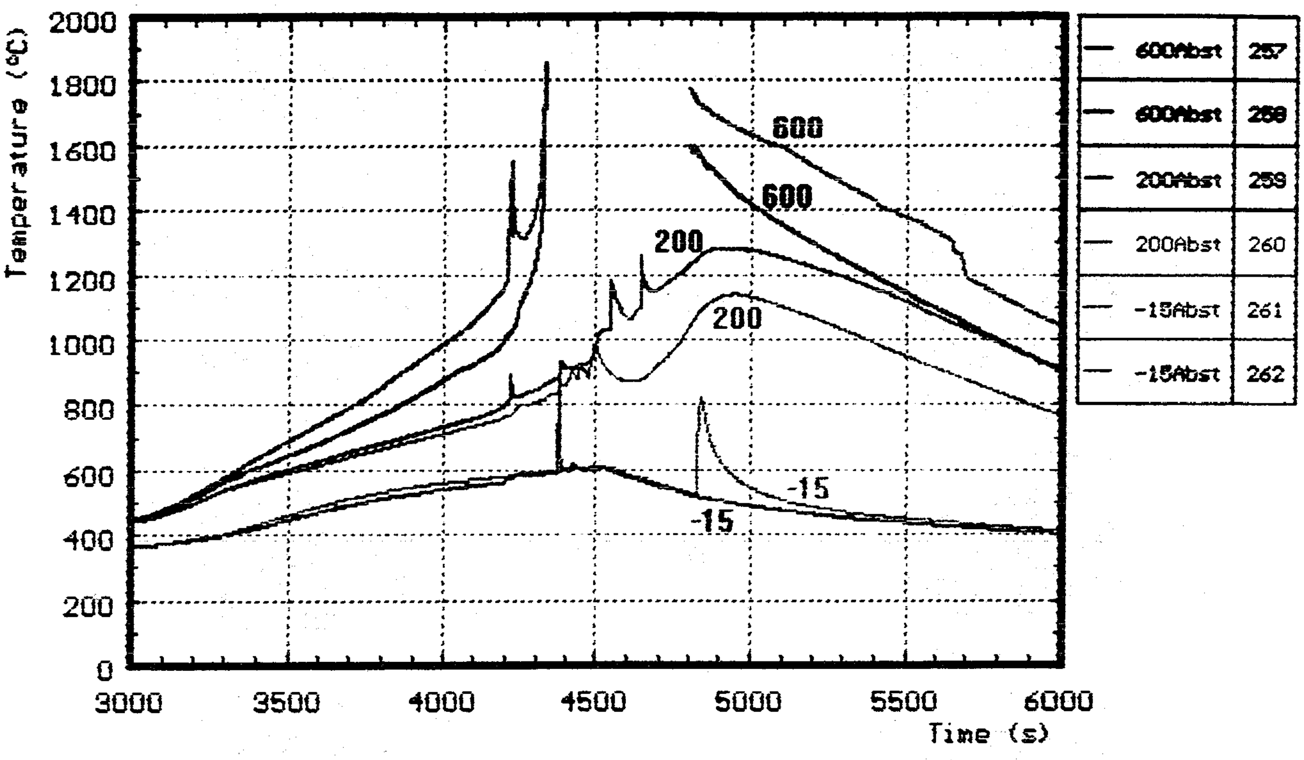

Fig. 36: CORA-W2; Temperatures of the spacers

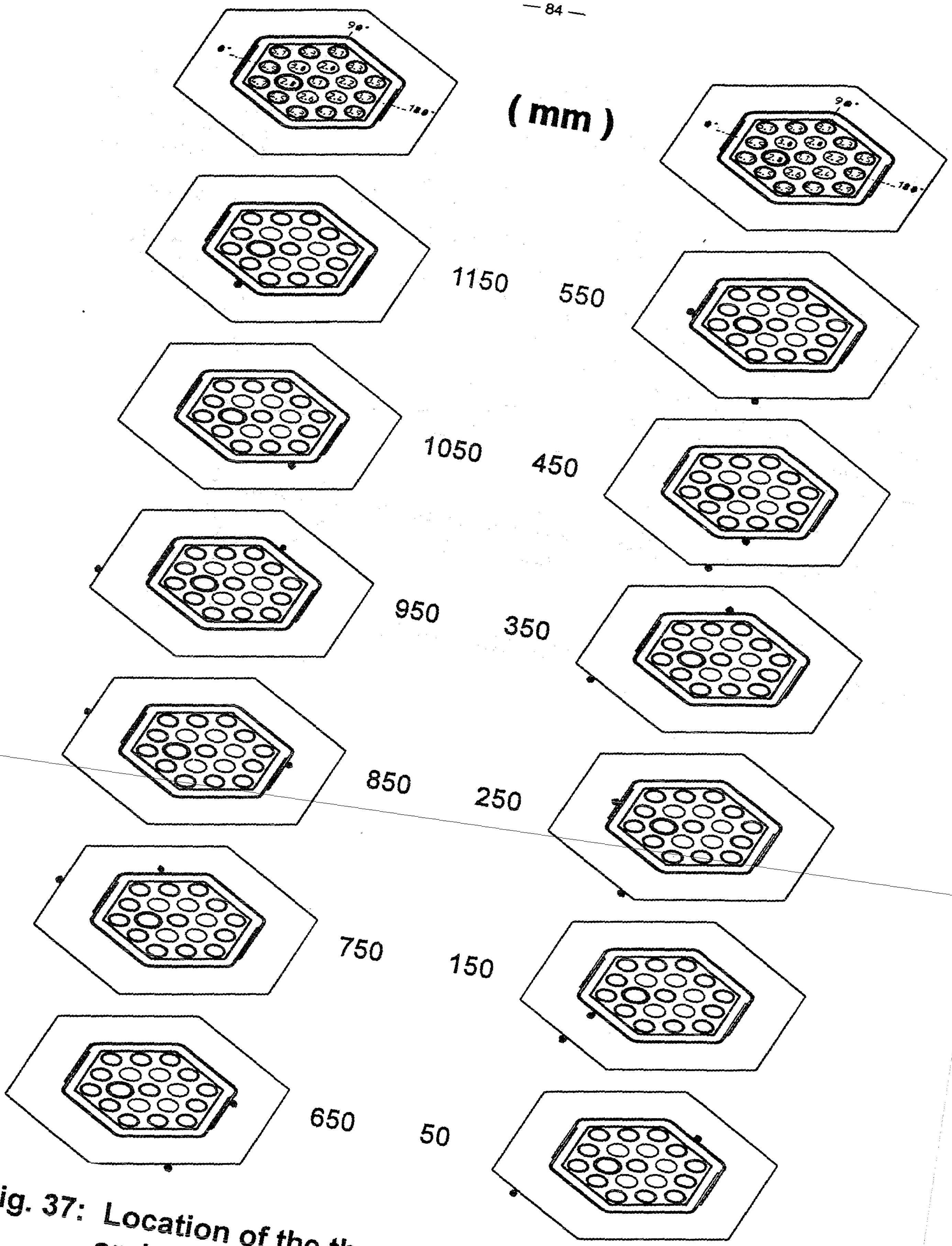

Fig. 37: Location of the thermocouples at shroud and shroud insulation (CORA-W2)

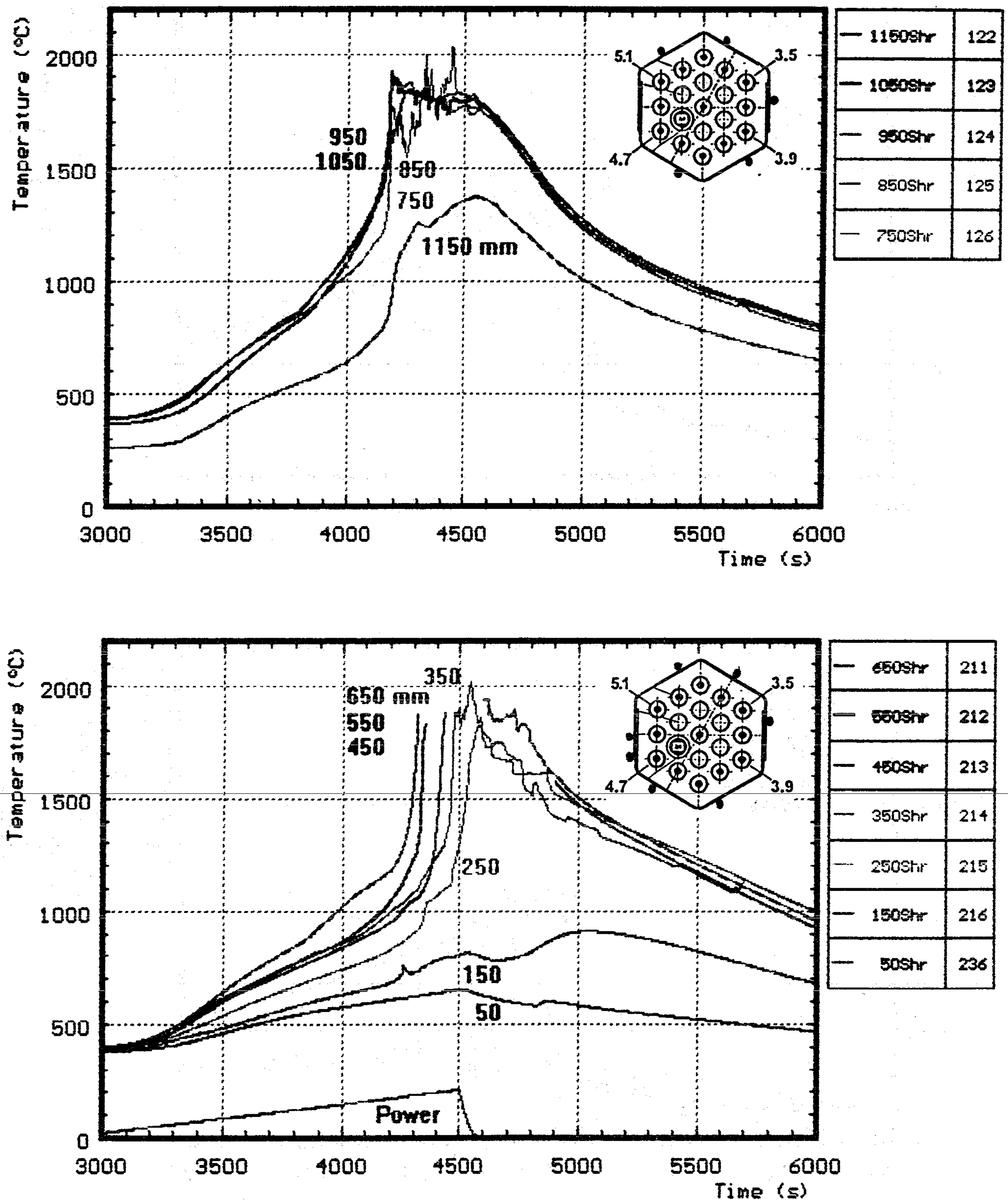

Fig. 38: CORA-W2; Temperatures of outer side of shroud

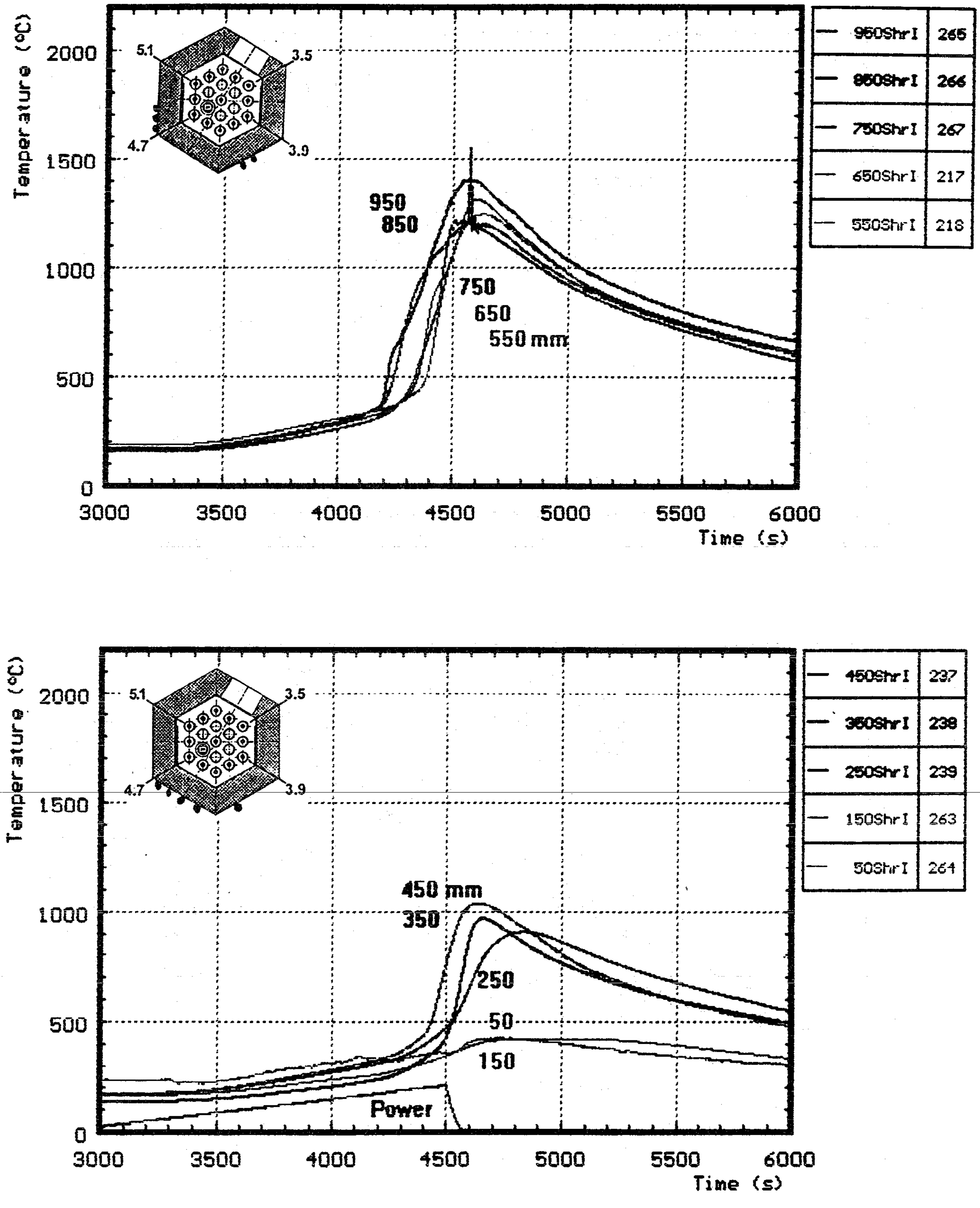

Fig. 39: CORA-W2; Temperatures of the shroud insulation

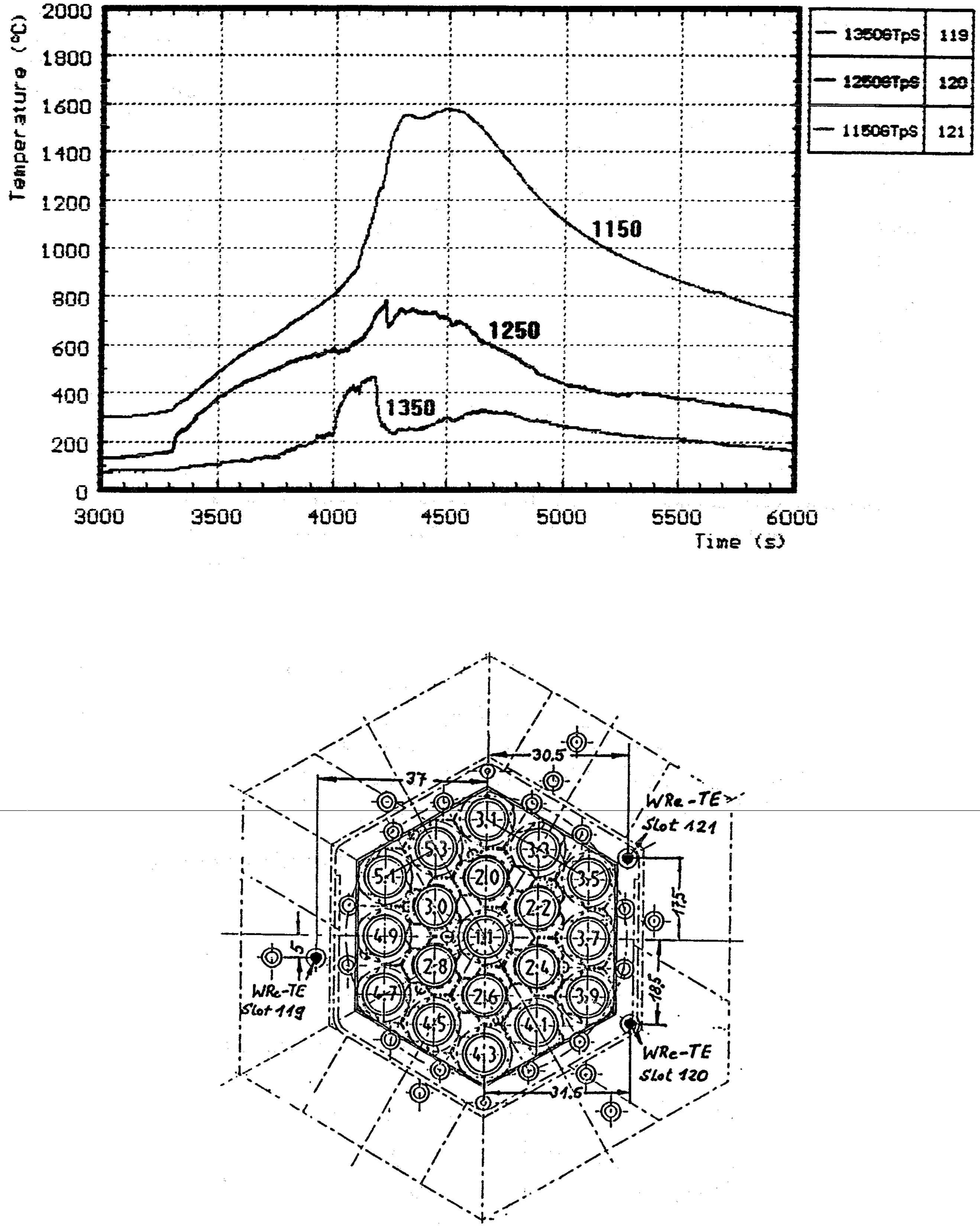

Fig. 40: CORA-W2; Gas temperatures above the heated zone (1150, 1250, 1350)

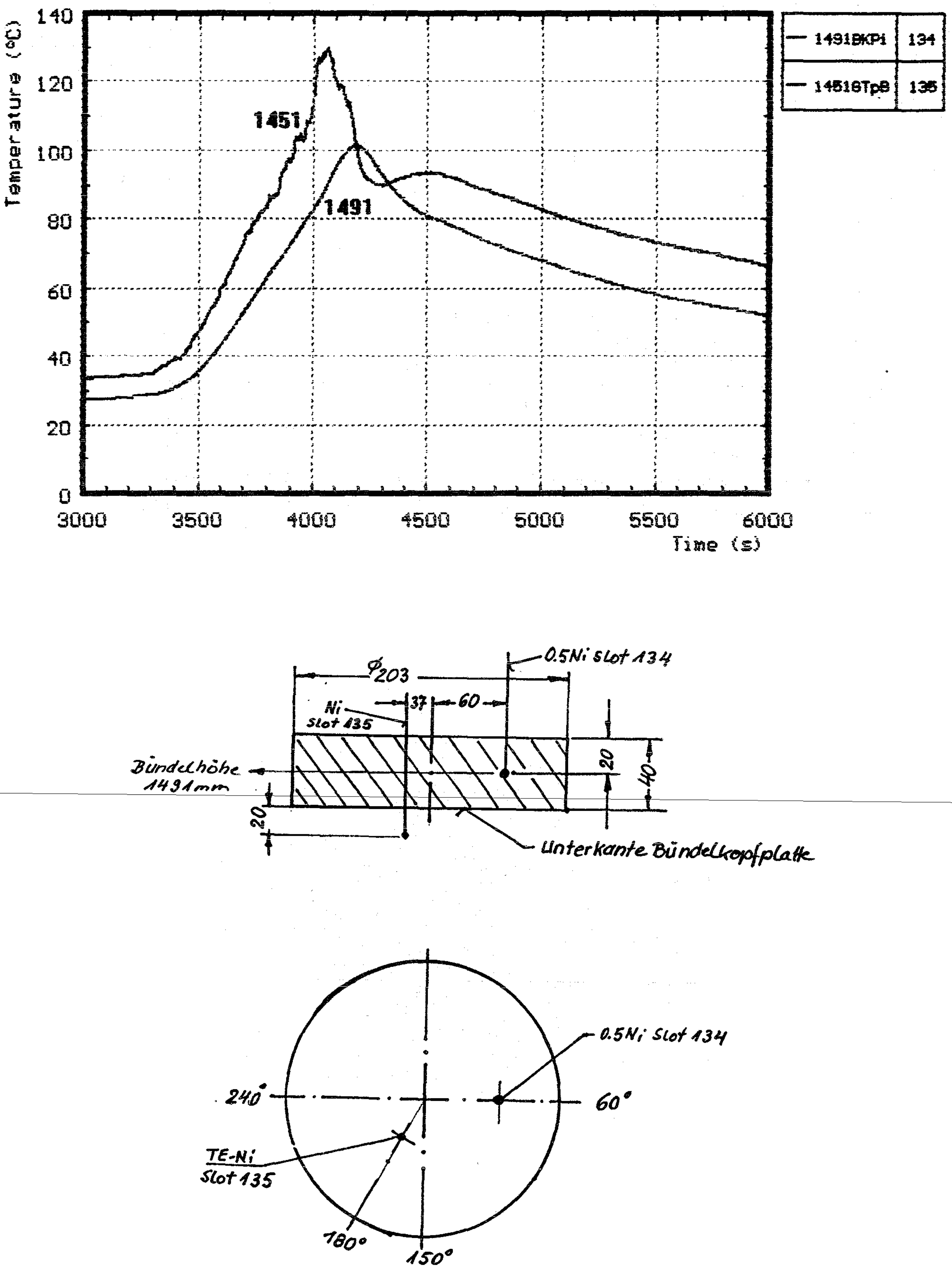

Fig. 41: CORA-W2; Temperature measured in and under the bundle head plate (1491, 1451 mm)

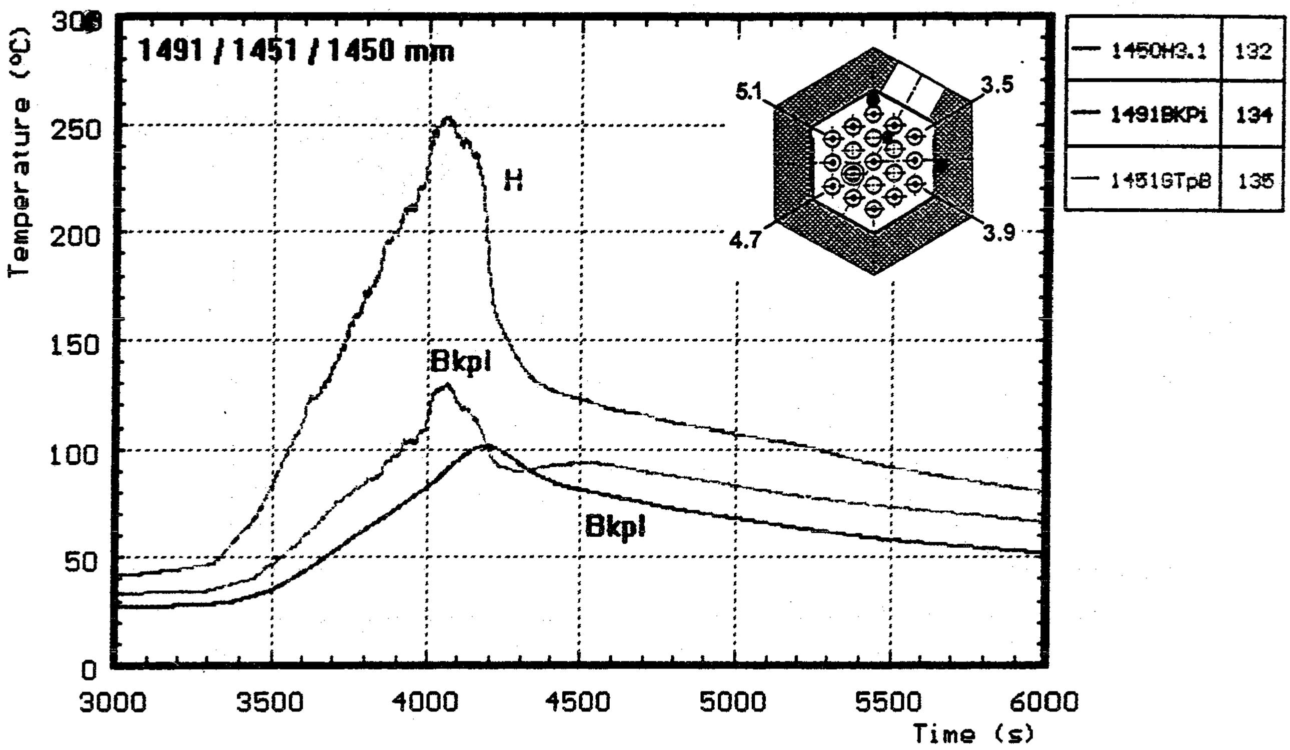

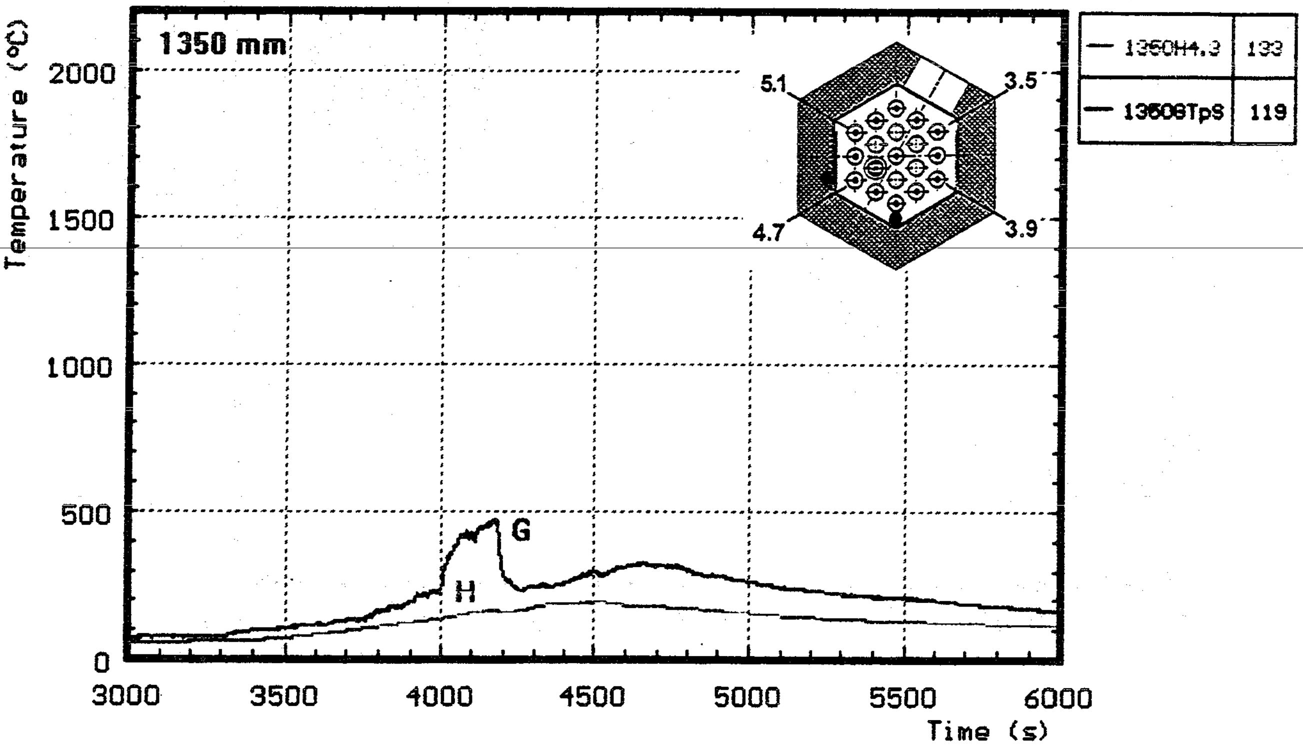

H : heated rods
G : gas temperature
Bkpl : bundle head plate

Fig. 42: CORA-W2; Temperatures at fixed elevations (1450, 1350 mm)

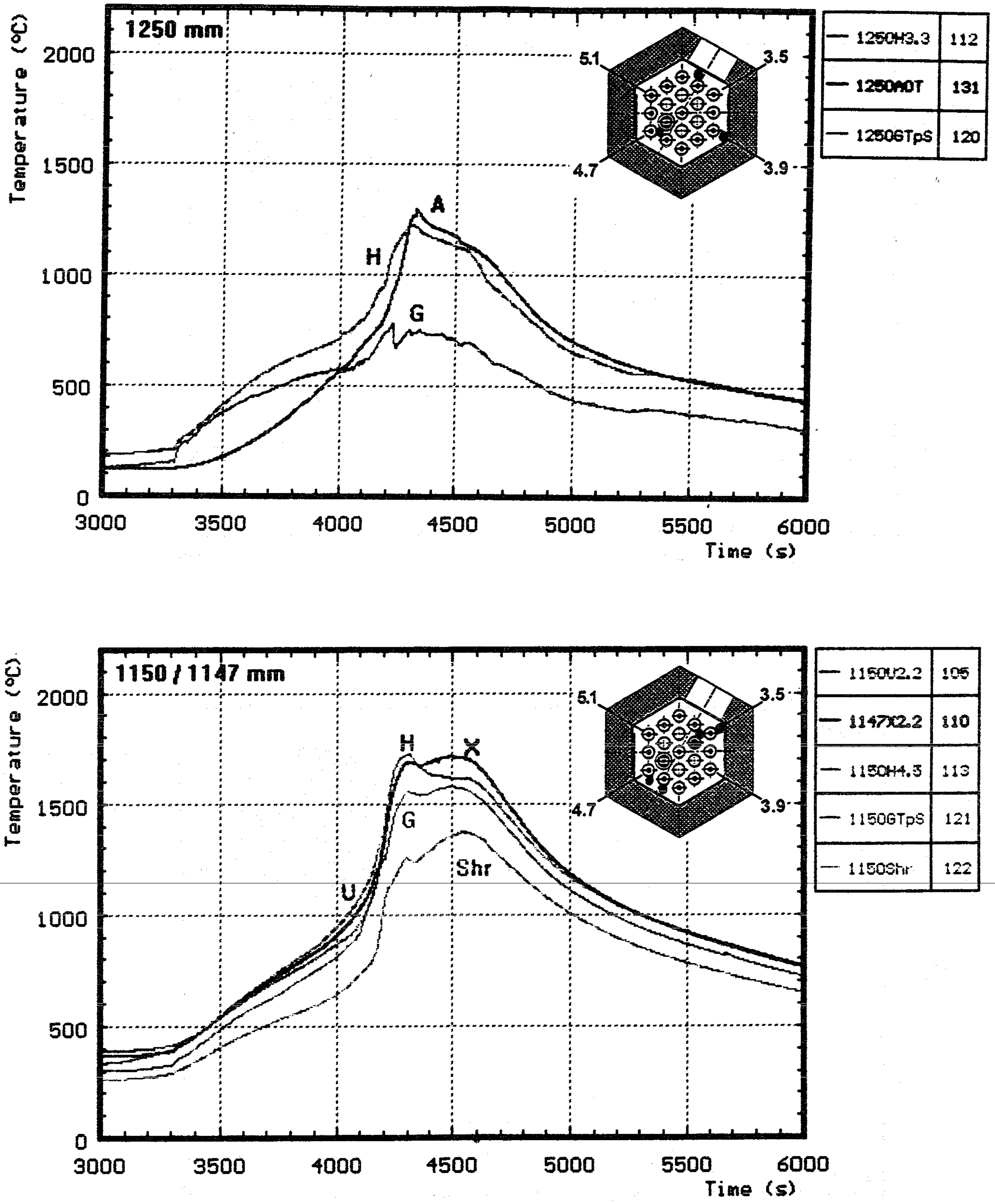

H : heated rods
U : unheated rods
X :on unheated rods

G : gas temperature
Shr : on shroud
A : on guide tube

Fig. 43: CORA-W2; Temperatures at fixed elevations (1250, 1150 mm)

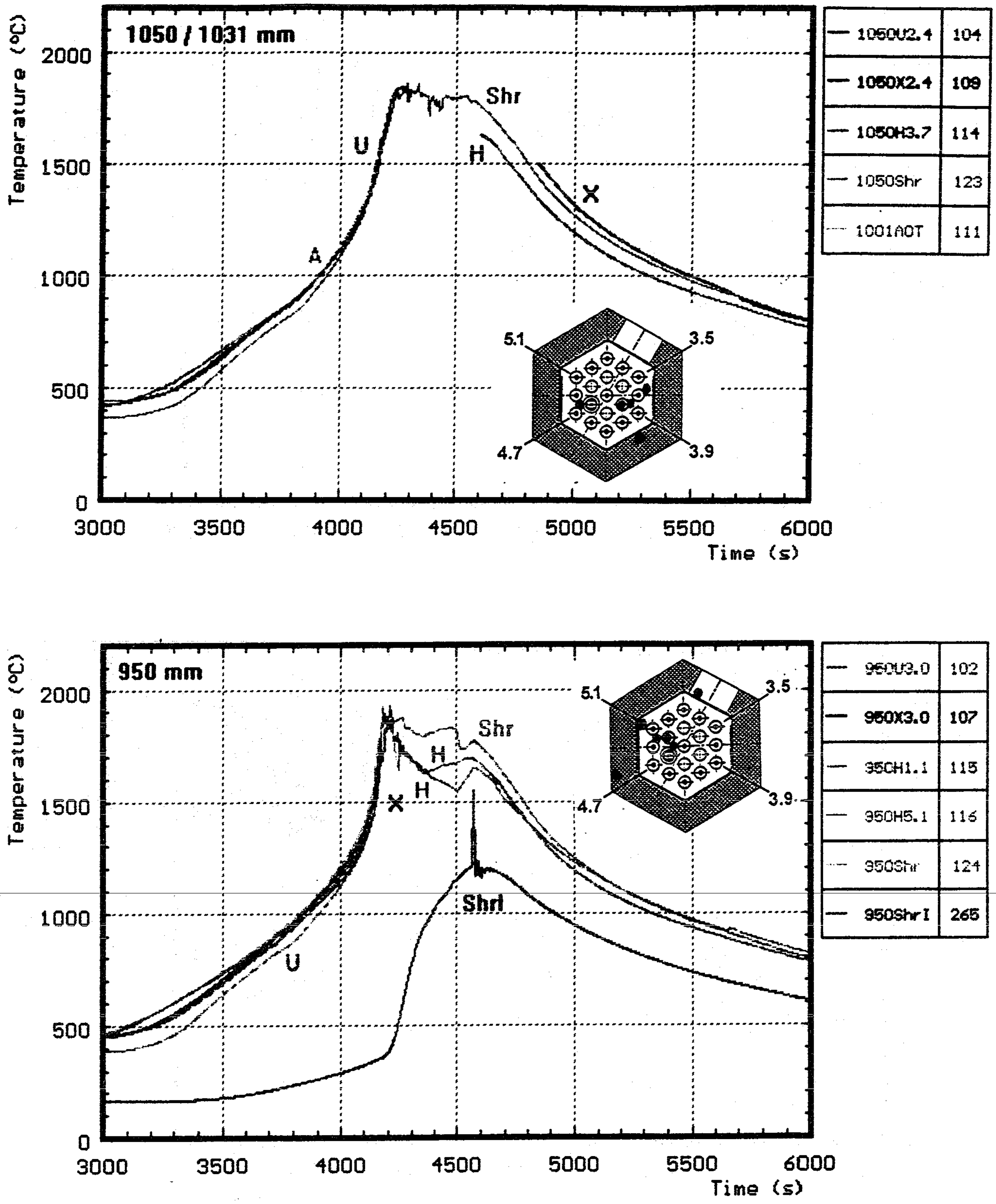

H : heated rods
U : unheated rods
X :on unheated rods
ShrI : shroud insulation
Shr : on shroud
A : on guide tube

Fig. 44: CORA-W2; Temperatures at fixed elevations (1050, 950 mm)

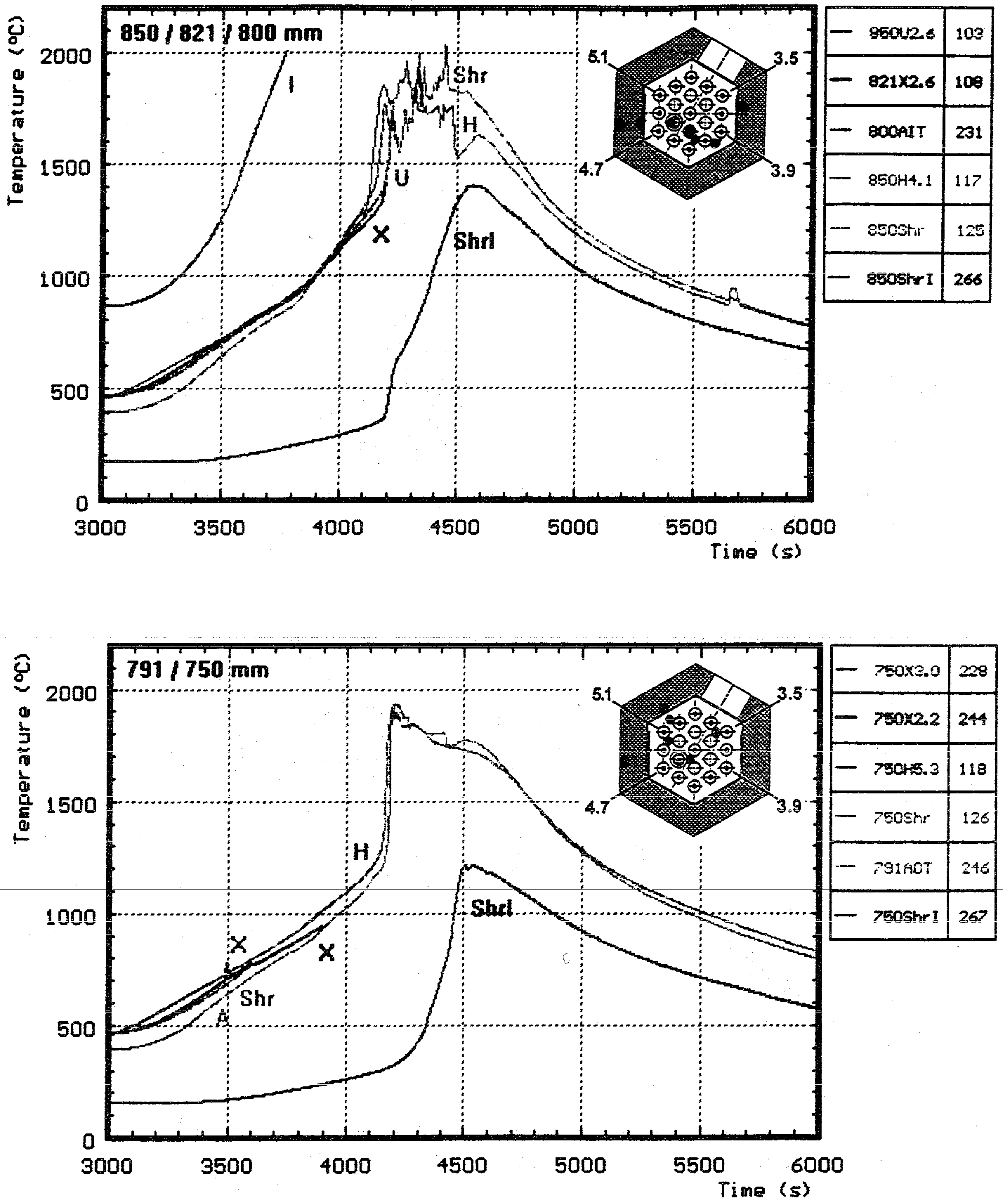

H : heated rods
U : unheated rods
X :on unheated rods
I : on absorber
ShrI : shroud insulation
Shr : on shroud
A : on guide tube

Fig. 45: CORA-W2; Temperatures at fixed elevations (850, 750 mm)

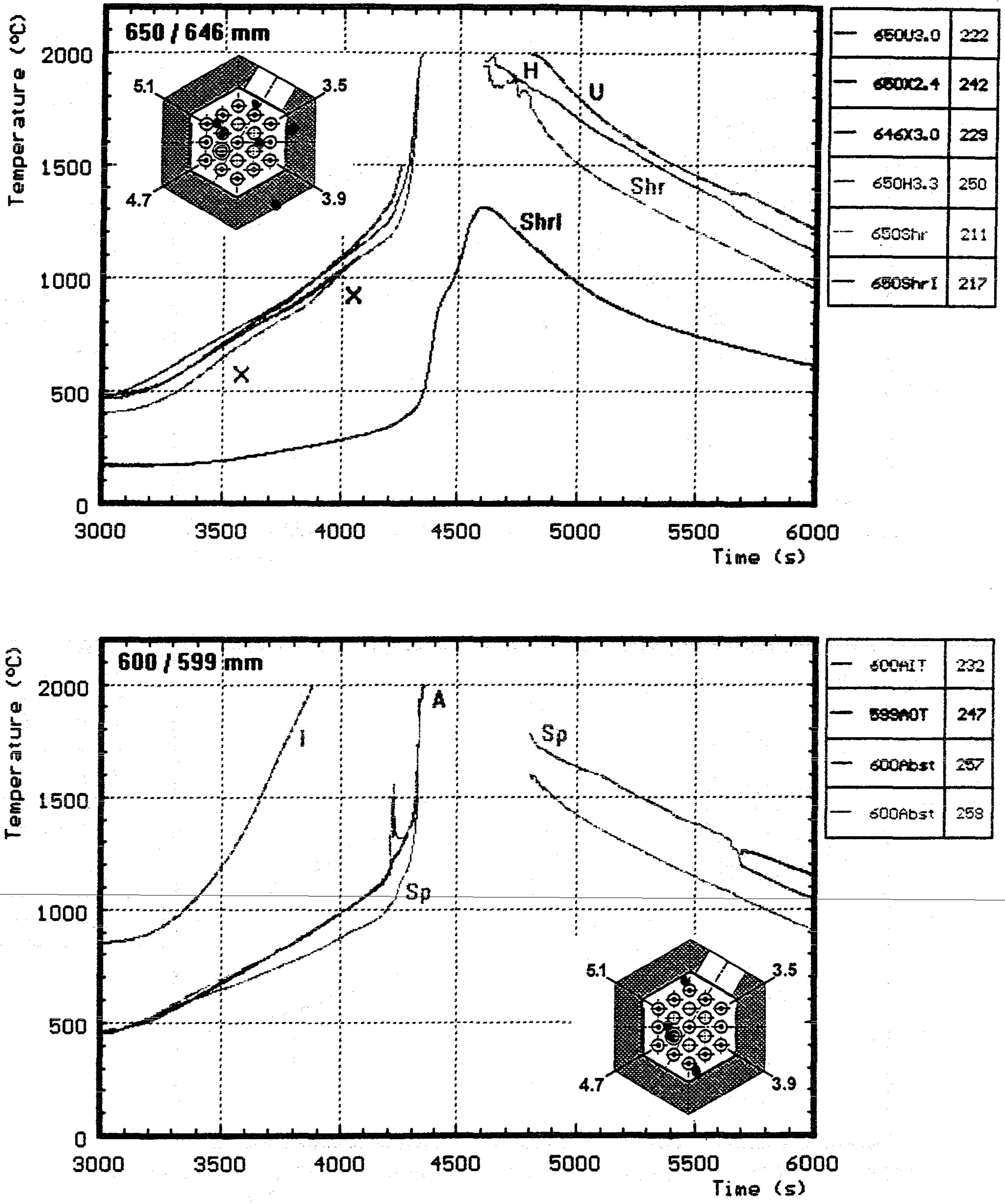

H : heated rods
U : unheated rods
X :on unheated rods
Sp : spacer
Shr : on shroud
ShrI : shroud insulation
I : on absorber
A : on guide tube

Fig. 46: CORA-W2; Temperatures at fixed elevations (650, 600 mm)

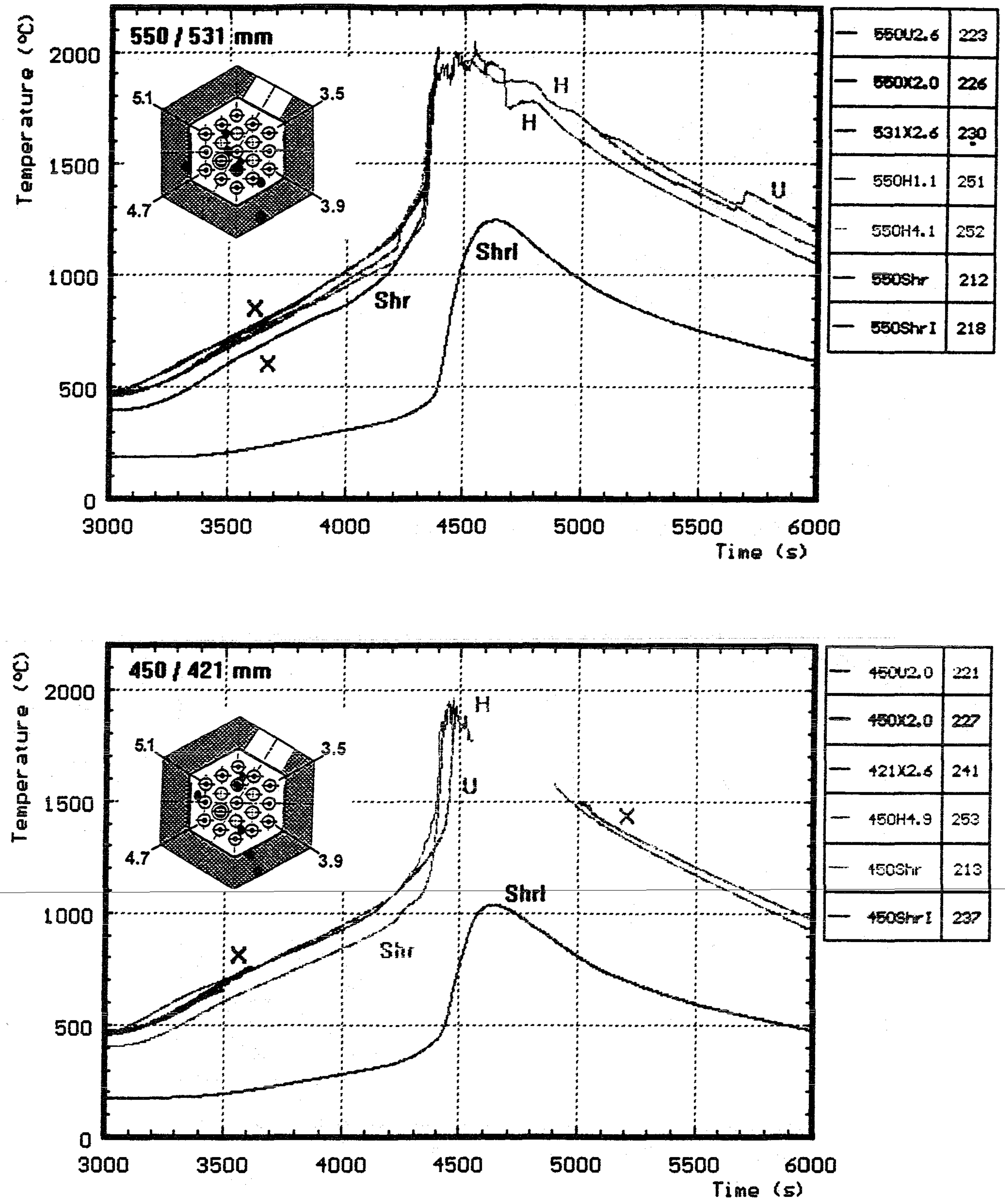

H : heated rods
U : unheated rods
X :on unheated rods

Shr : on shroud
ShrI : shroud insulation

Fig. 47: CORA-W2; Temperatures at fixed elevations (550, 450 mm)

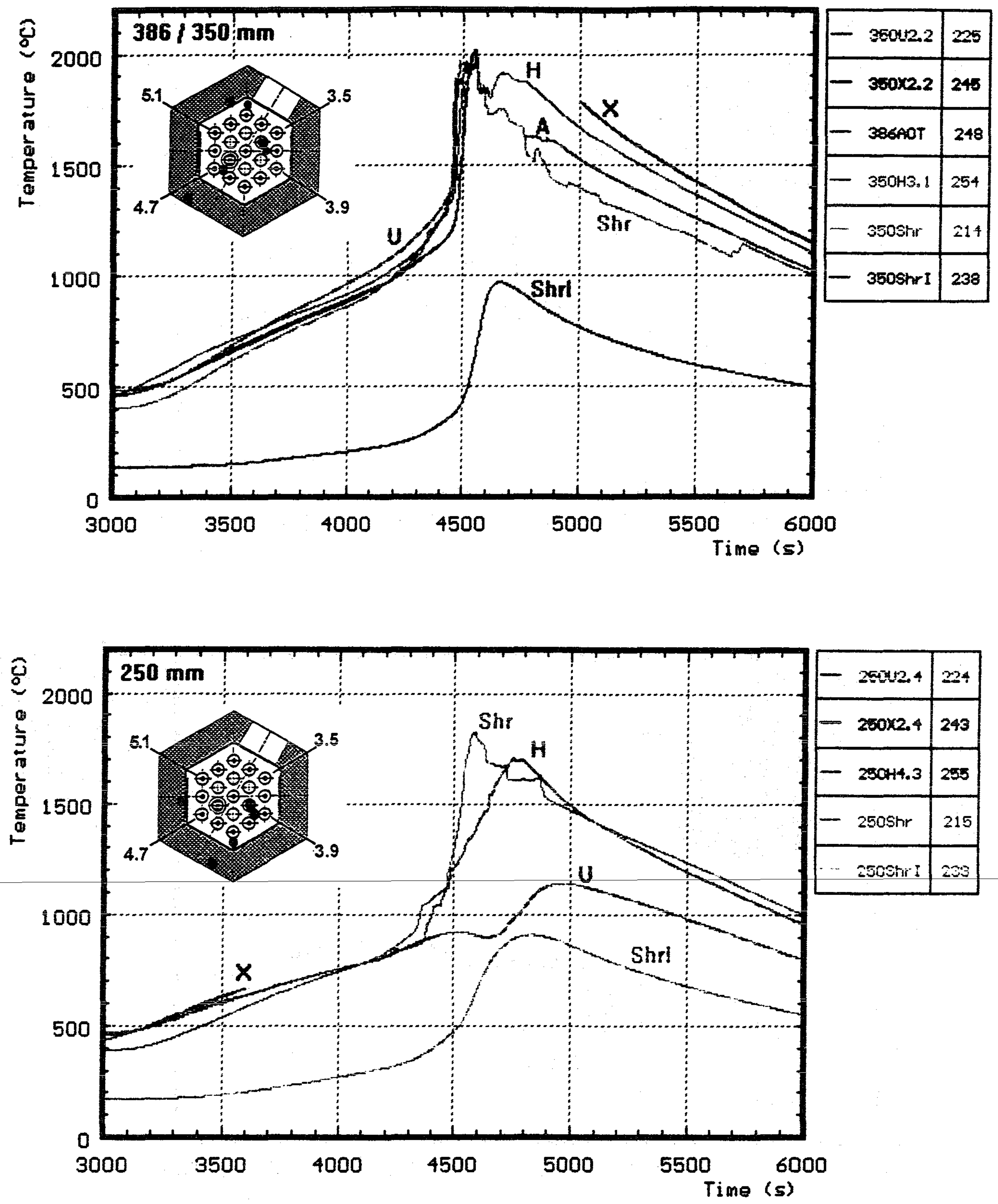

H : heated rods
U : unheated rods
X :on unheated rods

Shr : on shroud
ShrI : shroud insulation
A : on guide tube

Fig. 48: CORA-W2; Temperatures at fixed elevations (350, 250 mm)

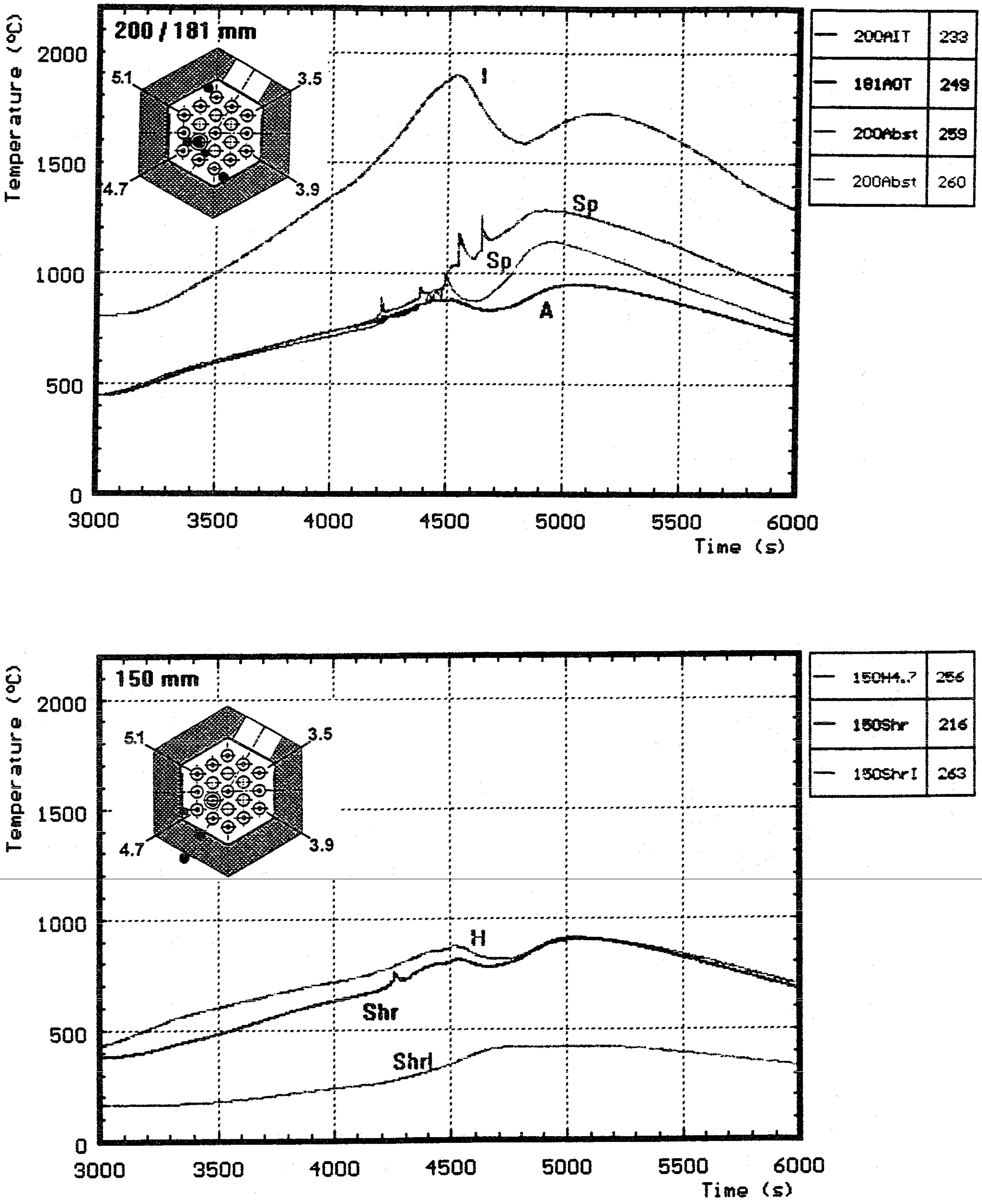

H : heated rods
I : on absorber
A : on guide tube

Shr : on shroud
ShrI : shroud insulation
Sp : spacer

Fig. 49: CORA-W2; Temperatures at fixed elevations (200, 150 mm)

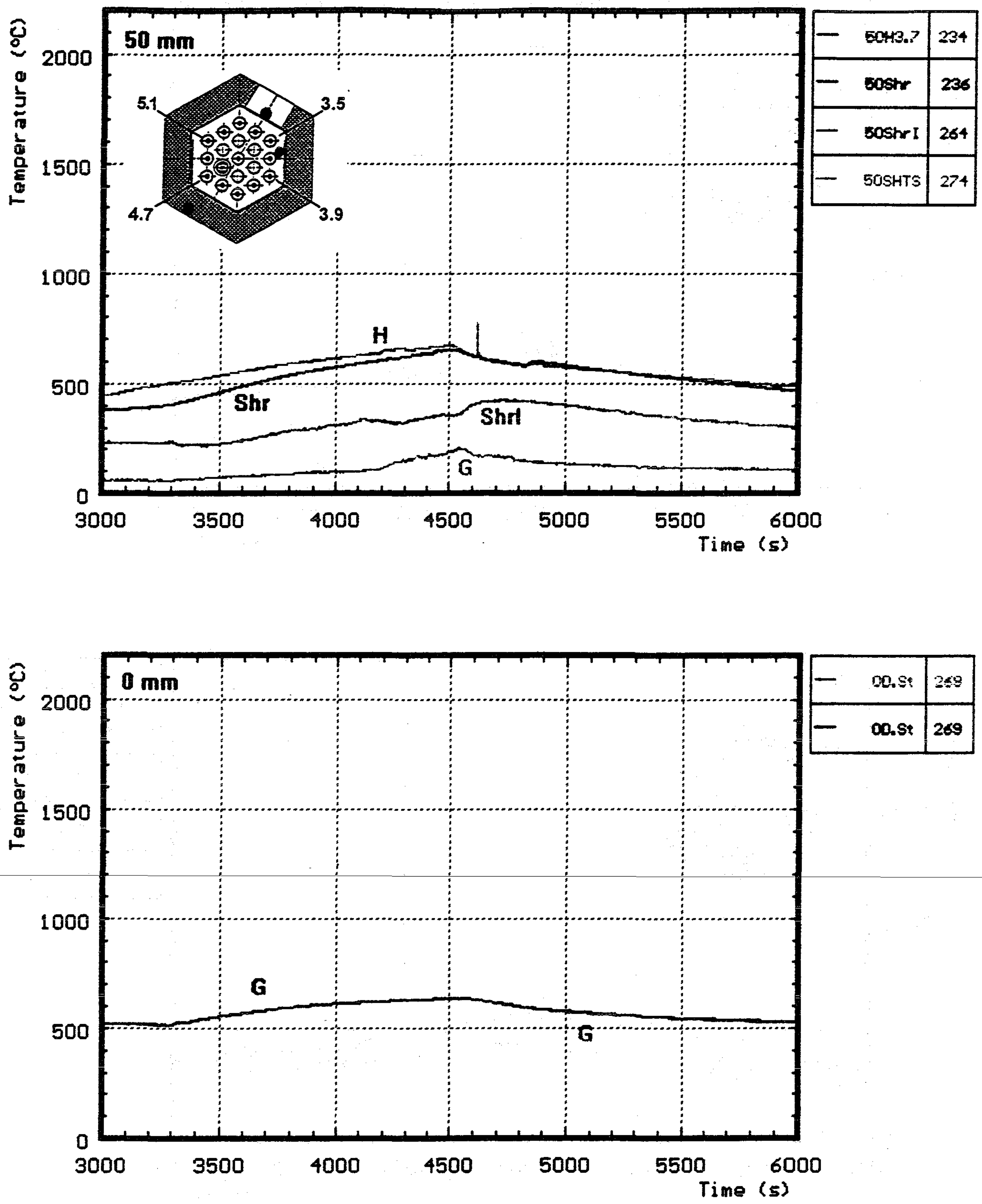

H : heated rods
G : gas temperature
Shr : on shroud
ShrI : shroud insulation

Fig. 50: CORA-W2; Temperatures at fixed elevations (50, 0 mm)

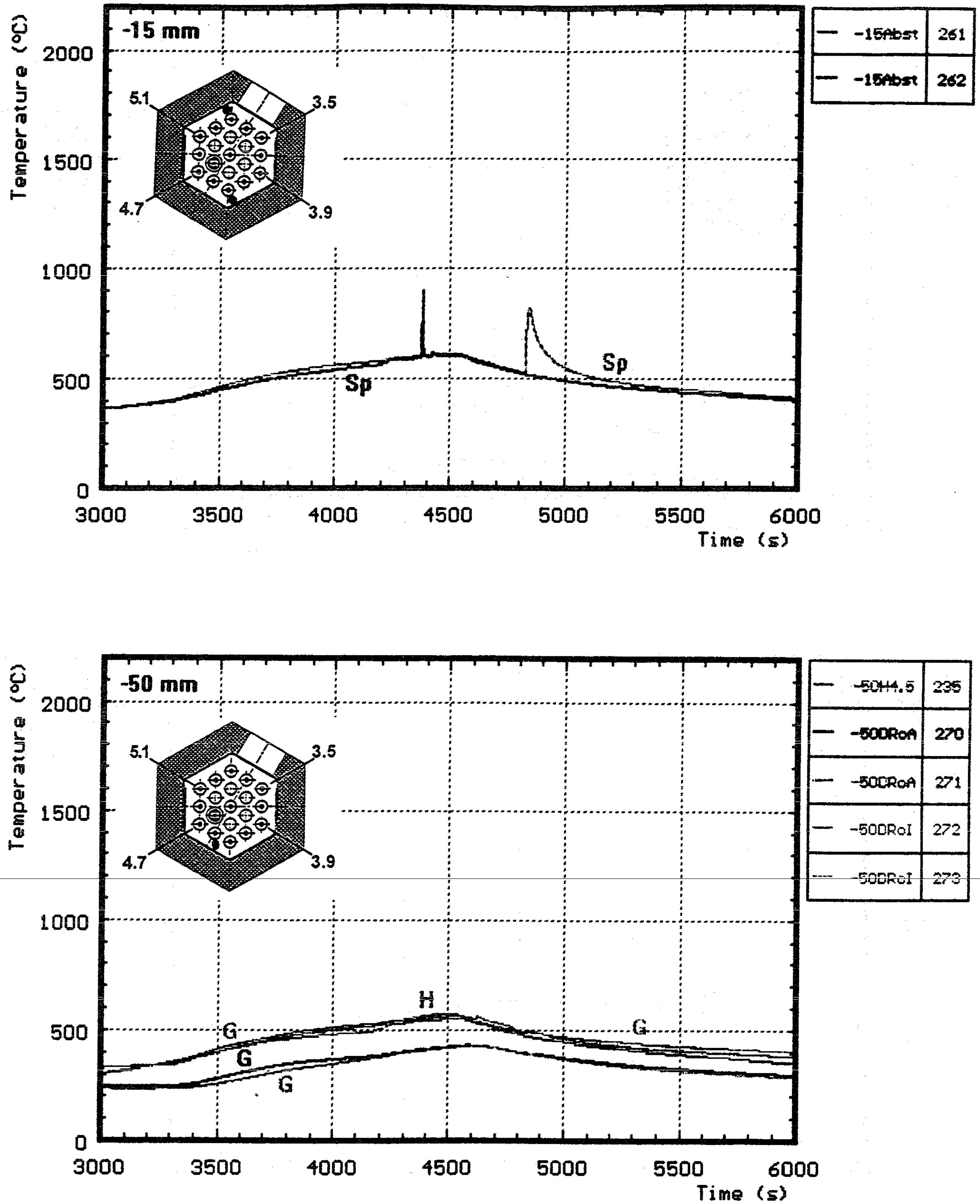

H	: heated rods	**Sp**	: spacer
G	: gas temperature		

Fig. 51: CORA-W2; Temperatures at fixed elevations (-15, -50 mm)

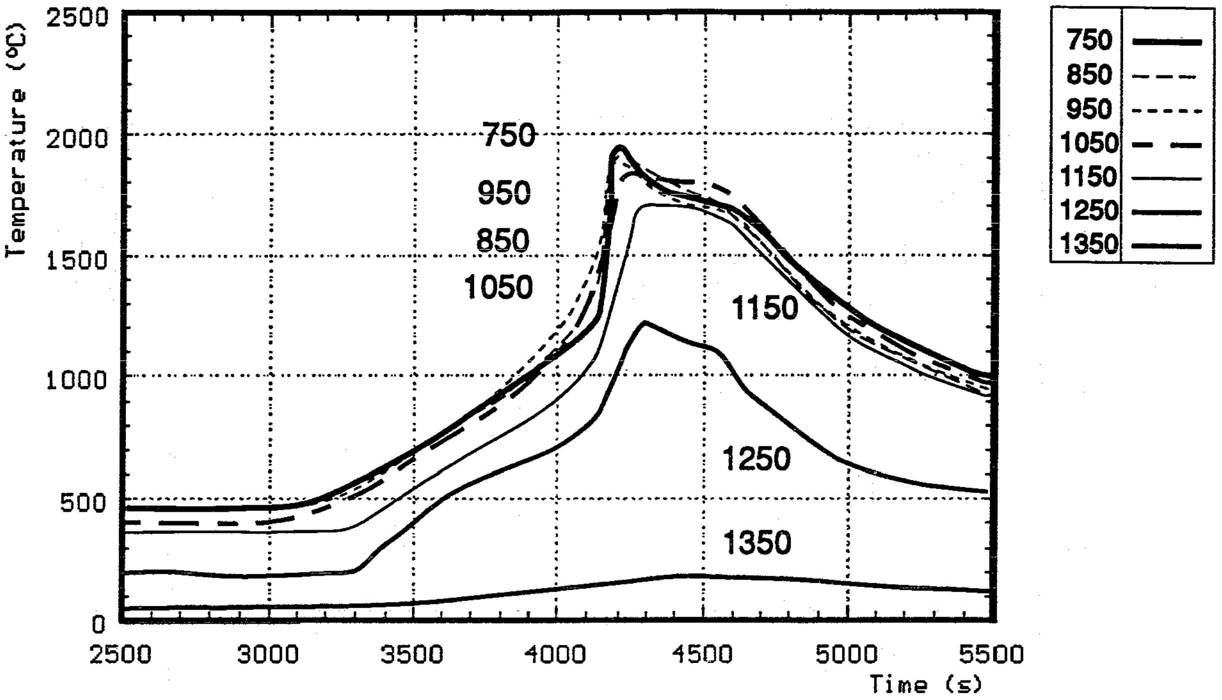

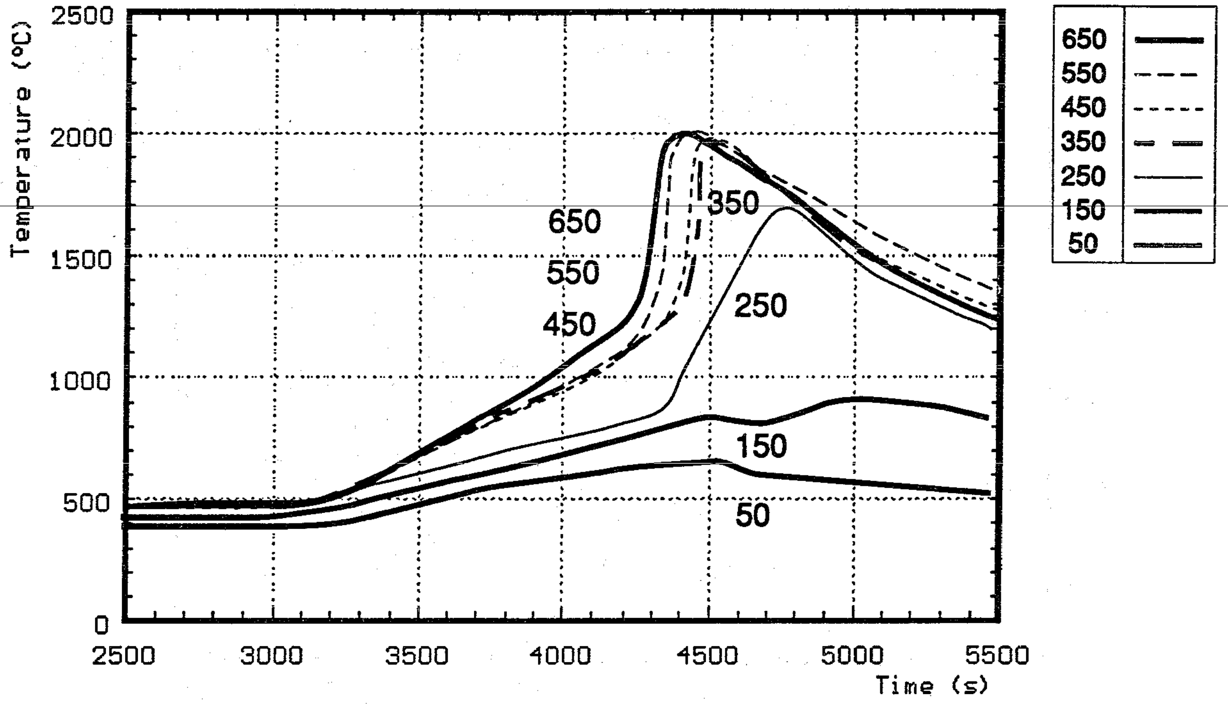

Fig. 52: CORA-W2; Best estimate bundle temperatures at different elevations

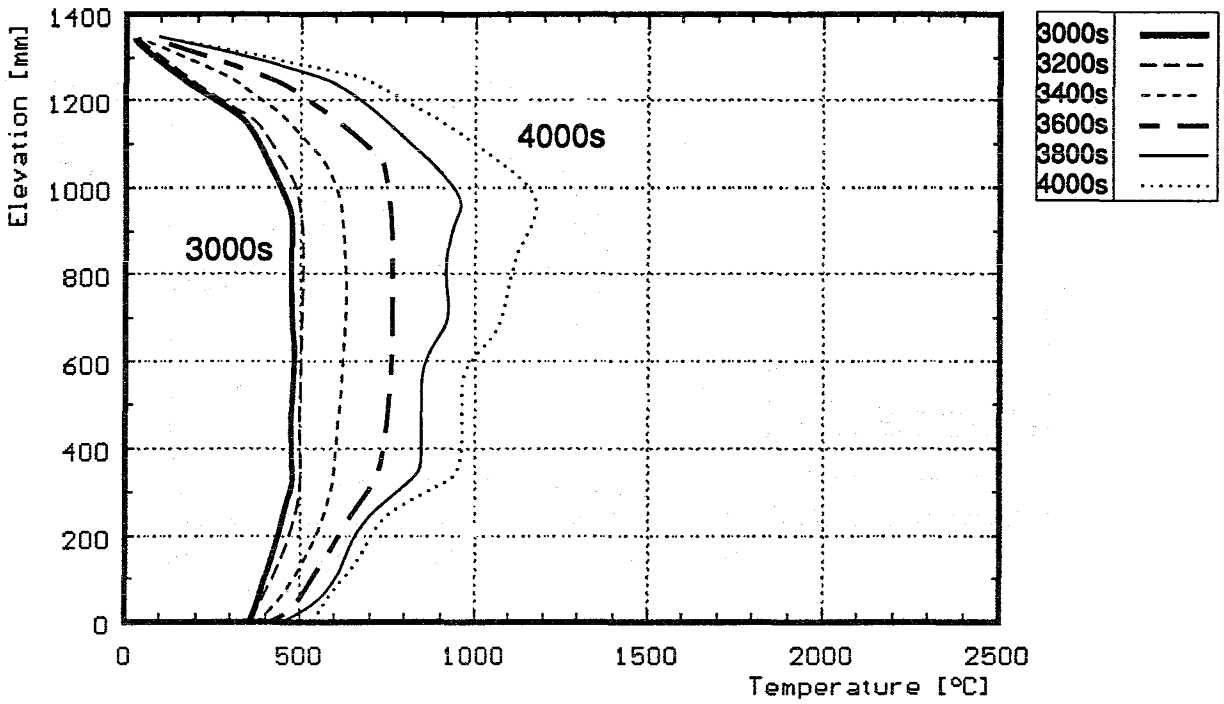

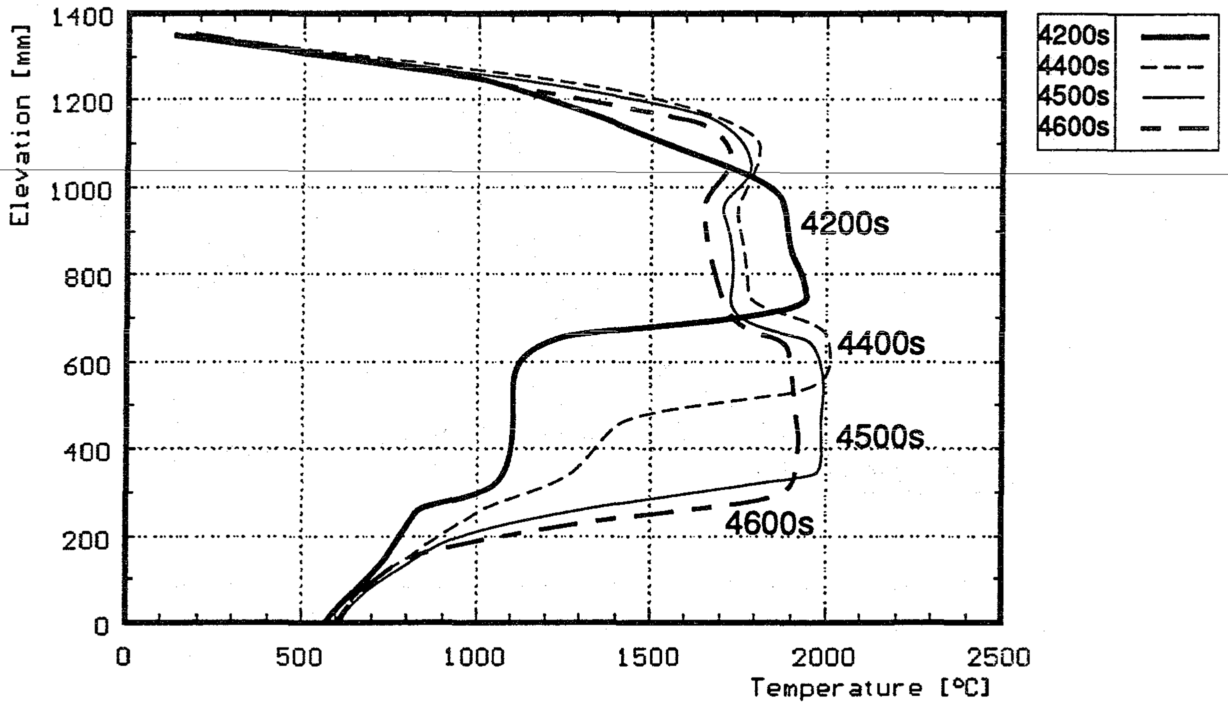

Fig. 53: Axial temperature distribution during the transient of test CORA-W2

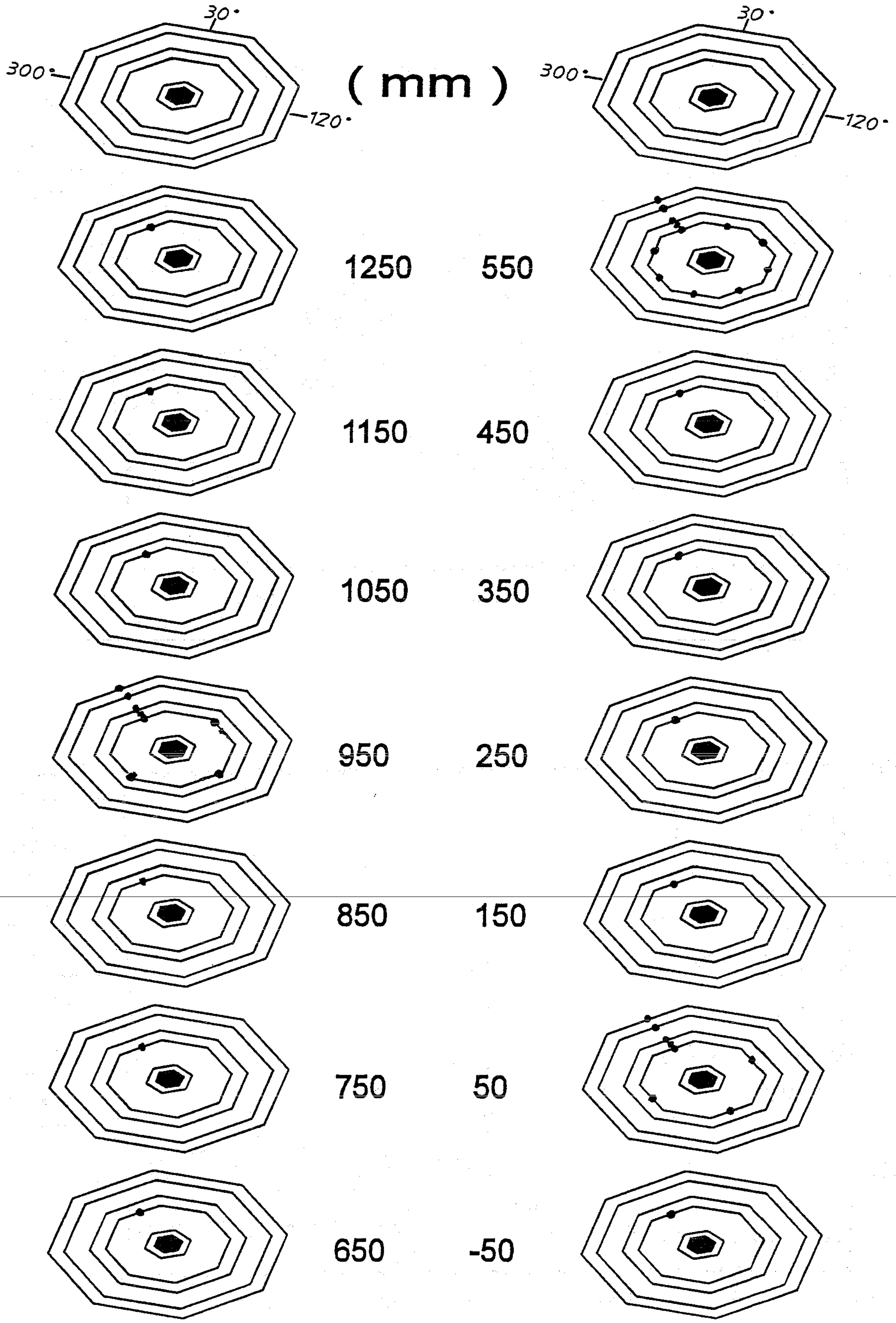

Fig. 54: Locations of thermocouples in the high temperature shield (CORA-W2)

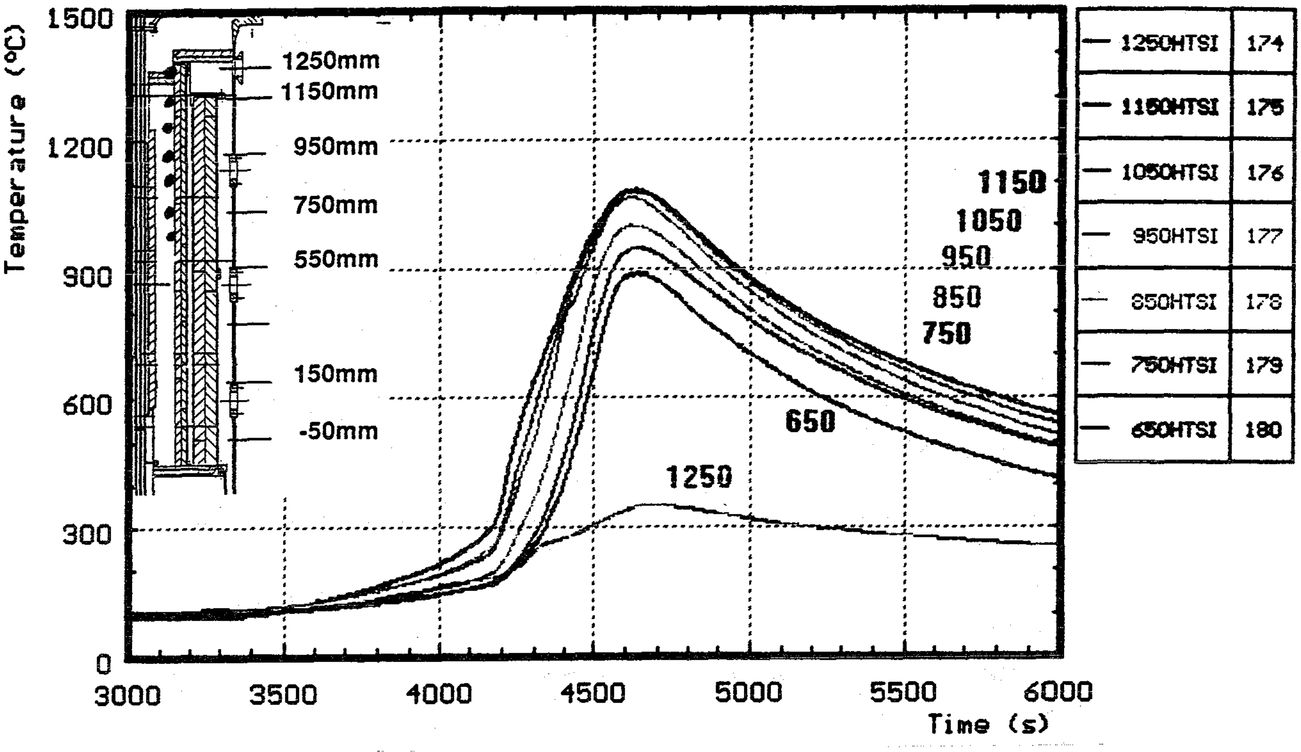

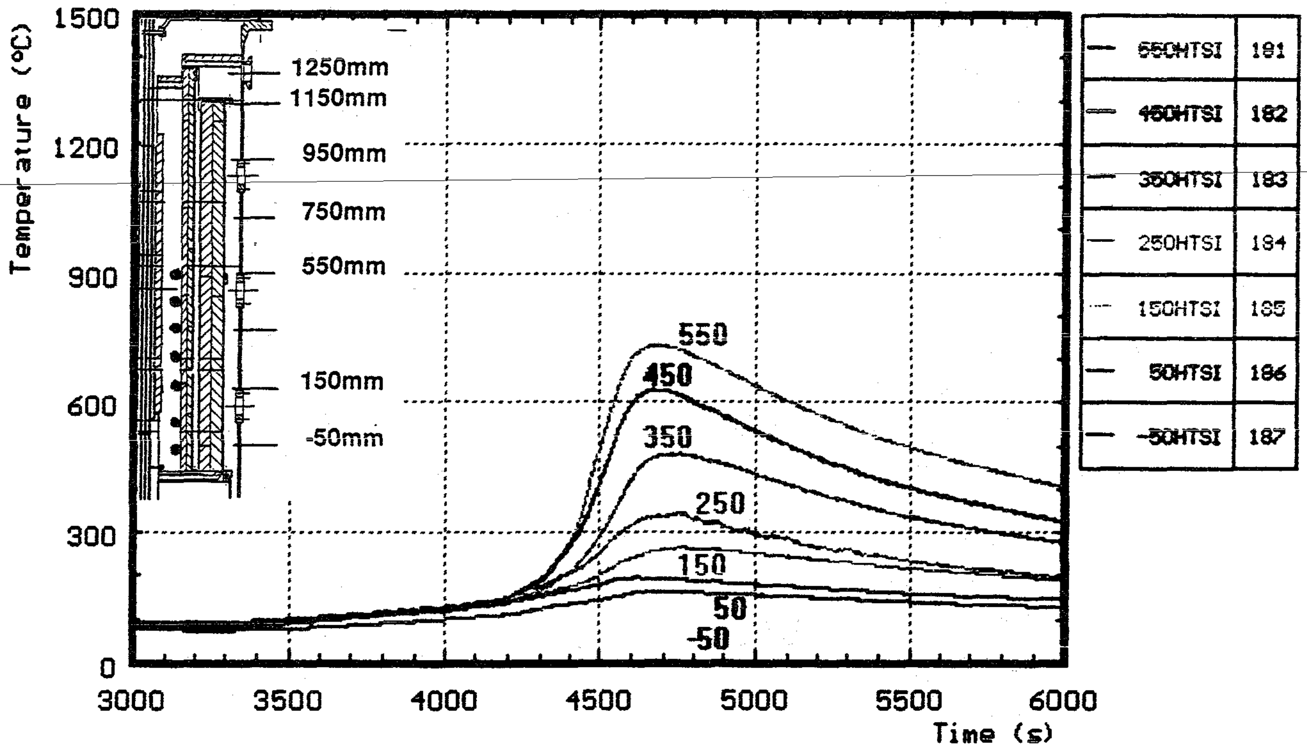

Fig. 56: CORA-W2; Temperatures of HTS, Temperature on inner surface, 153 mm radius

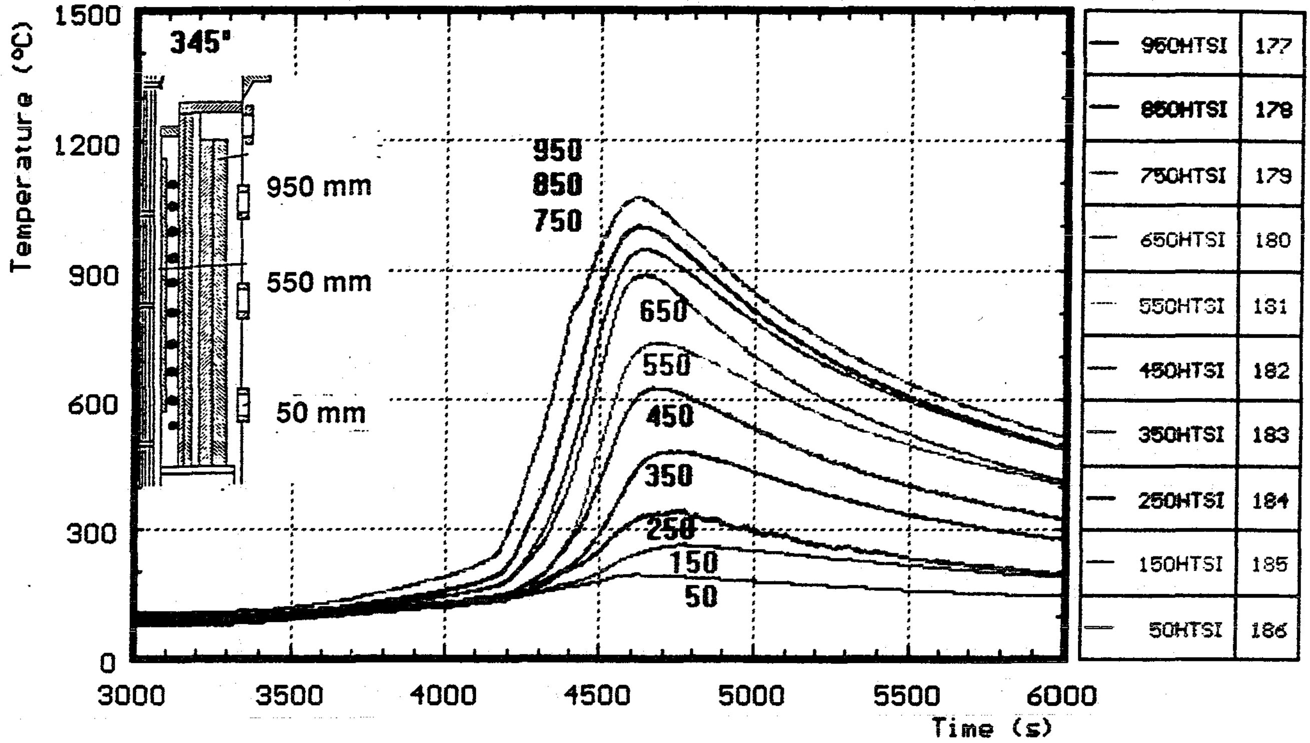

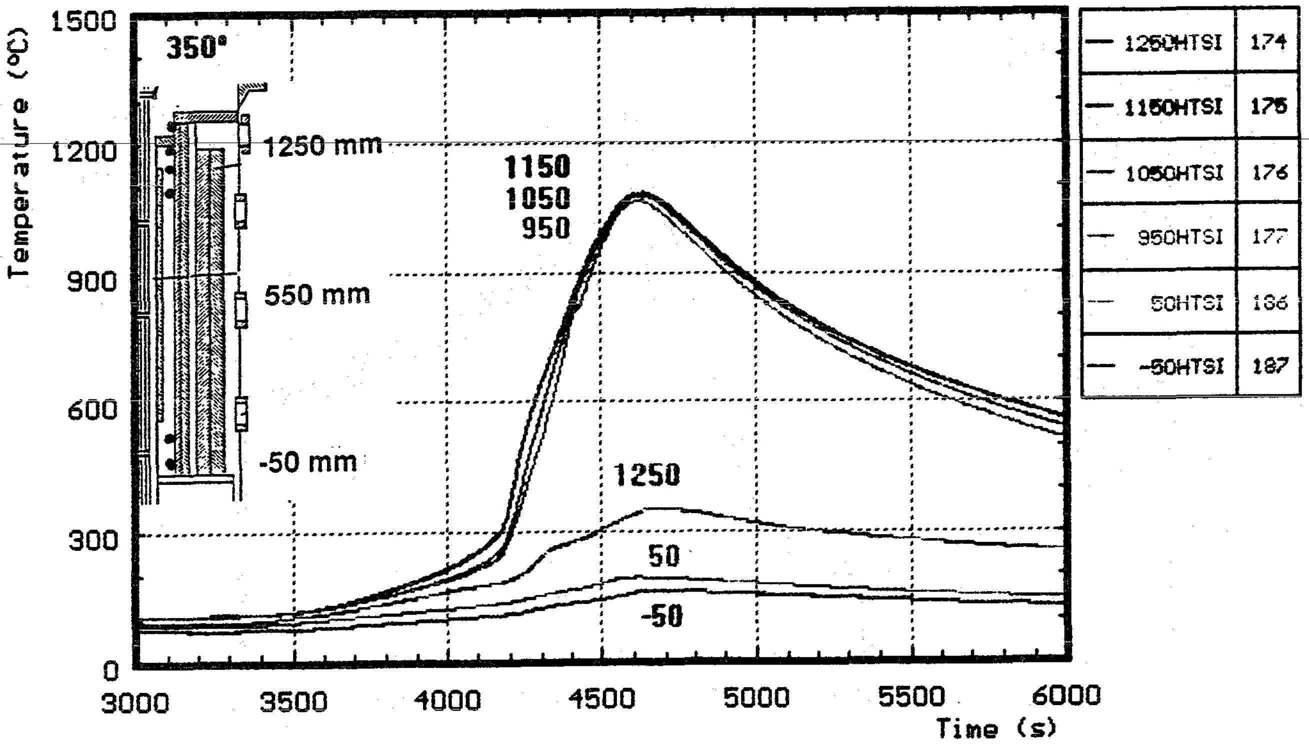

Fig. 57: CORA-W2; Temperatures of HTS, Temperature on inner surface, 153 mm radius

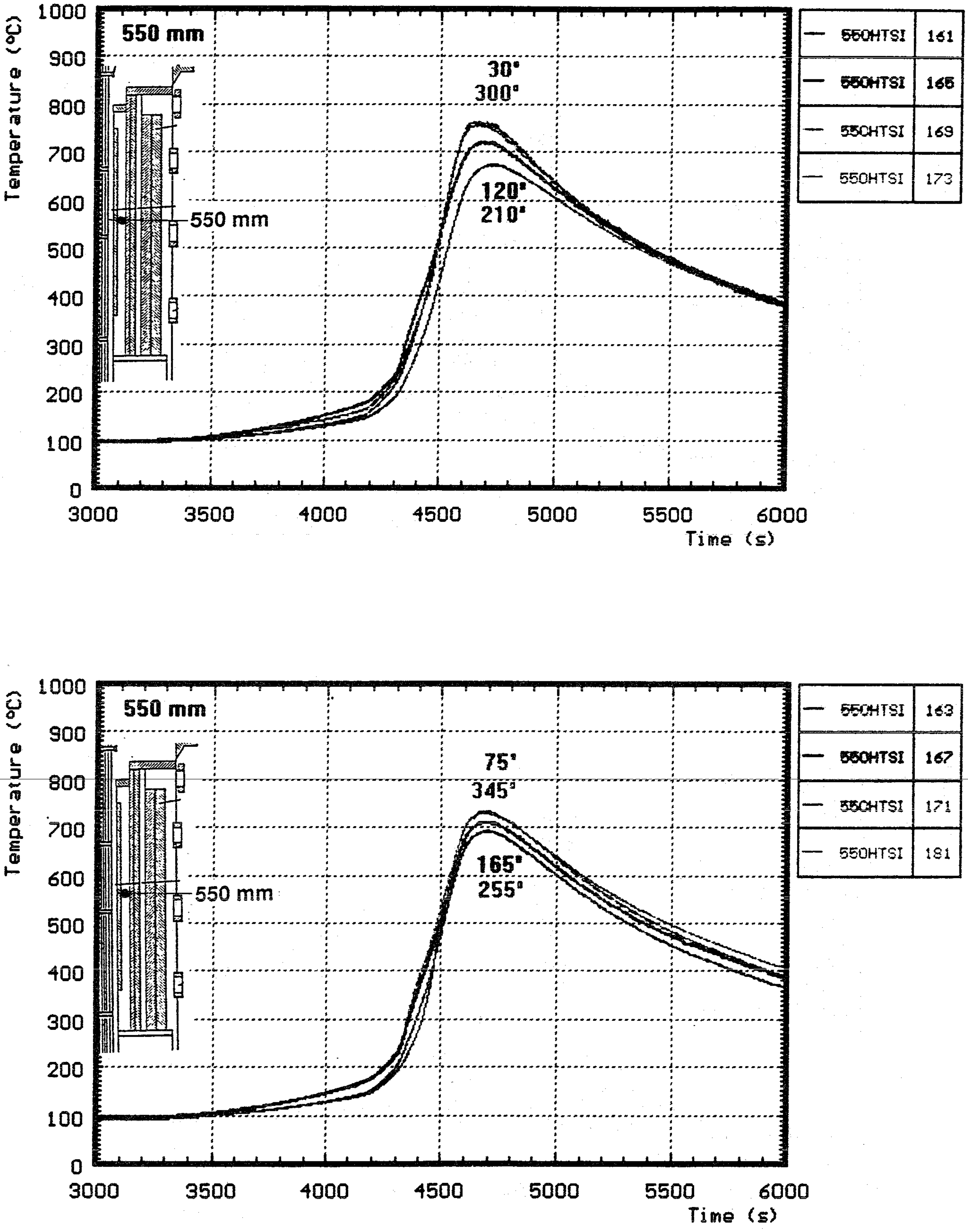

Fig. 58: CORA-W2; Temperatures of HTS, inner surface at 153 mm radius (550mm)

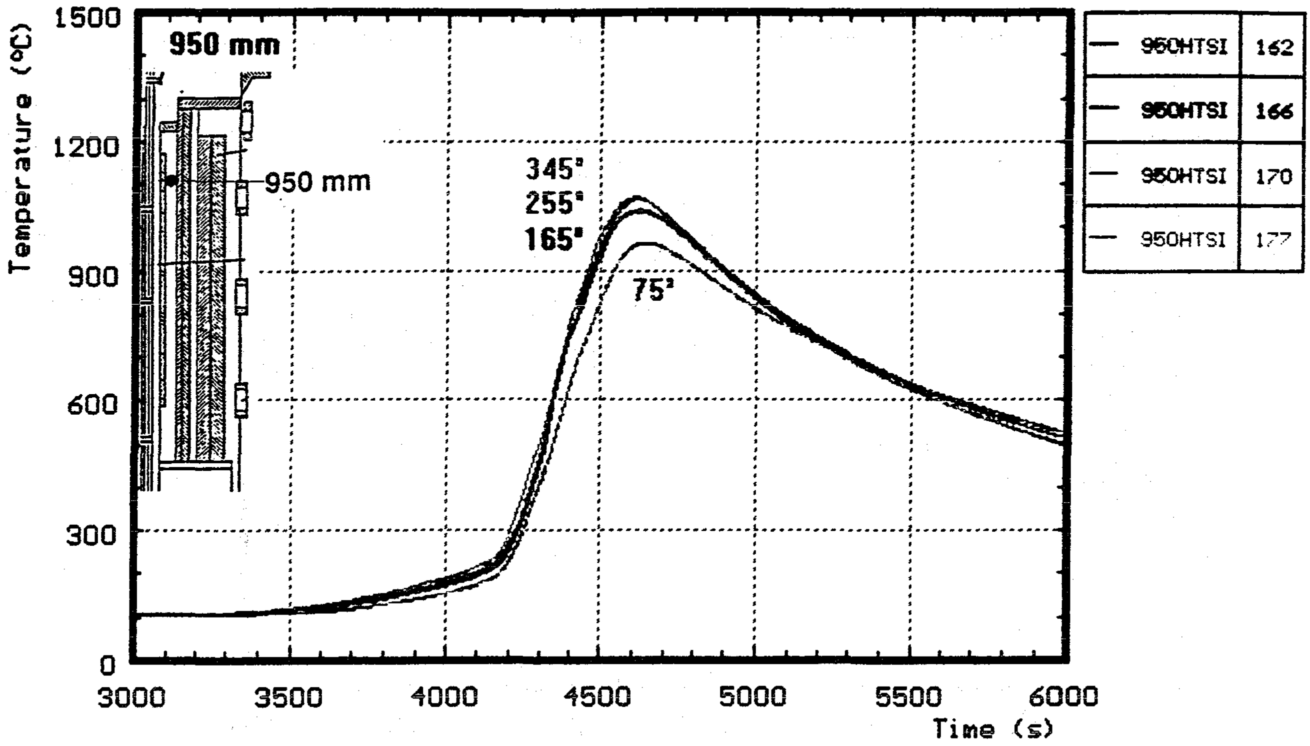

Fig. 59: CORA-W2; Temperatures of HTS, inner surface at 153 mm radius (950mm)

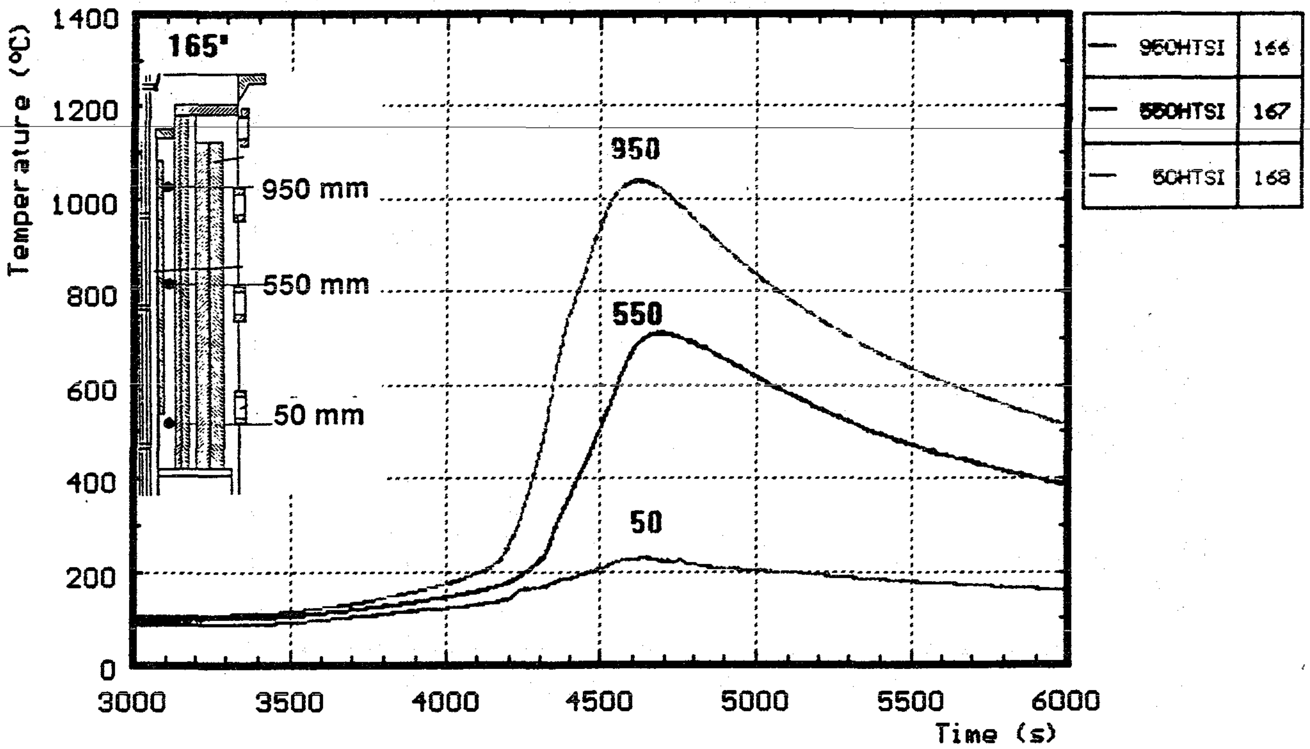

Fig. 60: CORA-W2; Temperatures of HTS, inner surface at 153 mm radius

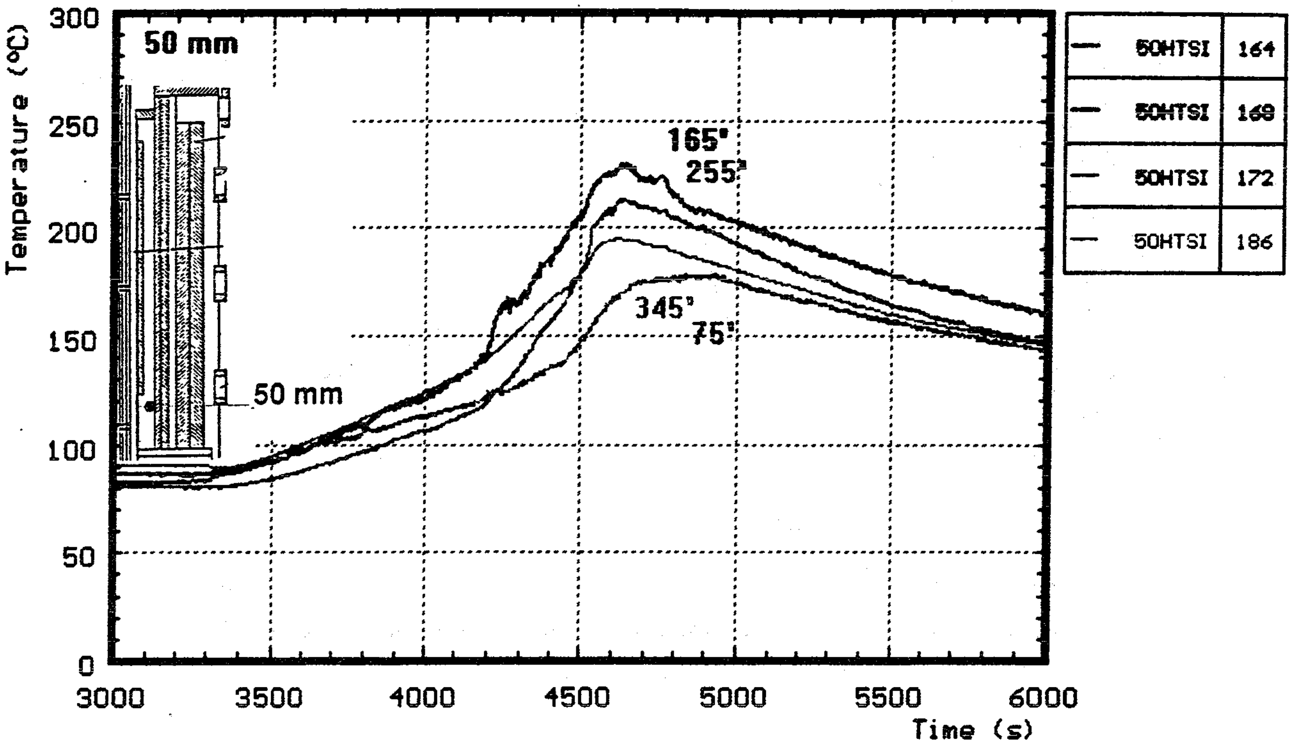

Fig. 61: CORA-W2; Temperatures of HTS, inner surface at 153 mm radius (50mm)

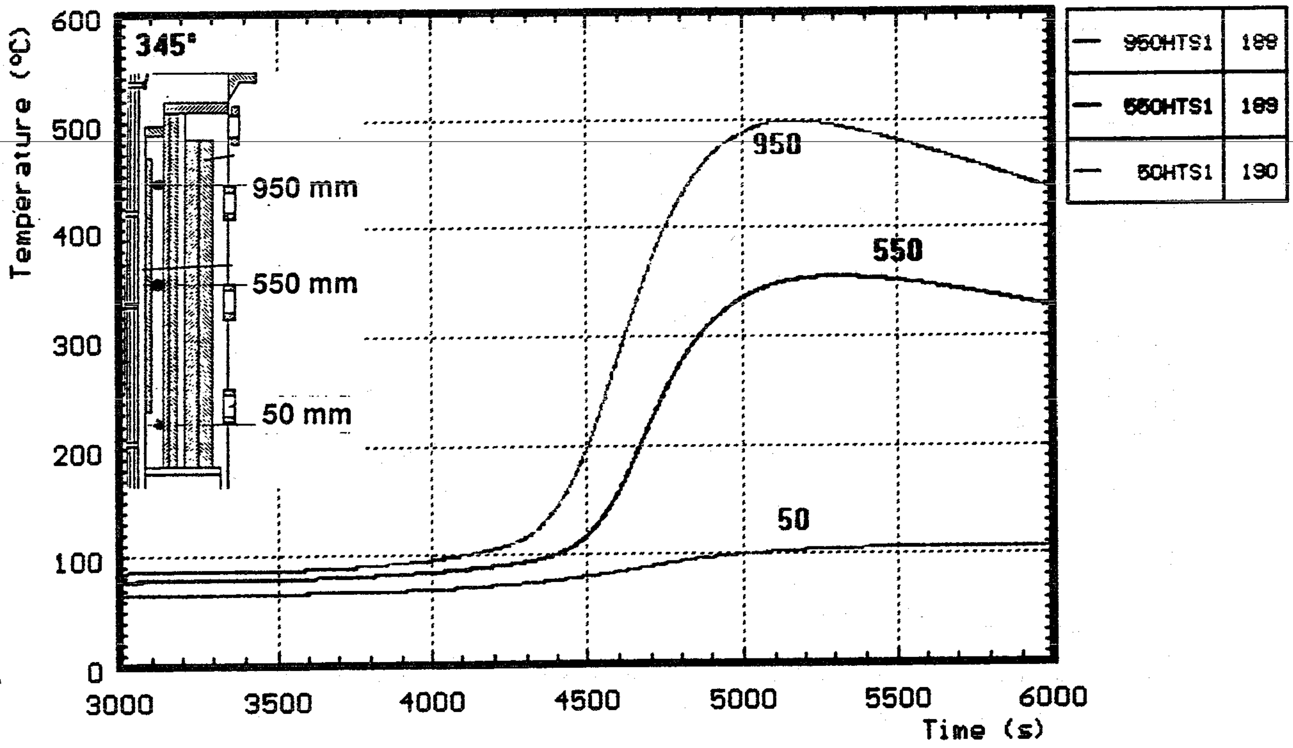

Fig. 62: CORA-W2; Temperatures of HTS, Temperatures in HT-shield at 172 mm radius

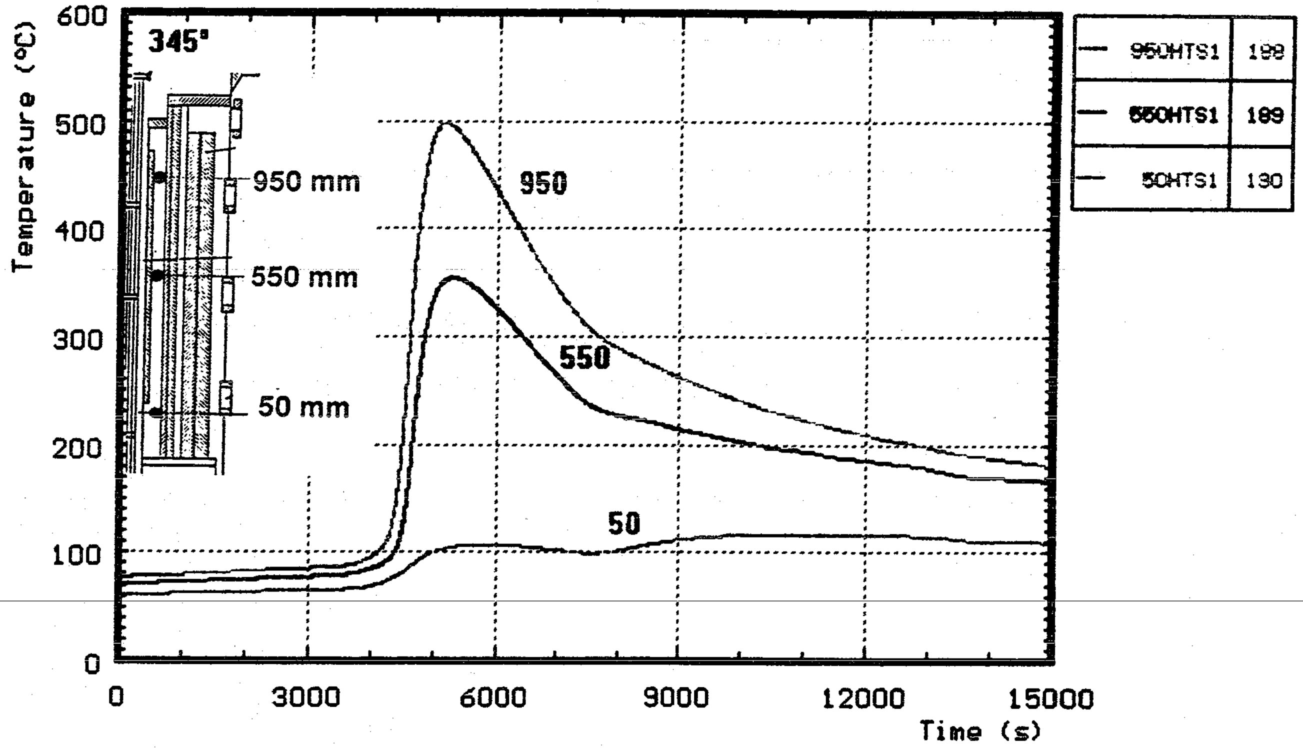

Fig. 63: CORA-W2; Temperatures of HTS, Temperatures in HT-shield at 172 mm radius (0 - 15000 s)

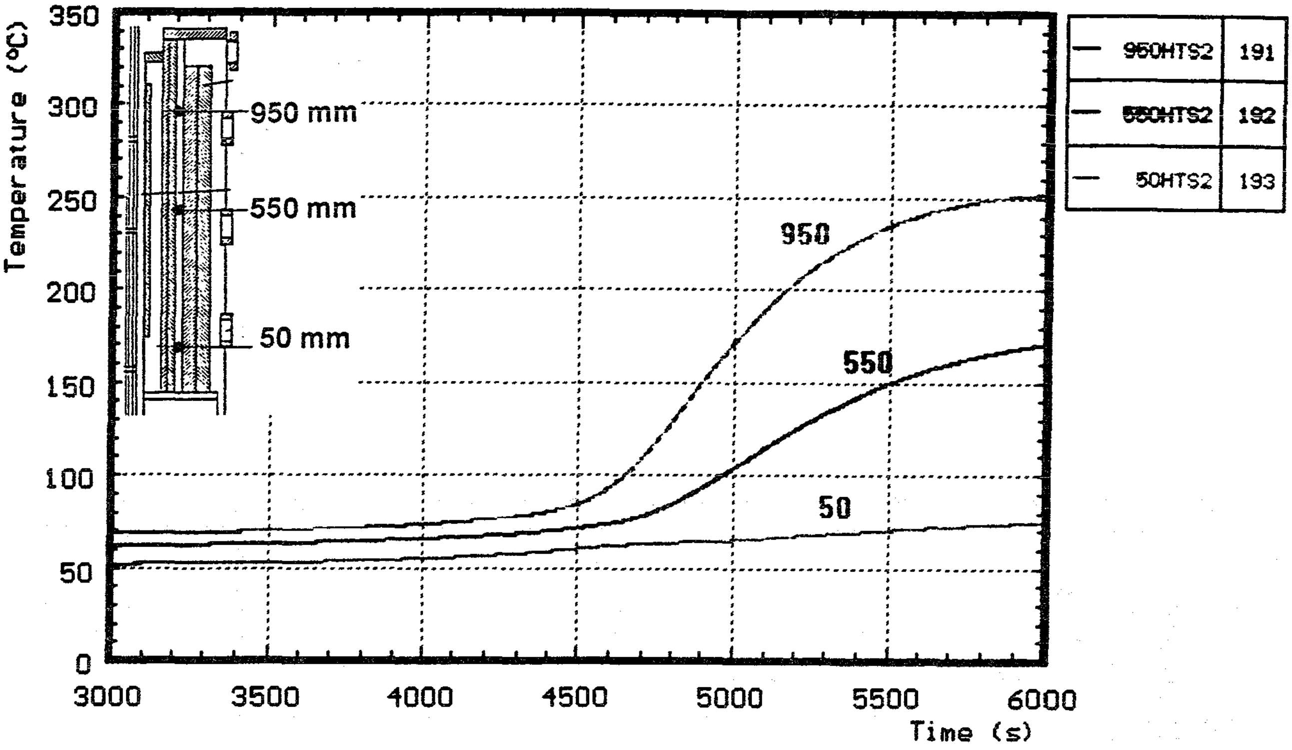

Fig. 64: CORA-W2; Temperatures of HTS, Temperatures in HT-shield at 192 mm radius

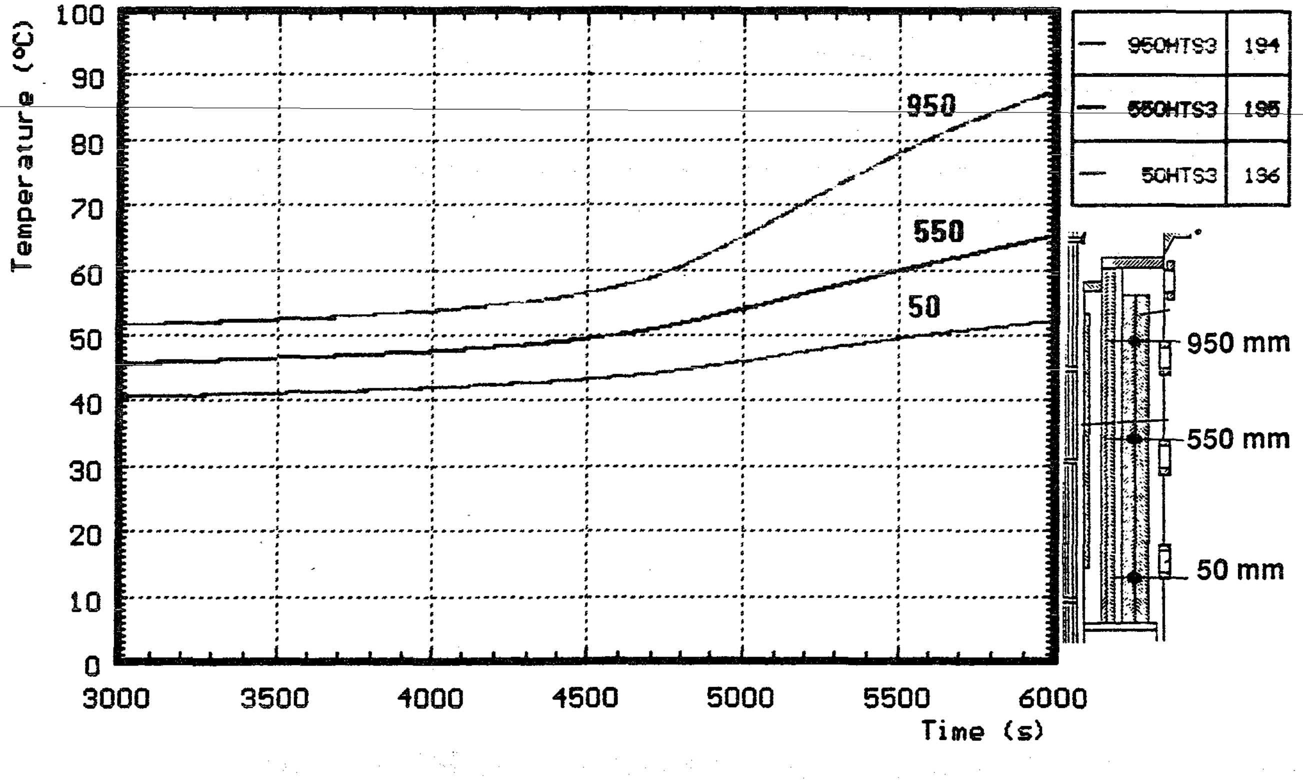

Fig. 65: CORA-W2; Temperatures of HTS, Temperatures in HT-shield at 255 mm radius

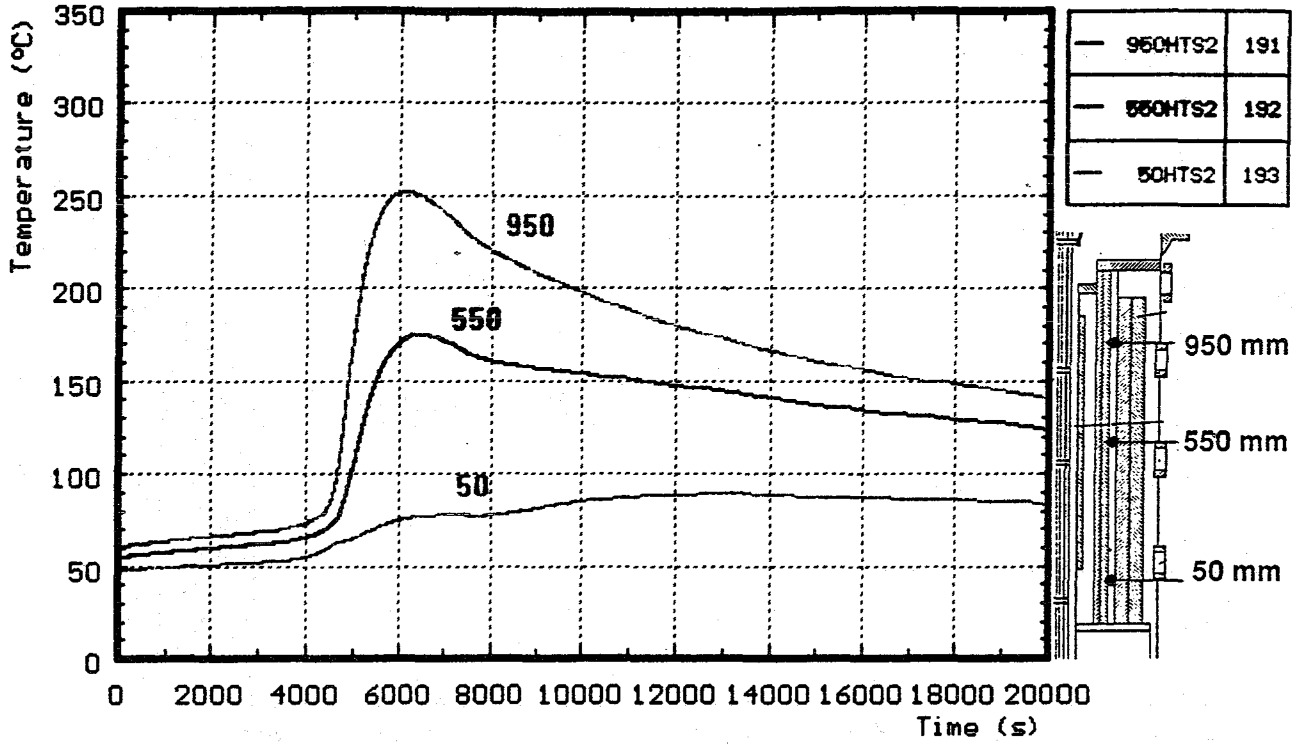

Fig. 66: CORA-W2; Temperatures of HTS, Temperatures in HT-shield at 192 mm radius (0 - 20000 s)

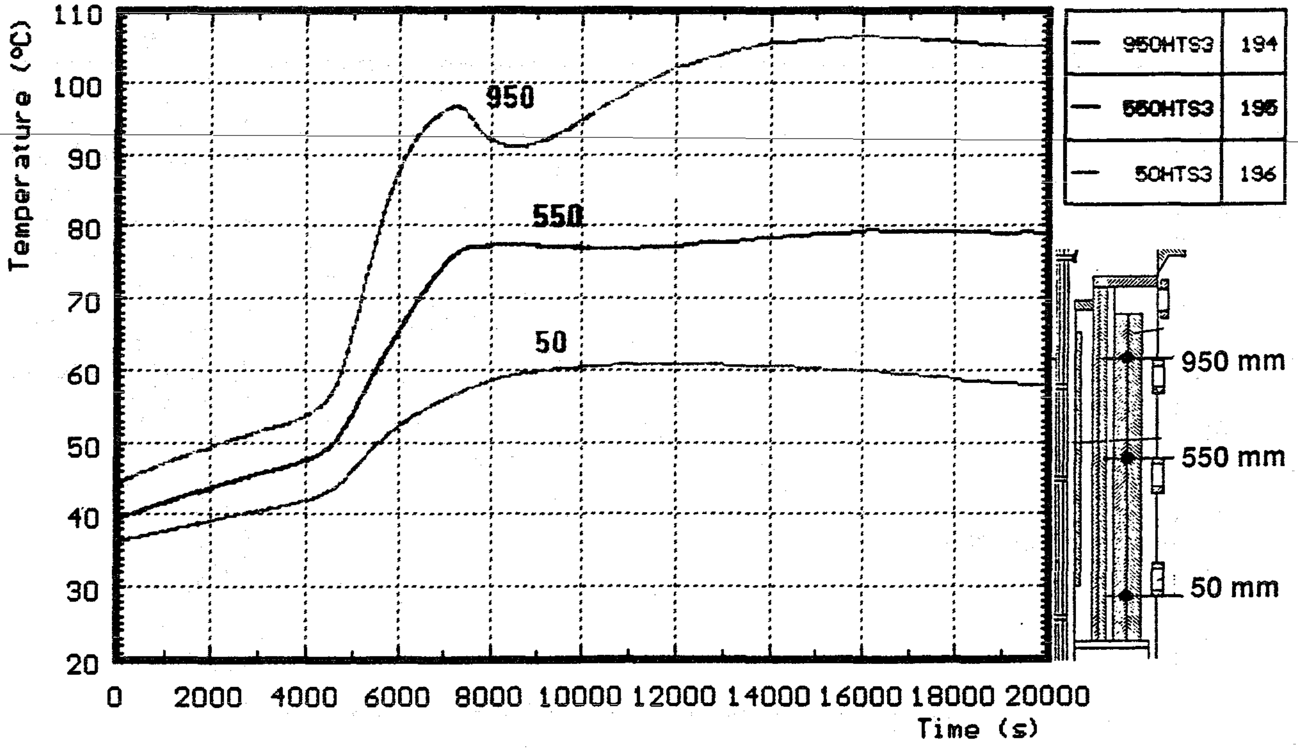

Fig. 67: CORA-W2; Temperatures of HTS, Temperatures in HT-shield at 255 mm radius (0 - 20000 s)

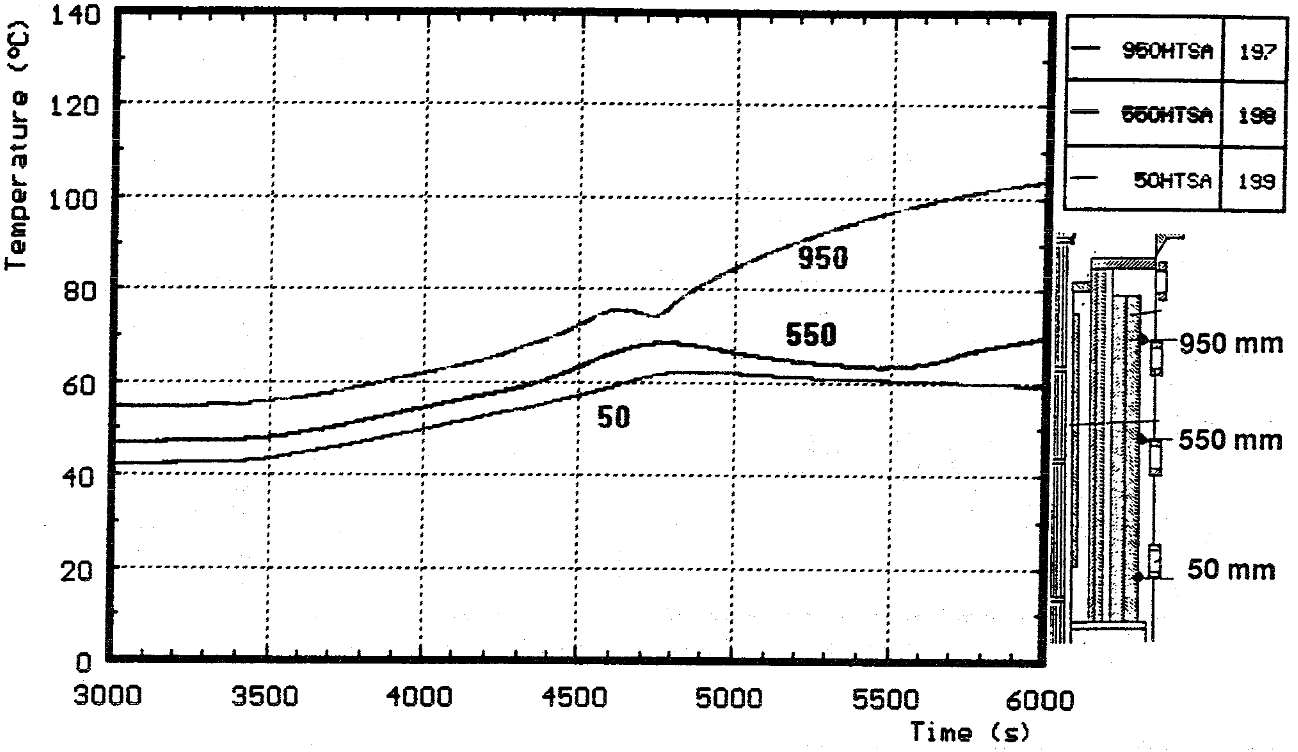

Fig. 68: CORA-W2; Temperatures of HTS, Temperatures in HT-shield at 293 mm radius

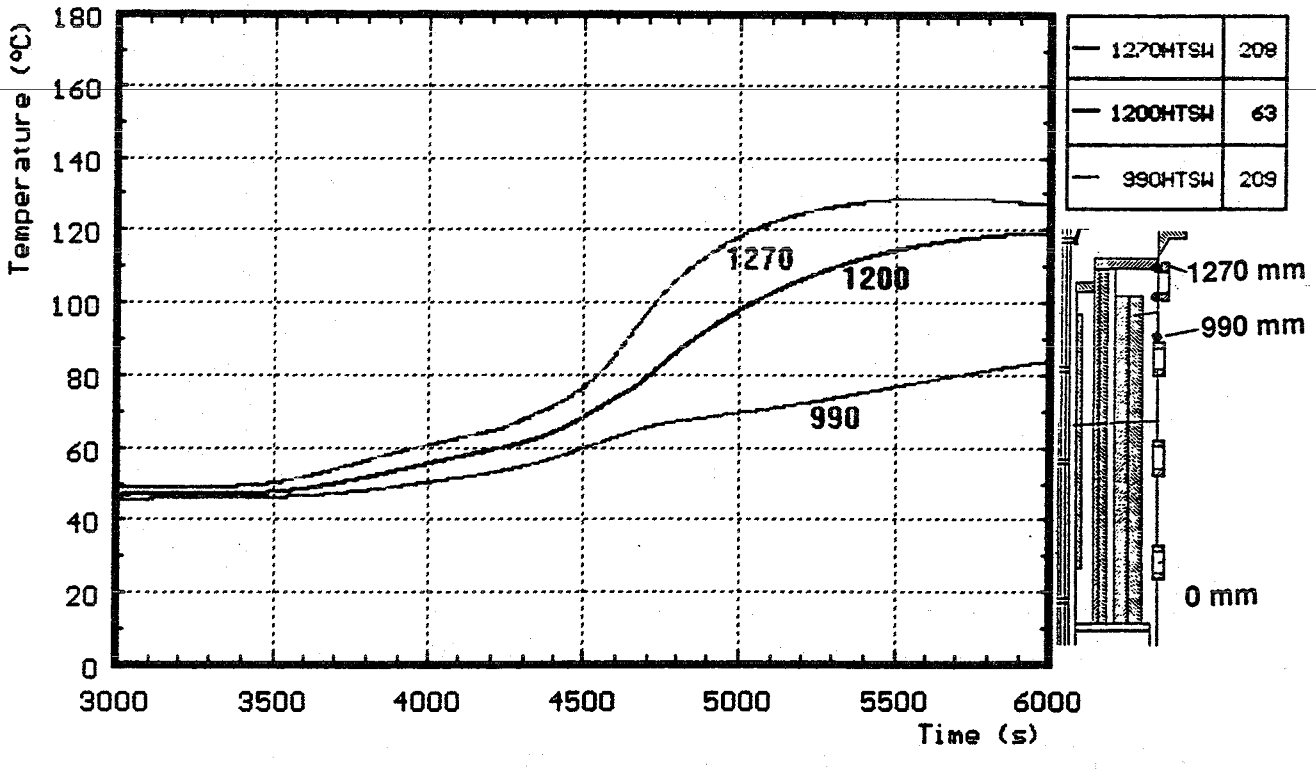

Fig. 69: CORA-W2; Temperatures of HTS, Temperatures on outer surface, 380 mm radius

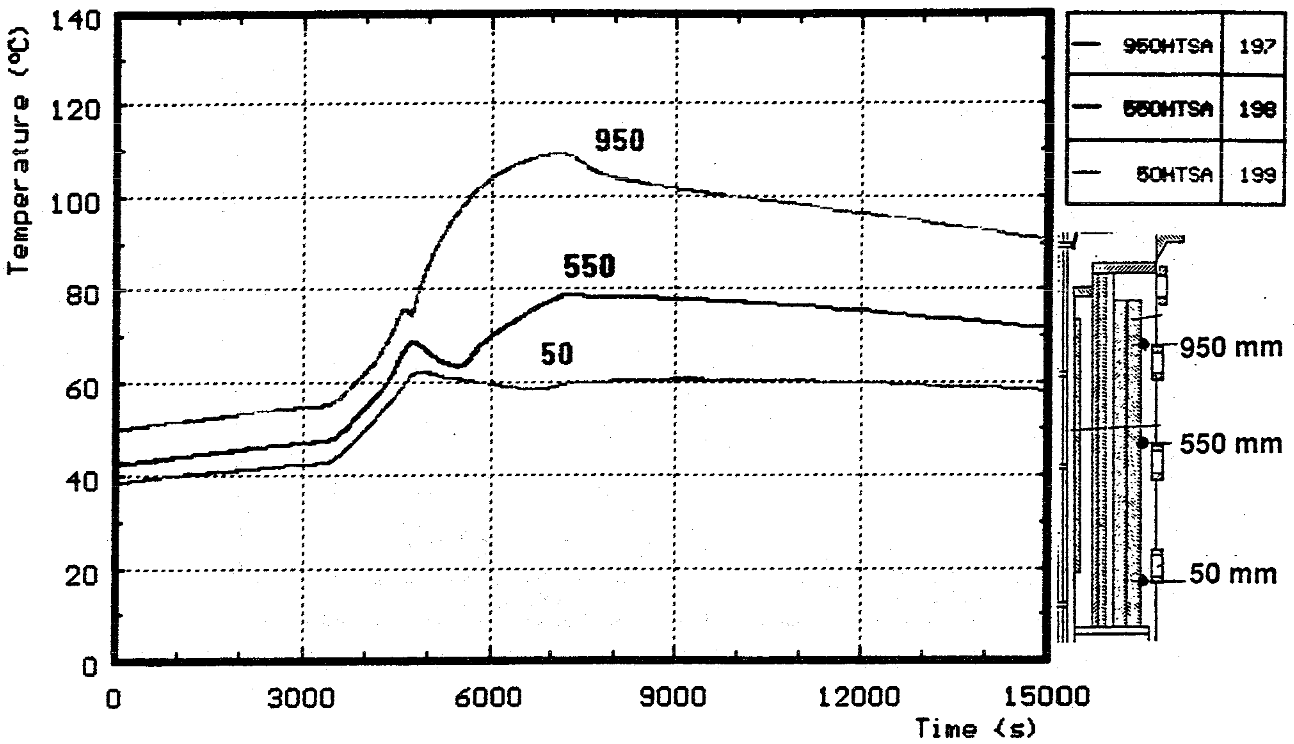

Fig. 70: CORA-W2; Temperatures of HTS, Temperatures in HT-shield at 293 mm radius (0 - 15000 s)

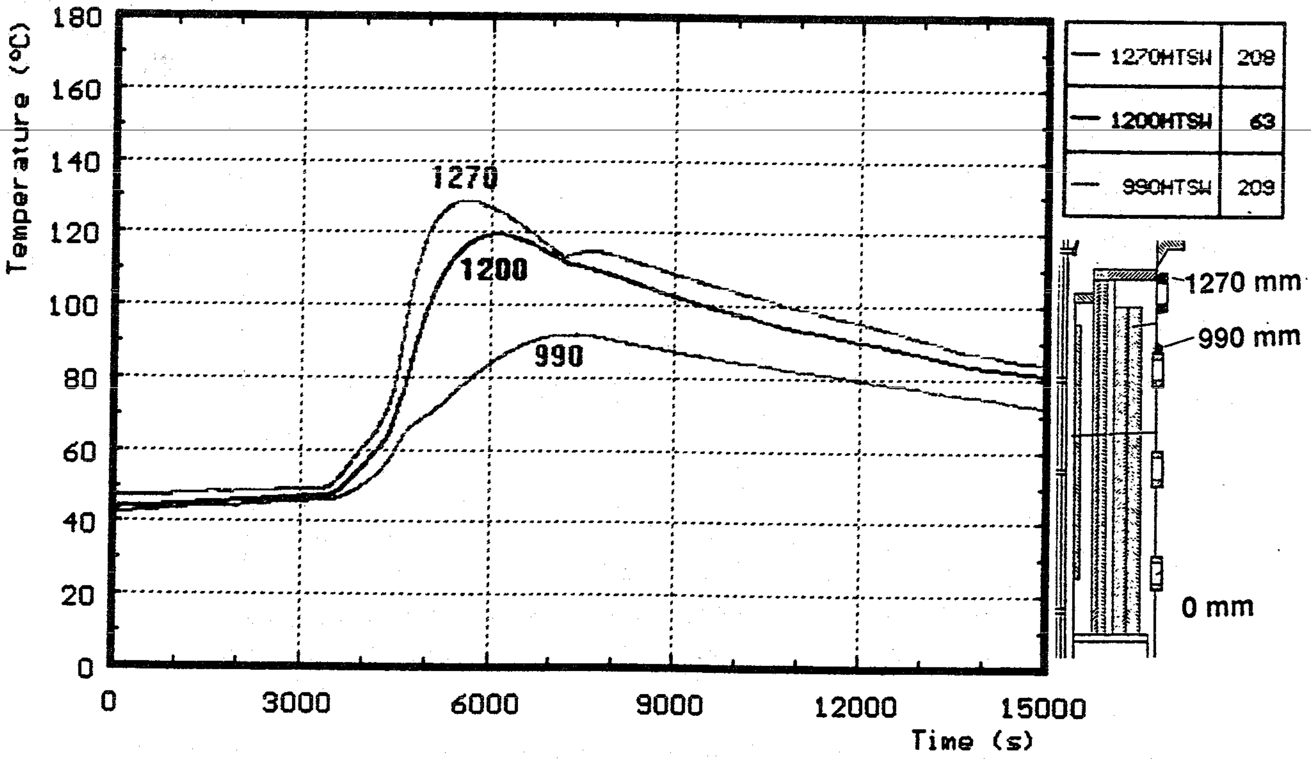

Fig. 71: CORA-W2; Temperatures of HTS, Temperatures on outer surface, 380 mm radius (0 - 15000 s)

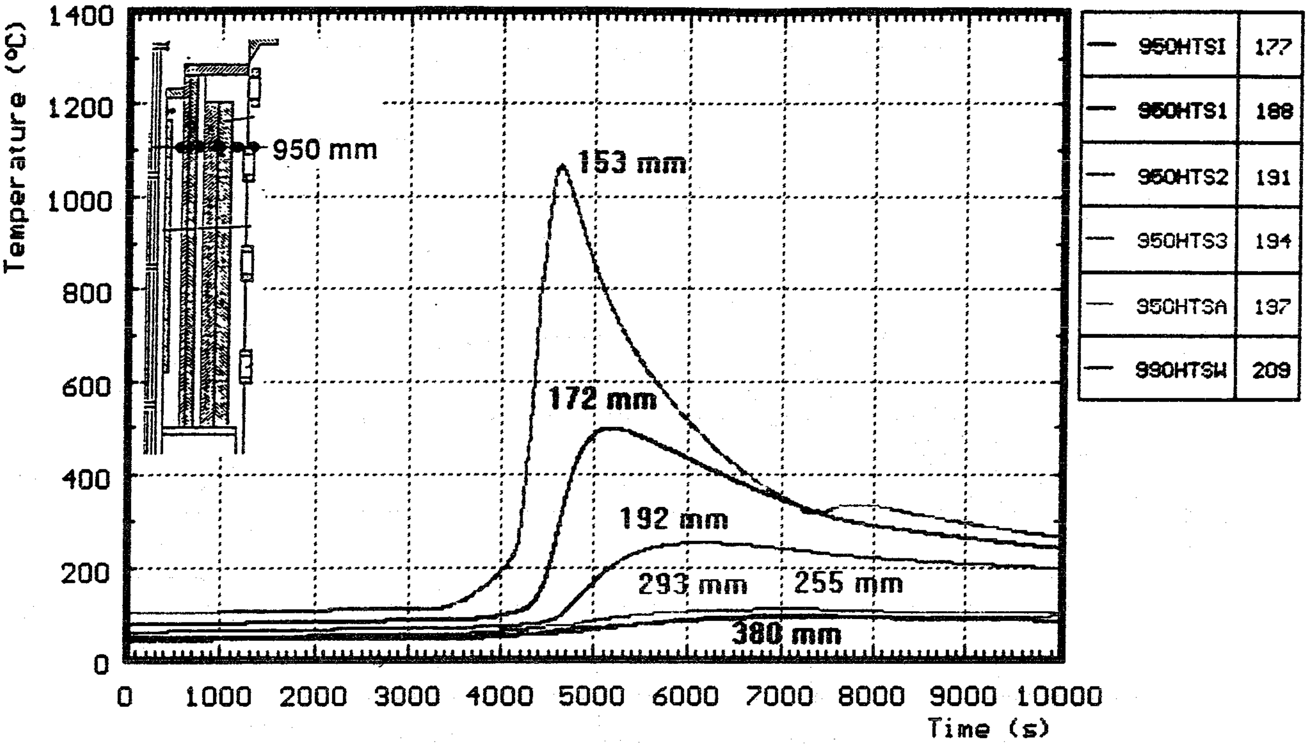

Fig. 72: CORA-W2; Temperatures of HTS, Radial dependence at 950 mm elevation (0 - 10000s)

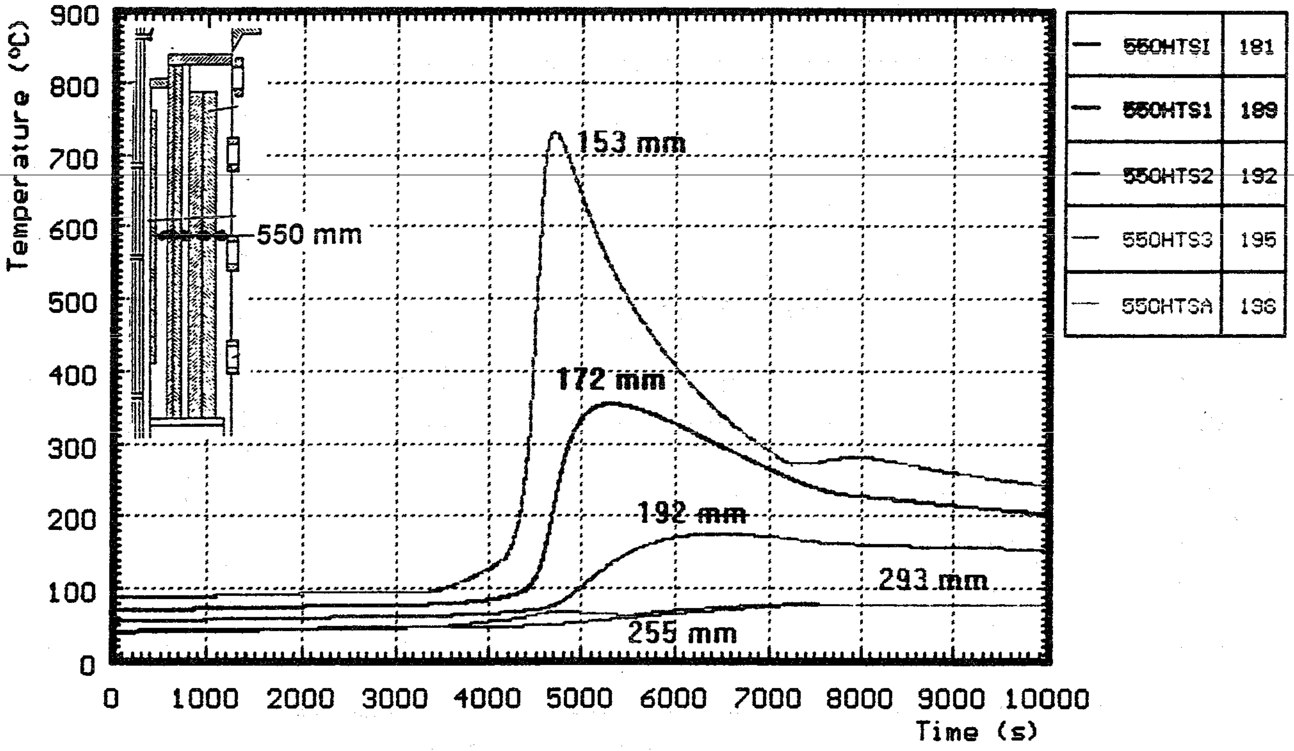

Fig. 73: CORA-W2; Temperatures of HTS, Radial dependence at 550 mm elevation (0 - 10000s)

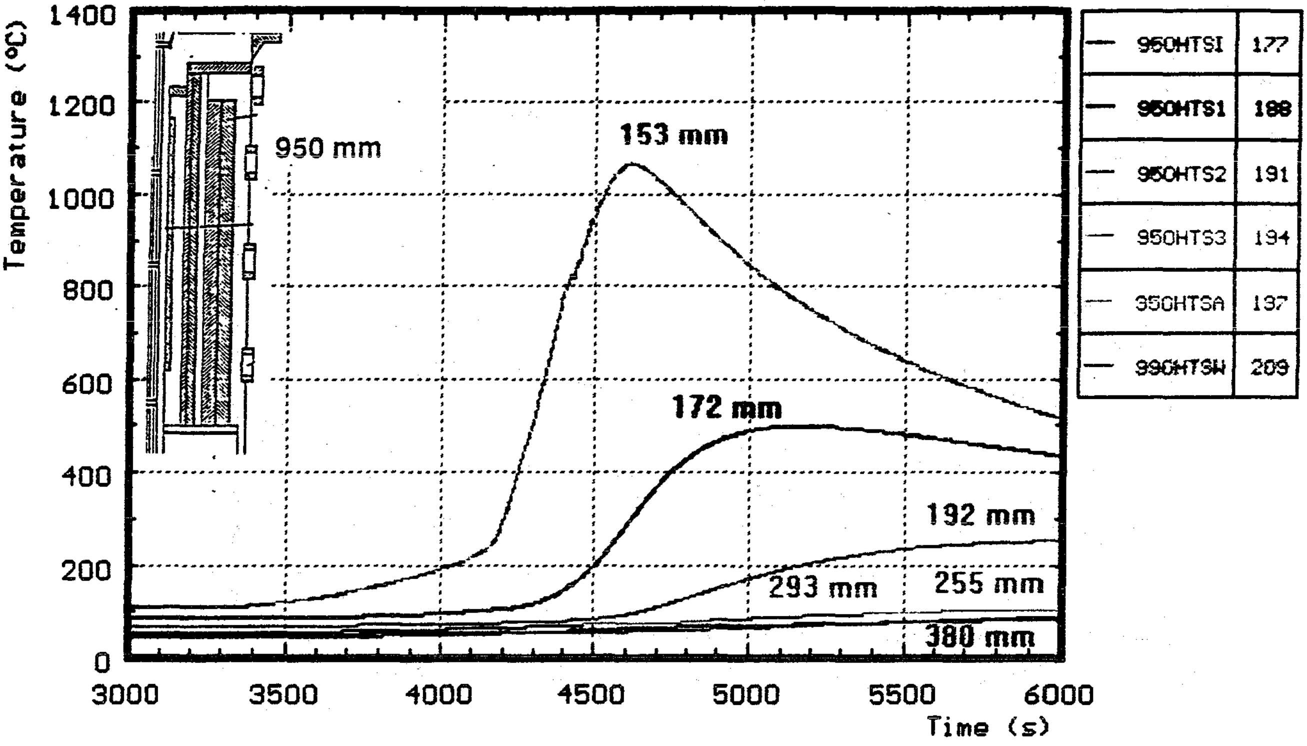

Fig. 74: CORA-W2; Temperatures of HTS, Radial dependence at 950 mm elevation (3000 - 6000s)

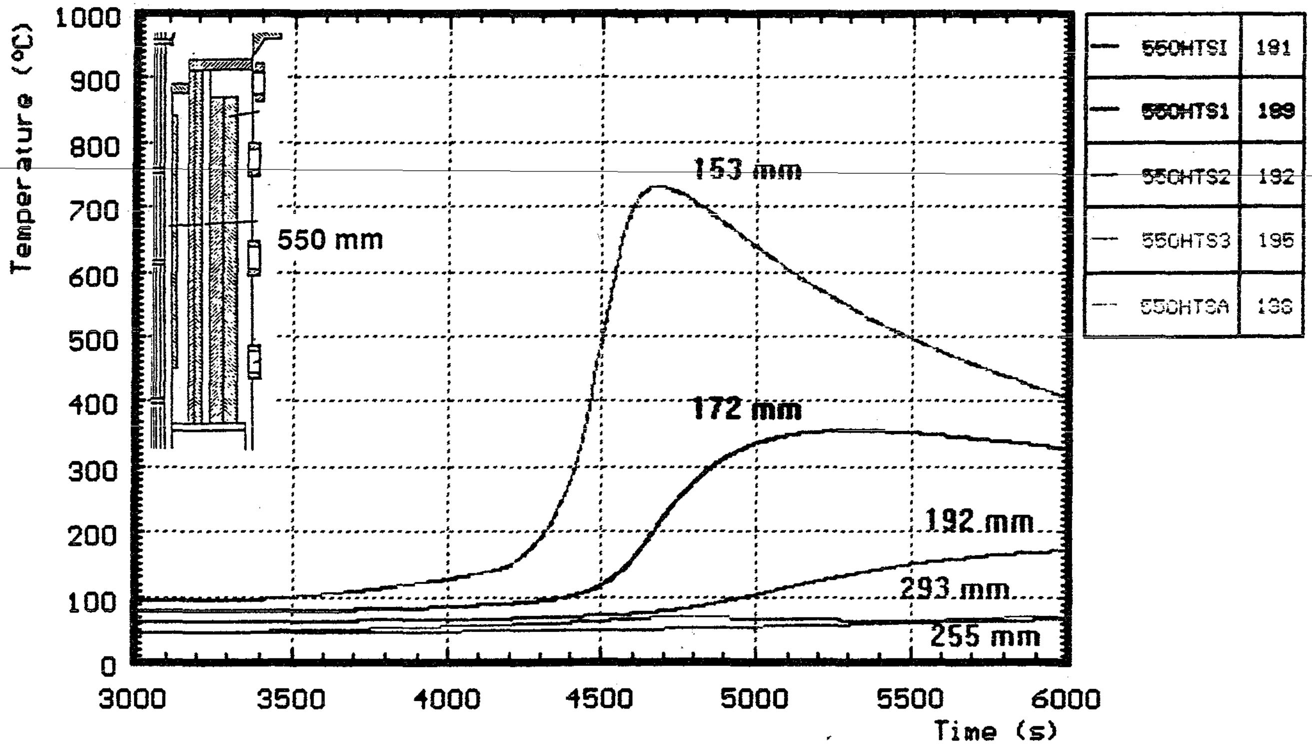

Fig. 75: CORA-W2; Temperatures of HTS, Radial dependence at 550 mm elevation (3000 - 6000s)

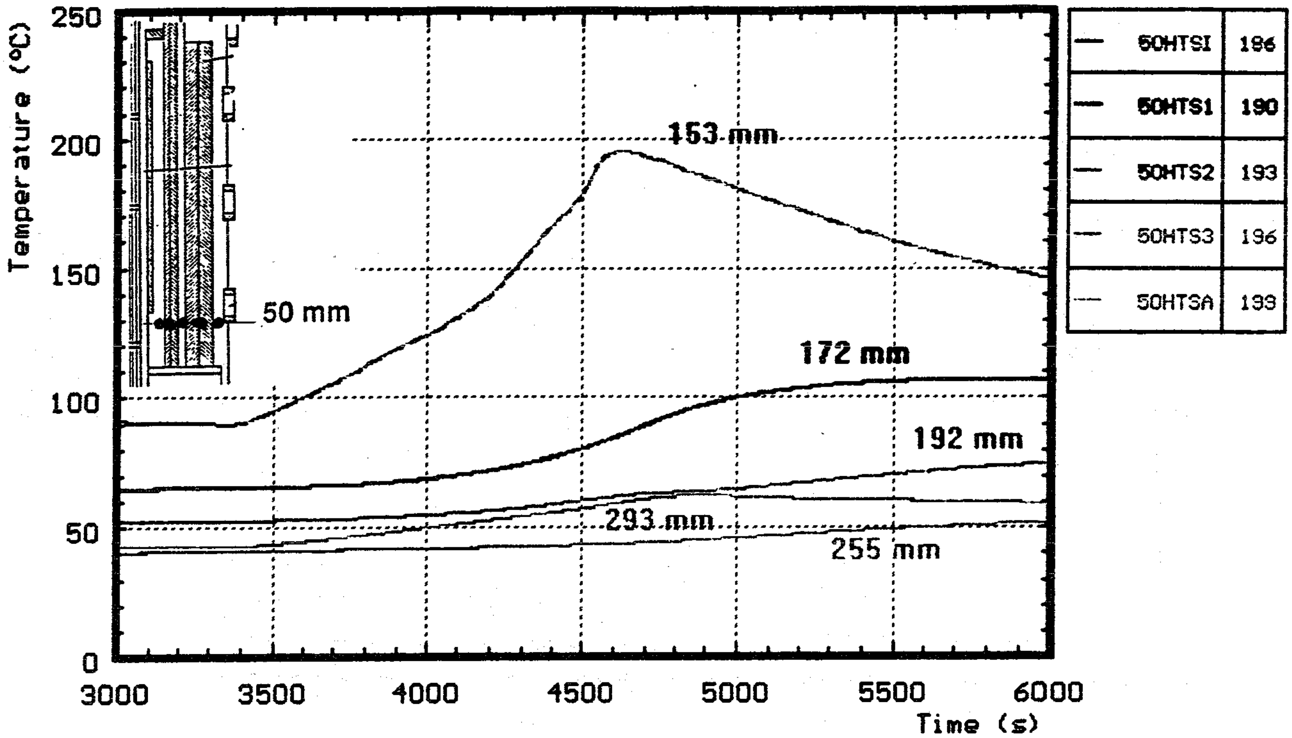

Fig. 76: CORA-W2; Temperatures of HTS, Radial dependence at 50 mm elevation (3000 - 6000s)

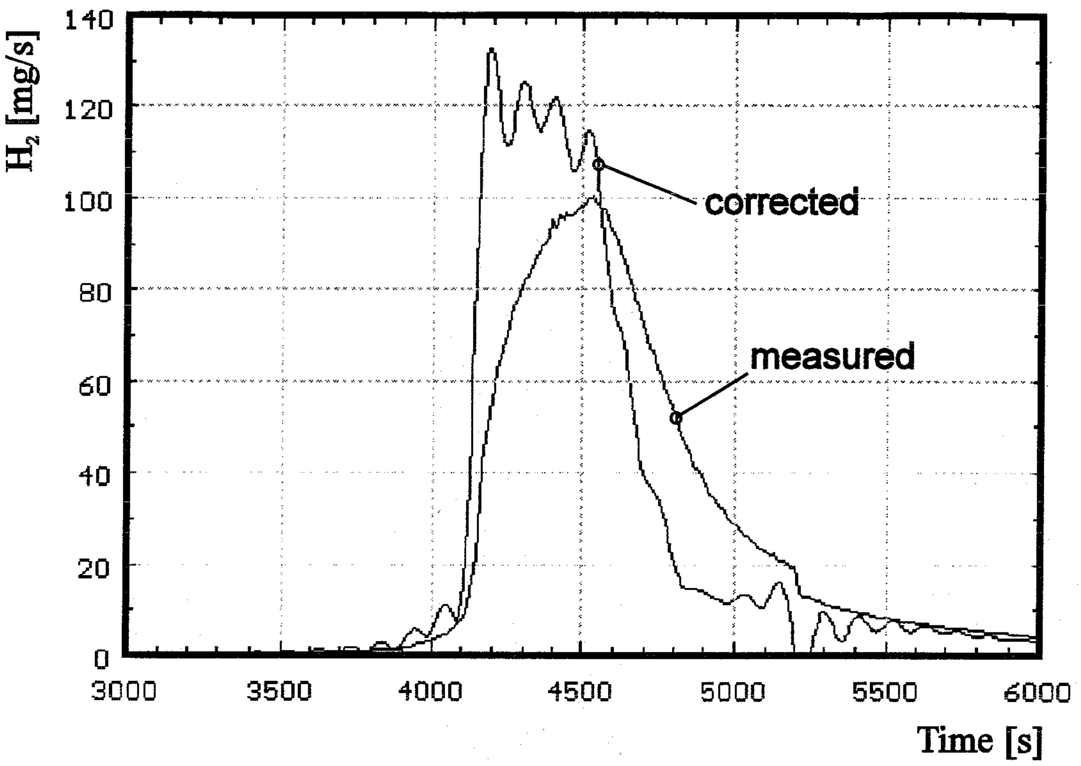

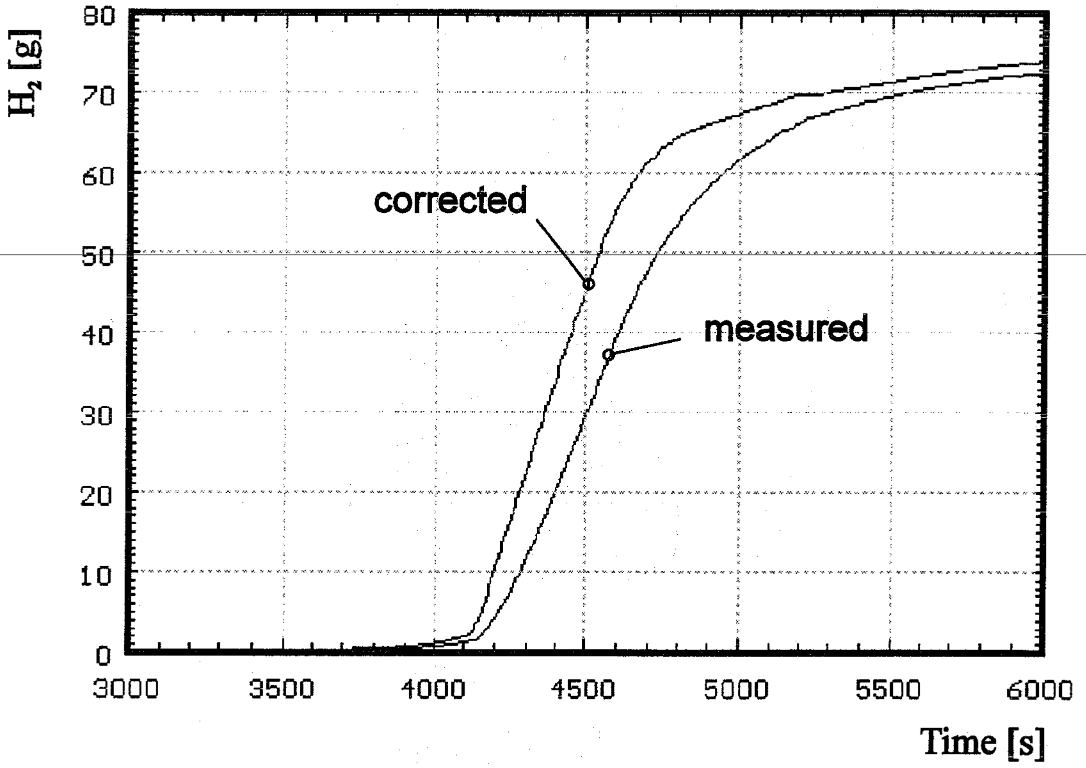

Fig. 77: Hydrogen production in test CORA-W2; production rate (top) and integral values (bottom)

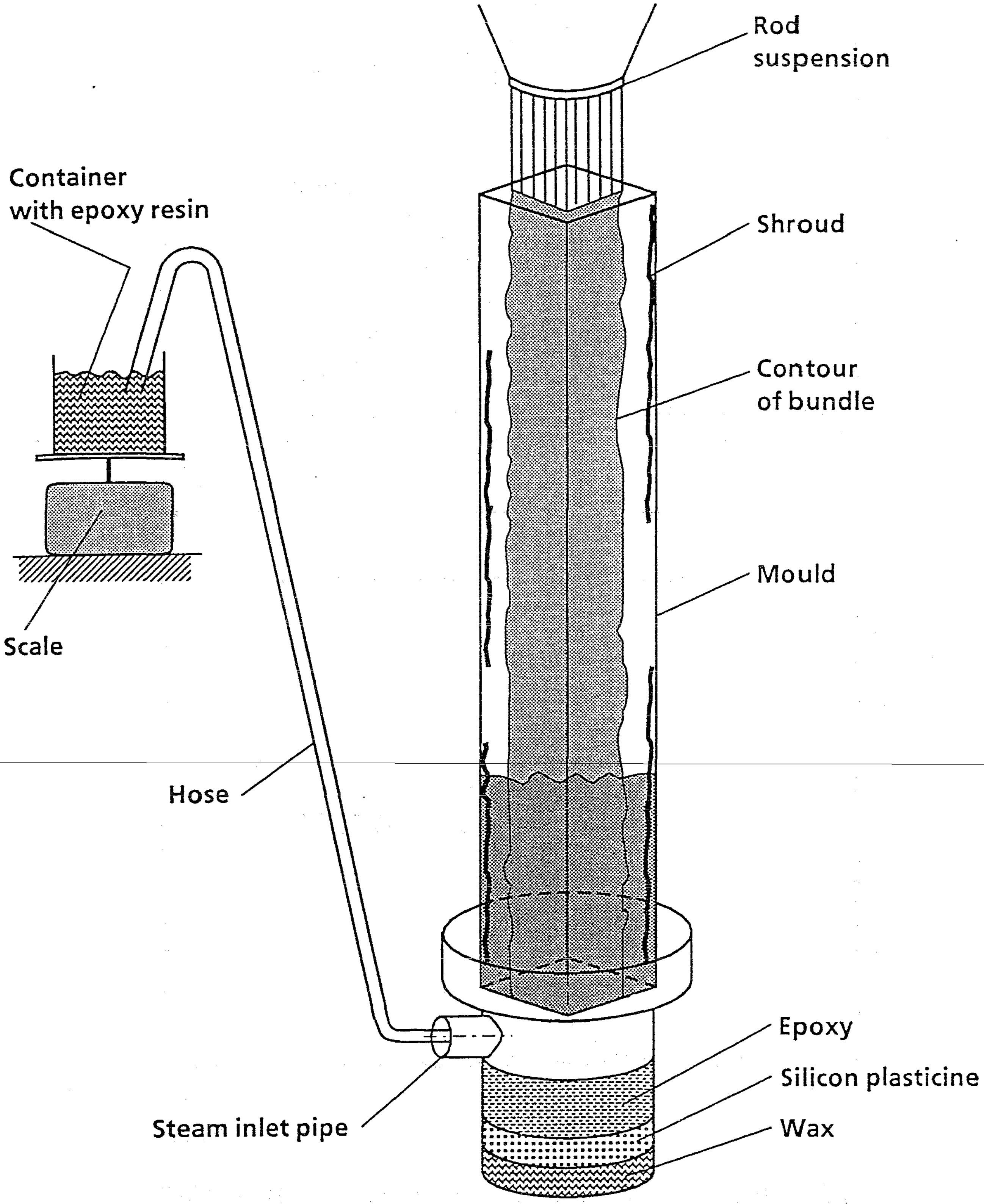

Fig. 78: CORA-W2; Epoxying process of the tested bundle

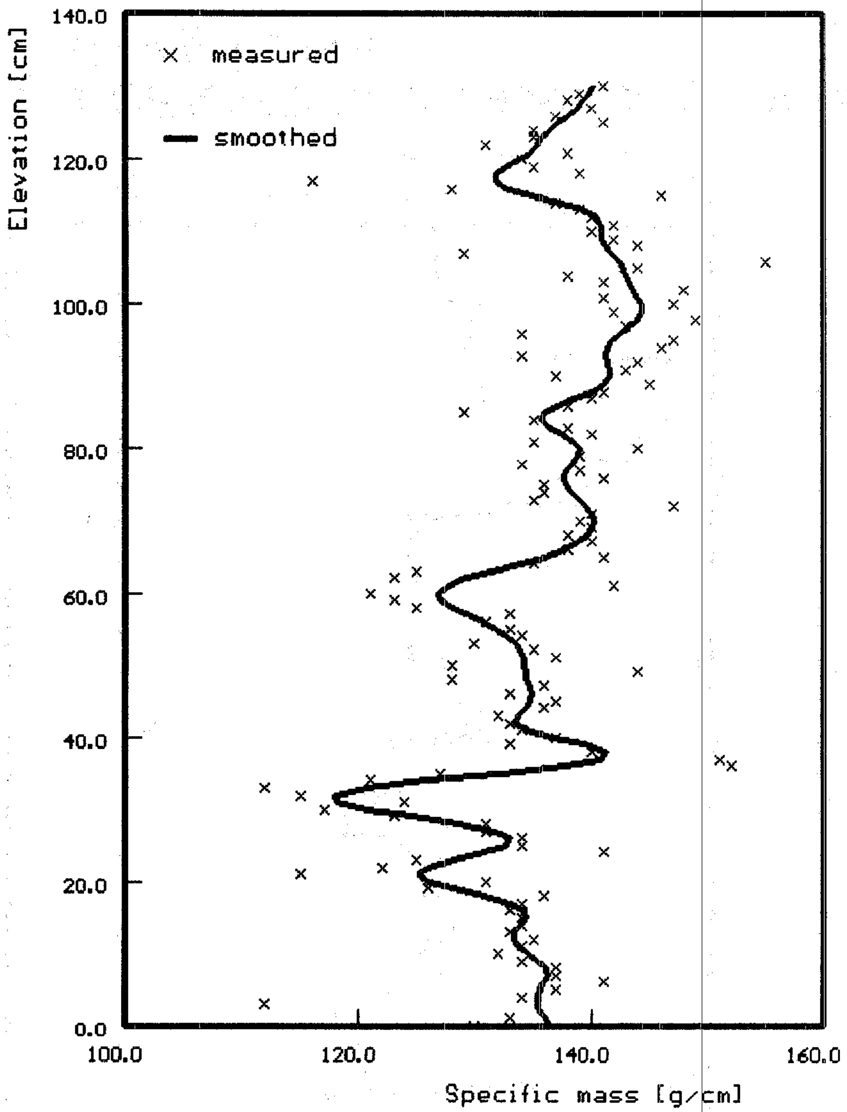

Fig. 79: CORA-W2; Axial distribution of the bundle fill up with epoxy resin

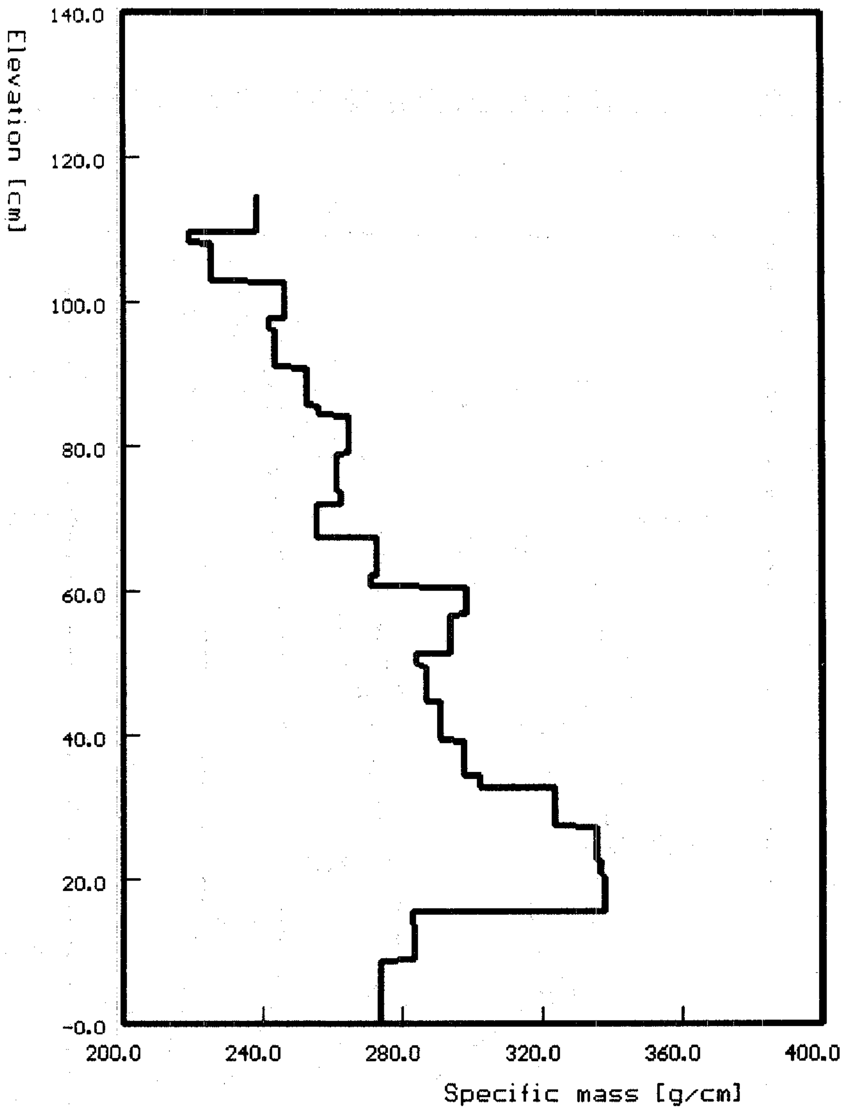

Fig. 80: CORA-W2; Axial mass distribution of bundle segments filled with epoxy resin

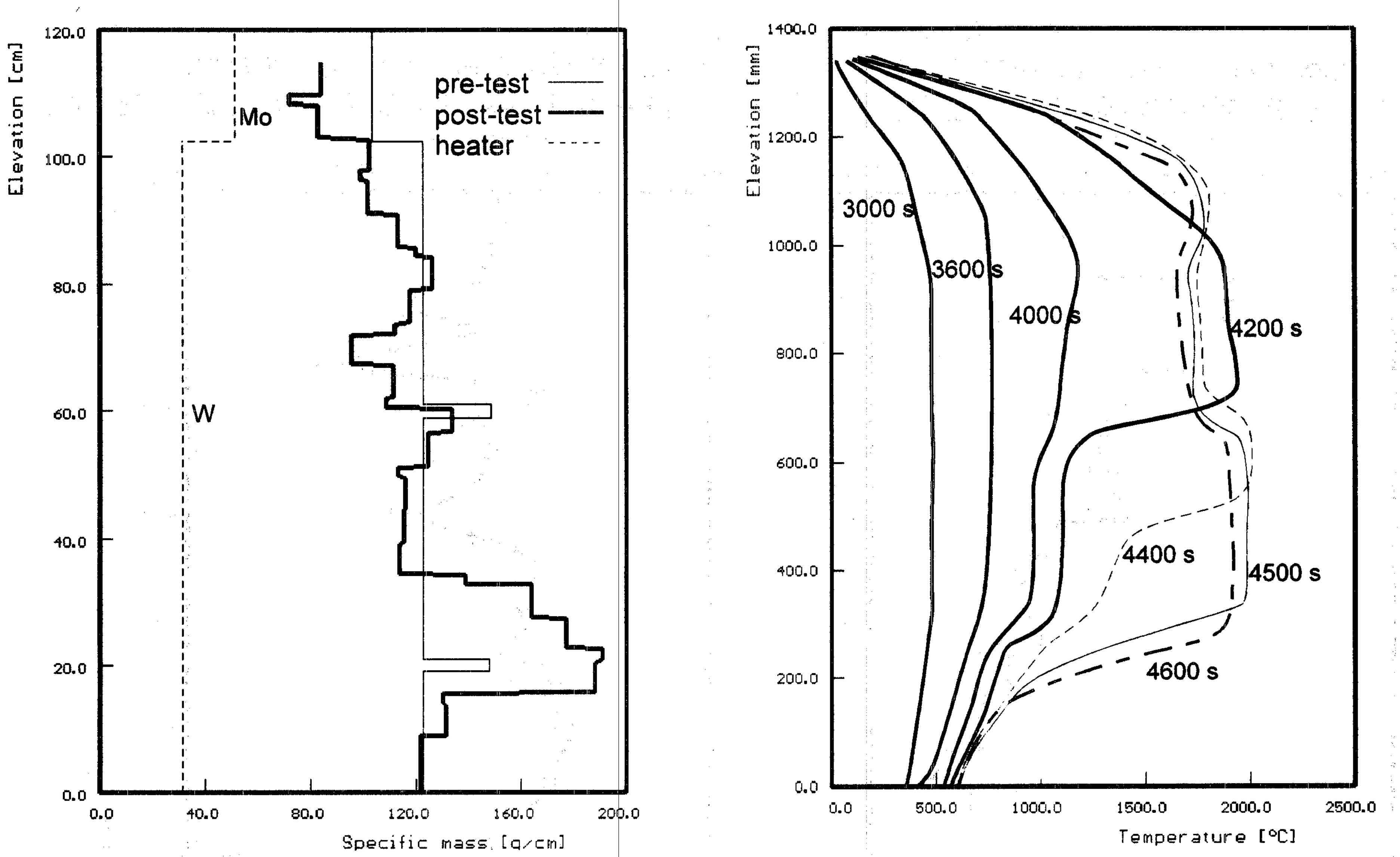

Fig. 81: CORA-W2; Axial mass distribution after the test and axial temperature distribution during the test

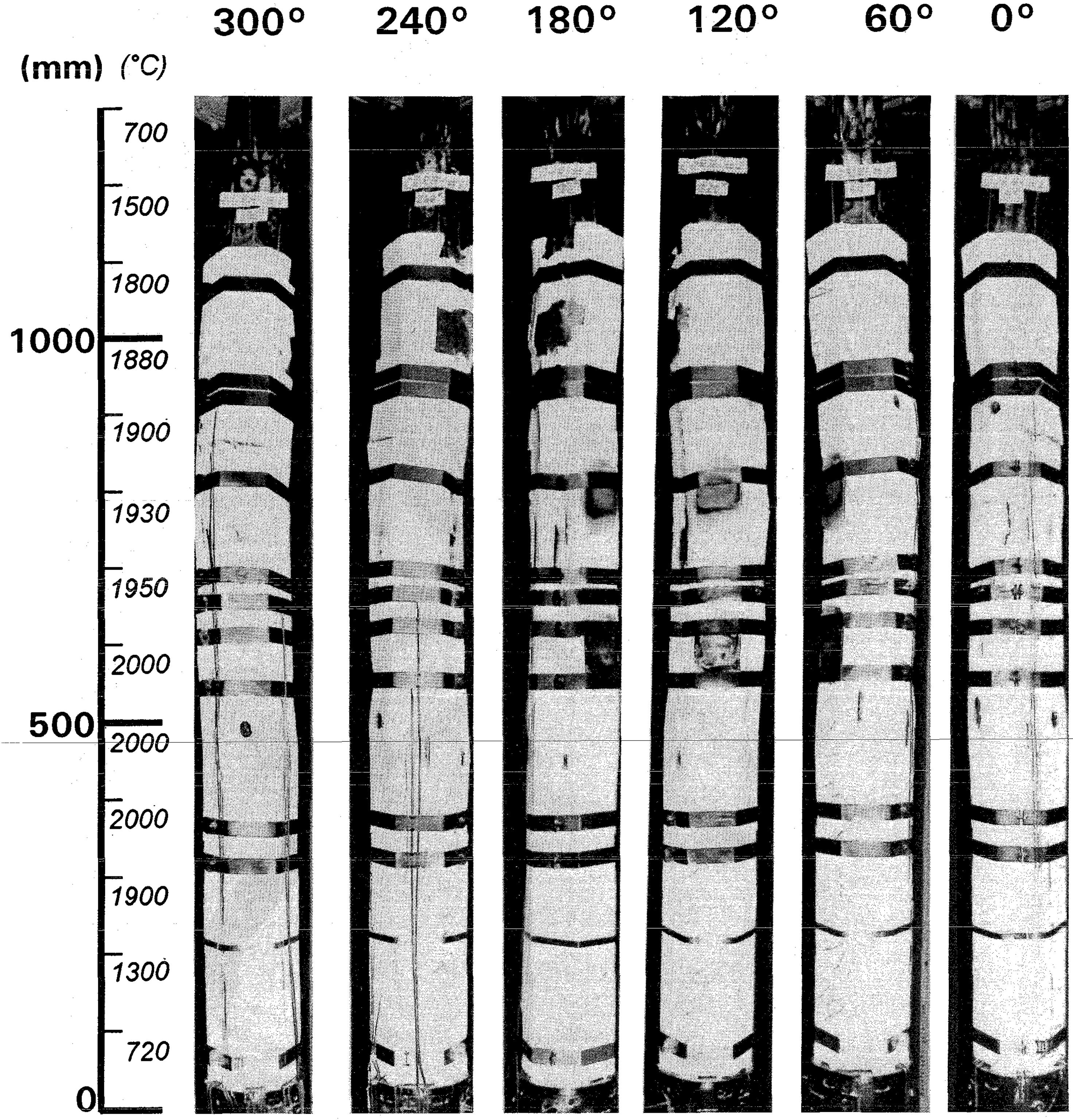

Fig. 82: CORA-W2; Posttest appearance of the entire bundle length

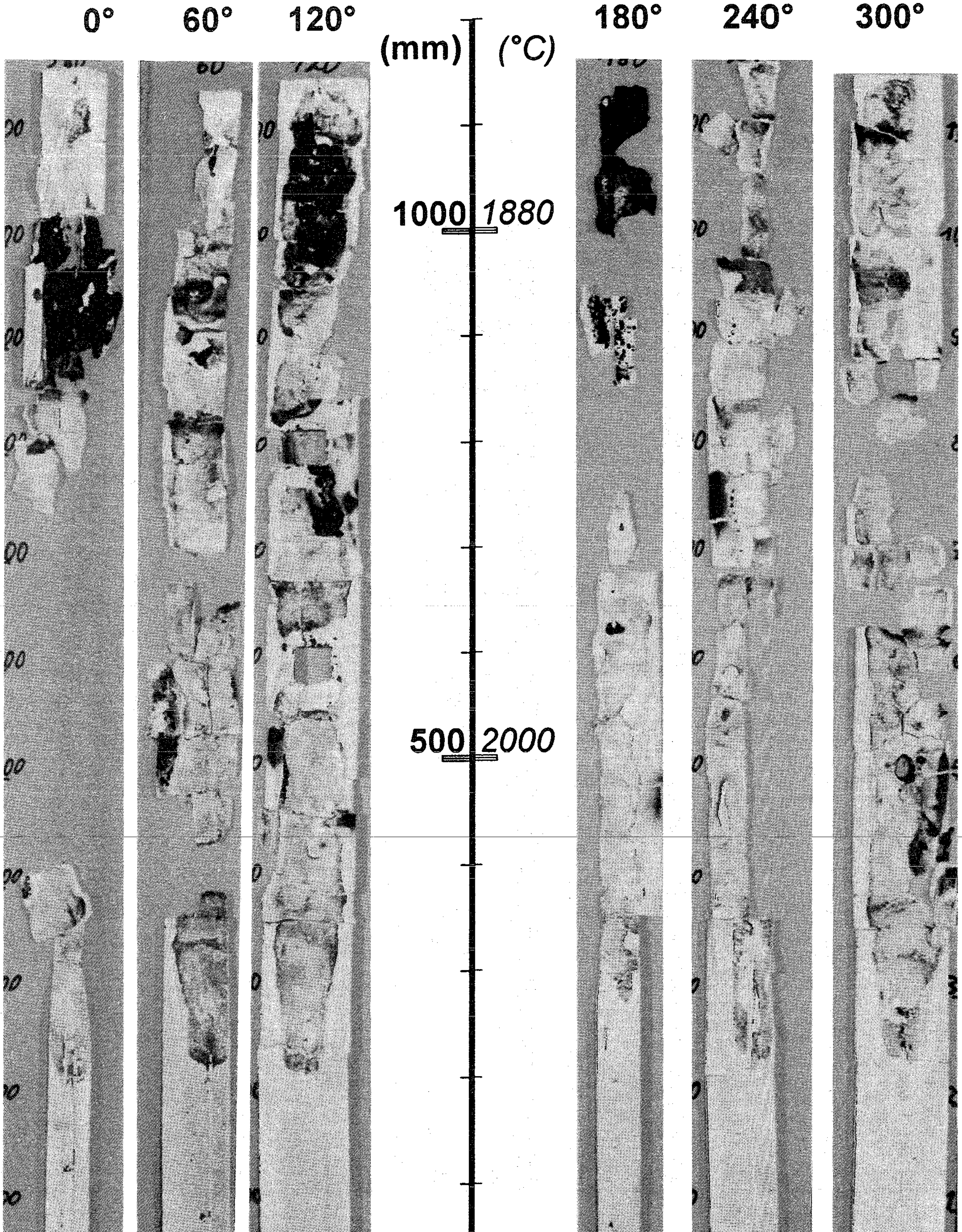

Fig. 83: CORA-W2; Posttest view of the inner side of the shroud insulation

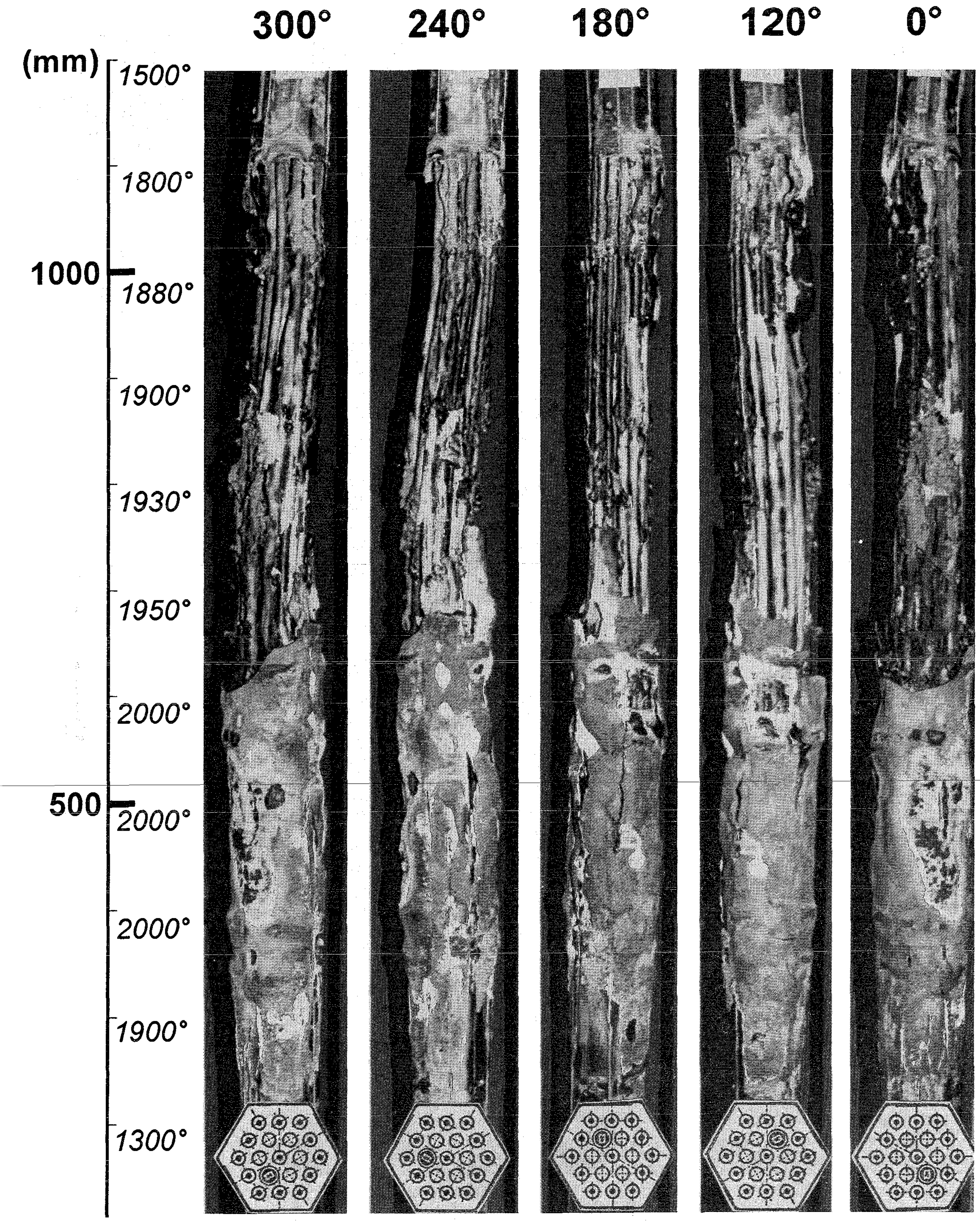

Fig. 84: Posttest view of bundle CORA-W2 after partial removal of shroud

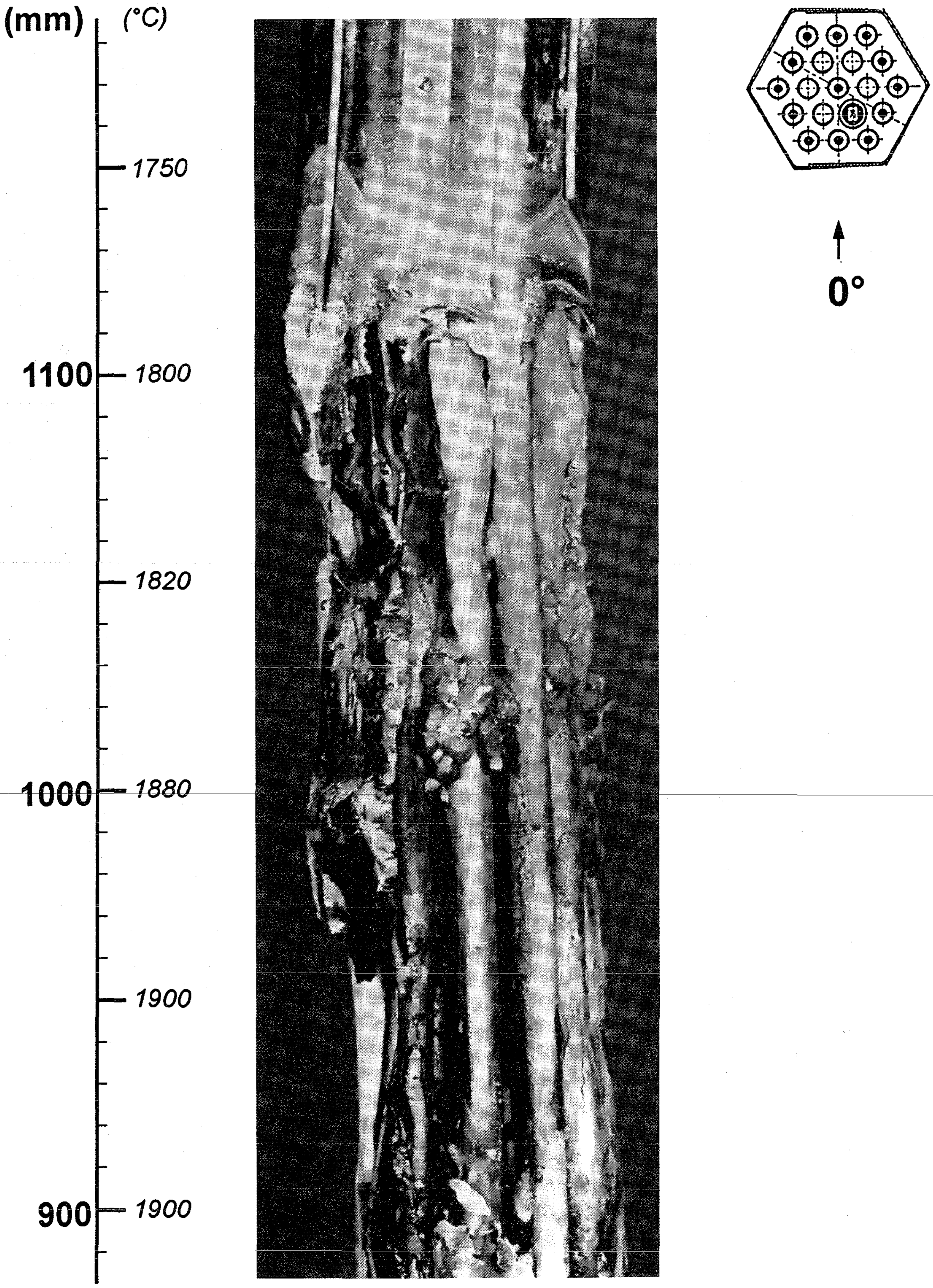

Fig. 85: Posttest view, 0° orientation

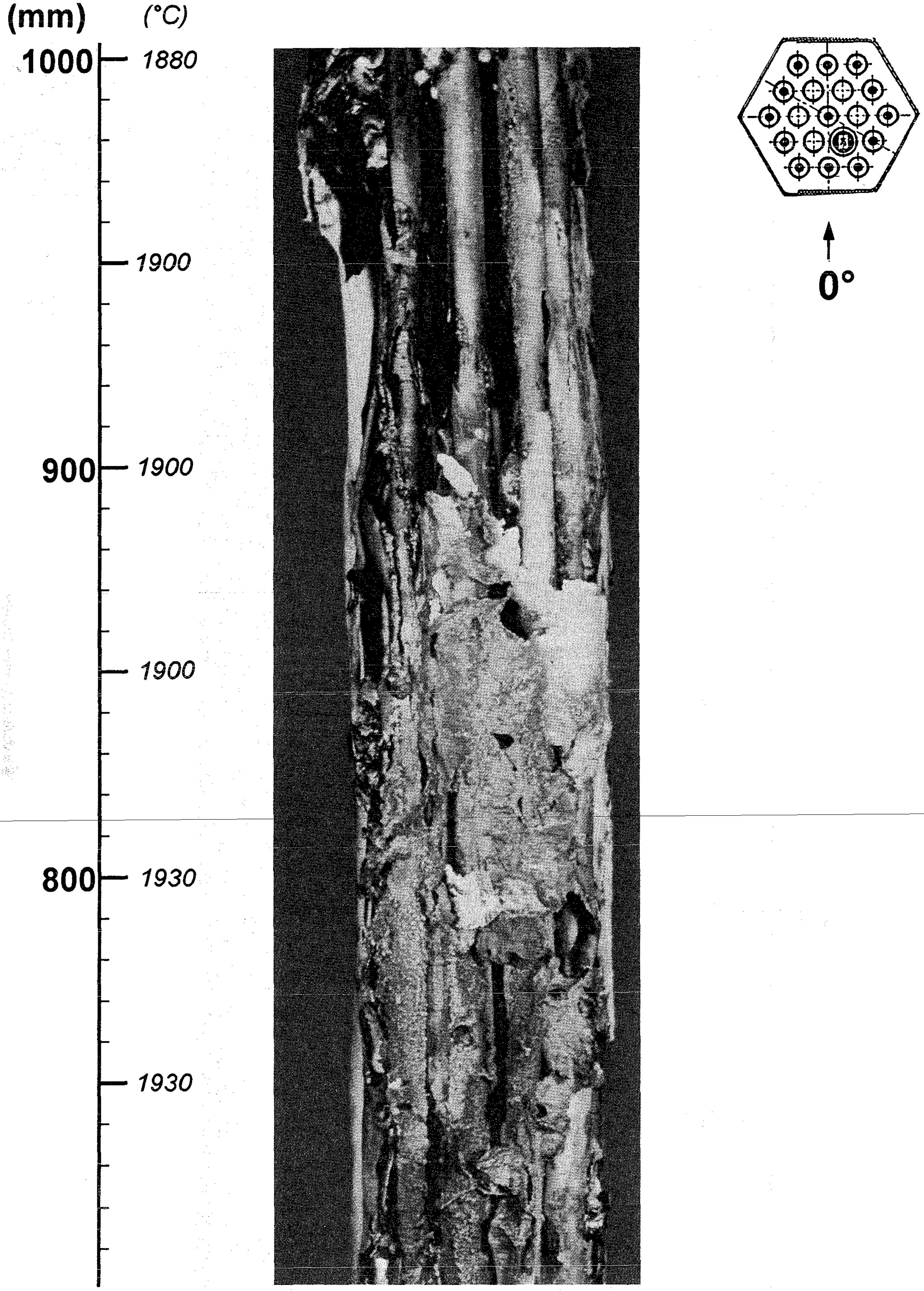

Fig. 86: Posttest view, 0° orientation

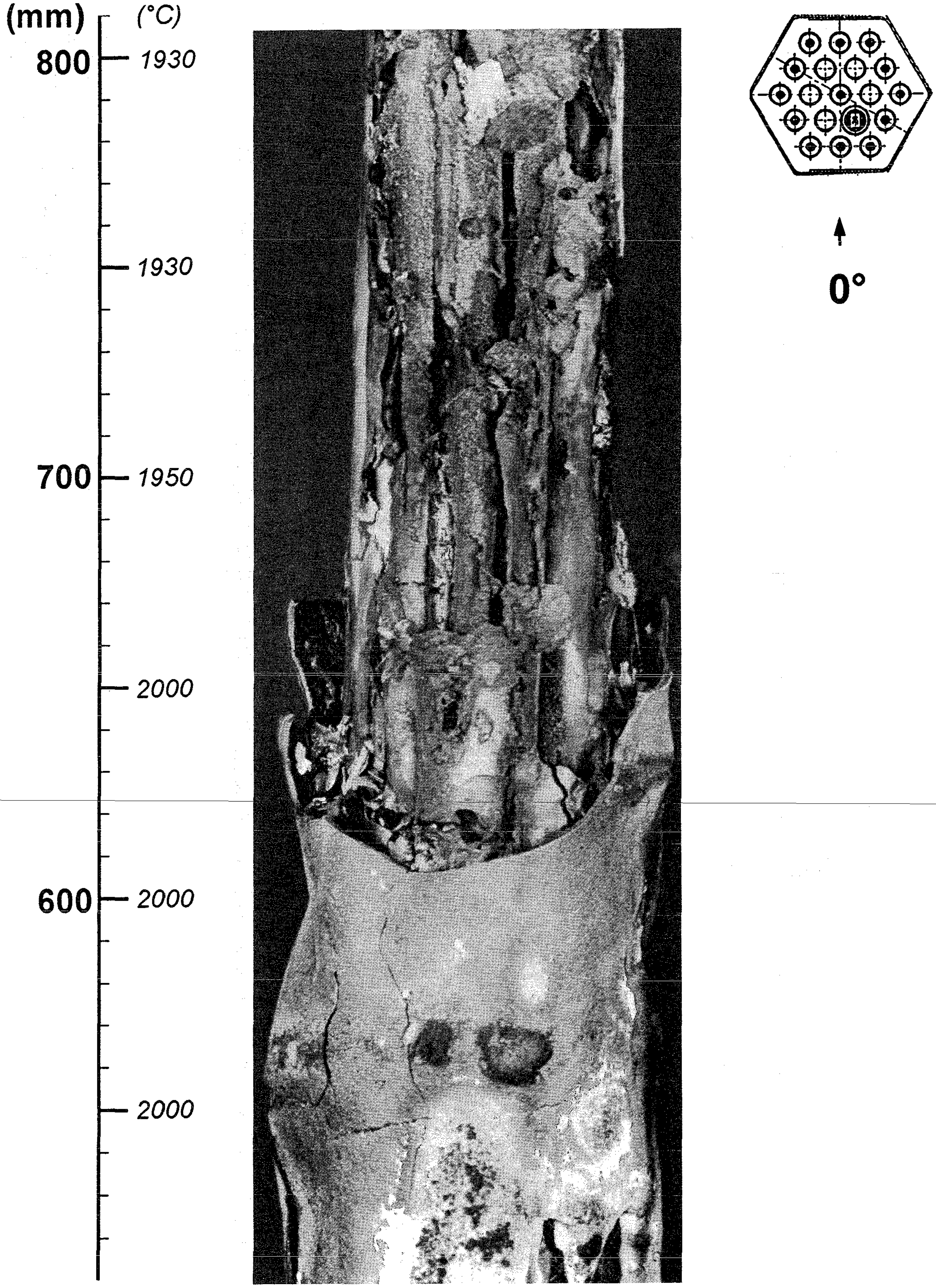

Fig. 87: Posttest view, 0° orientation

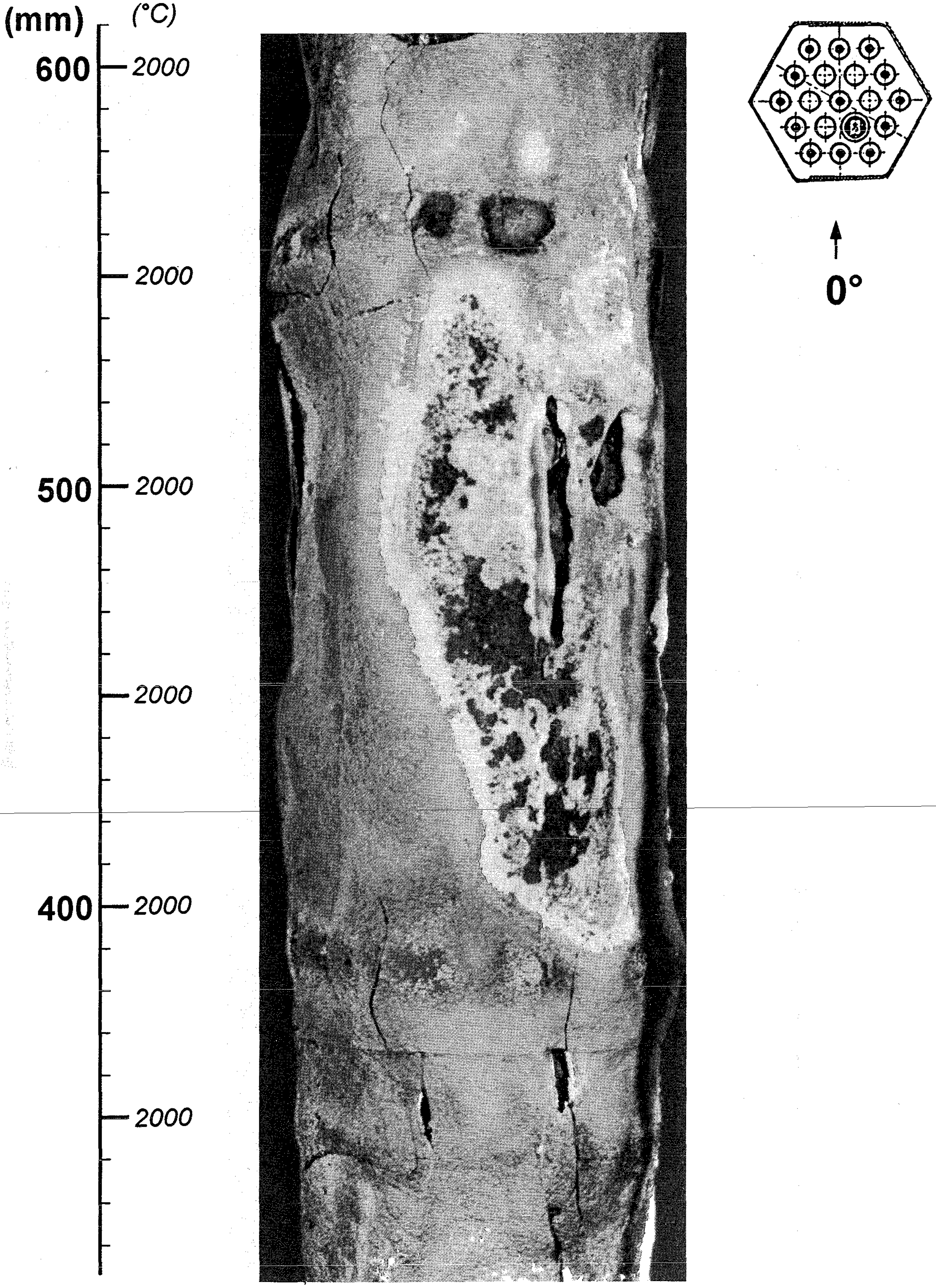

Fig. 88: Posttest view, 0° orientation

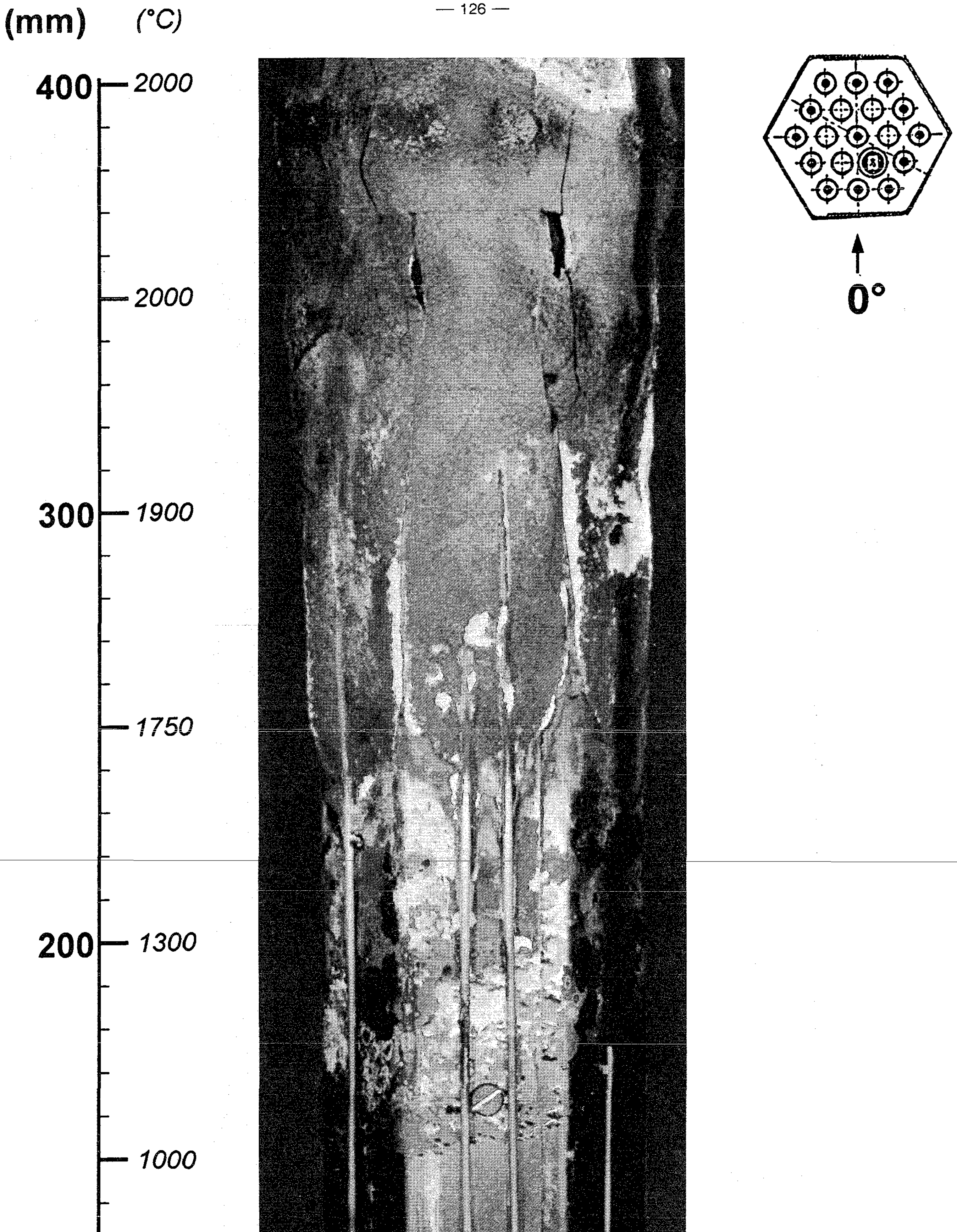

Fig. 89: Posttest view, 0° orientation

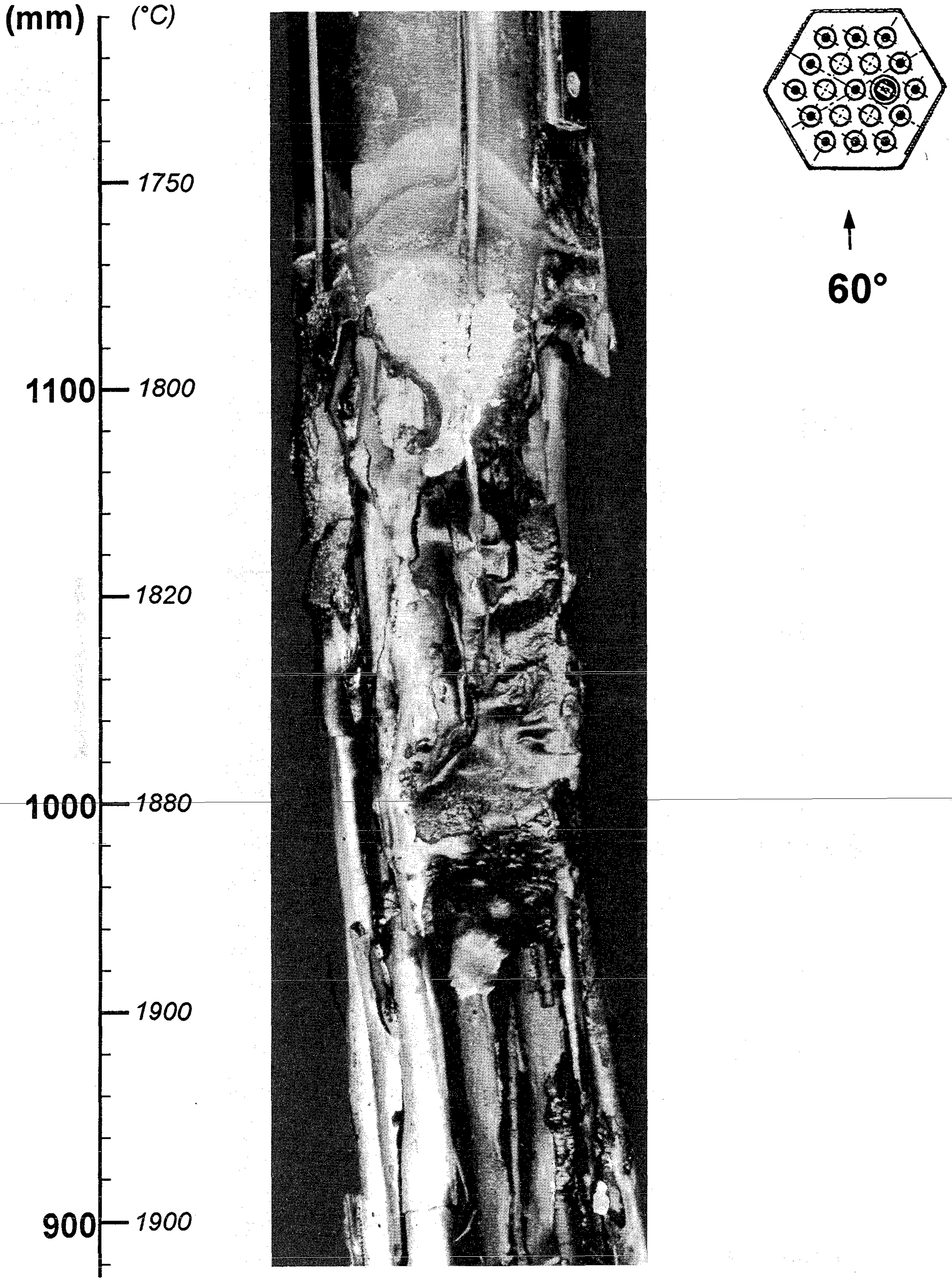

Fig. 90: Posttest view, 60° orientation

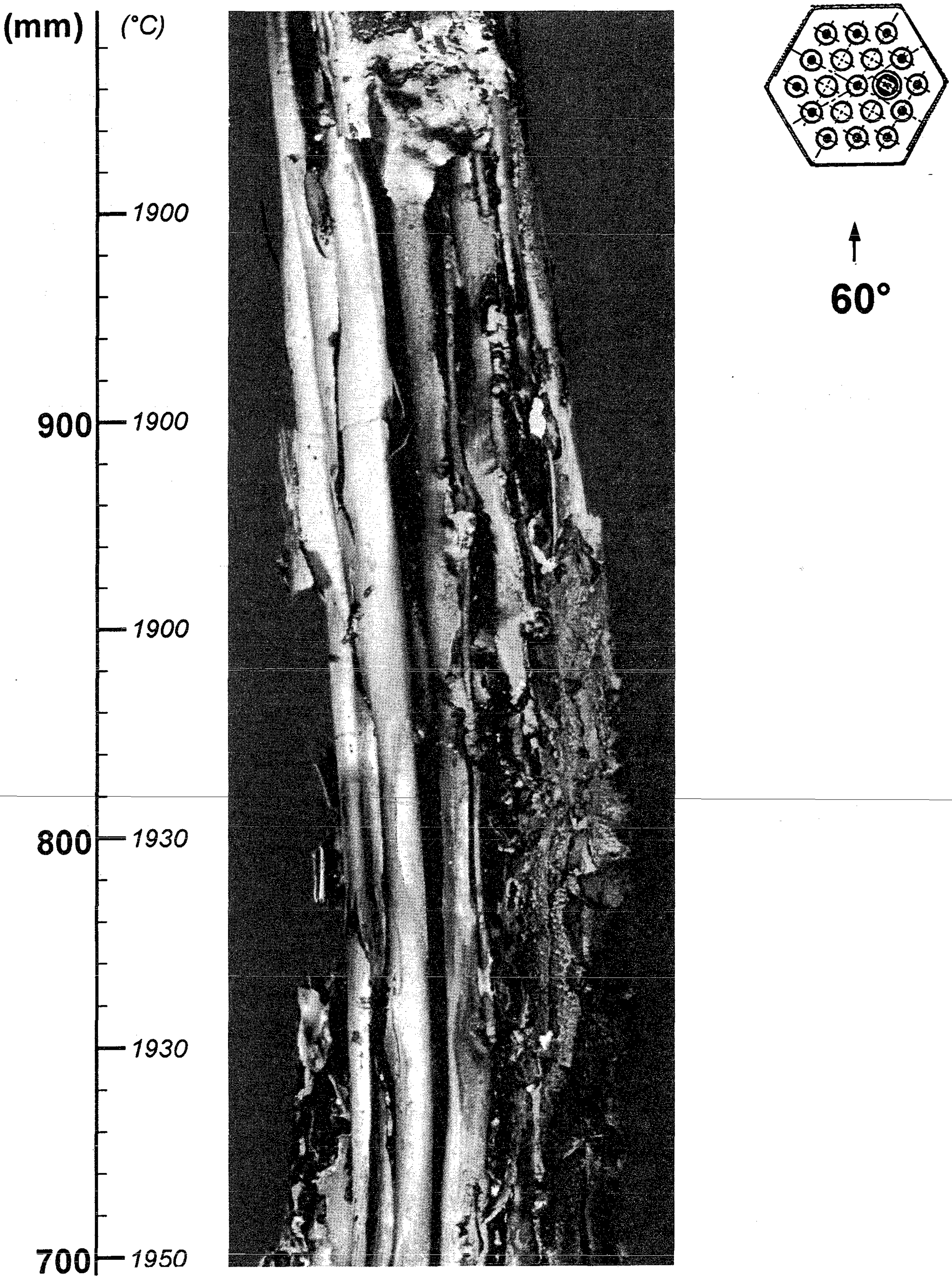

Fig. 91: Posttest view, 60° orientation

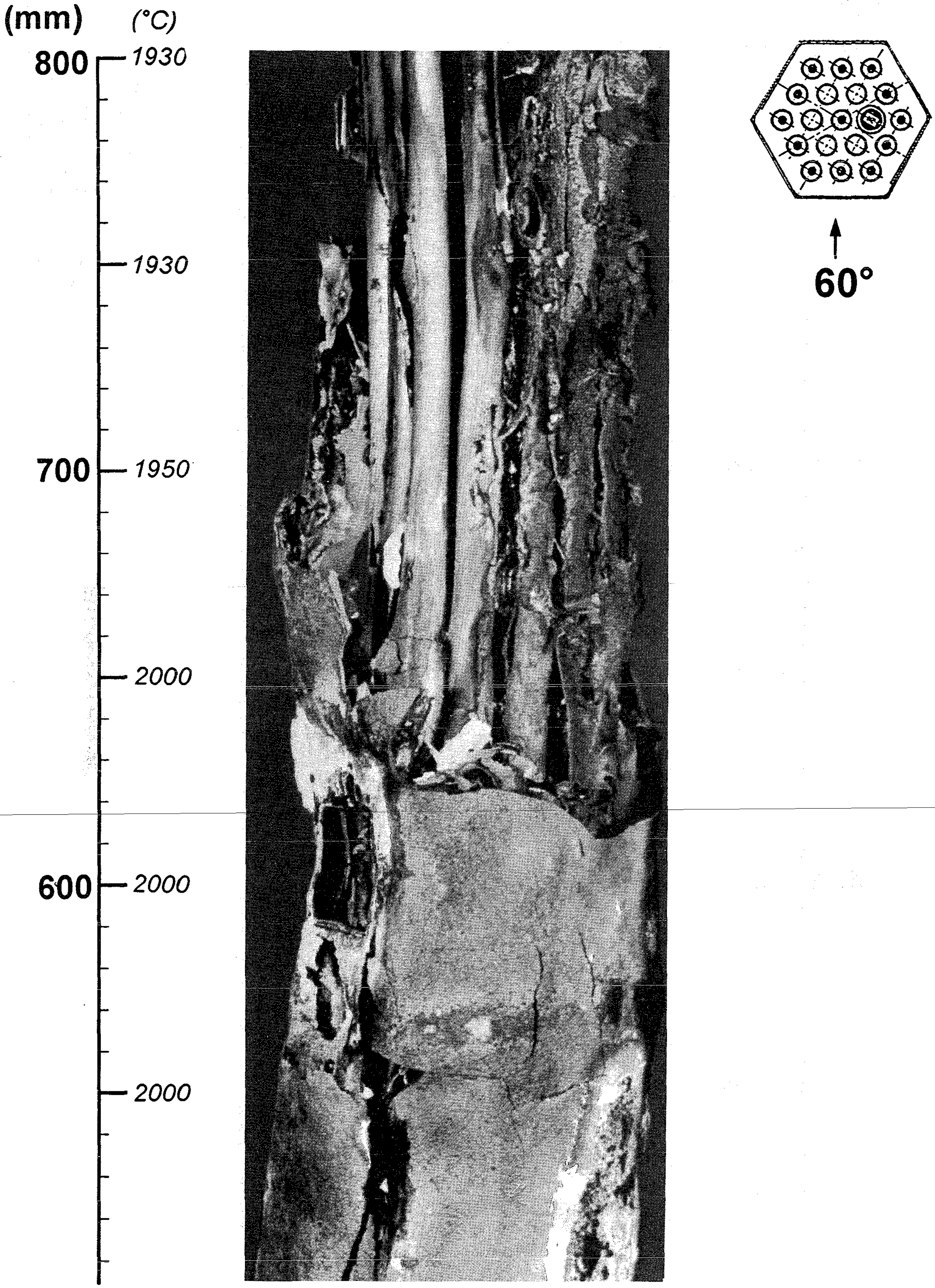

Fig. 92: Posttest view, 60° orientation

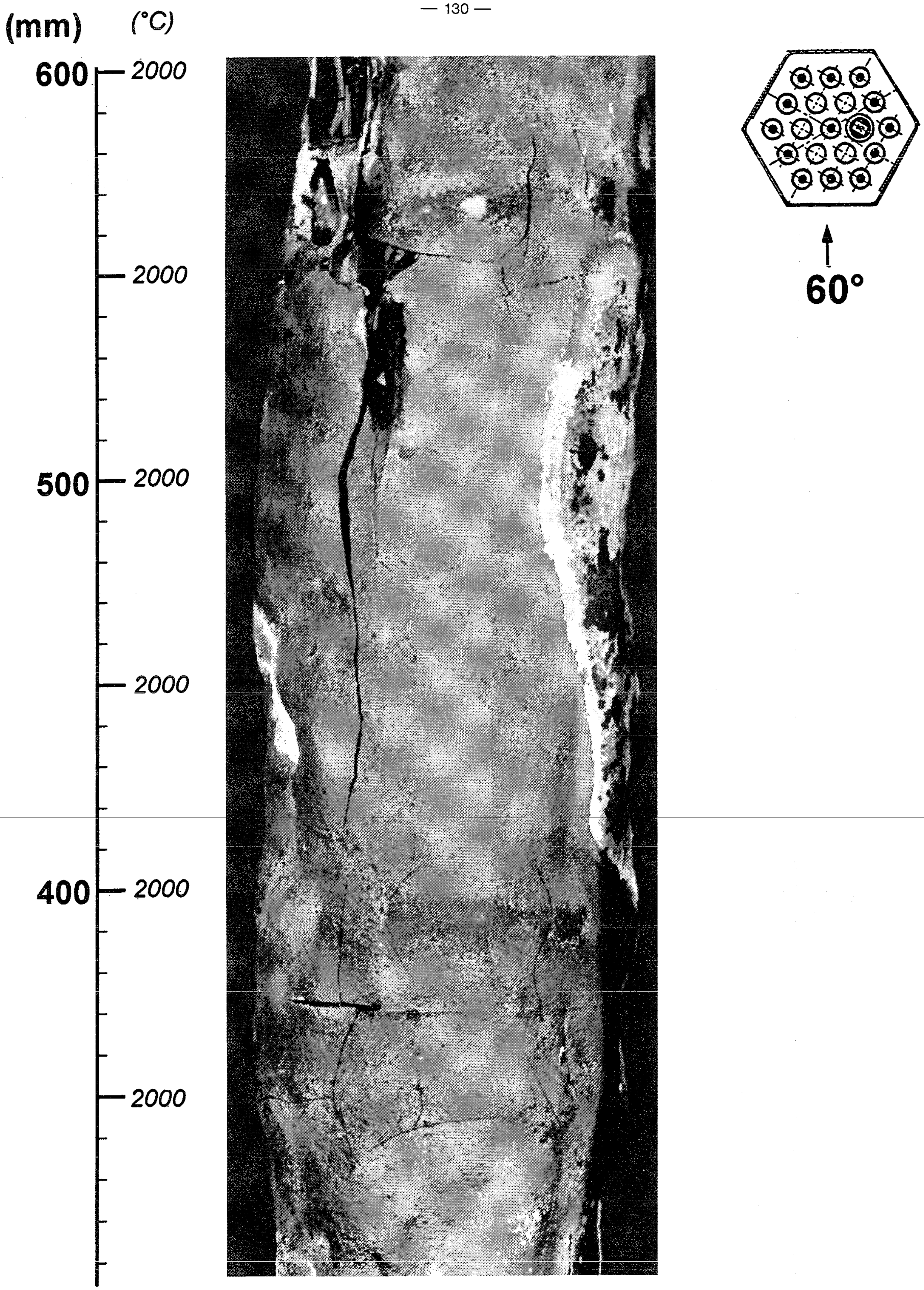

Fig. 93: Posttest view, 60° orientation

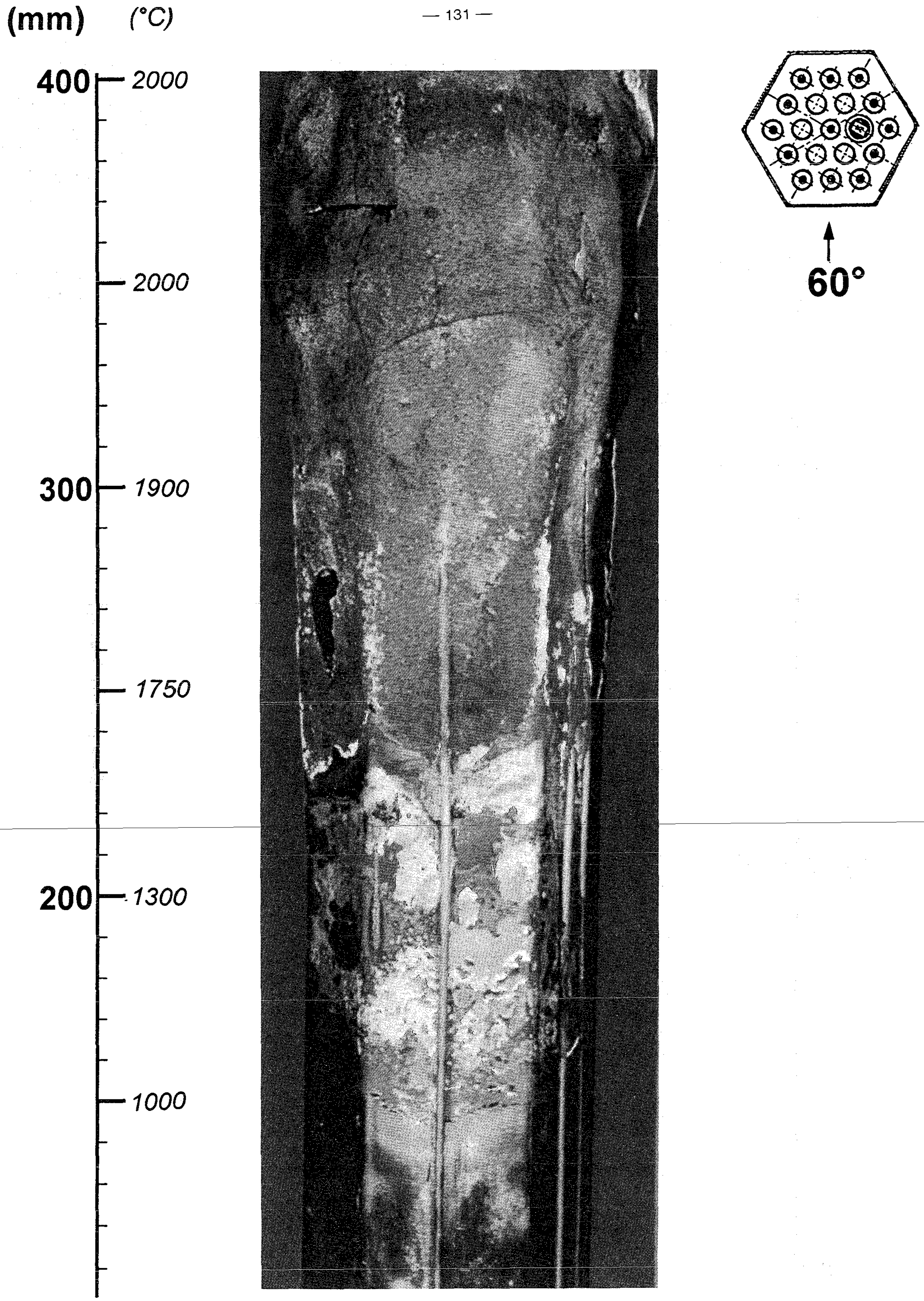

Fig. 94: Posttest view, 60° orientation

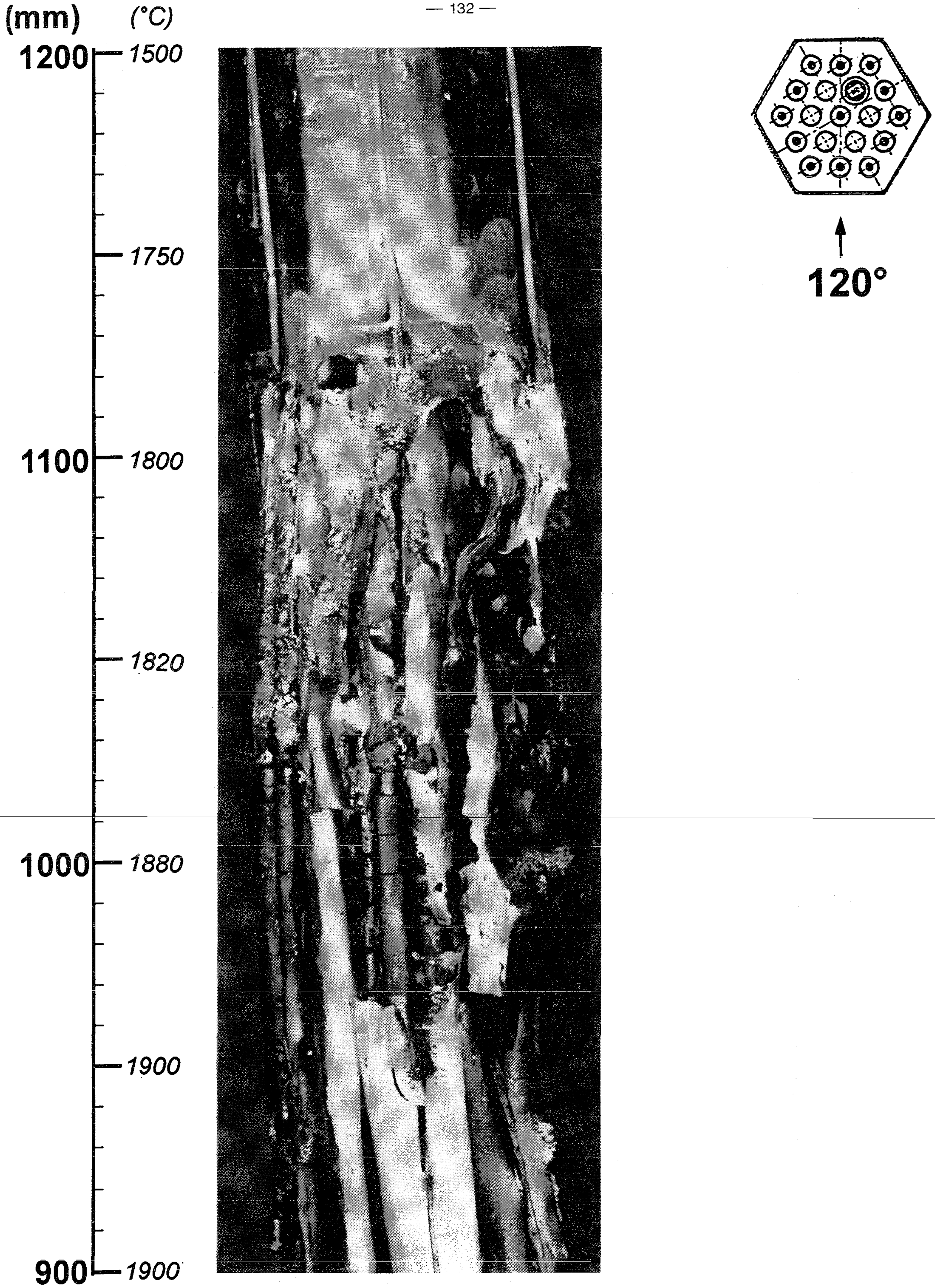

Fig. 95: Posttest view, 120° orientation

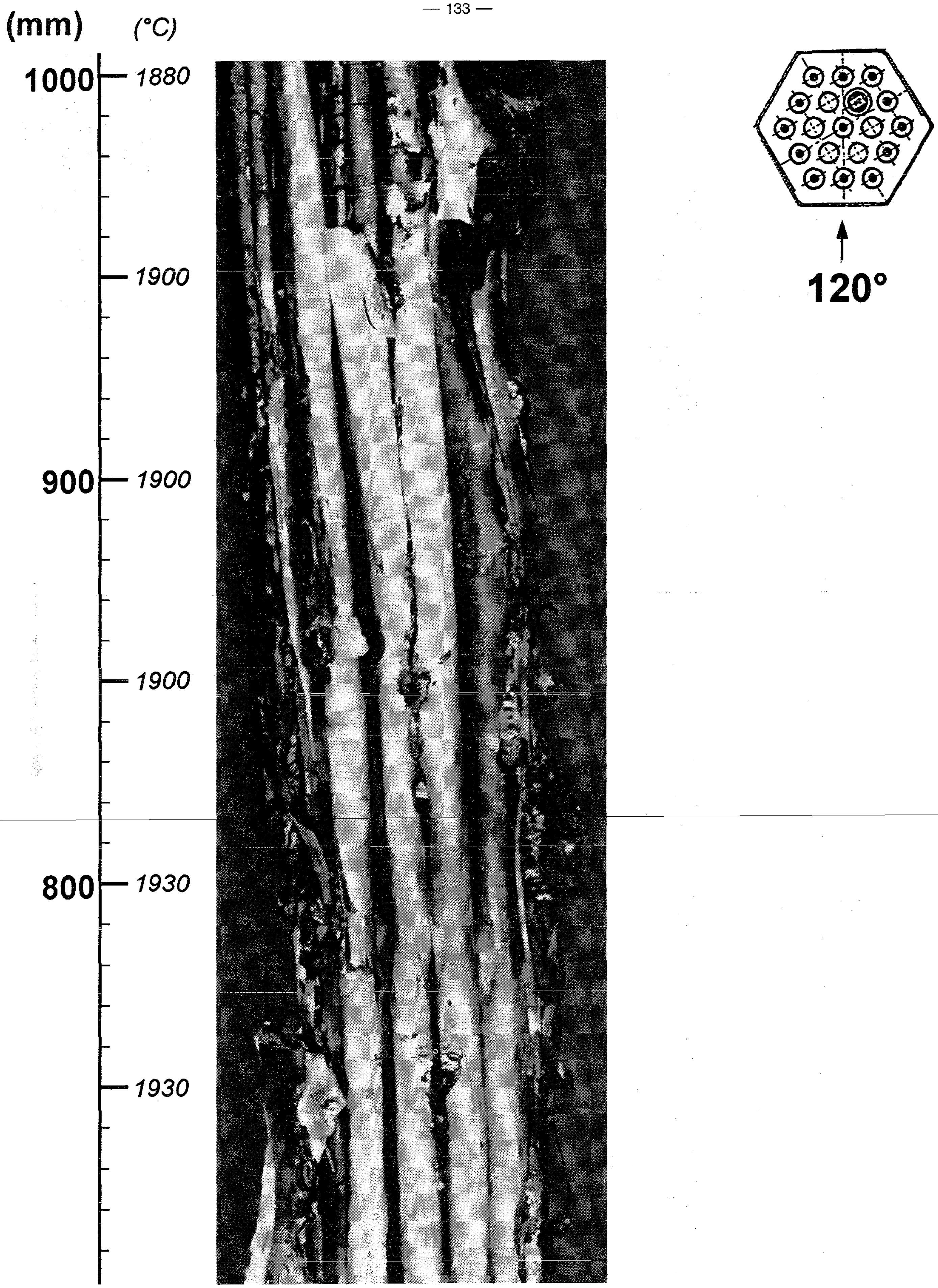

Fig. 96: Posttest view, 120° orientation

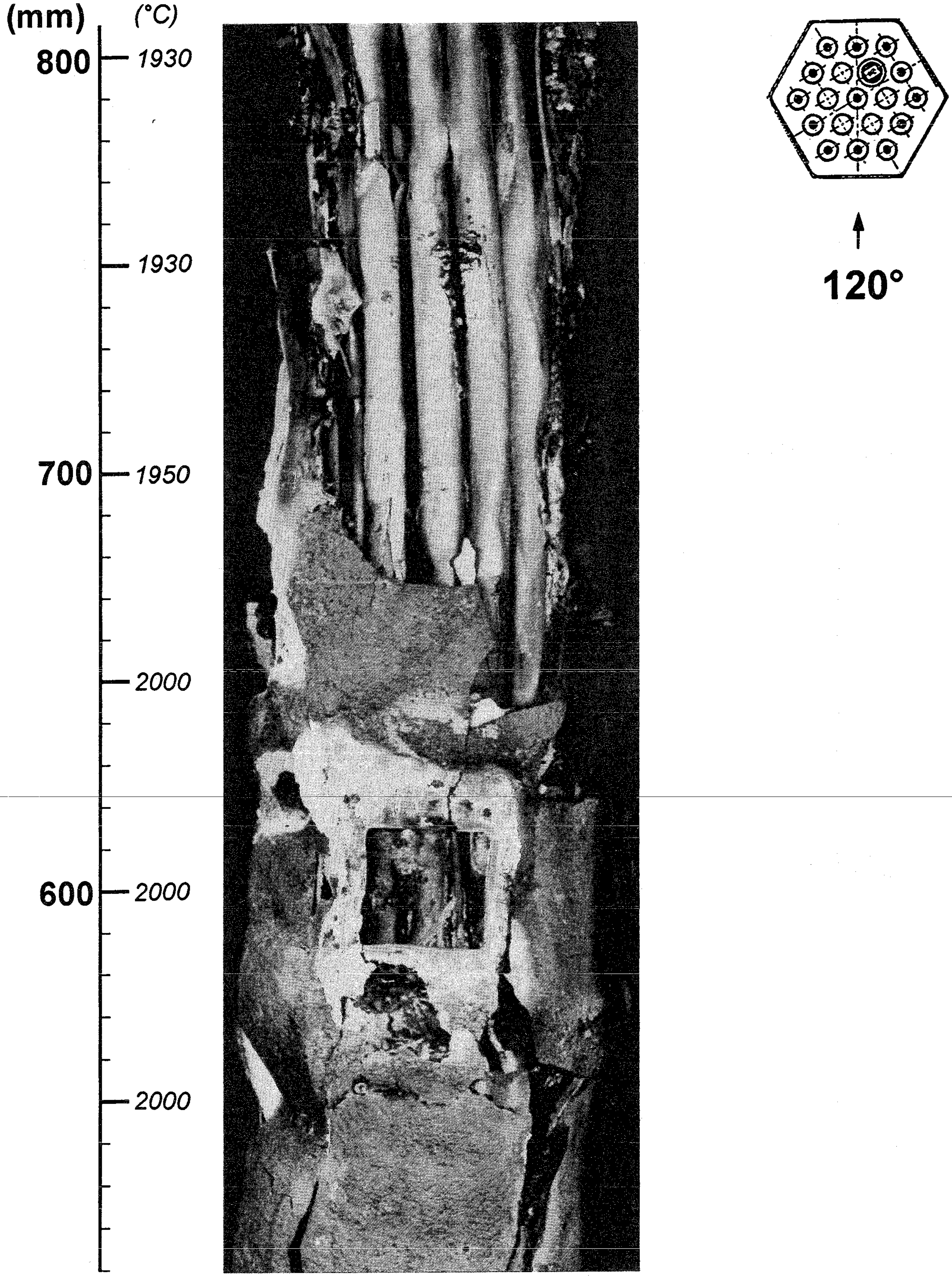

Fig. 97: Posttest view, 120° orientation

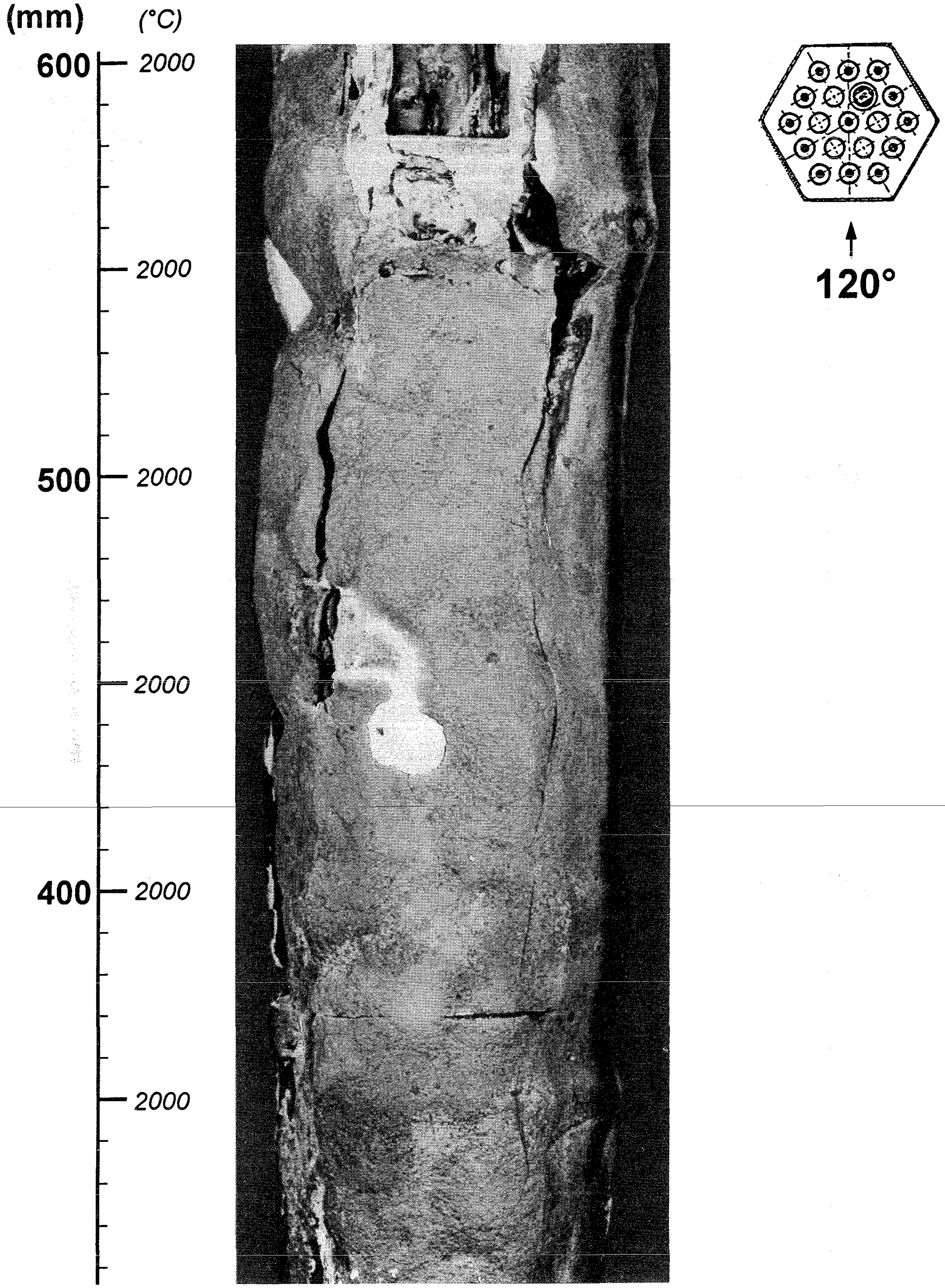

Fig. 98: Posttest view, 120° orientation

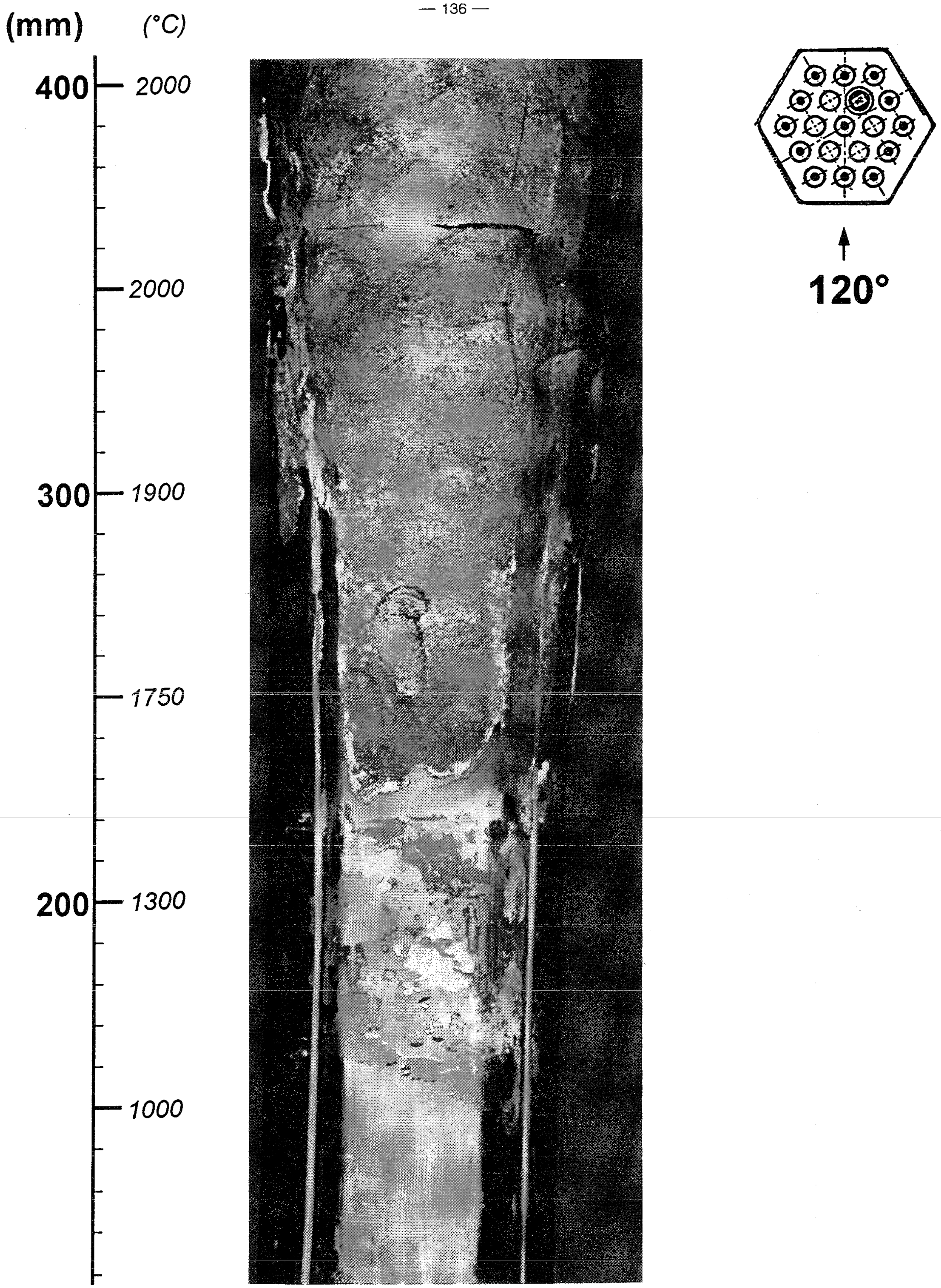

Fig. 99: Posttest view, 120° orientation

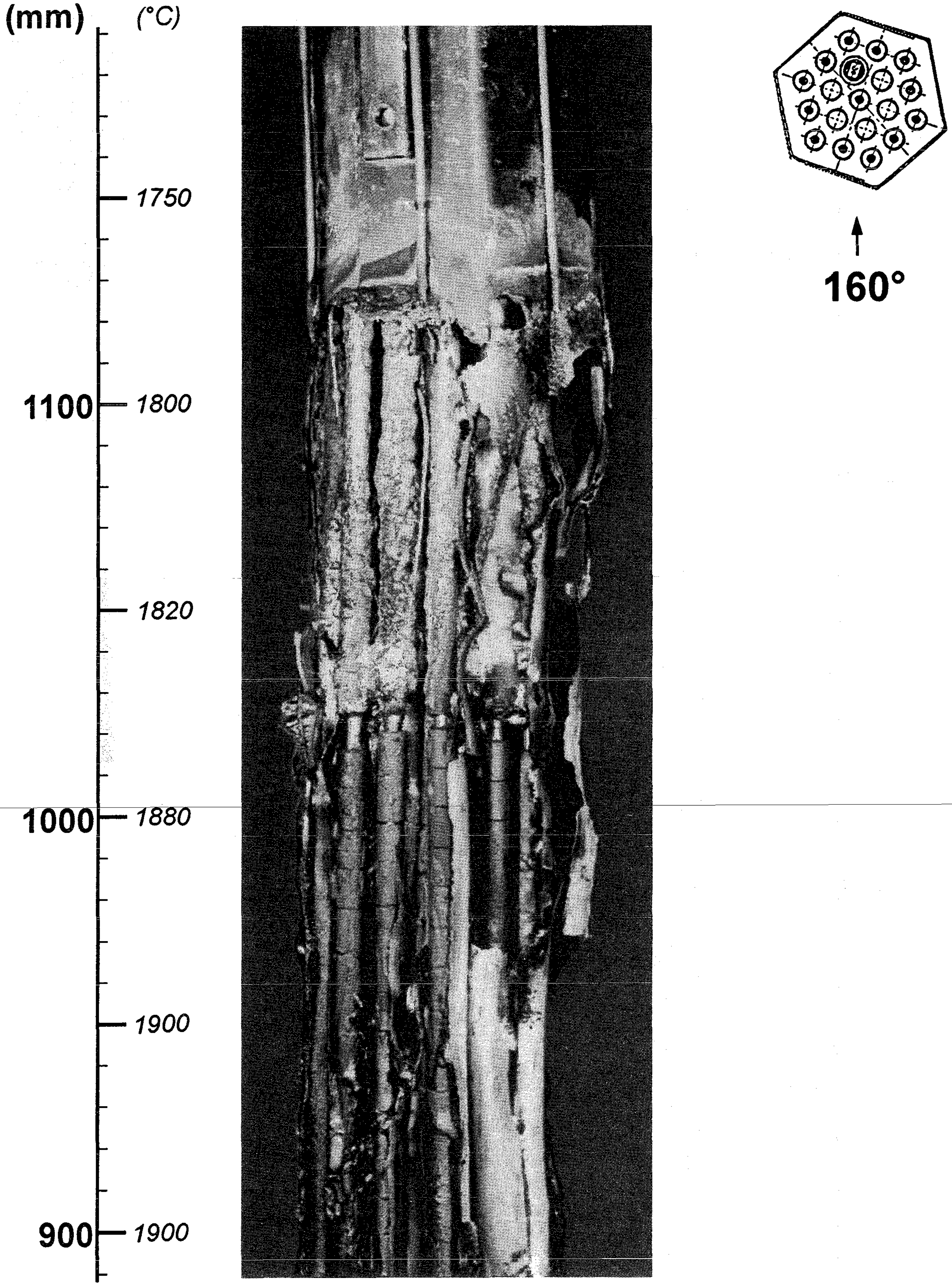

Fig. 100: Posttest view, 160° orientation

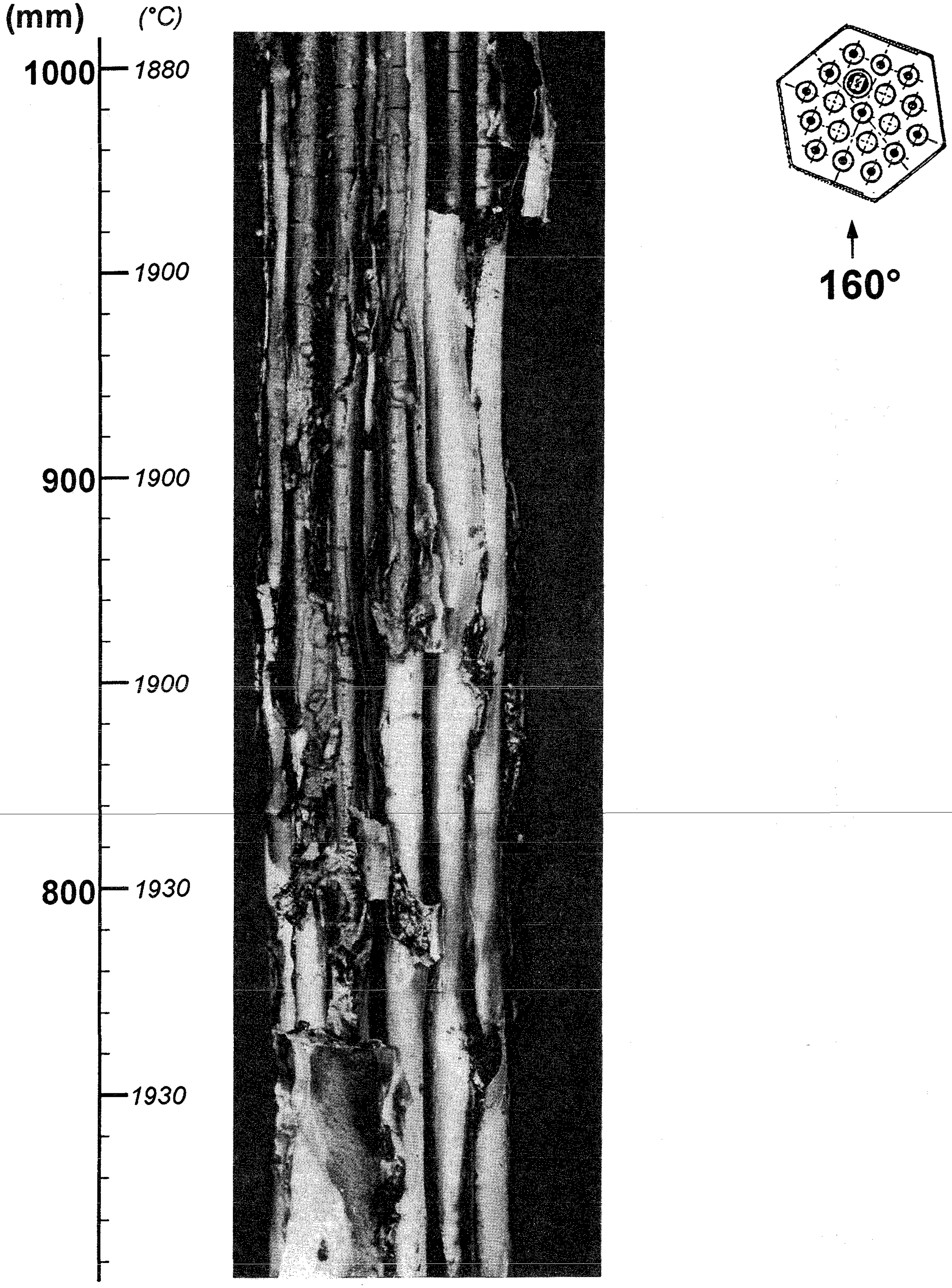

Fig. 101: Posttest view, 160° orientation

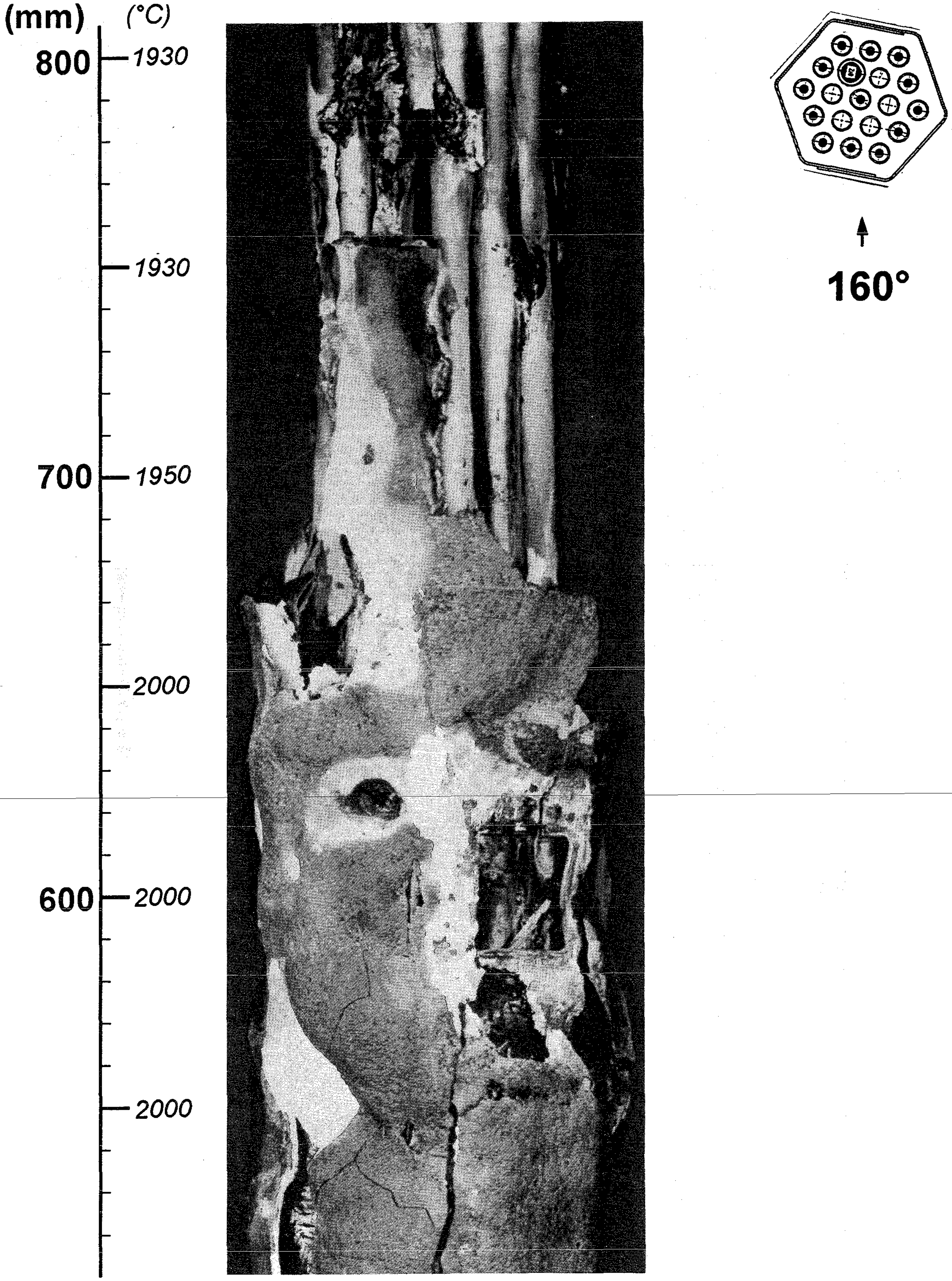

Fig. 102: Posttest view, 160° orientation

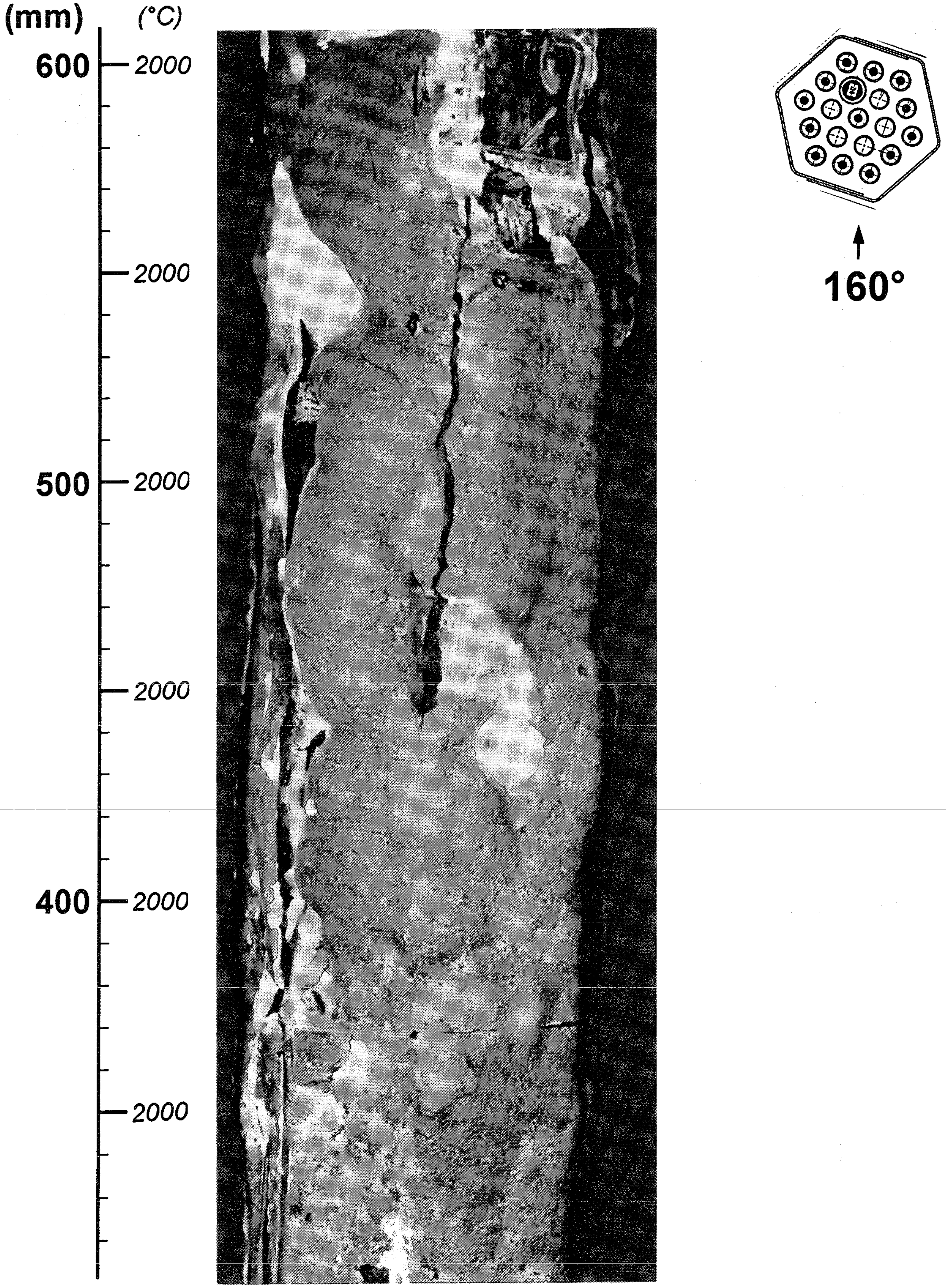

Fig. 103: Posttest view, 160° orientation

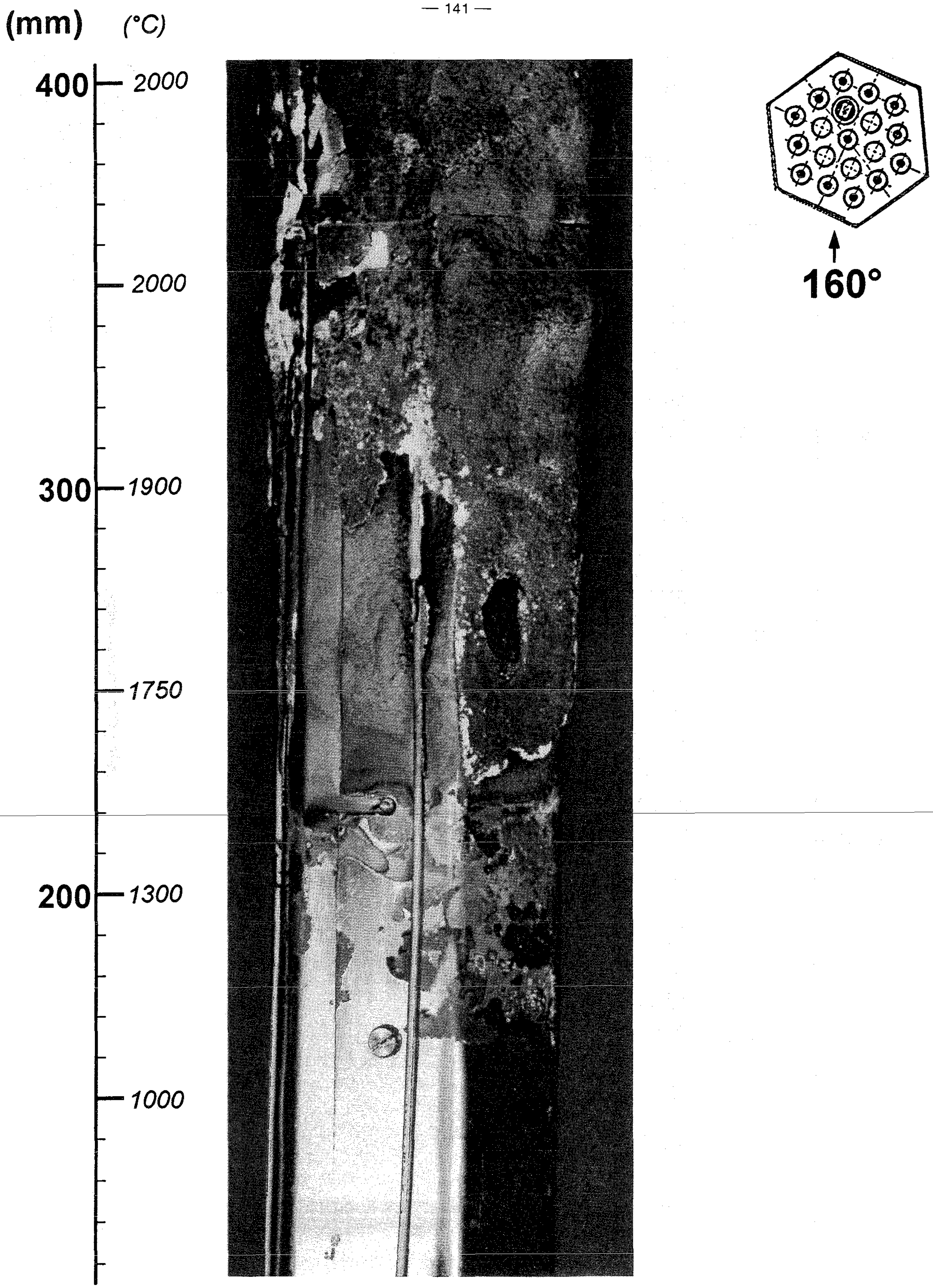

Fig. 104: Posttest view, 160° orientation

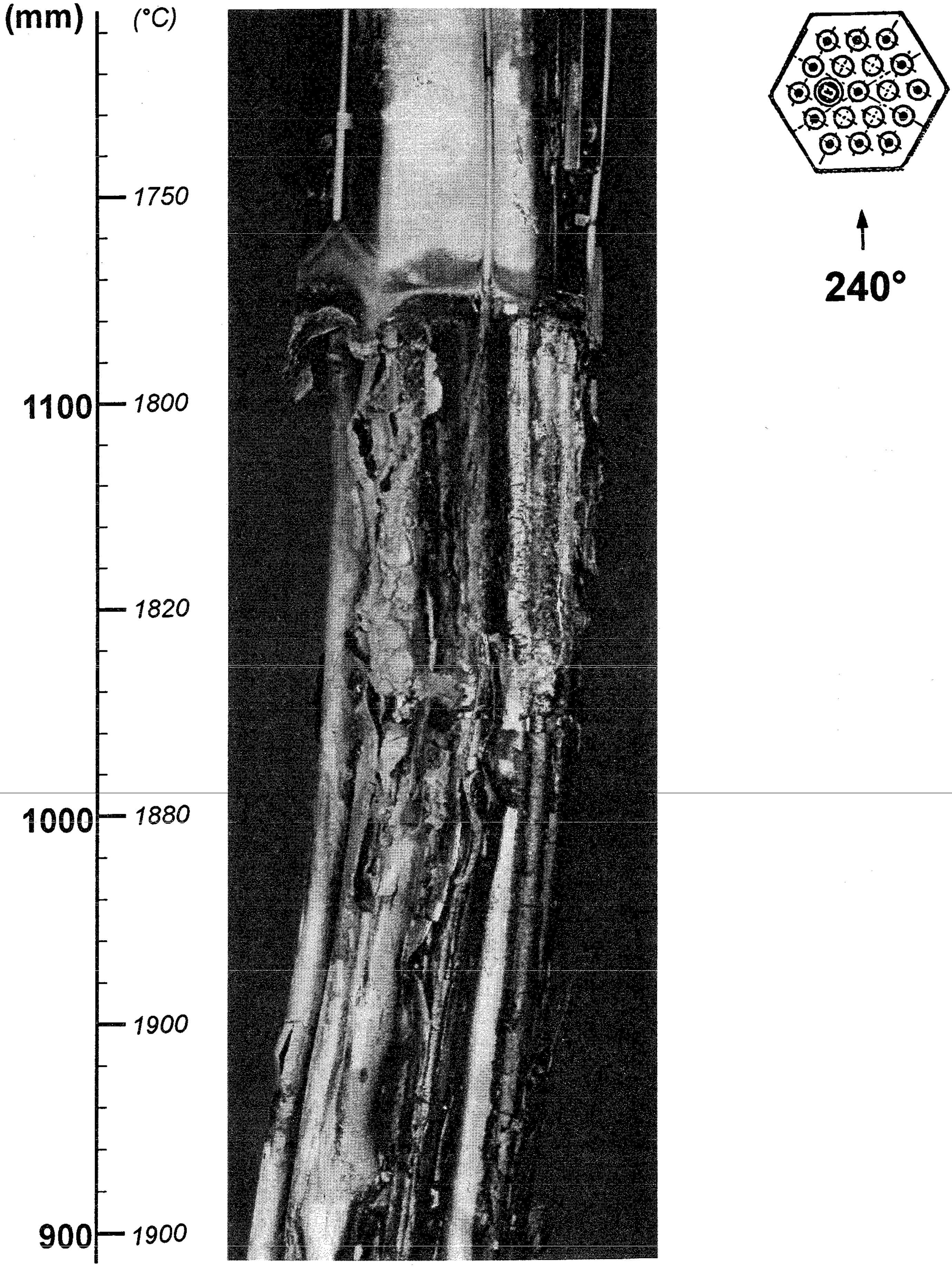

Fig. 105: Posttest view, 240° orientation

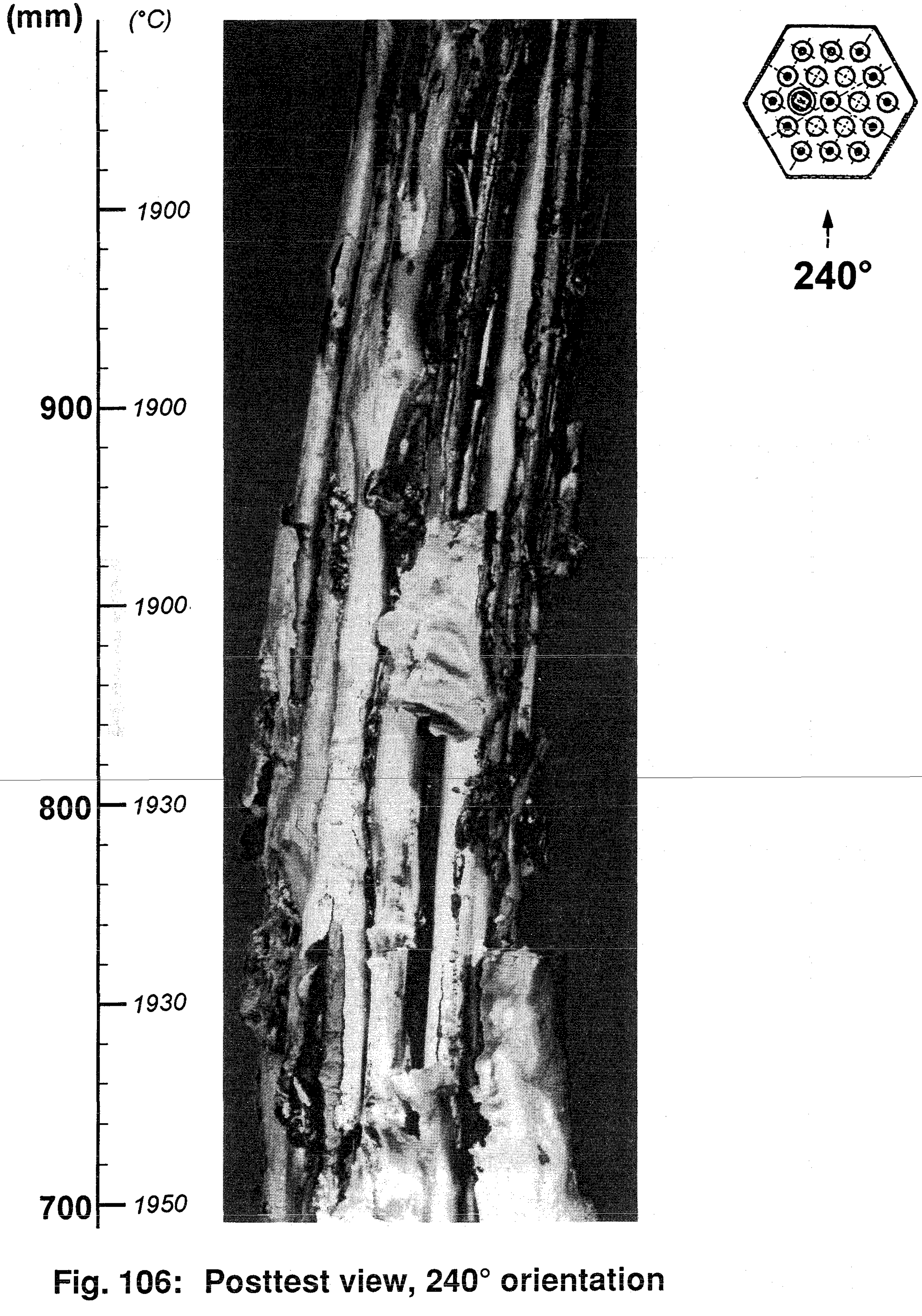

Fig. 106: Posttest view, 240° orientation

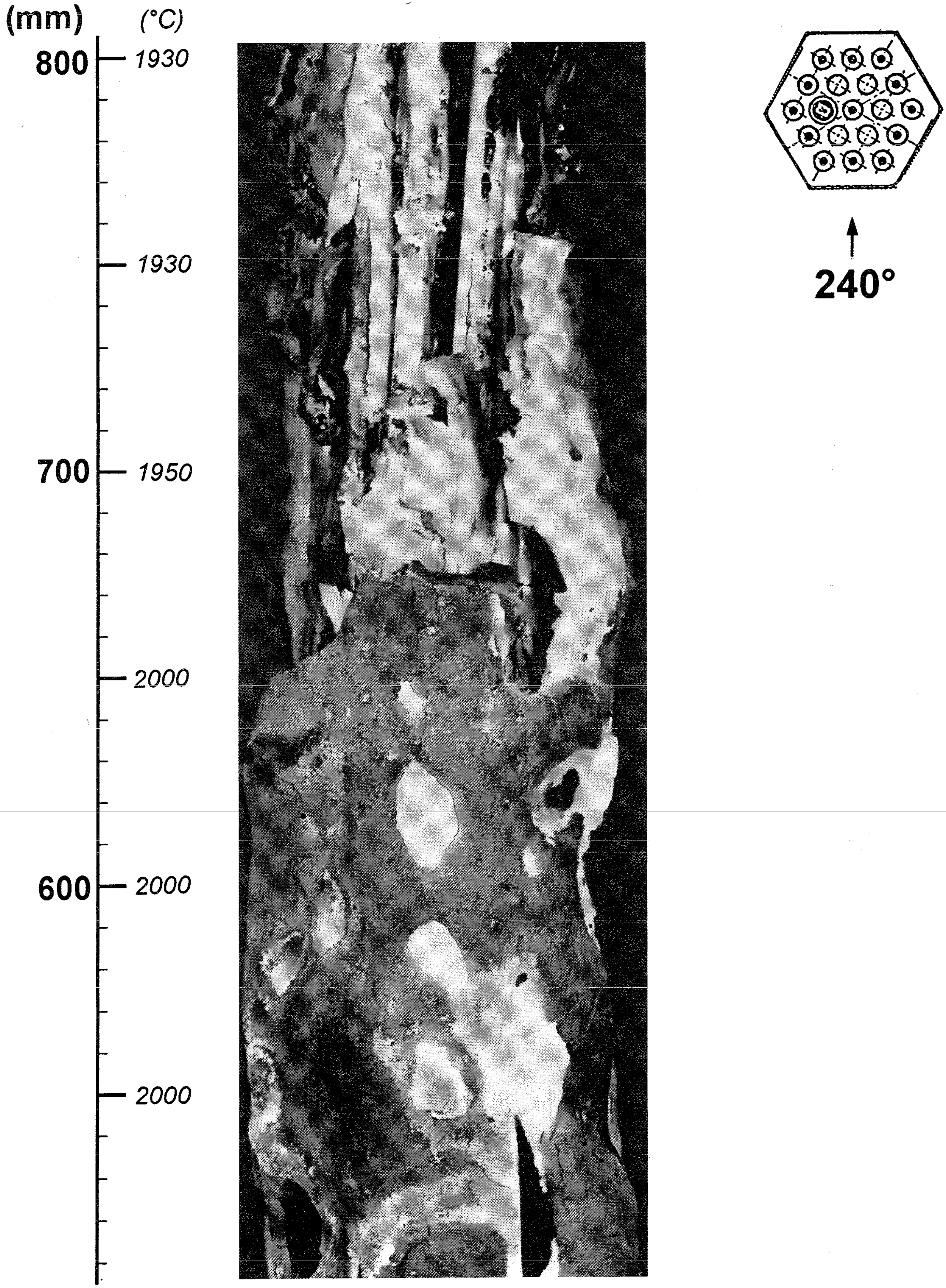

Fig. 107: Posttest view, 240° orientation

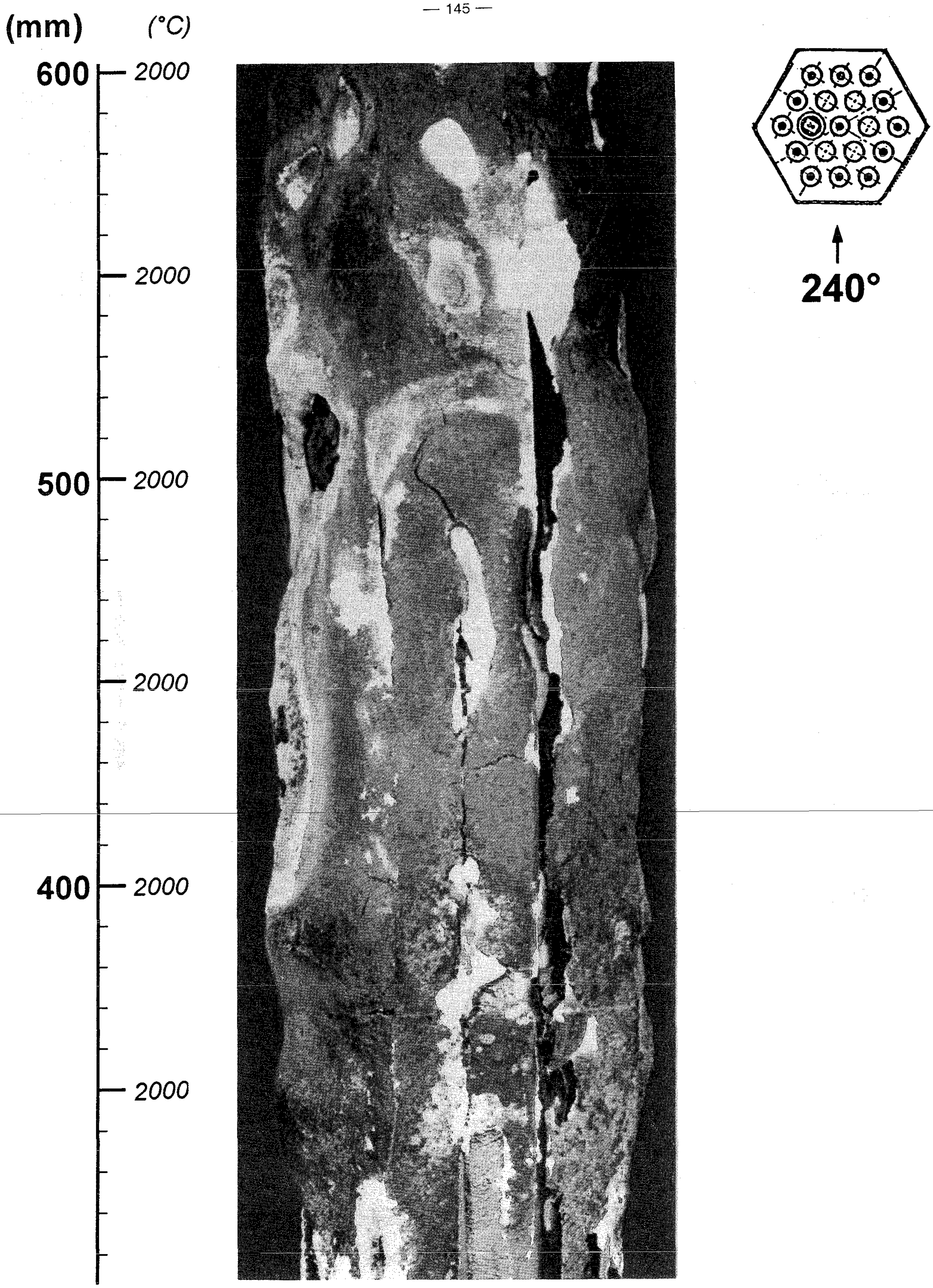

Fig. 108: Posttest view, 240° orientation

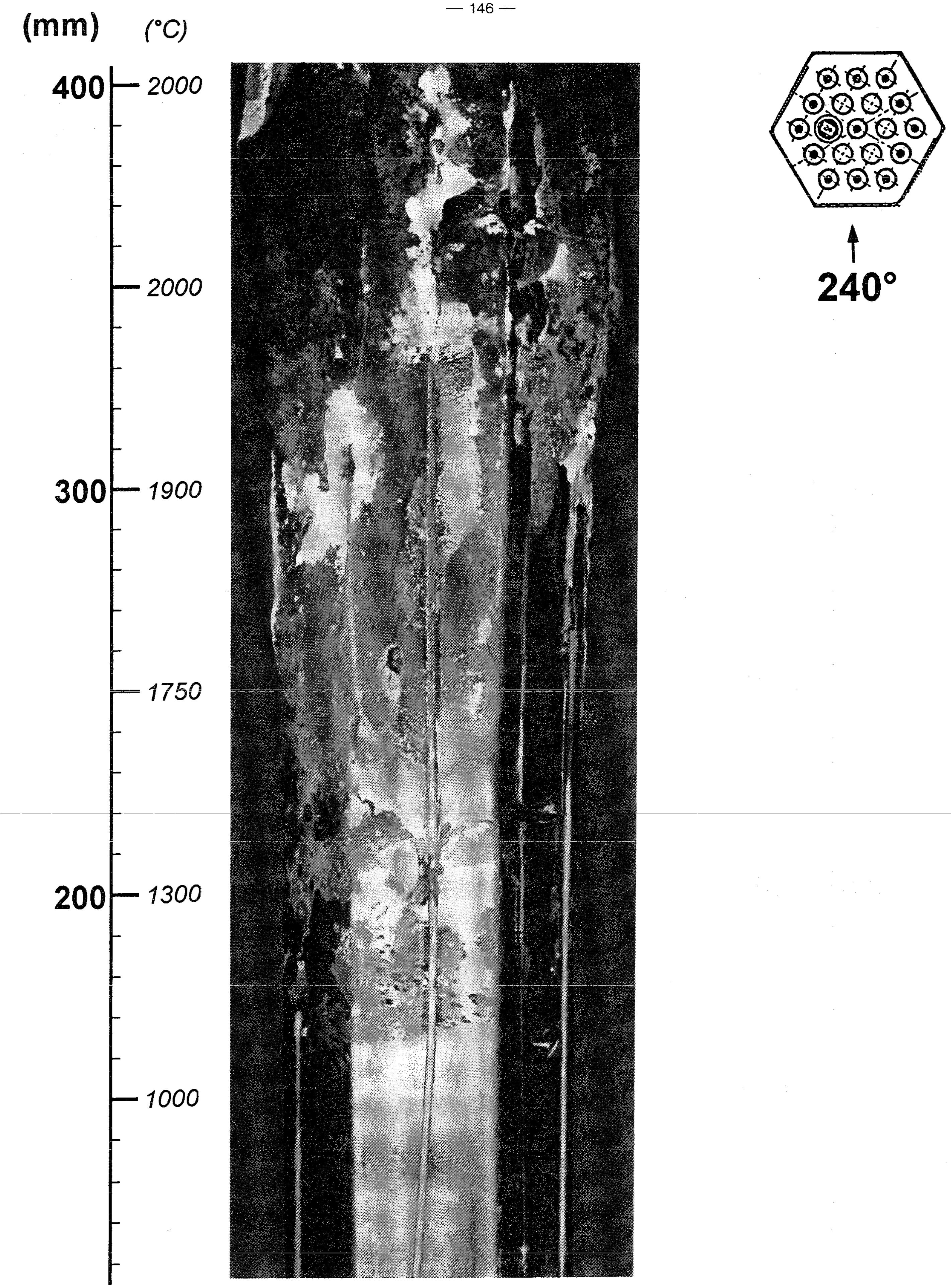

Fig. 109: Posttest view, 240° orientation

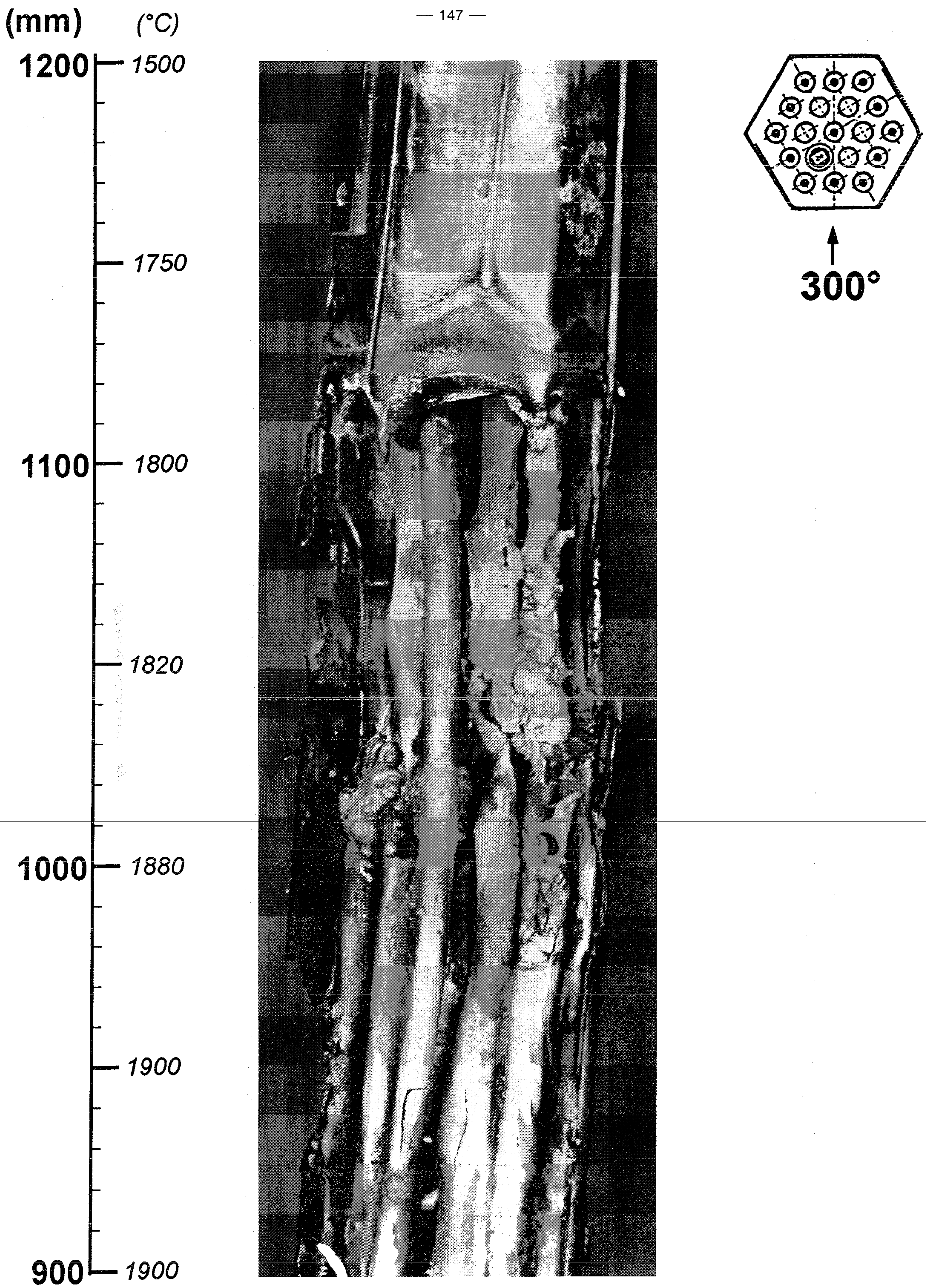

Fig. 110: Posttest view, 300° orientation

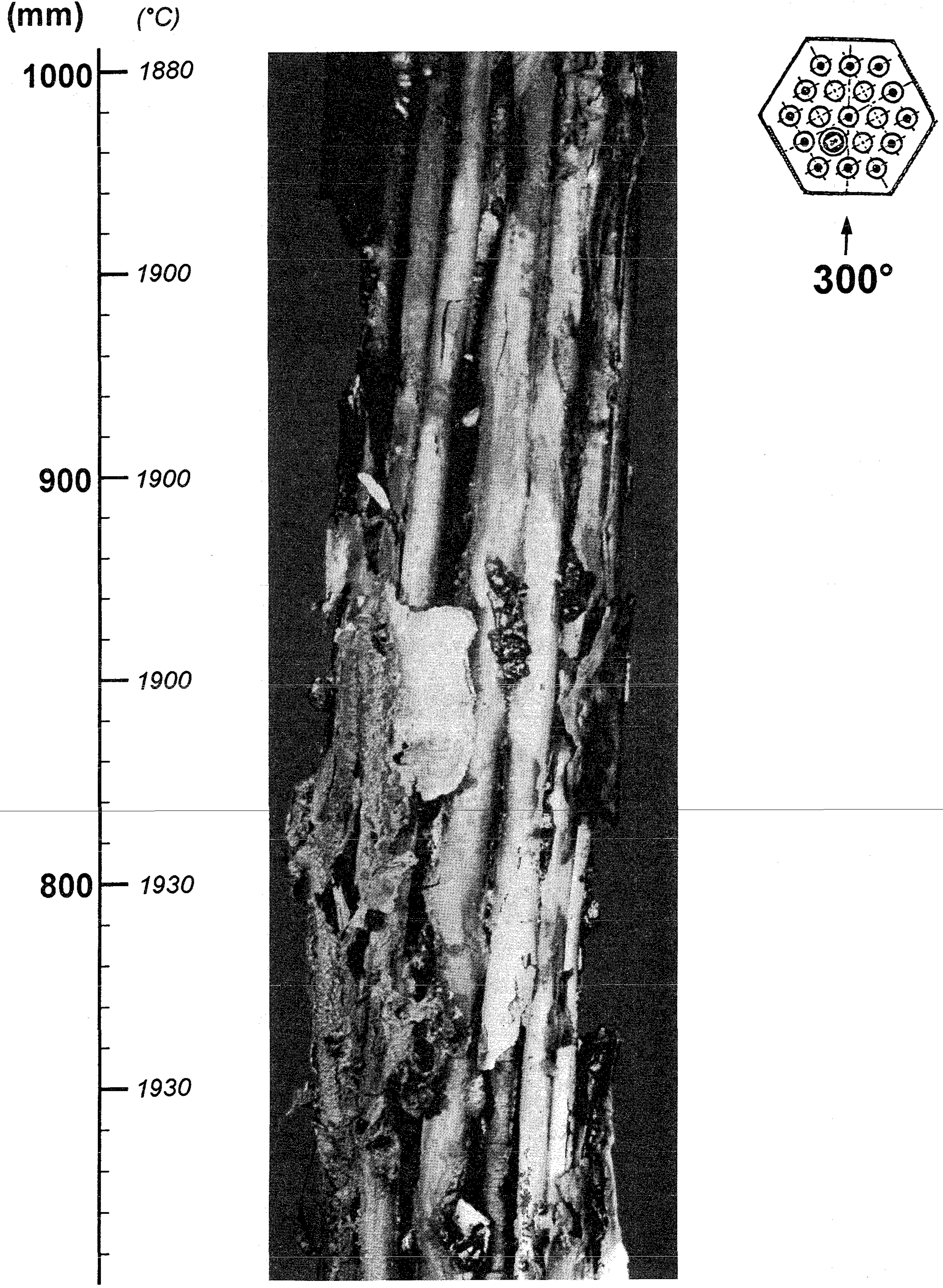

Fig. 111: Posttest view, 300° orientation

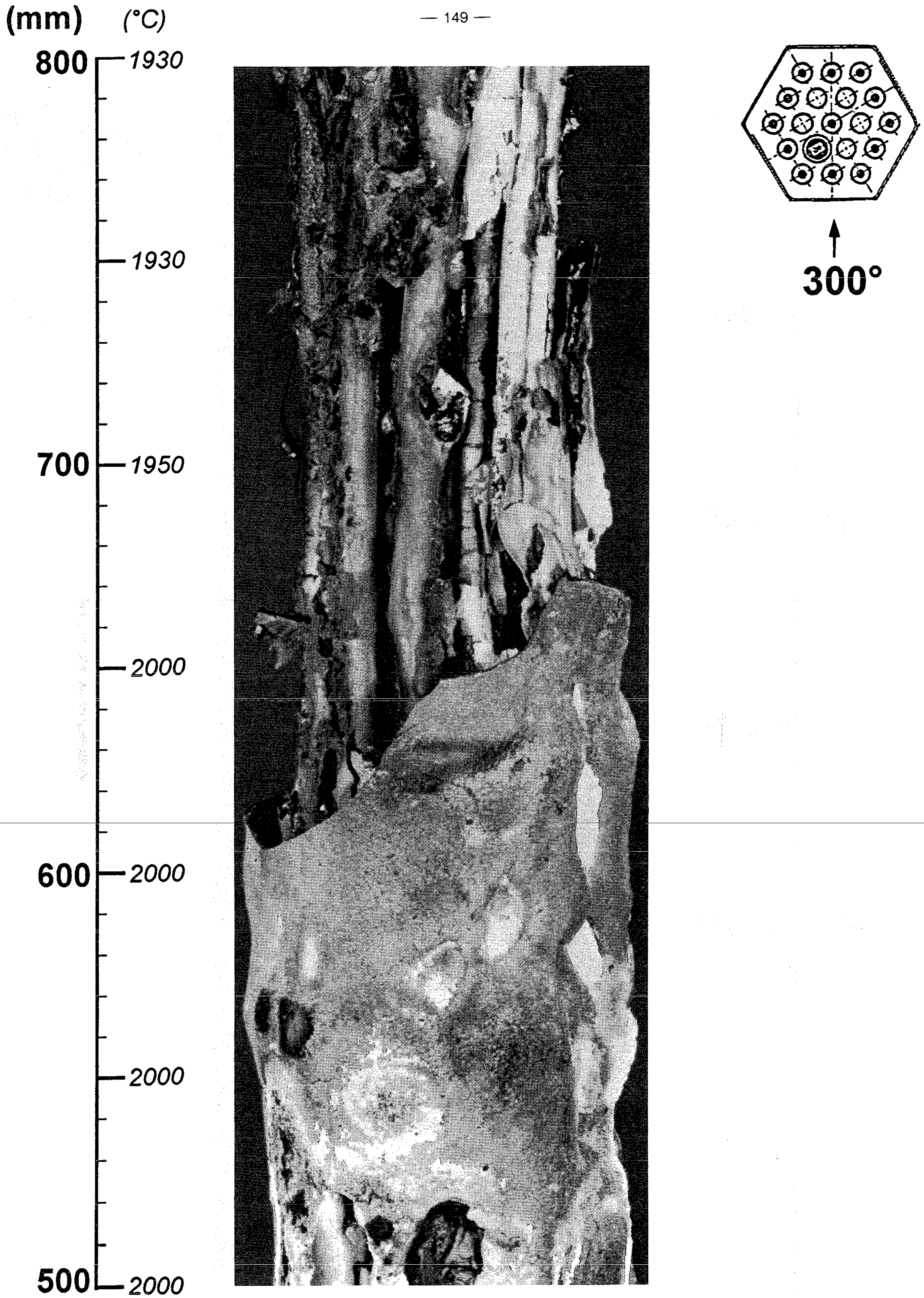

Fig. 112: Posttest view, 300° orientation

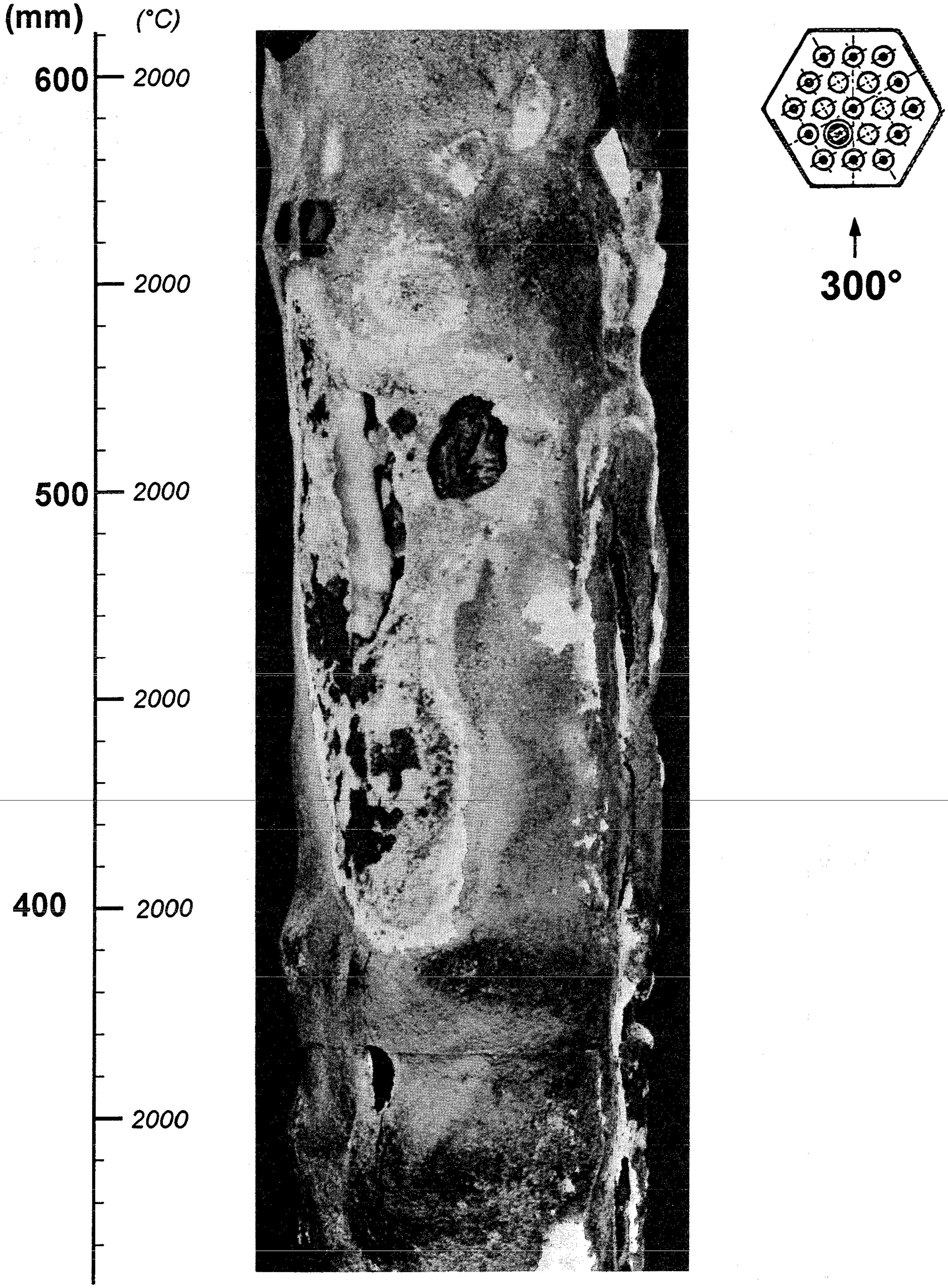

Fig. 113: Posttest view, 300° orientation

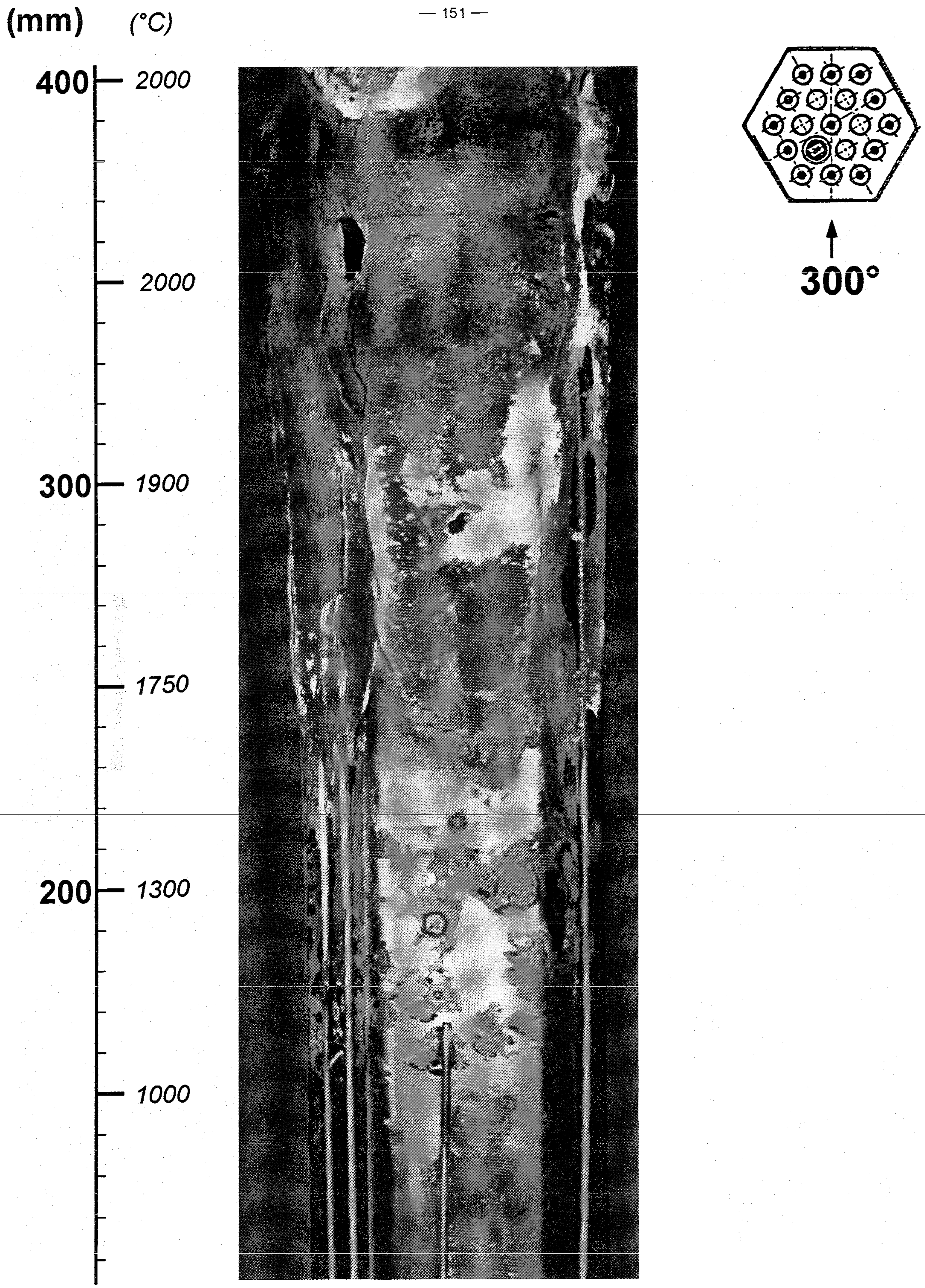

Fig. 114: Posttest view, 300° orientation

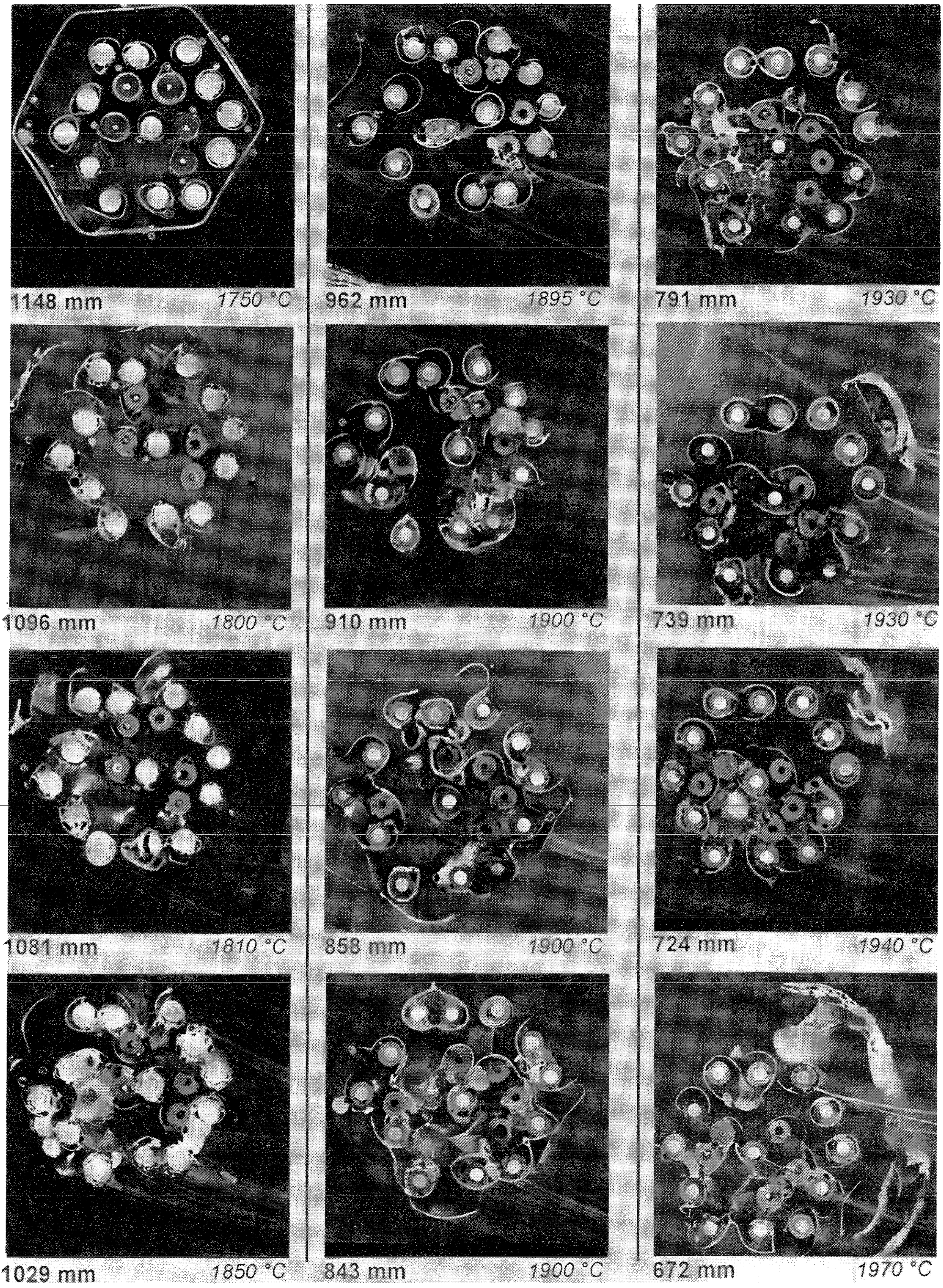

1148 mm 1750 °C

1096 mm 1800 °C

1081 mm 1810 °C

1029 mm 1850 °C

962 mm 1895 °C

910 mm 1900 °C

858 mm 1900 °C

843 mm 1900 °C

791 mm 1930 °C

739 mm 1930 °C

724 mm 1940 °C

672 mm 1970 °C

(top)

Fig. 115: Horizontal cross sections of bundle CORA-W2, top planes (1148 - 672 mm)

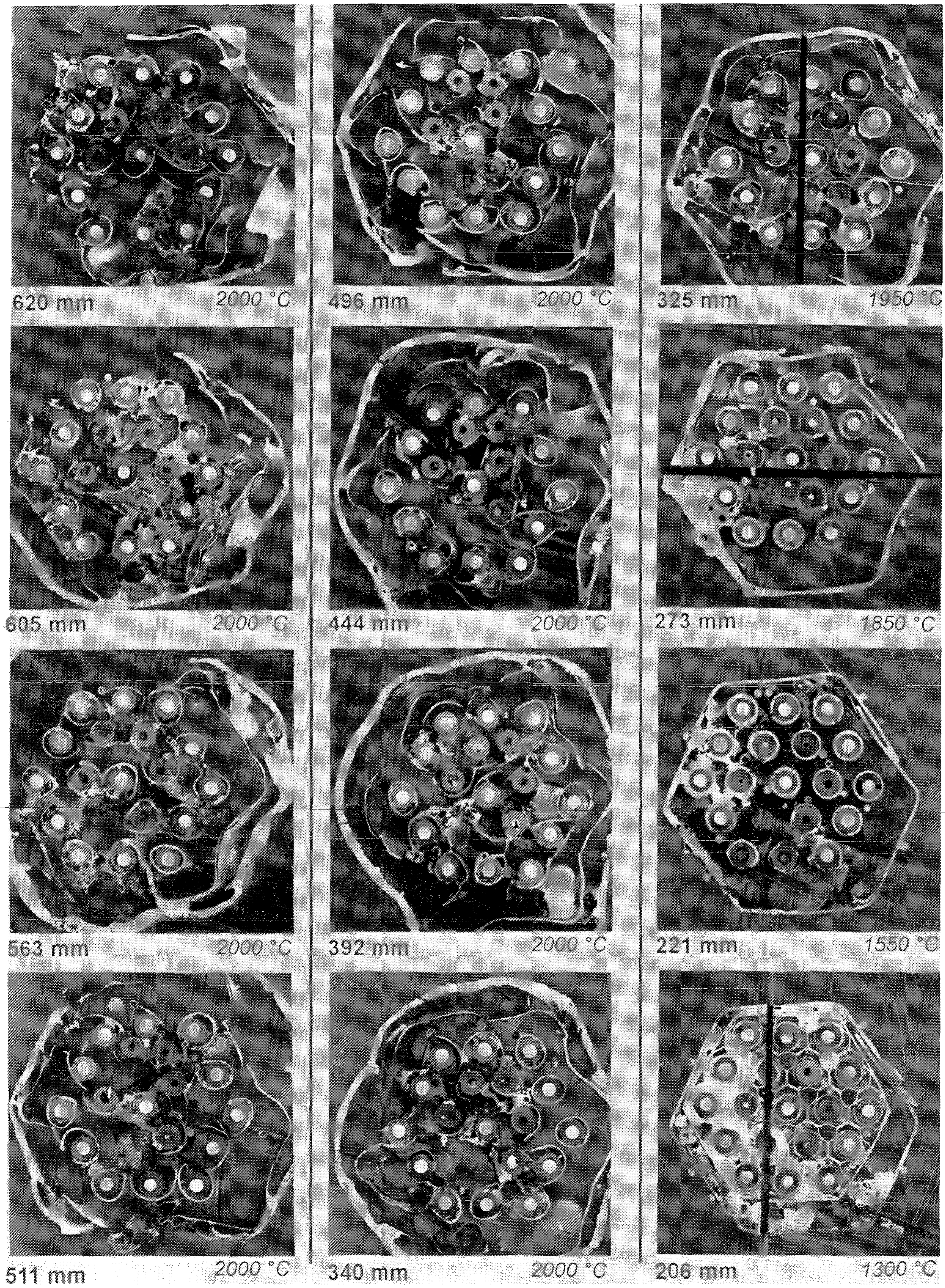

620 mm 2000 °C
496 mm 2000 °C
325 mm 1950 °C

605 mm 2000 °C
444 mm 2000 °C
273 mm 1850 °C

563 mm 2000 °C
392 mm 2000 °C
221 mm 1550 °C

511 mm 2000 °C
340 mm 2000 °C
206 mm 1300 °C

(top)

Fig. 116: Horizontal cross sections of bundle CORA-W2, top planes (620 - 206 mm)

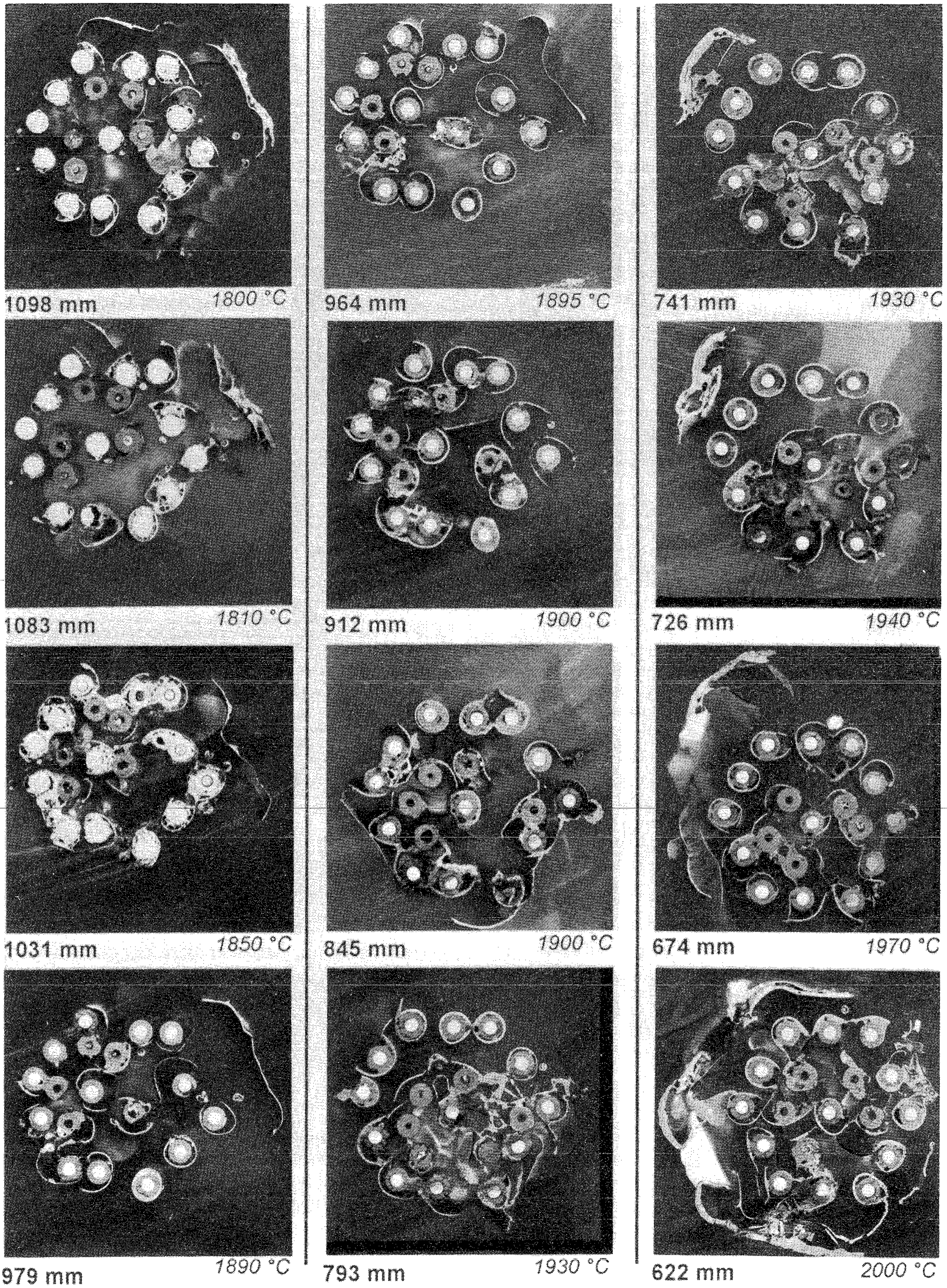

1098 mm 1800 °C
1083 mm 1810 °C
1031 mm 1850 °C
979 mm 1890 °C
964 mm 1895 °C
912 mm 1900 °C
845 mm 1900 °C
793 mm 1930 °C
741 mm 1930 °C
726 mm 1940 °C
674 mm 1970 °C
622 mm 2000 °C

(bottom)

Fig. 117: Horizontal cross sections of bundle CORA-W2, bottom planes (1098 - 622 mm)

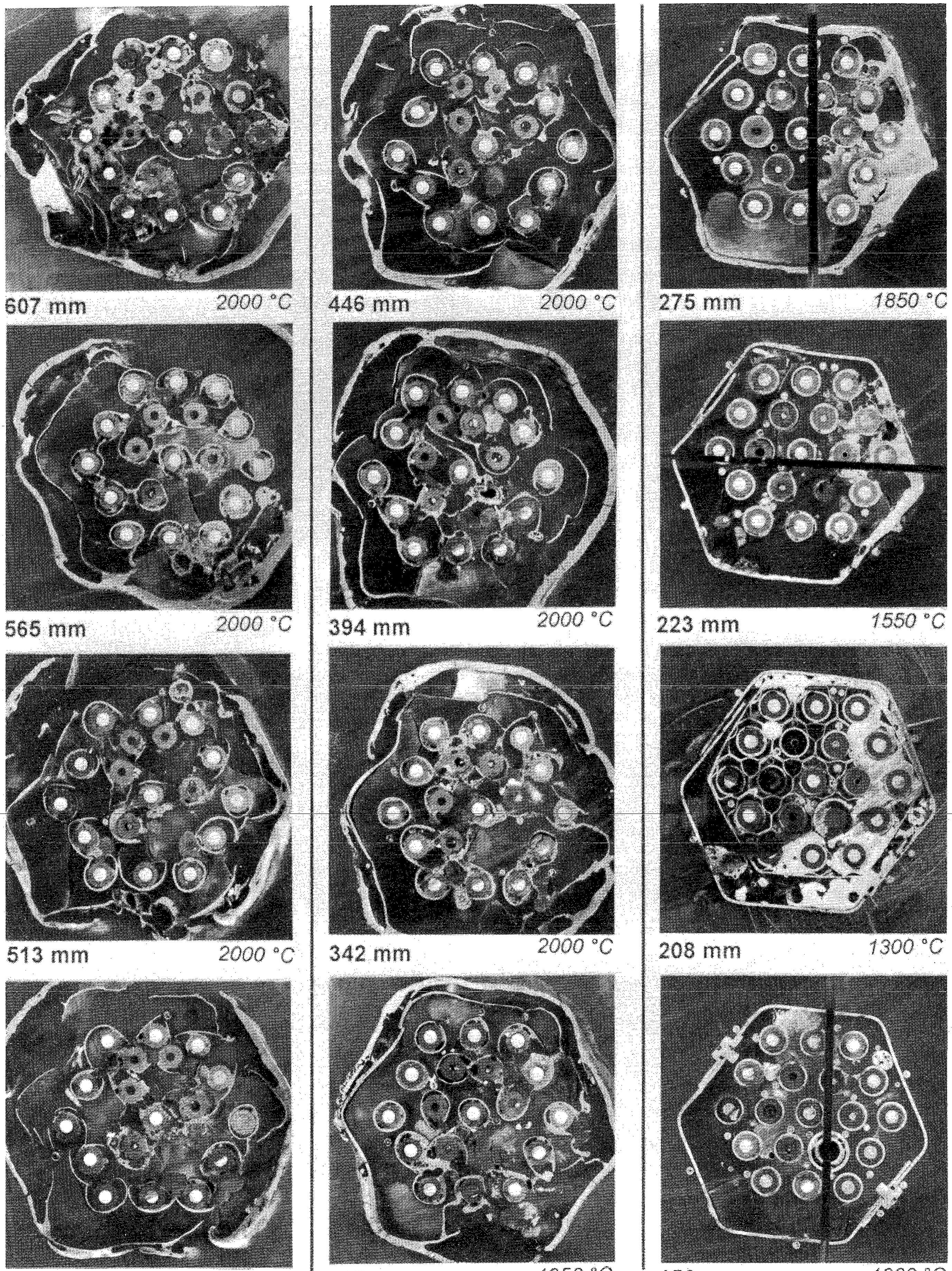

607 mm 2000 °C

565 mm 2000 °C

513 mm 2000 °C

498 mm 2000 °C

446 mm 2000 °C

394 mm 2000 °C

342 mm 2000 °C

327 mm 1950 °C

275 mm 1850 °C

223 mm 1550 °C

208 mm 1300 °C

156 mm 1000 °C

(bottom)

Fig. 118: Horizontal cross sections of bundle CORA-W2, bottom planes (607 - 156 mm)

top

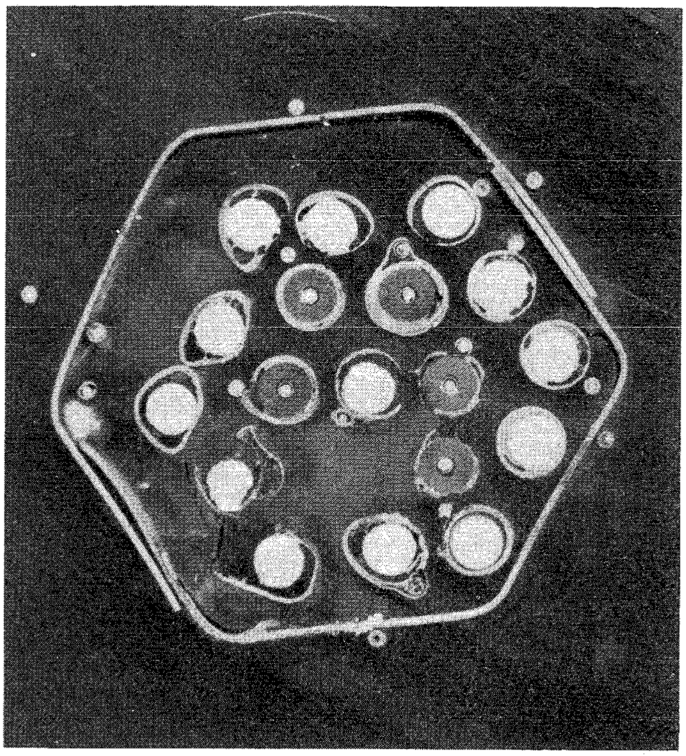

1750°C

1148 mm

bottom

top

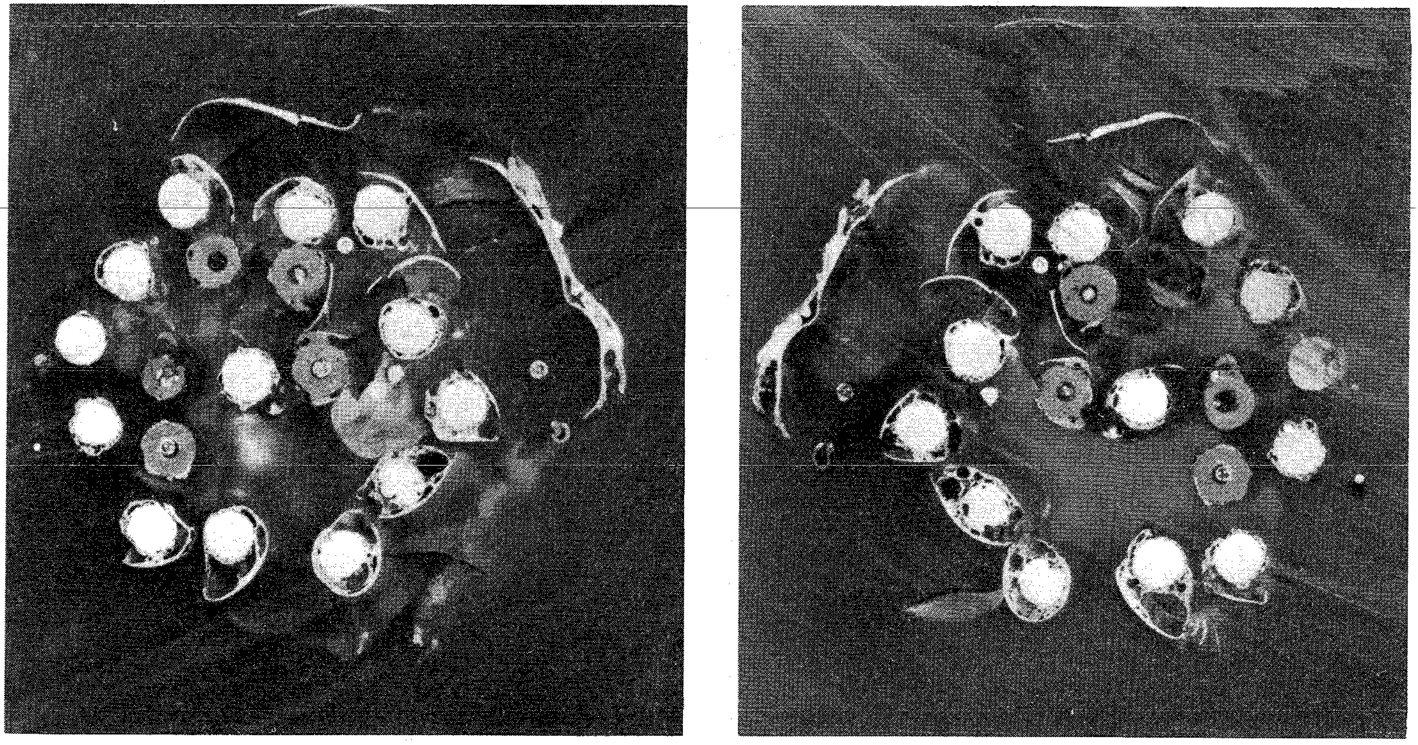

1098 mm

1800°C

1096 mm

Fig. 119: Horizontal cross sections of bundle CORA-W2, enlarged views of sections at 1148, 1098, and 1096 mm

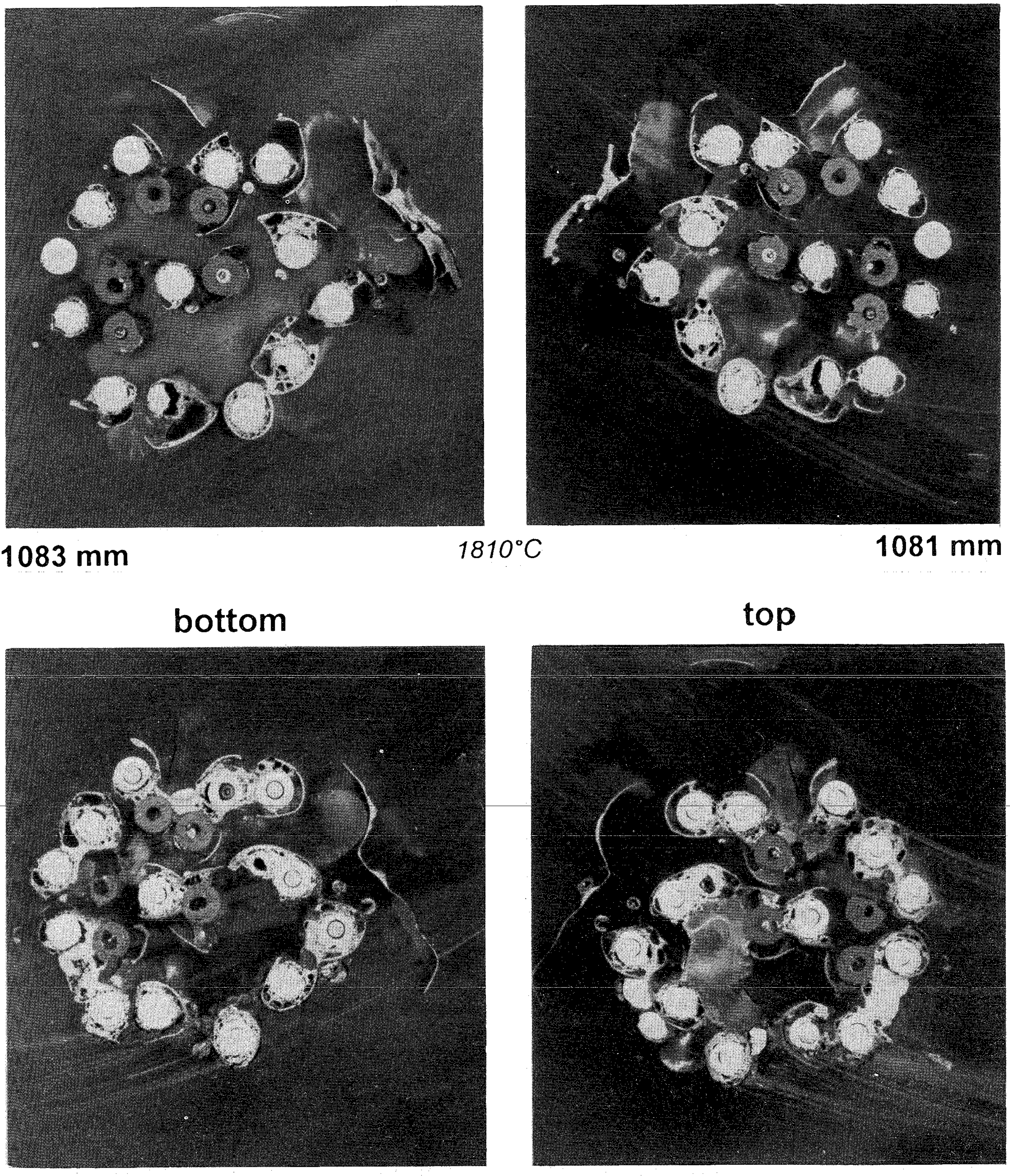

bottom

top

1083 mm

1810°C

1081 mm

bottom

top

1031 mm

1850°C

1029 mm

Fig. 120: Horizontal cross sections of bundle CORA-W2, enlarged views of sections at 1083, 1081, 1031 and 1029 mm

bottom top

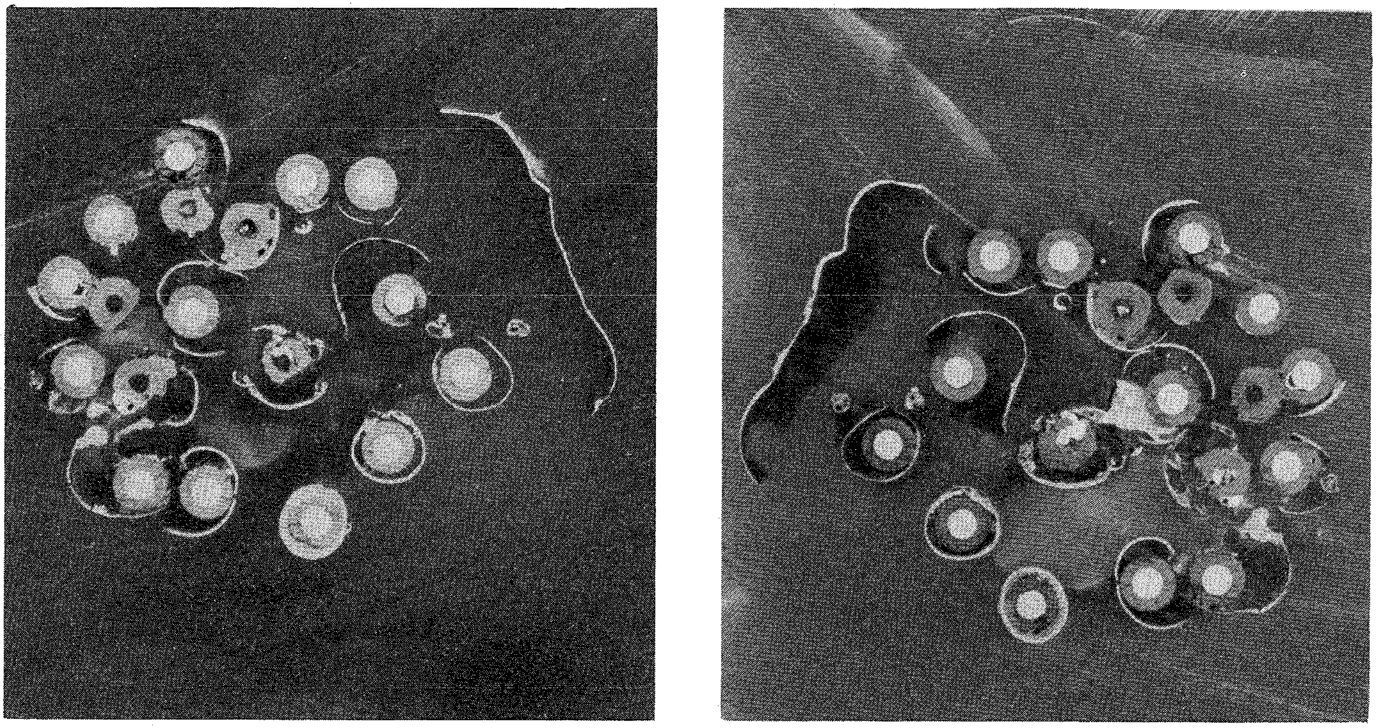

979 mm *1890°C* 977 mm

bottom top

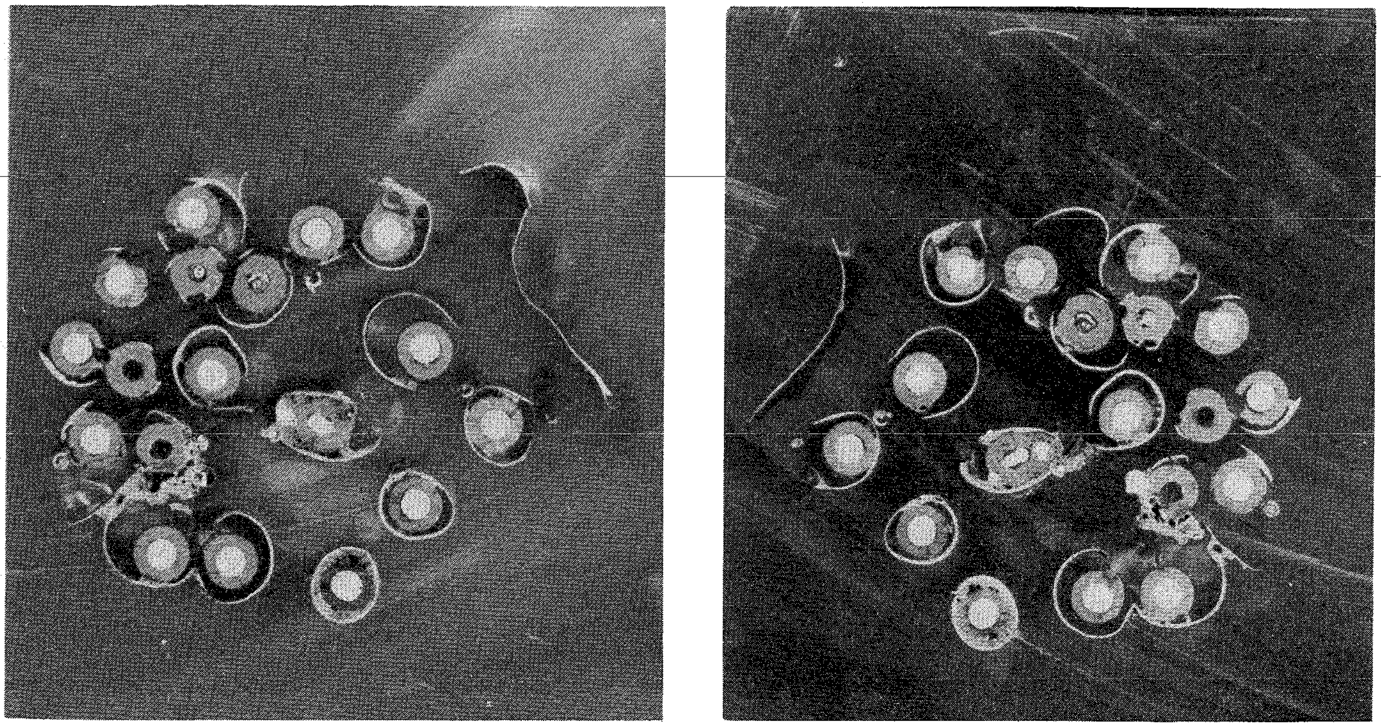

964 mm *1895°C* 962 mm

Fig. 121: Horizontal cross sections of bundle CORA-W2, enlarged views of sections at 979, 977, 964 and 962 mm

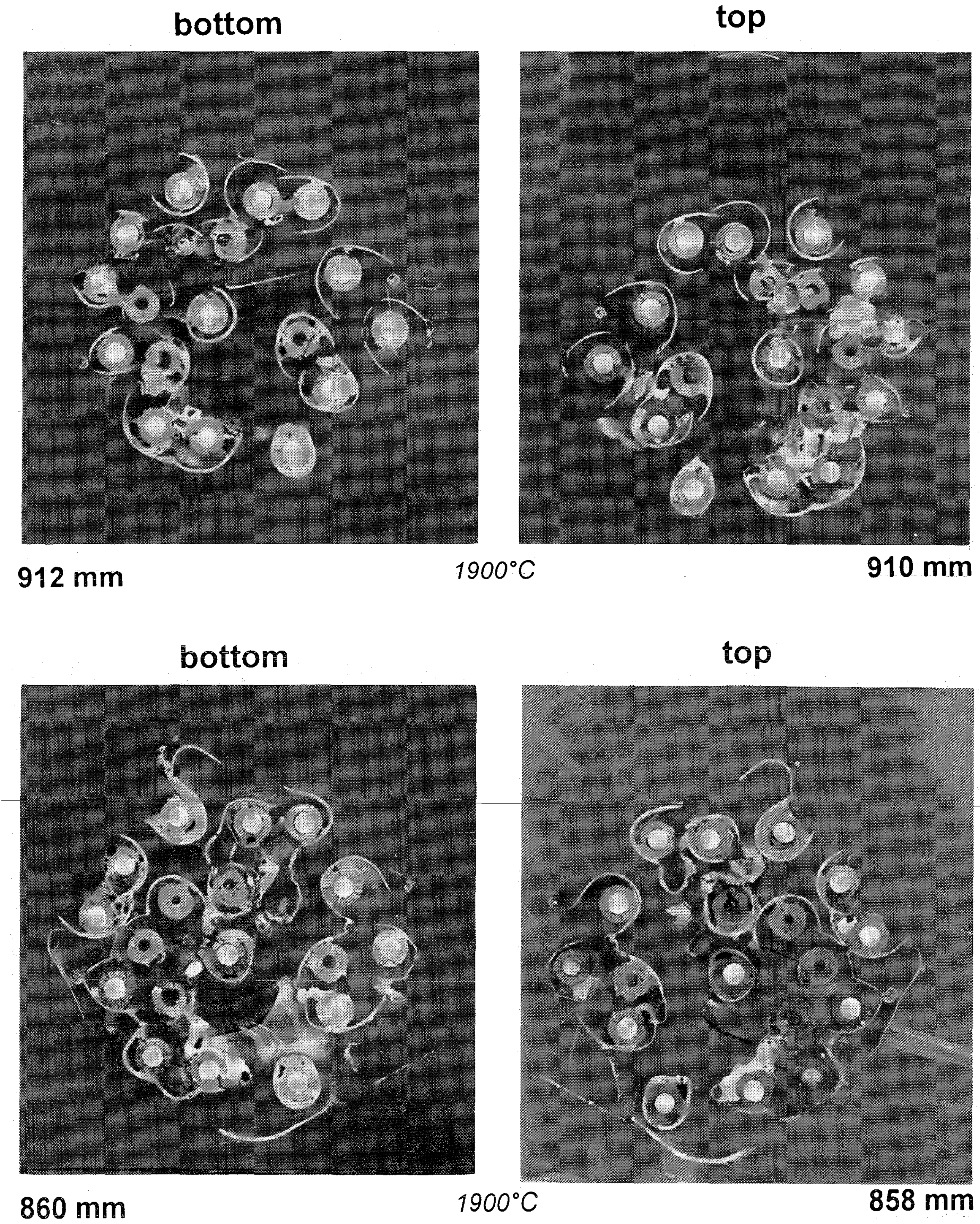

Fig. 122: Horizontal cross sections of bundle CORA-W2, enlarged views of sections at 912, 910, 860 and 858 mm

bottom top

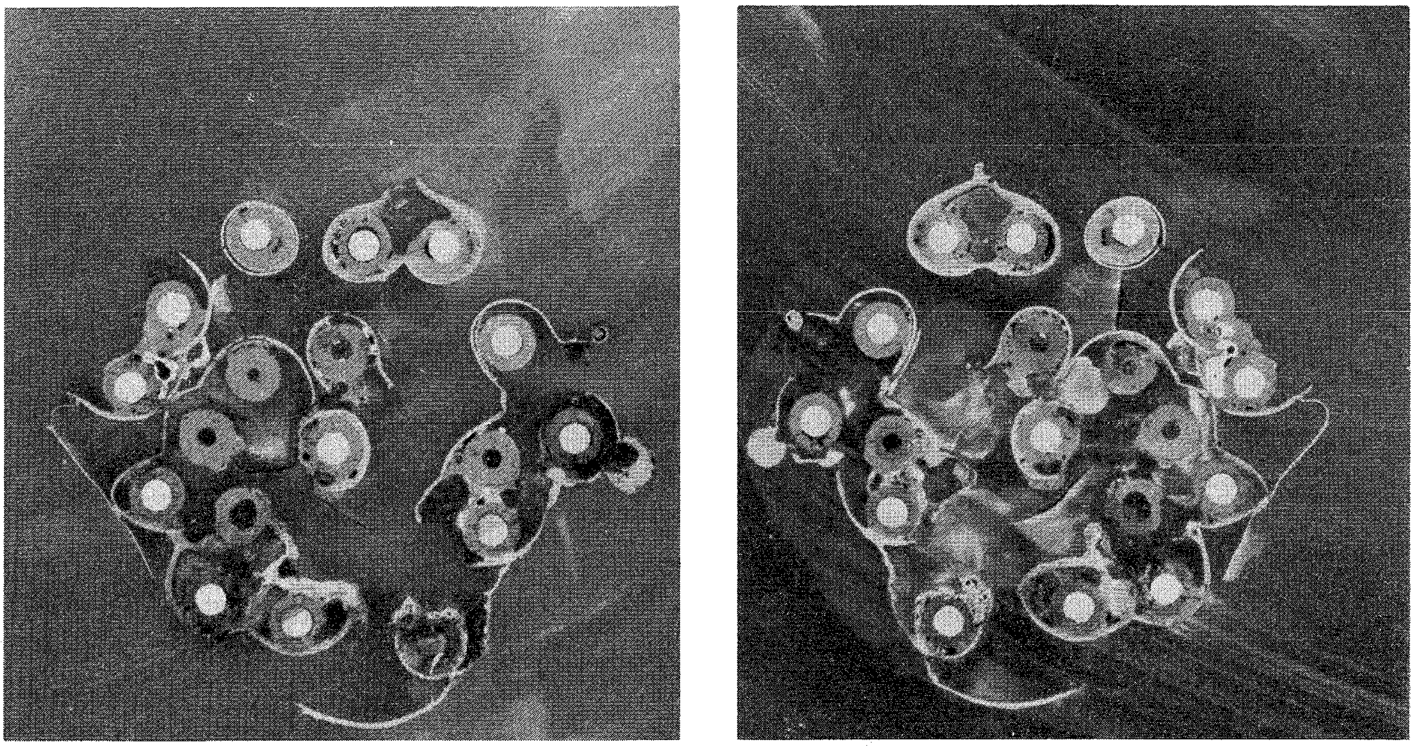

845 mm *1900°C* 843 mm

bottom top

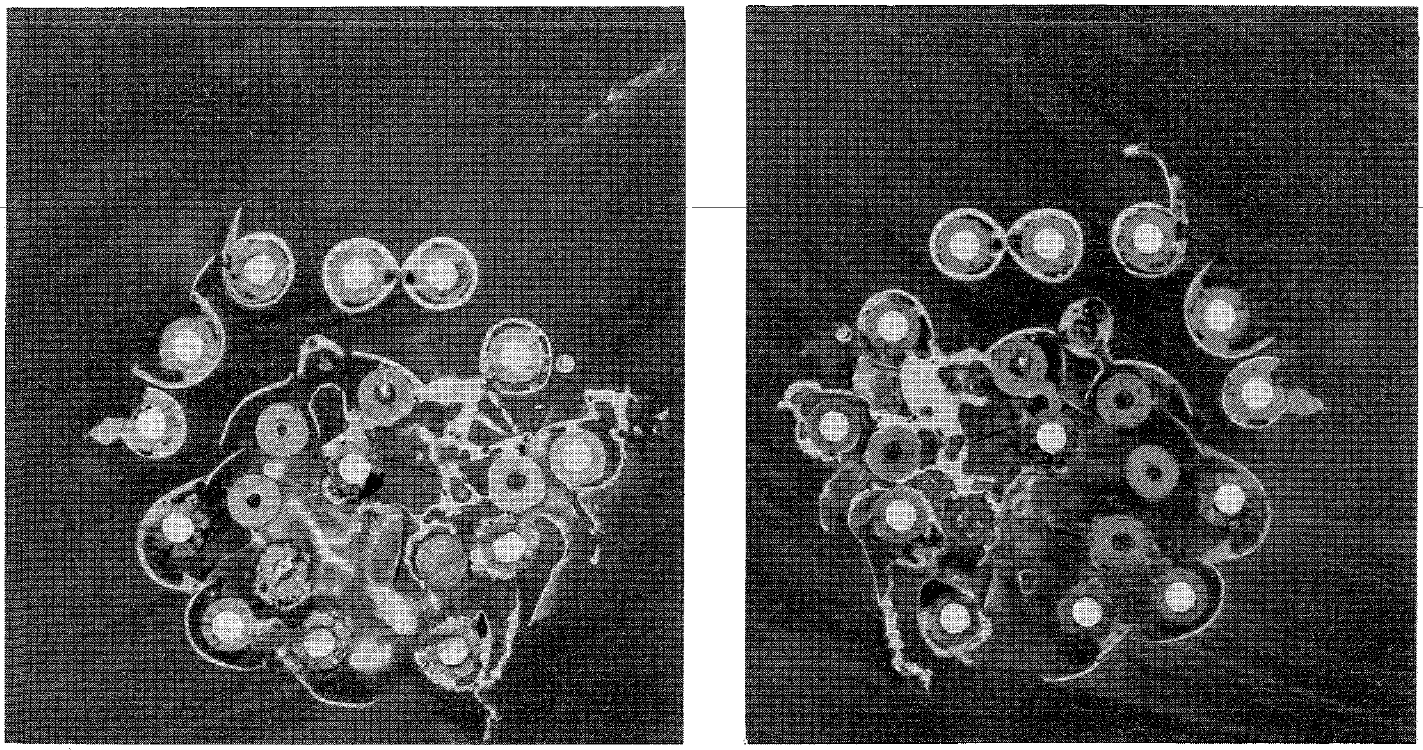

793 mm *1930°C* 791 mm

Fig. 123: Horizontal cross sections of bundle CORA-W2, enlarged views of sections at 845, 843, 793 and 791 mm

bottom top

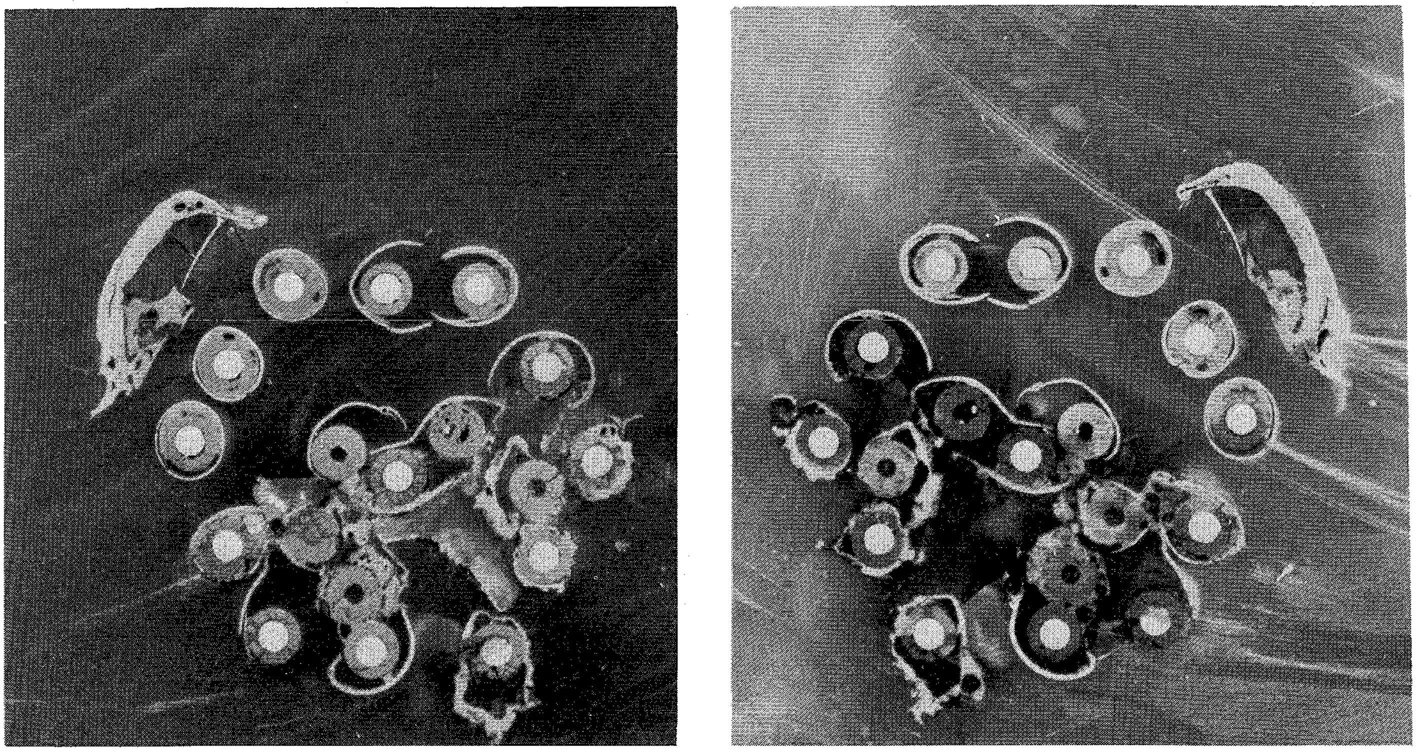

741 mm 1930°C 739 mm

bottom top

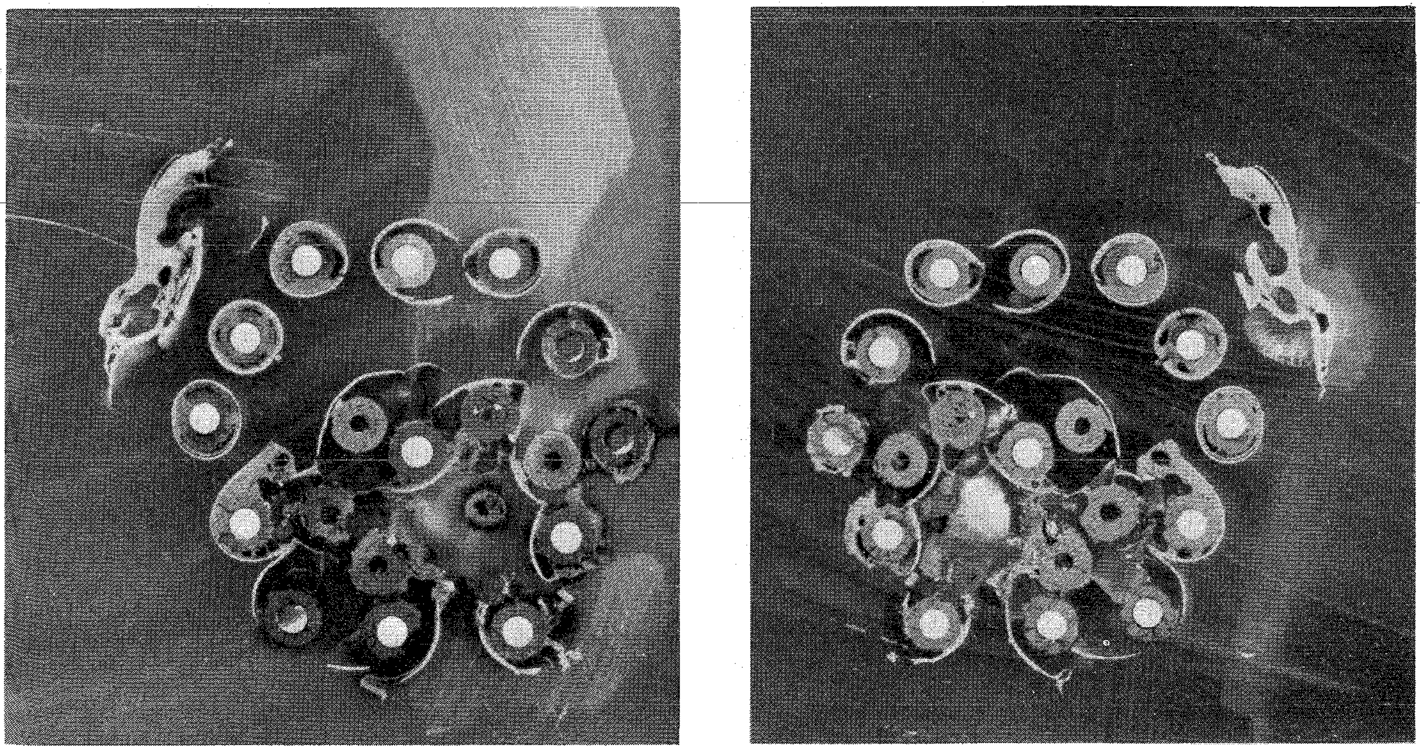

726 mm 1940°C 724 mm

Fig. 124: Horizontal cross sections of bundle CORA-W2, enlarged views of sections at 741, 739, 726 and 724 mm

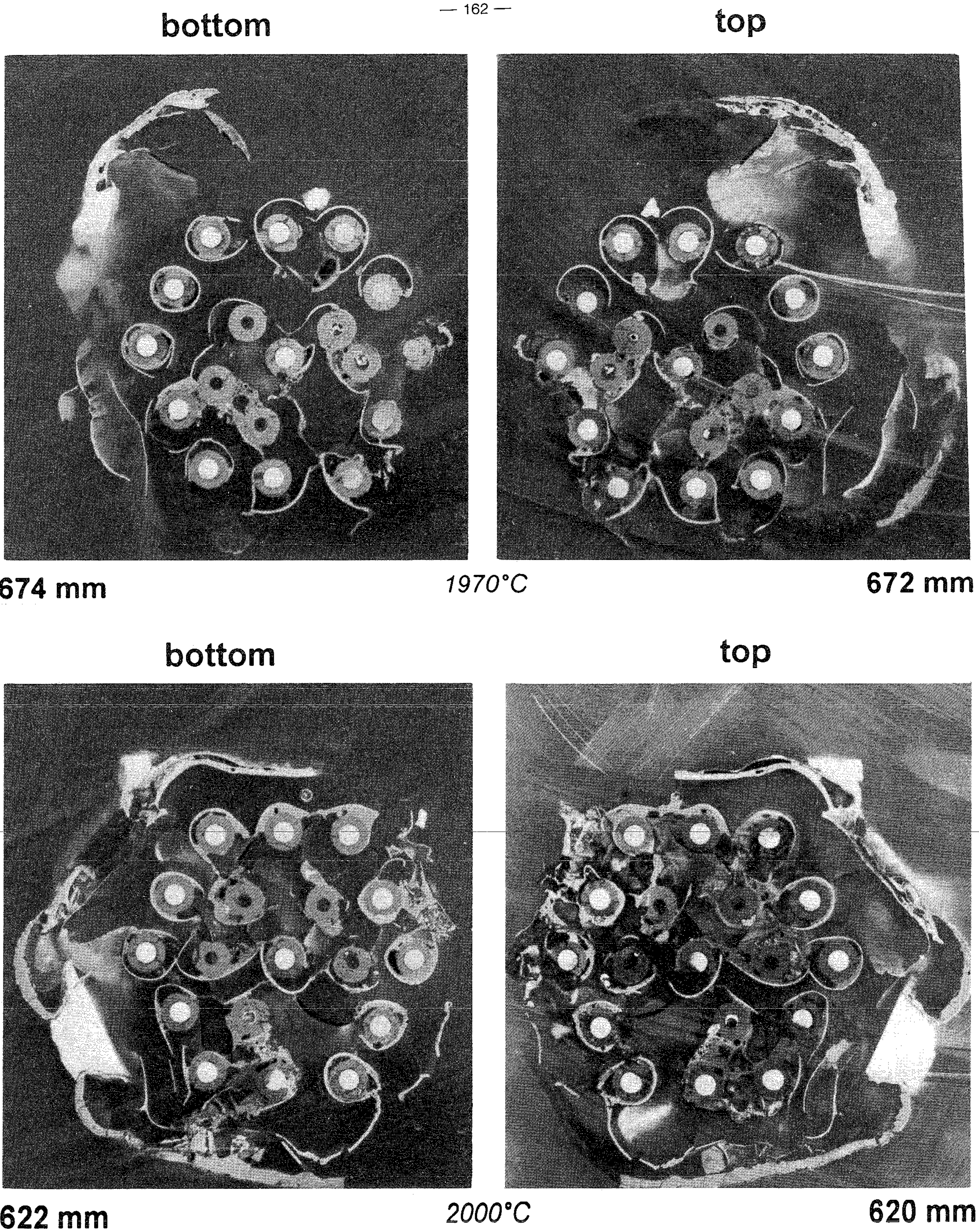

Fig. 125: Horizontal cross sections of bundle CORA-W2, enlarged views of sections at 674, 672, 622 and 620 mm

bottom top

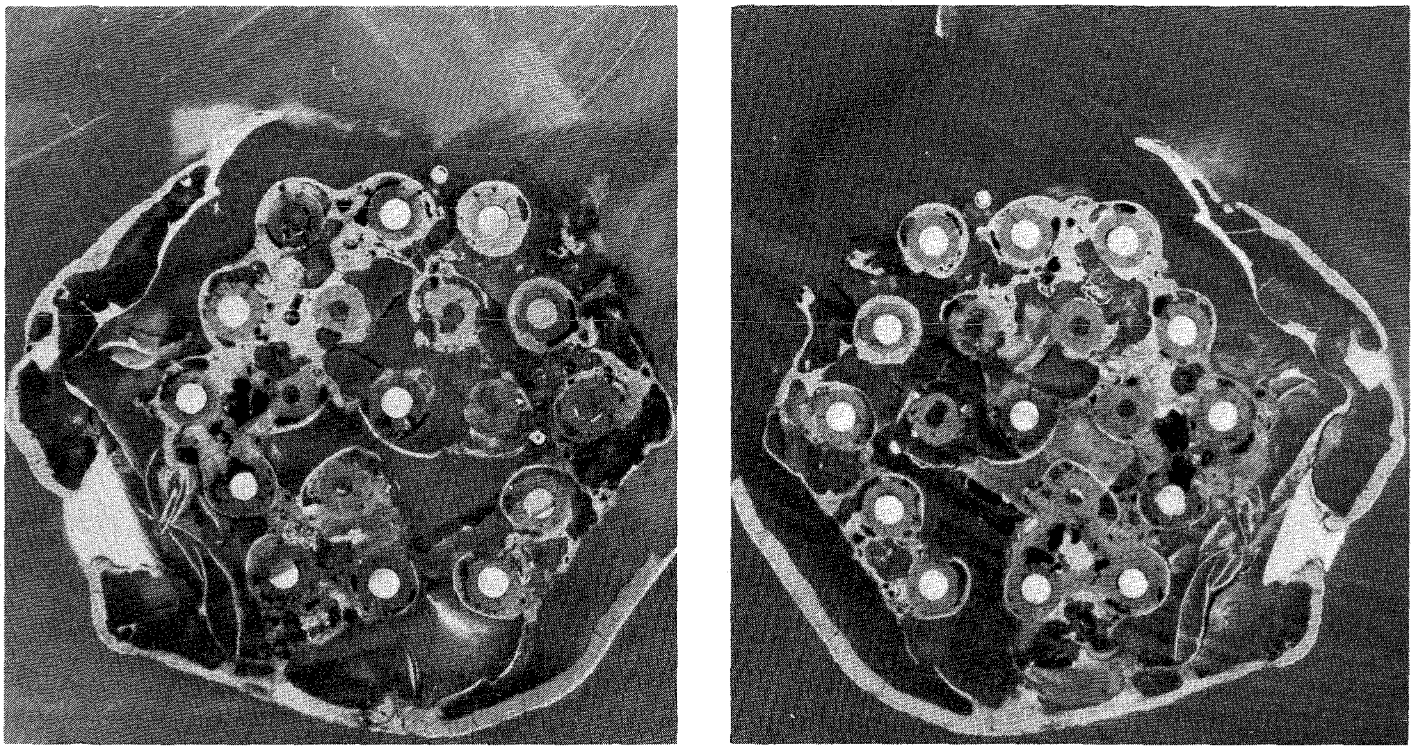

607 mm *2000°C* 605 mm

bottom top

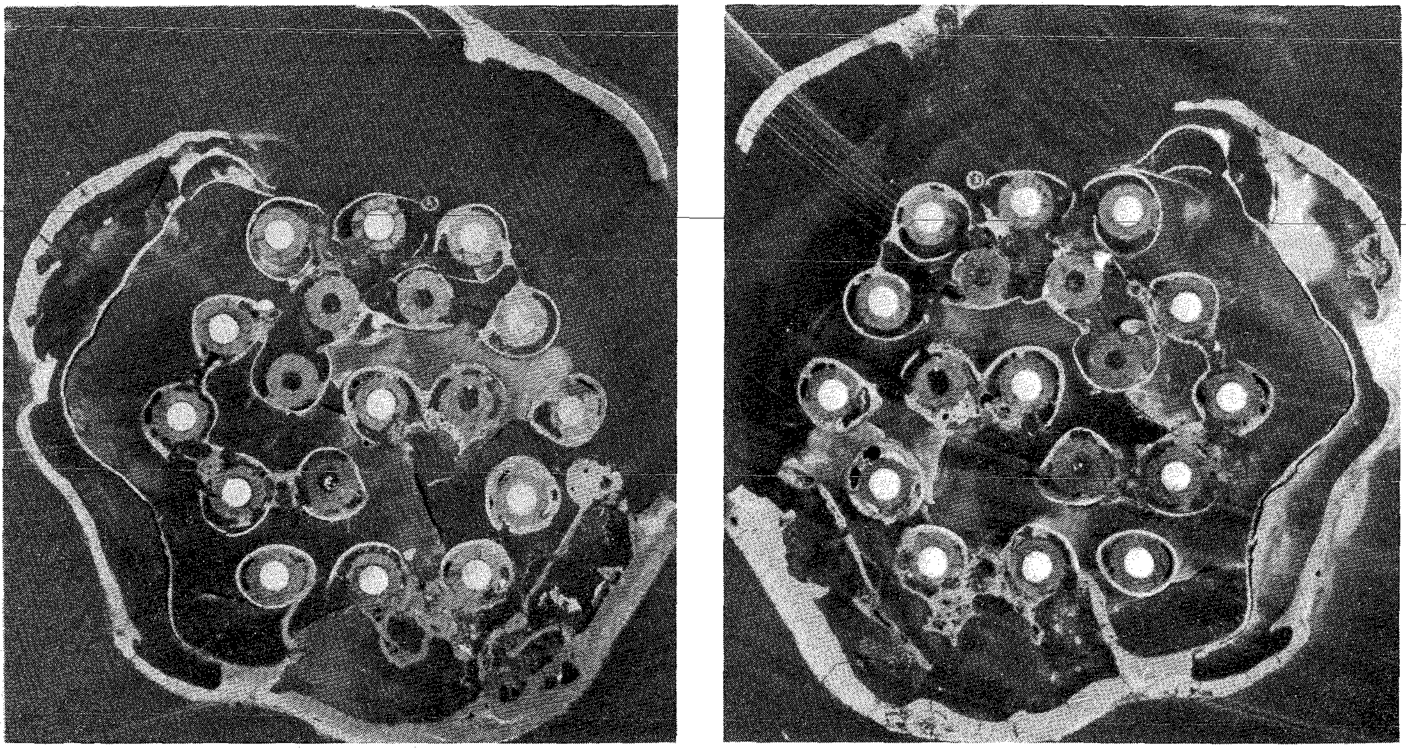

565 mm *2000°C* 563 mm

Fig. 126: Horizontal cross sections of bundle CORA-W2, enlarged views of sections at 607, 605, 565 and 563 mm

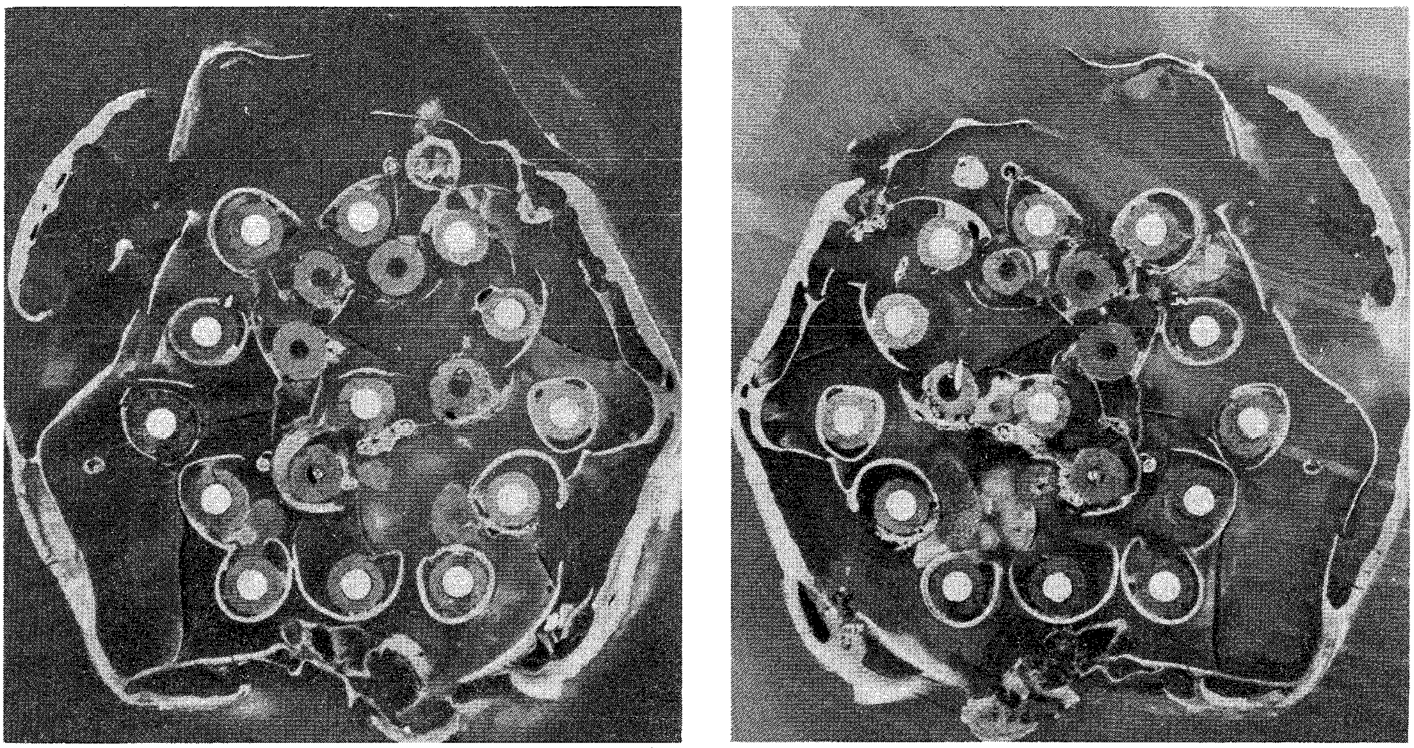

bottom

top

513 mm

2000°C

511 mm

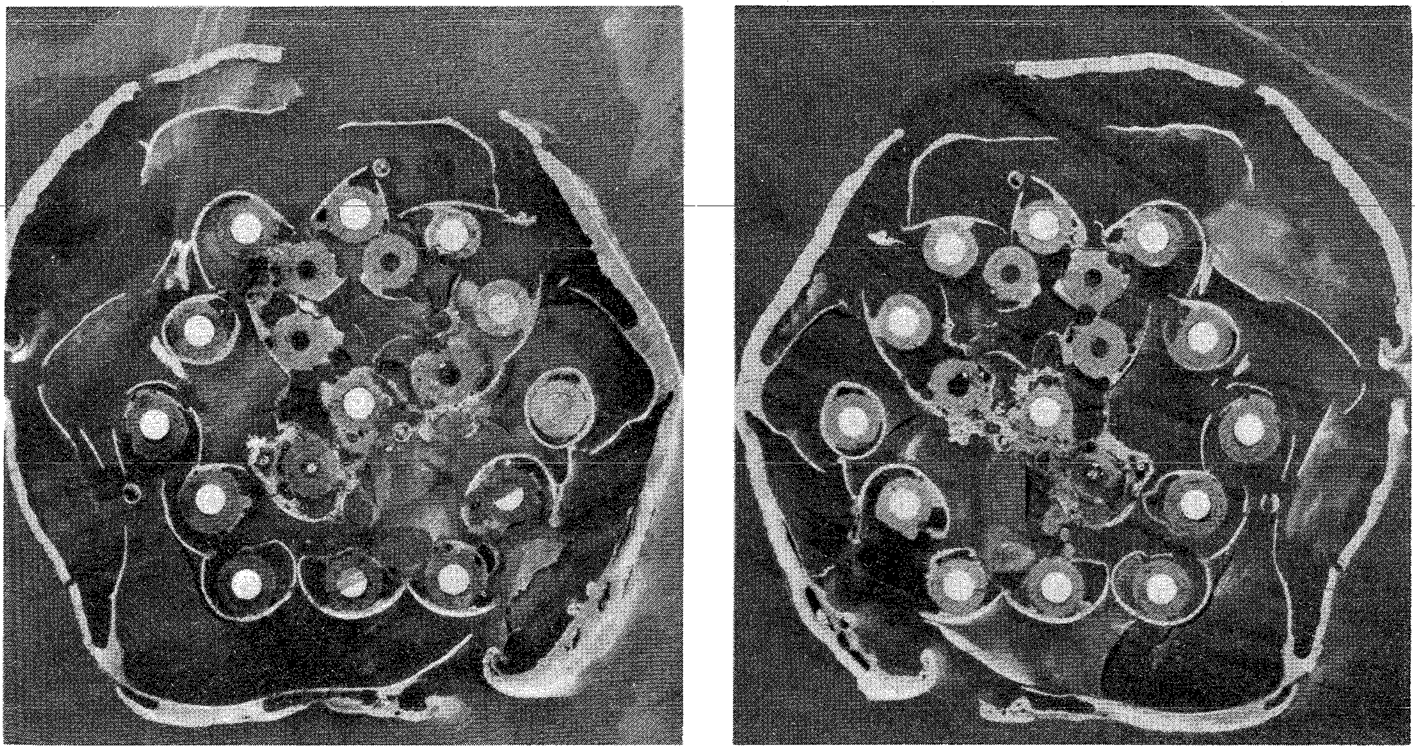

bottom

top

498 mm

2000°C

496 mm

Fig. 127: Horizontal cross sections of bundle CORA-W2, enlarged views of sections at 513, 511, 498 and 496 mm

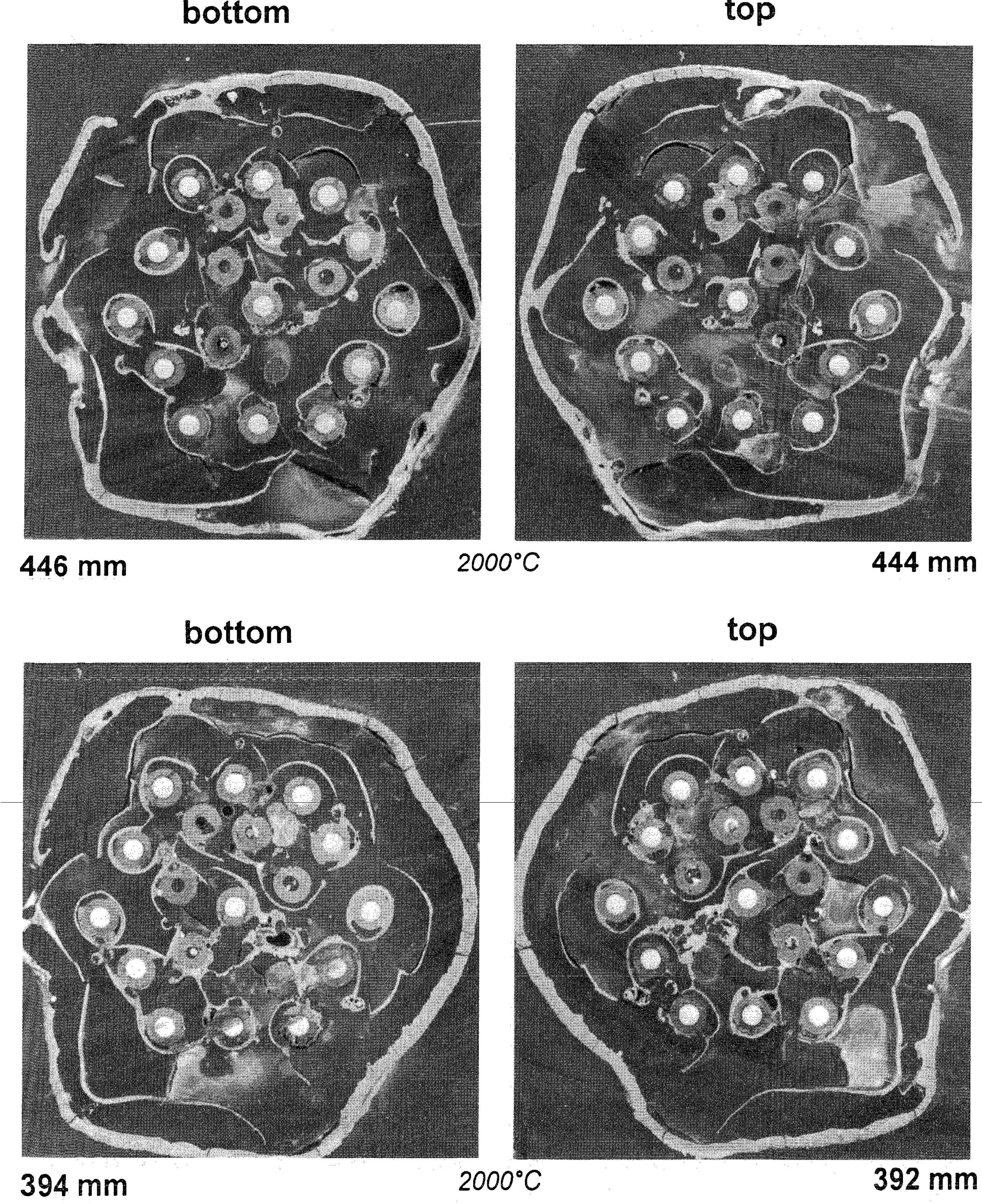

Fig. 128: Horizontal cross sections of bundle CORA-W2, enlarged views of sections at 446, 444, 394 and 392 mm

bottom **top**

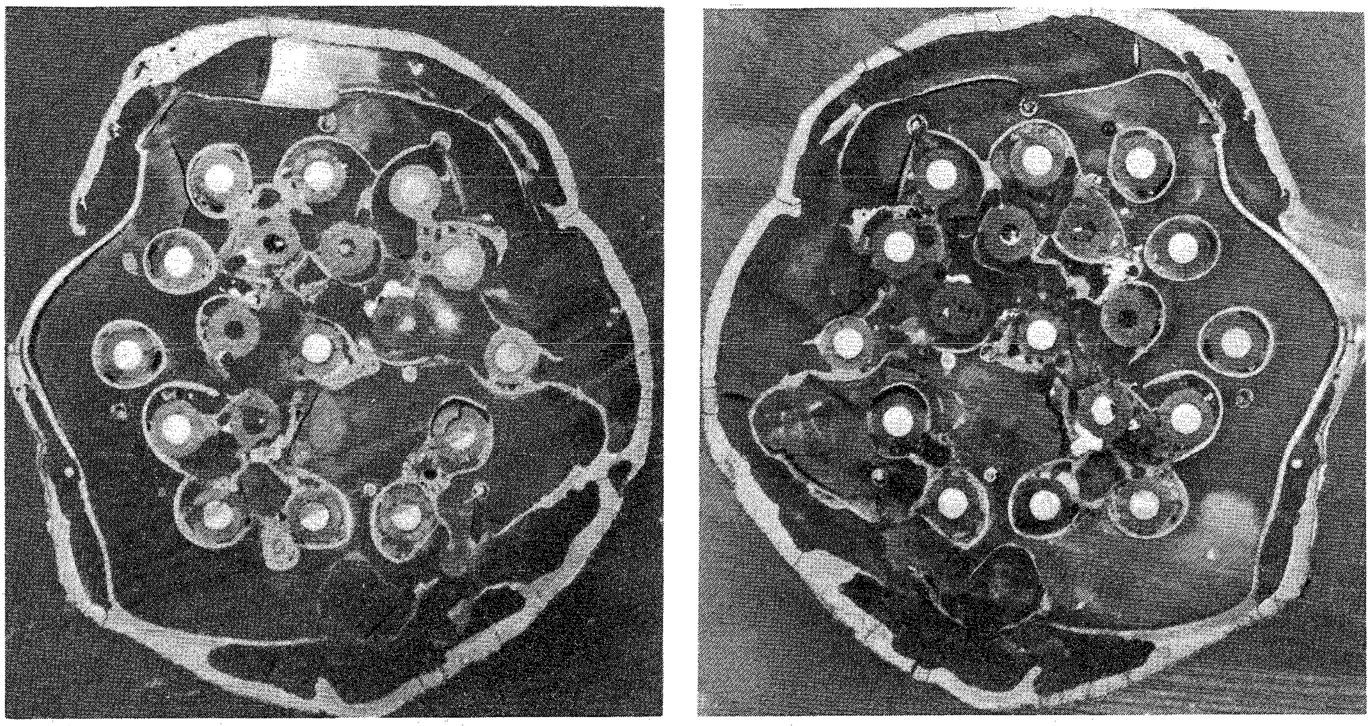

342 mm *2000°C* **340 mm**

bottom **top**

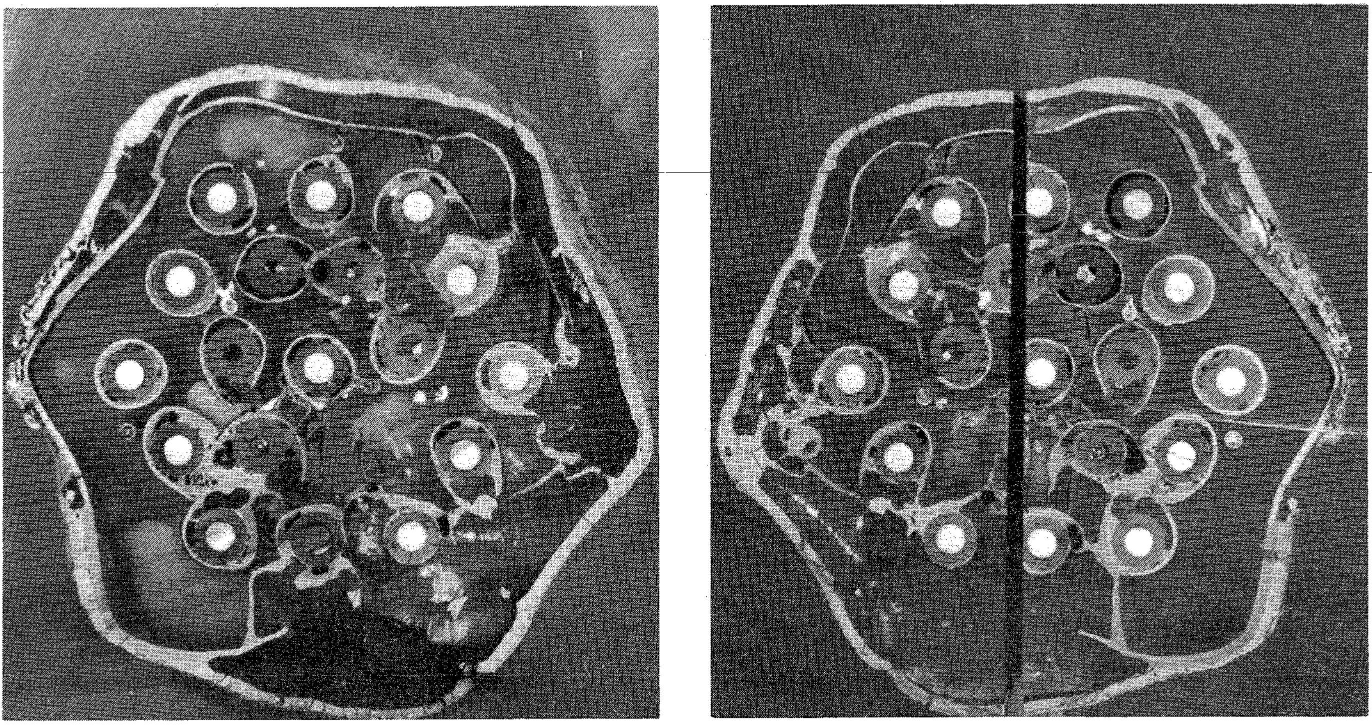

327 mm *1950°C* **325 mm**

Fig. 129: Horizontal cross sections of bundle CORA-W2, enlarged views of sections at 342, 340, 327 and 325 mm

bottom top

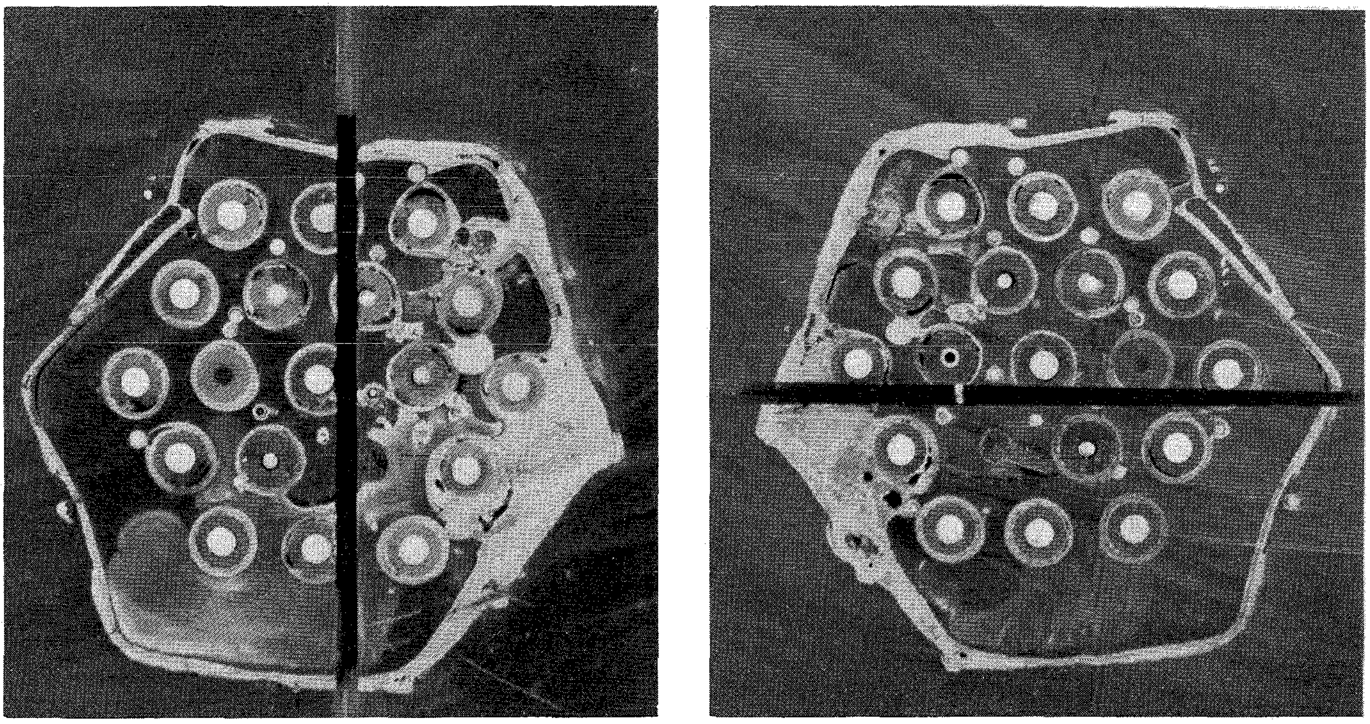

275 mm *1850°C* 273 mm

bottom top

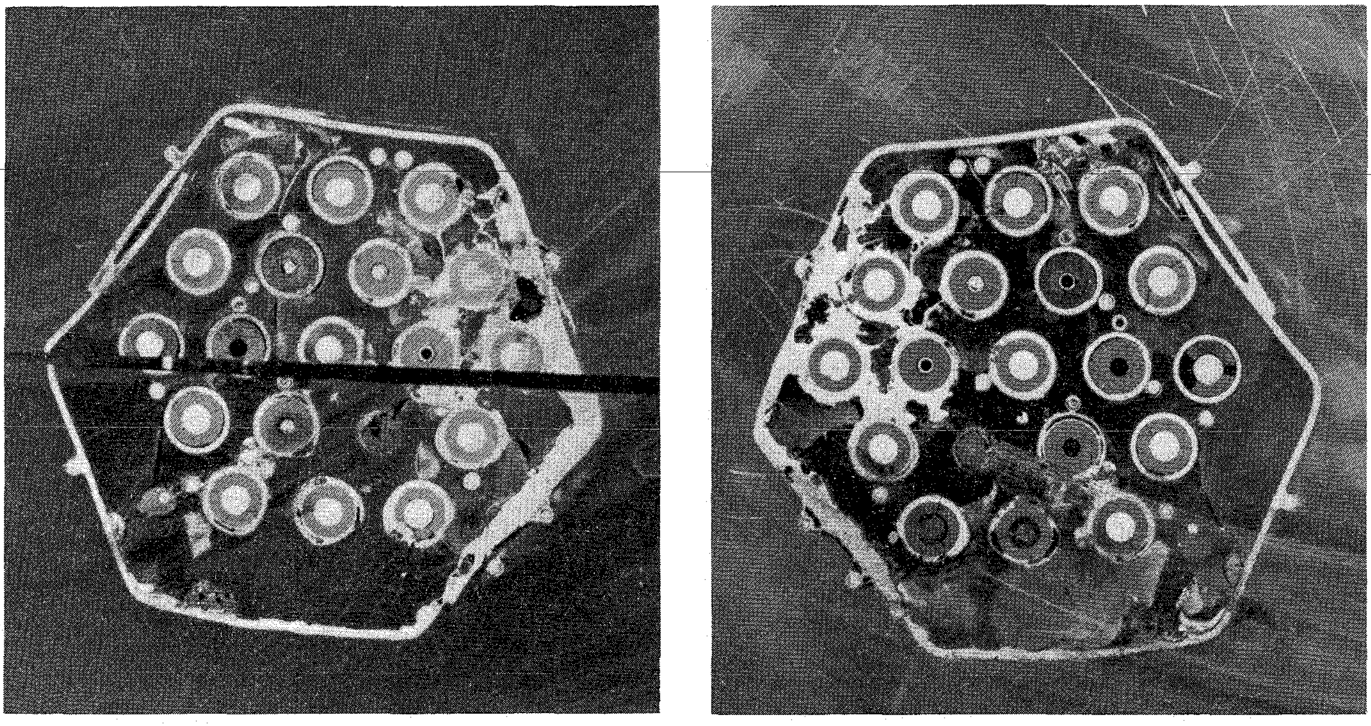

223 mm *1550°C* 221 mm

Fig. 130: Horizontal cross sections of bundle CORA-W2, enlarged views of sections at 275, 273, 223 and 221 mm

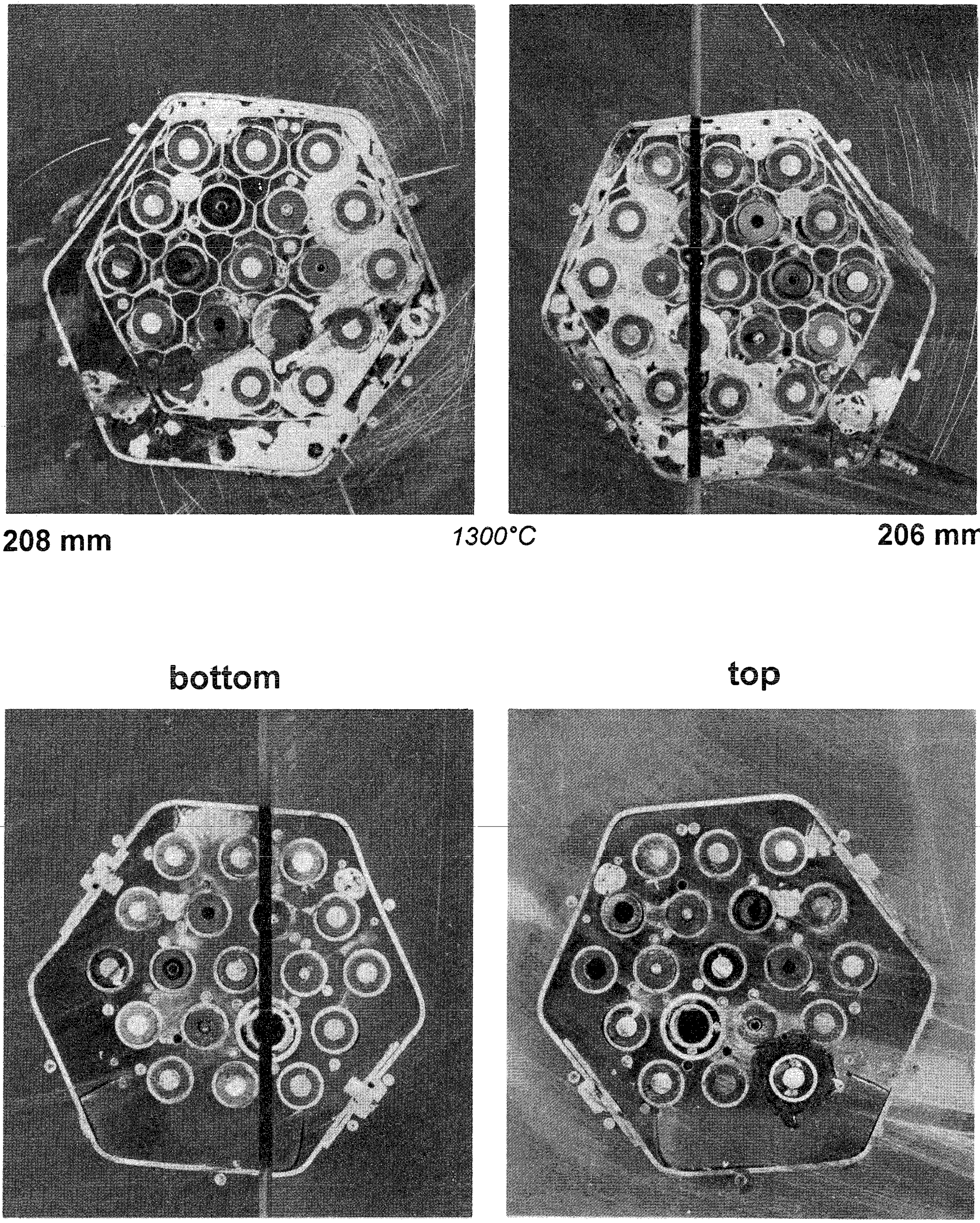

Fig. 131: Horizontal cross sections of bundle CORA-W2, enlarged views of sections at 208, 206, 156 and 154 mm

bottom **top**

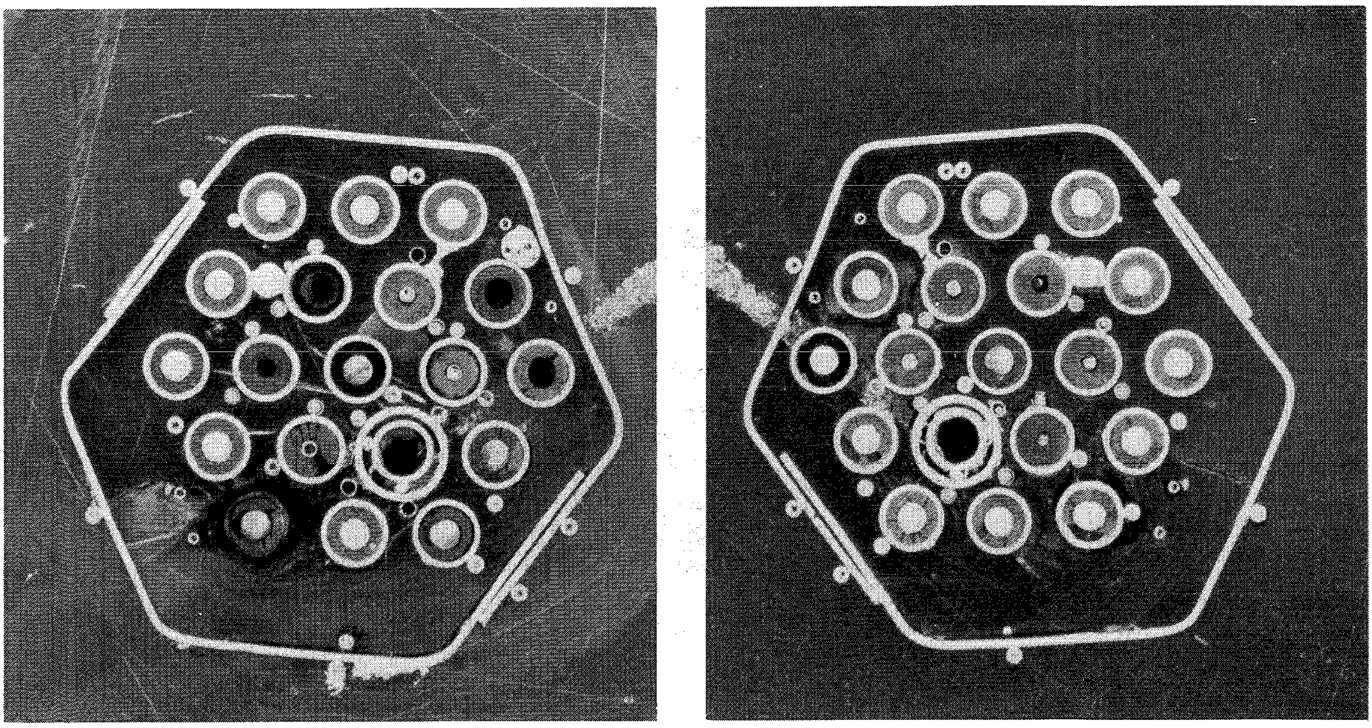

141 mm *950°C* **139 mm**

bottom **top**

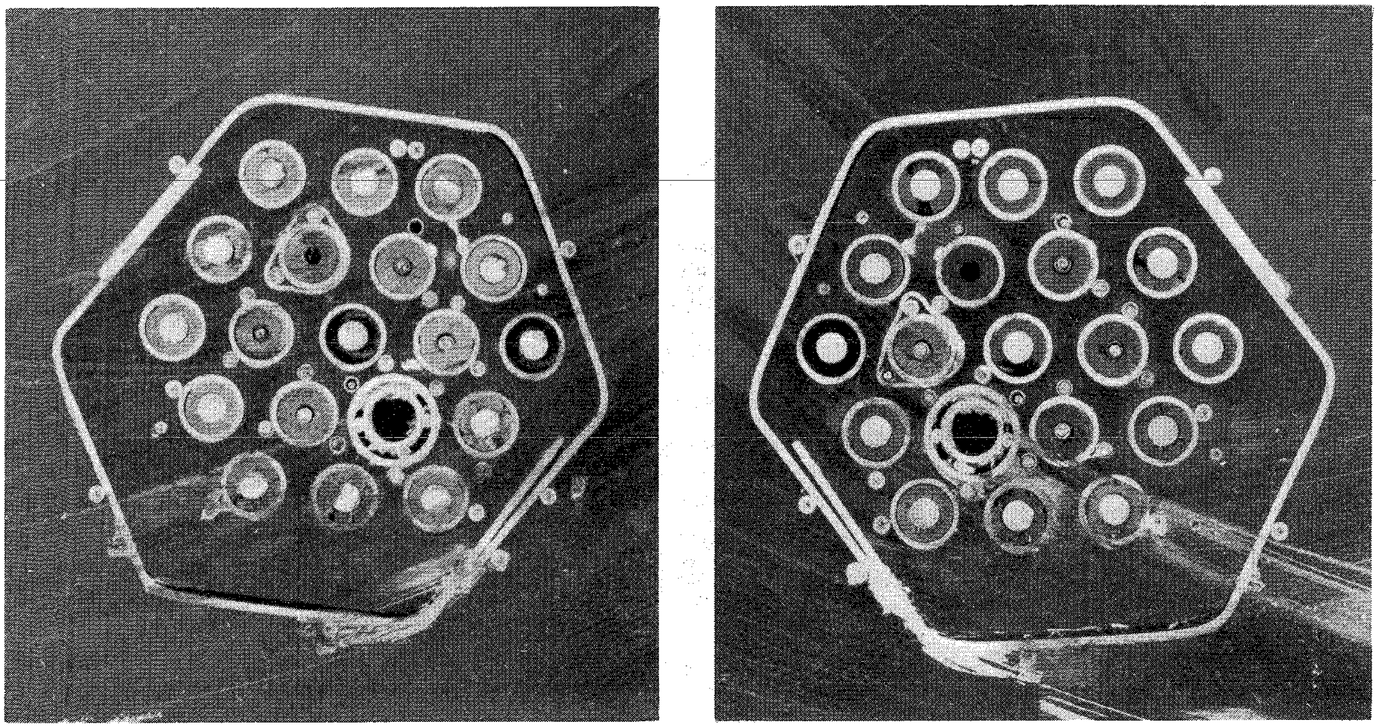

89 mm *700°C* **87 mm**

Fig. 132: **Horizontal cross sections of bundle CORA-W2, enlarged views of sections at 141, 139, 89 and 87 mm**

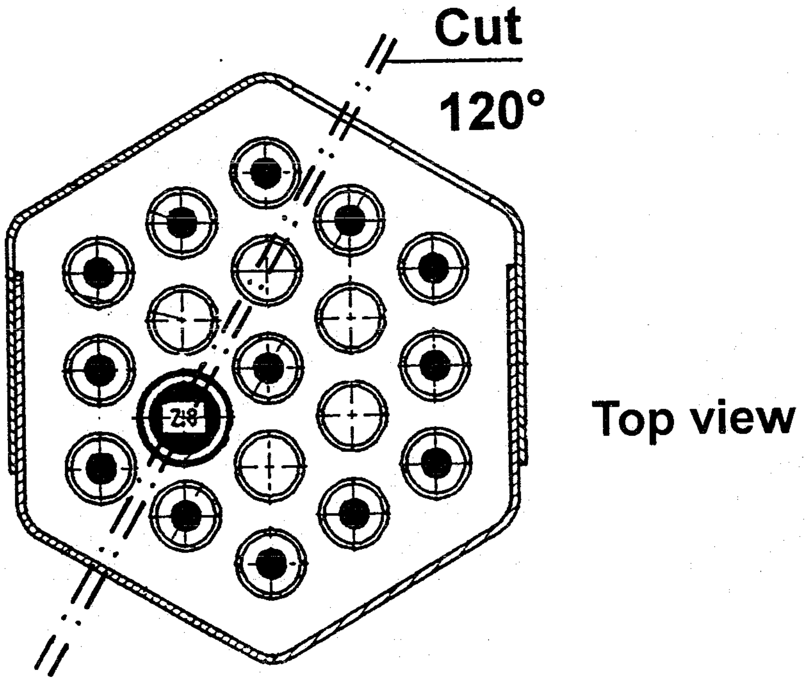

Fig. 133: Position of longitudinal cuts through samples CORA-W2-d and CORA-W2-f

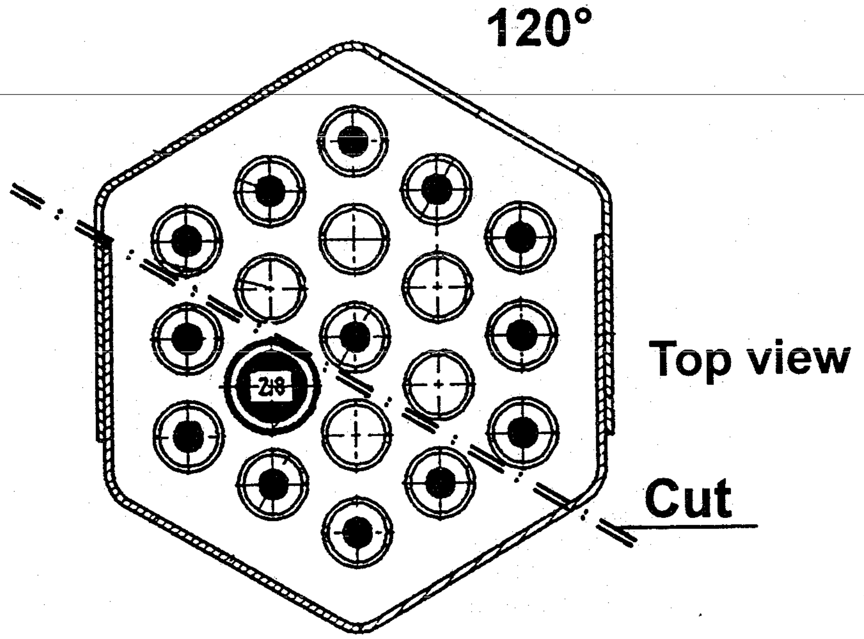

Fig. 134: Position of longitudinal cut through sample CORA-W2-e

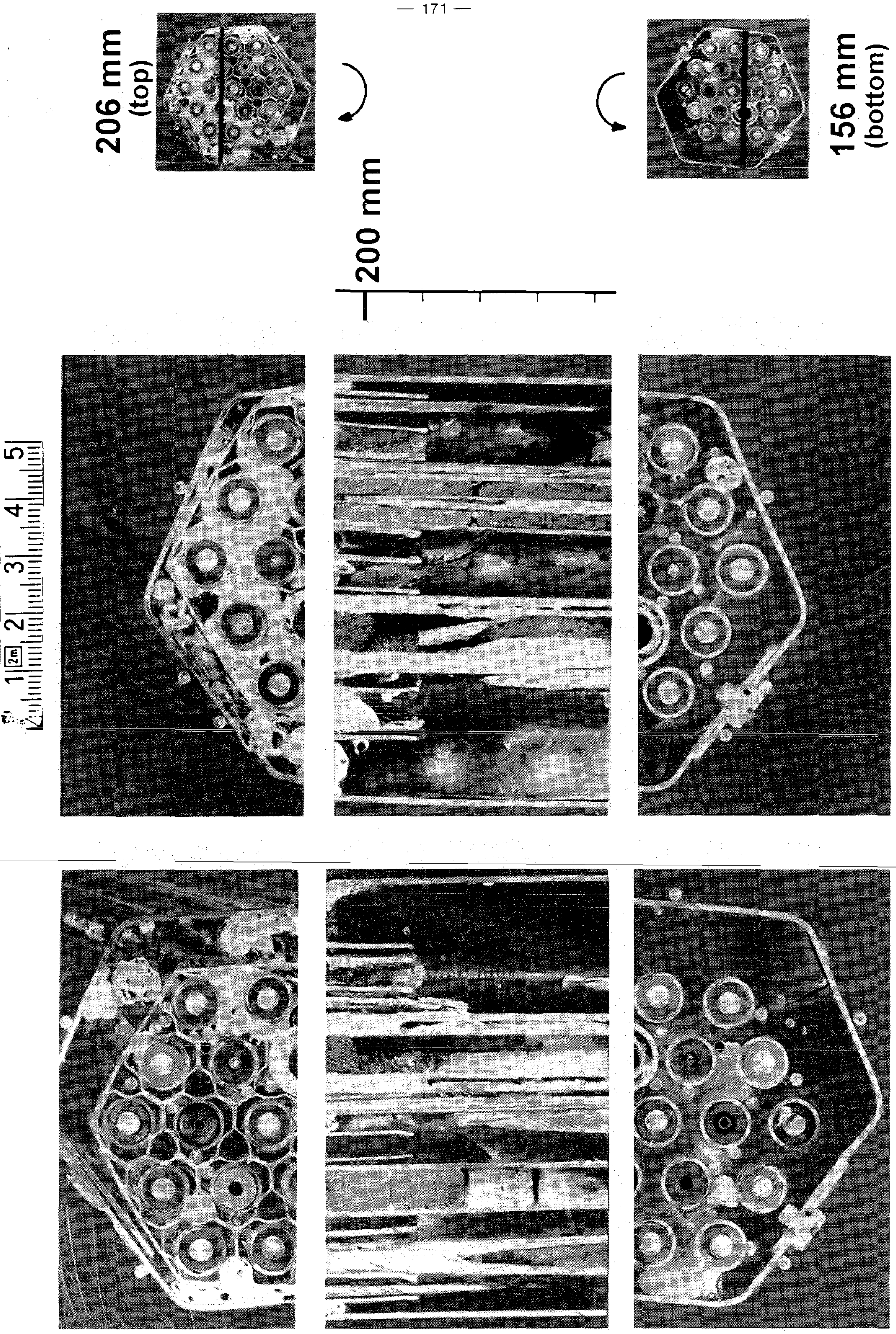

Fig. 135: Vertical cross section of bundle CORA-W2-d, 156 mm - 206 mm

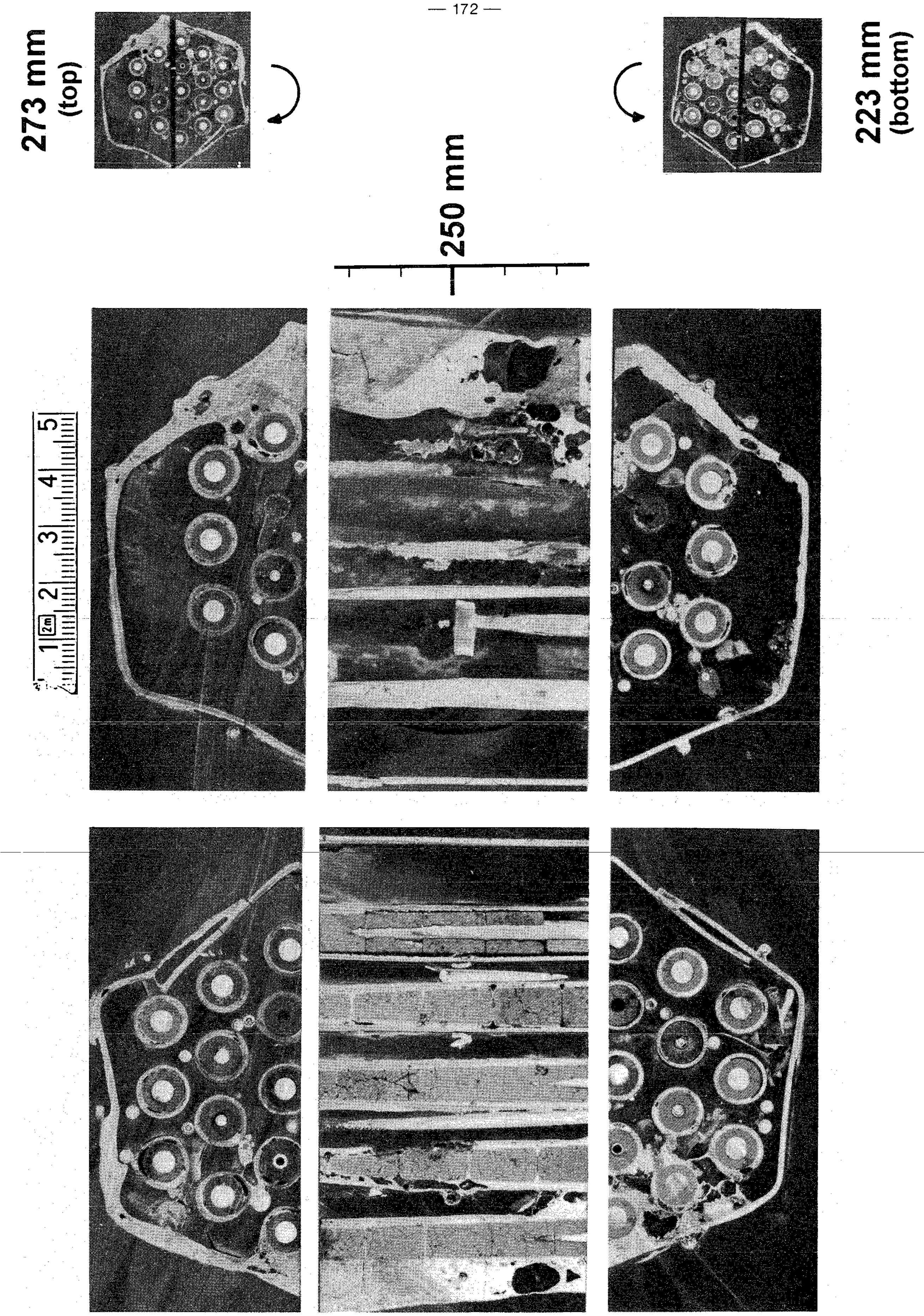

Fig. 136: Vertical cross section of bundle CORA-W2-e, 223 mm - 273 mm

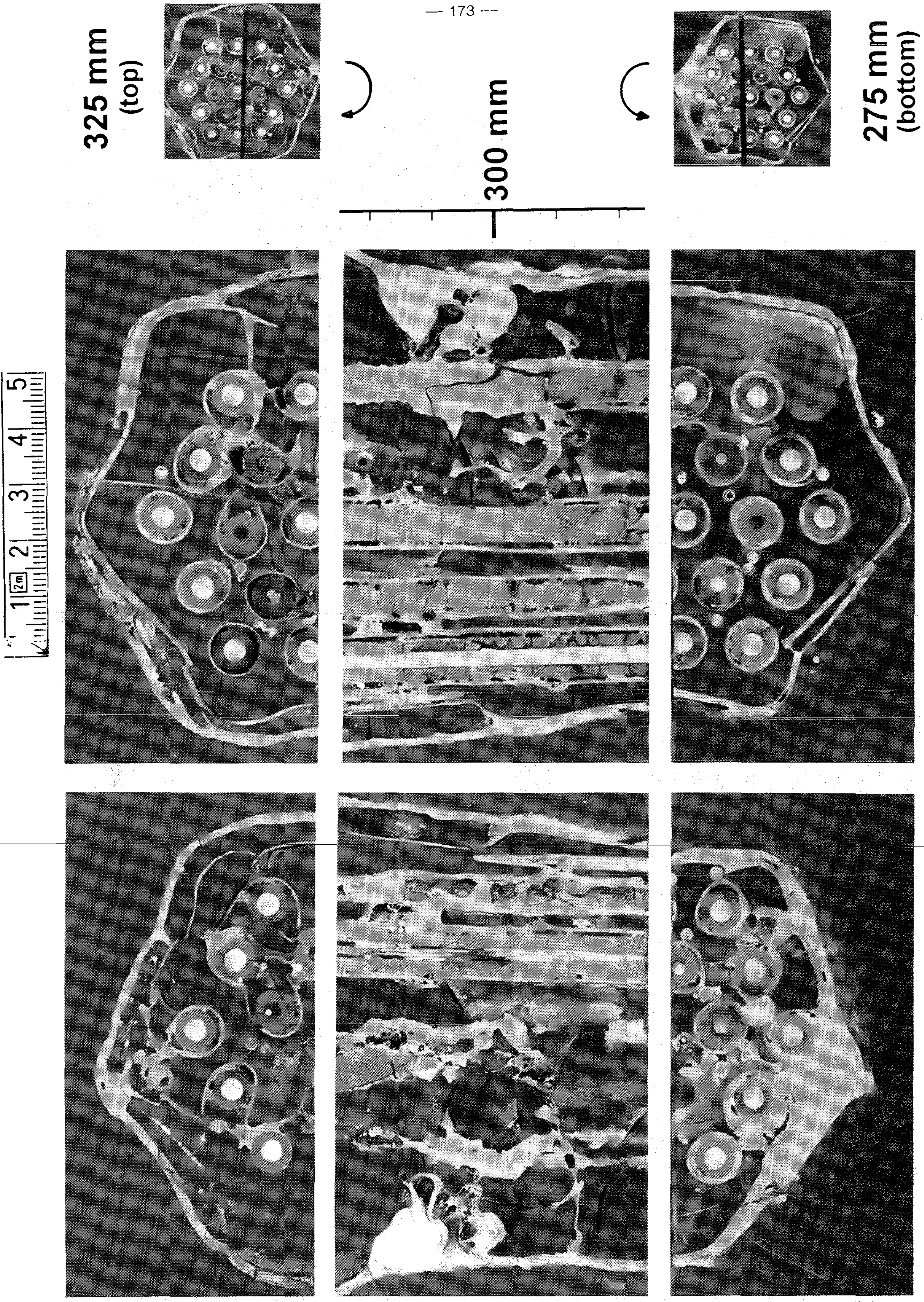

Fig. 137: Vertical cross section of bundle CORA-W2-f, 275 mm - 325 mm

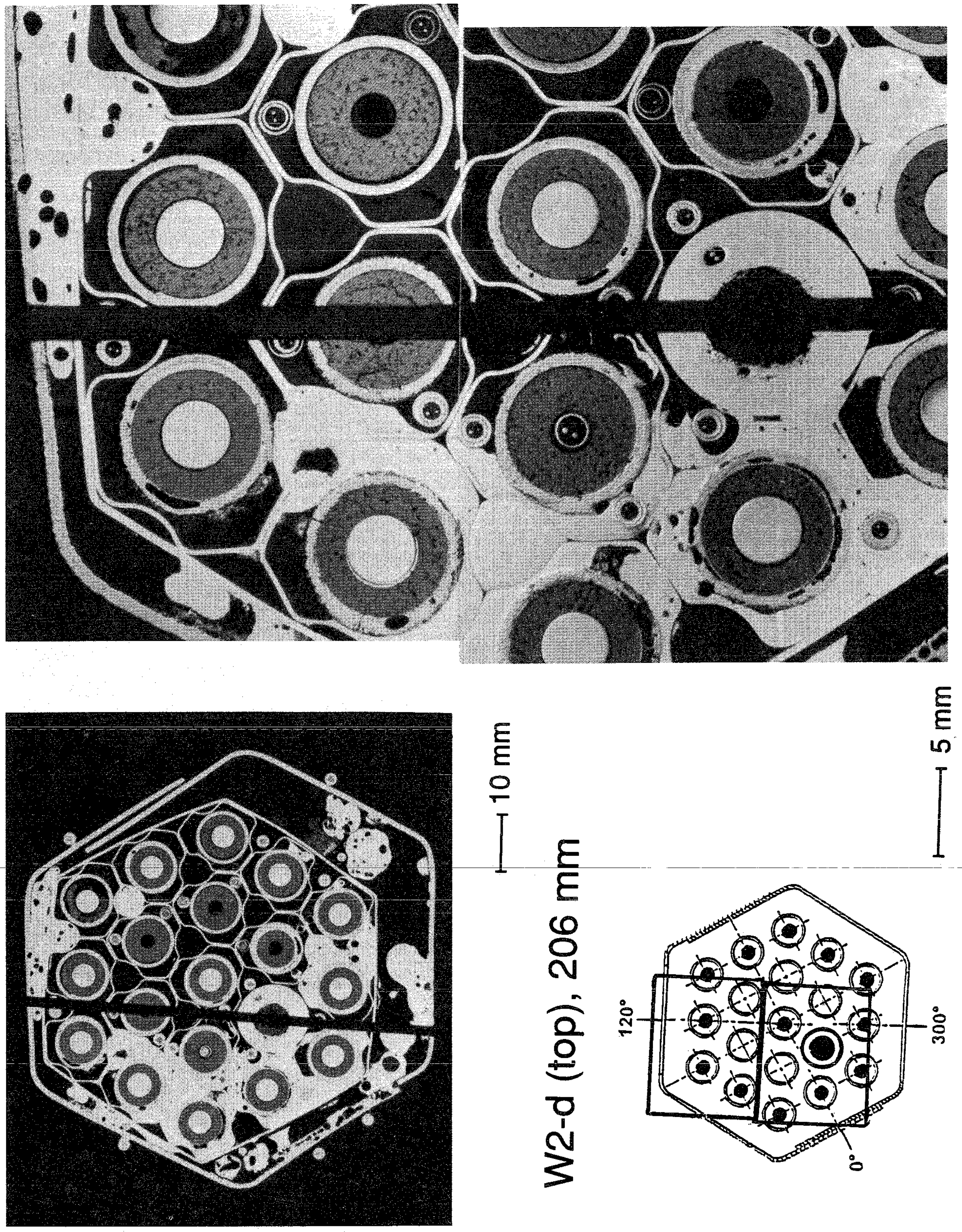

Fig. 138: Cross section CORA-W2-d (top), elevation 206 mm; overview

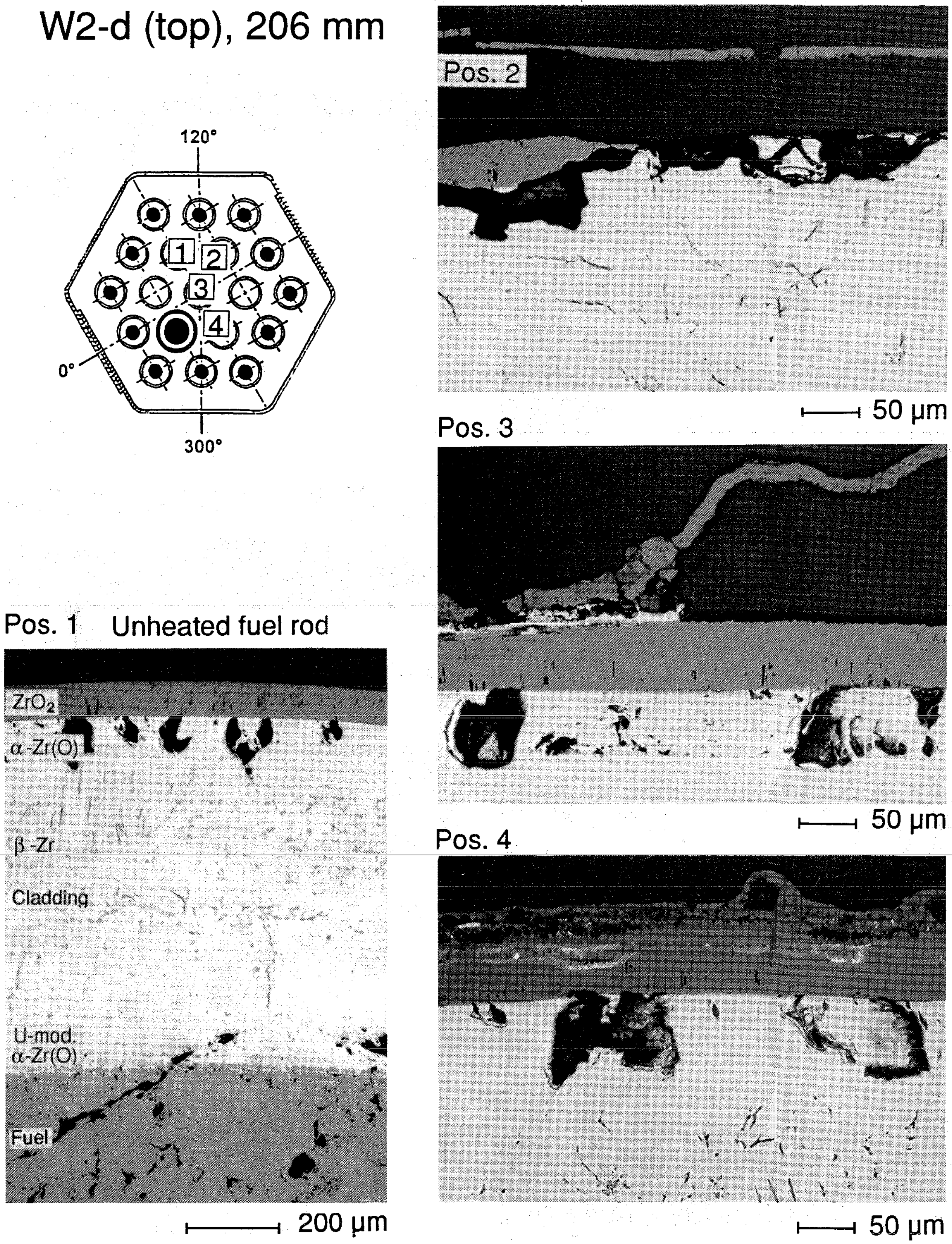

Fig. 139: Cross section CORA-W2-d (top), elevation 206 mm; cladding oxidation

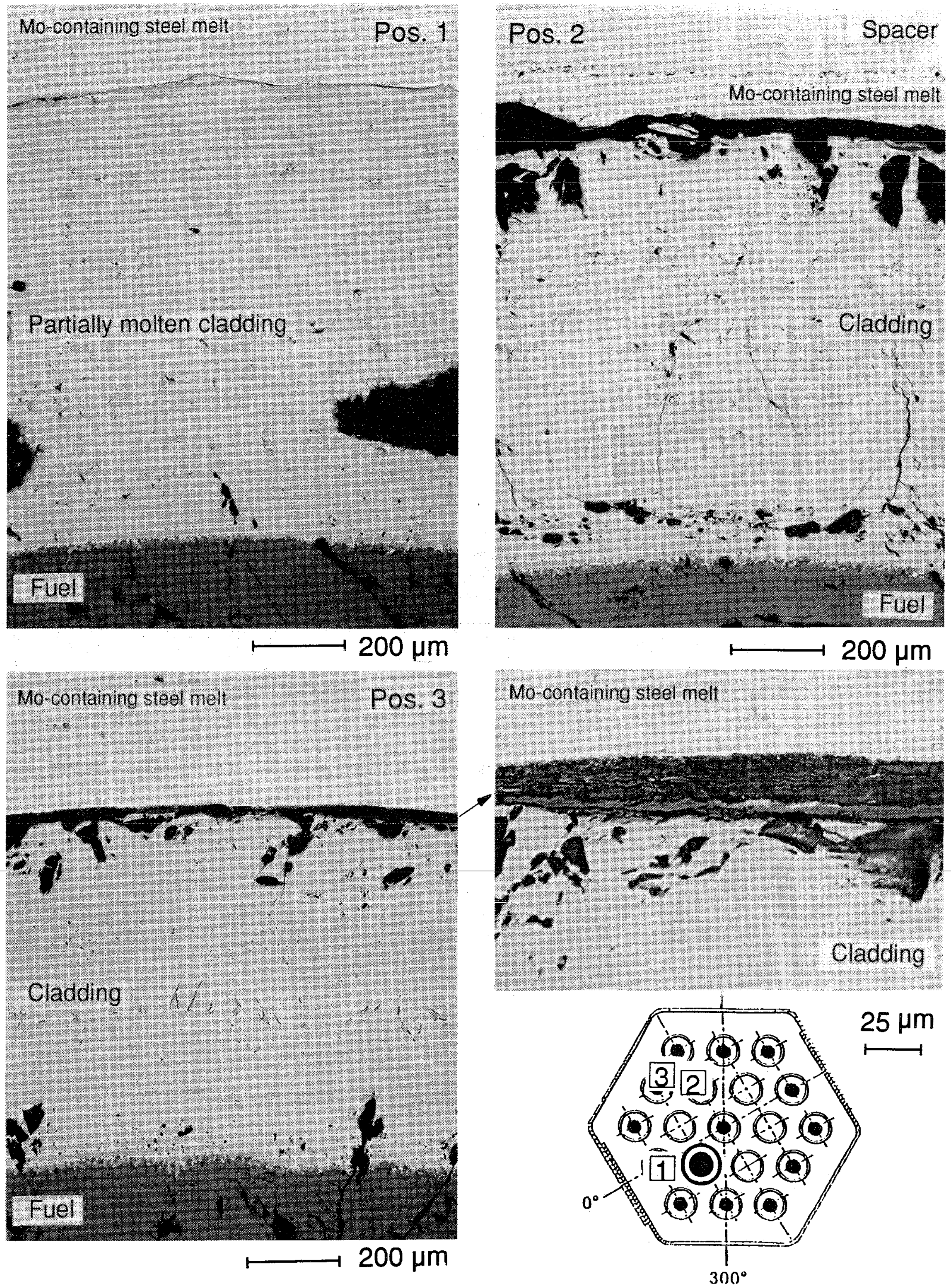

Fig. 140: **Cross section CORA-W2-d (top), elevation 206 mm; cladding in contact with metallic melt**

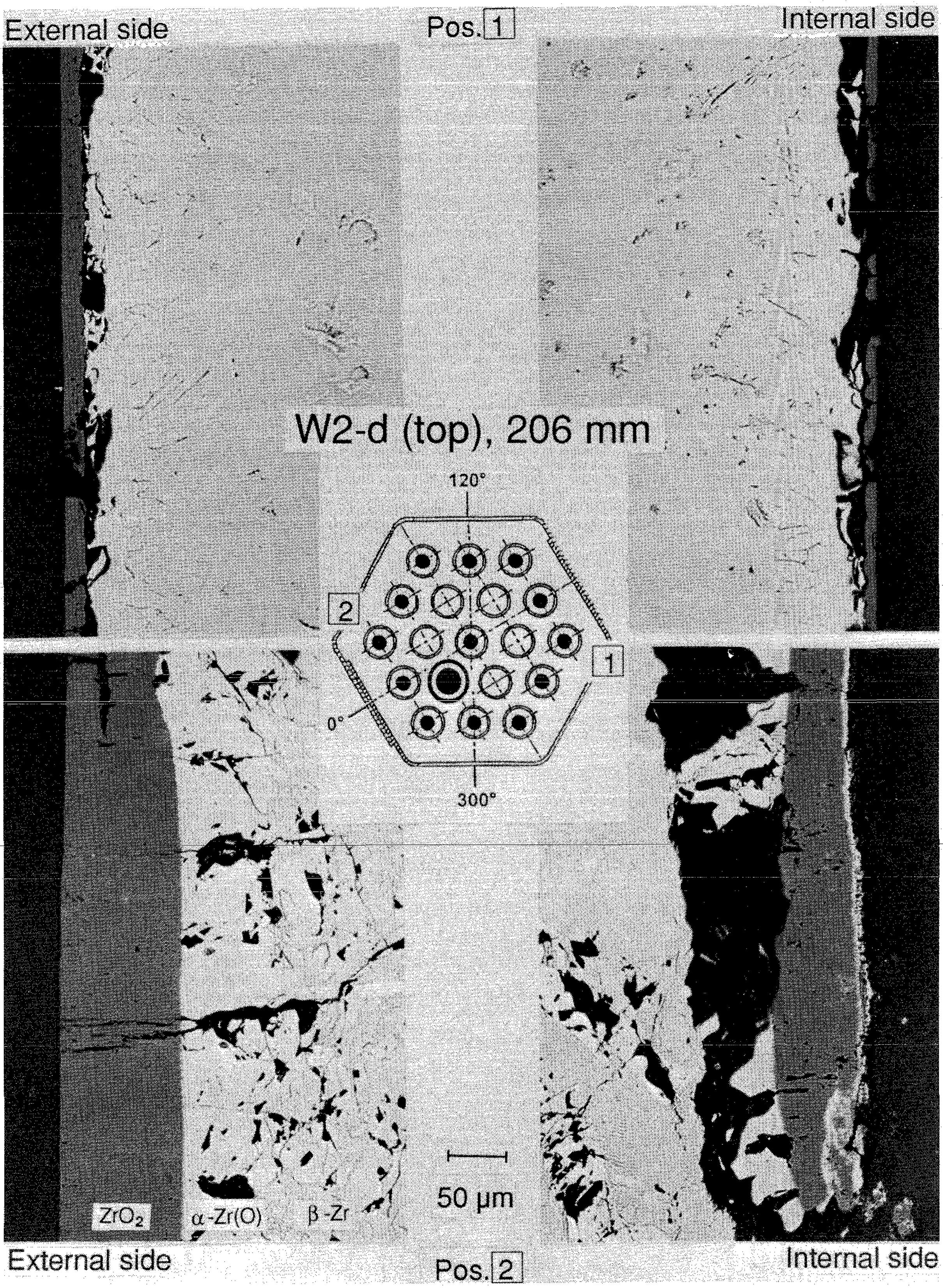

Fig. 141: Cross section CORA-W2-d (top), elevation 206 mm; shroud oxidation

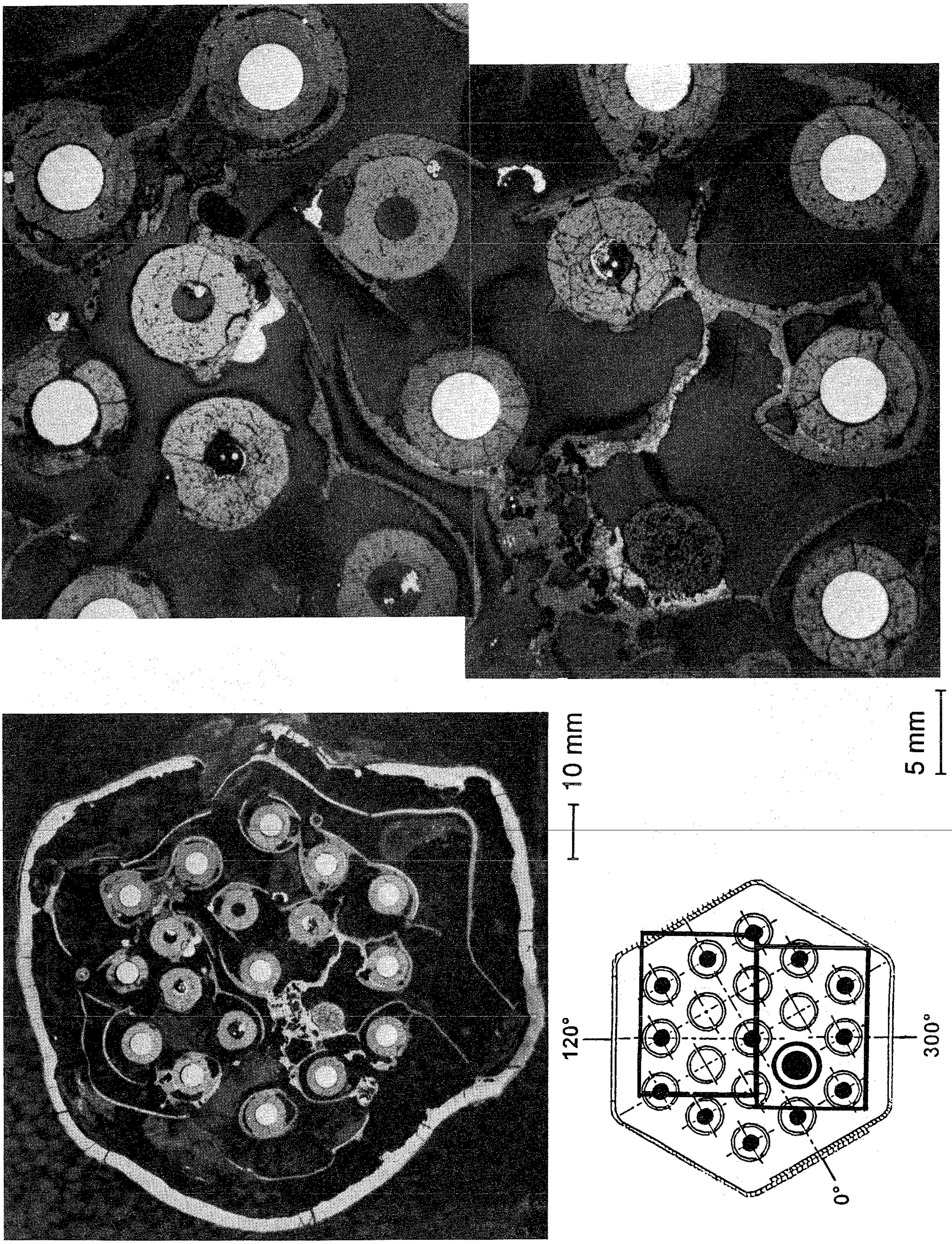

Fig. 142: Cross section CORA-W2-g (top), elevation 392 mm; overview

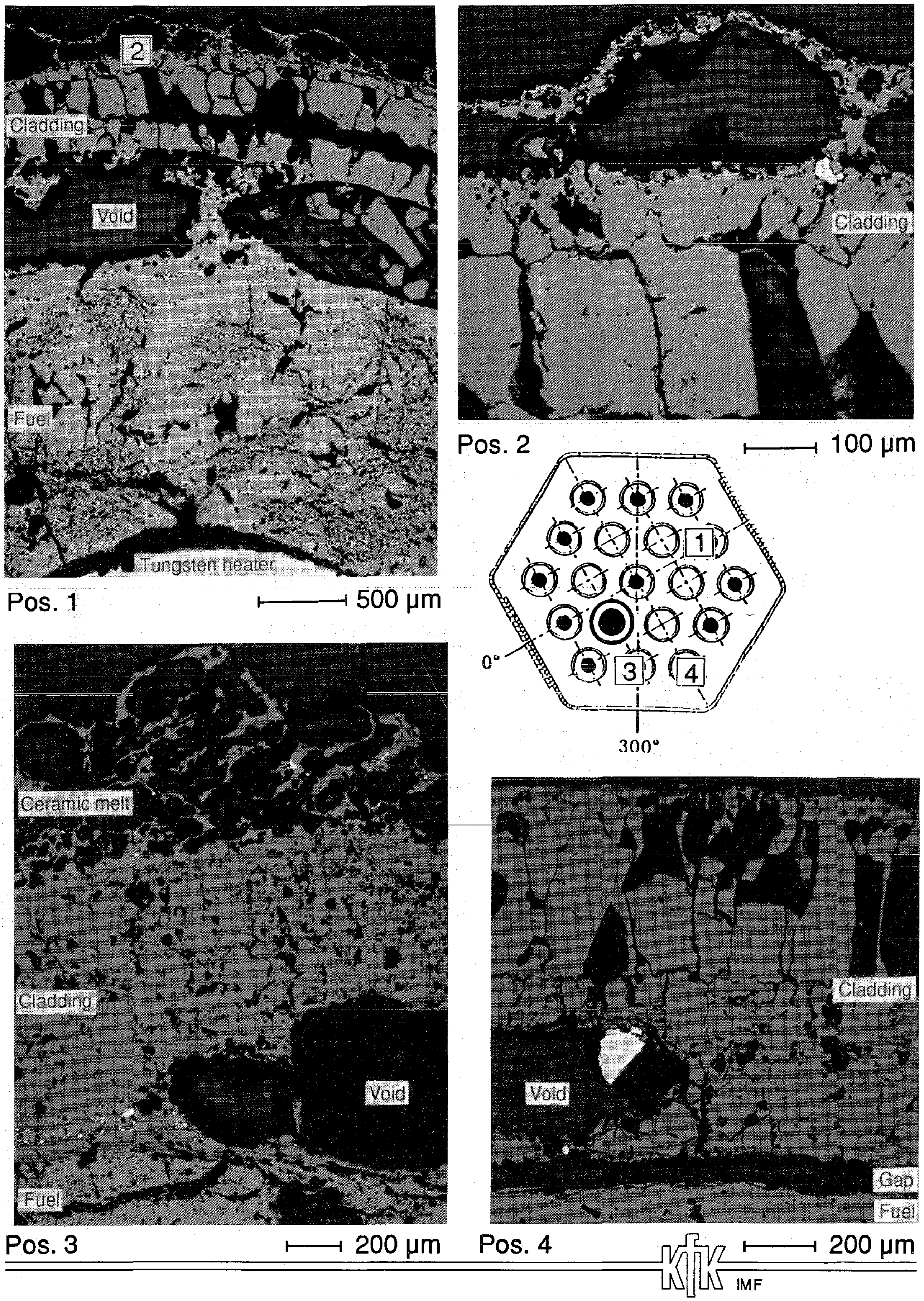

Pos. 1 500 µm

Pos. 2 100 µm

Pos. 3 200 µm

Pos. 4 200 µm

Fig. 143: **Cross Section CORA-W2-g (top), elevation 392 mm; cladding oxidation**

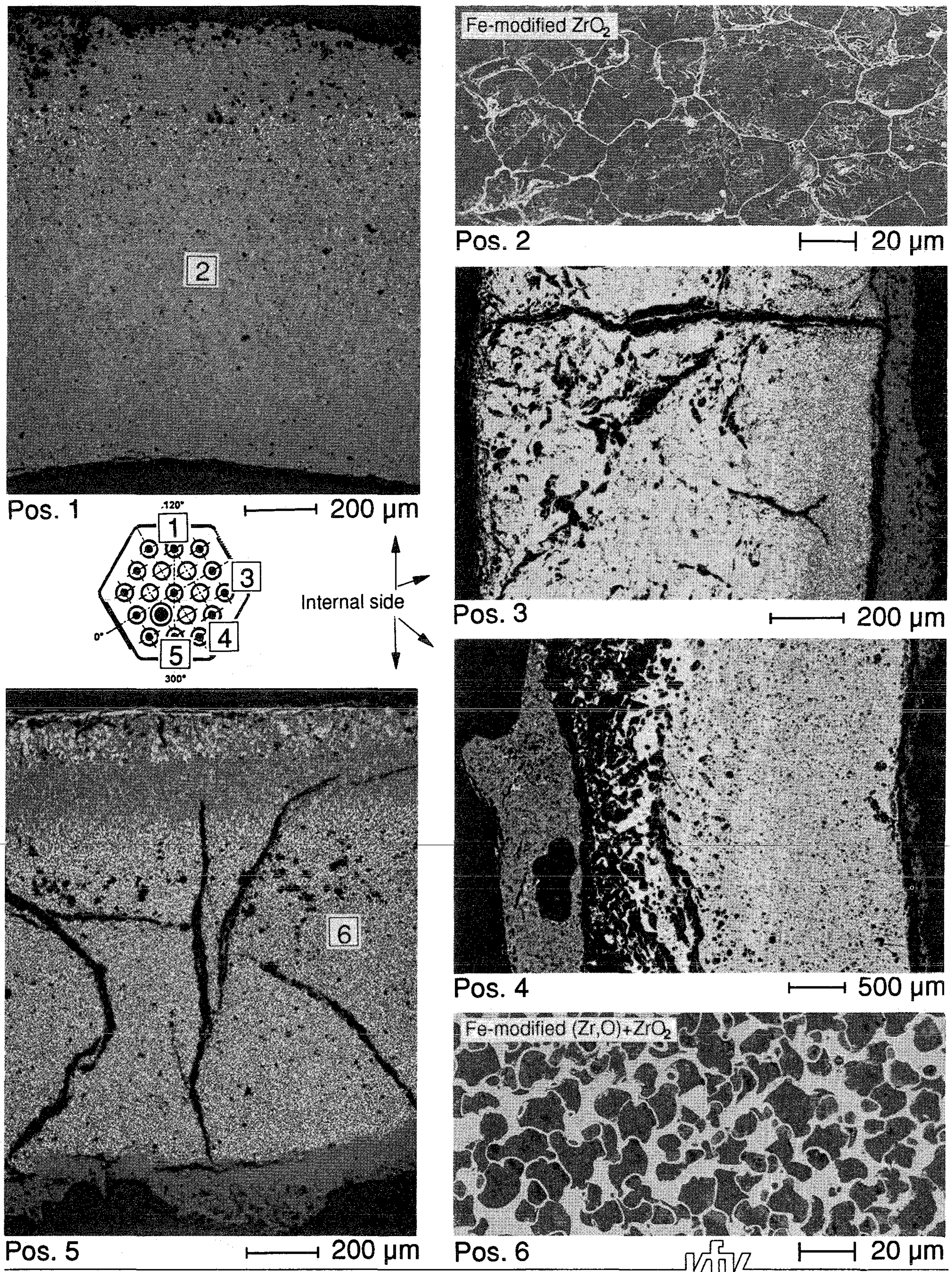

KfK IMF

Fig. 144: Cross section CORA-W2-g (top), elevation 392 mm; shroud oxidation

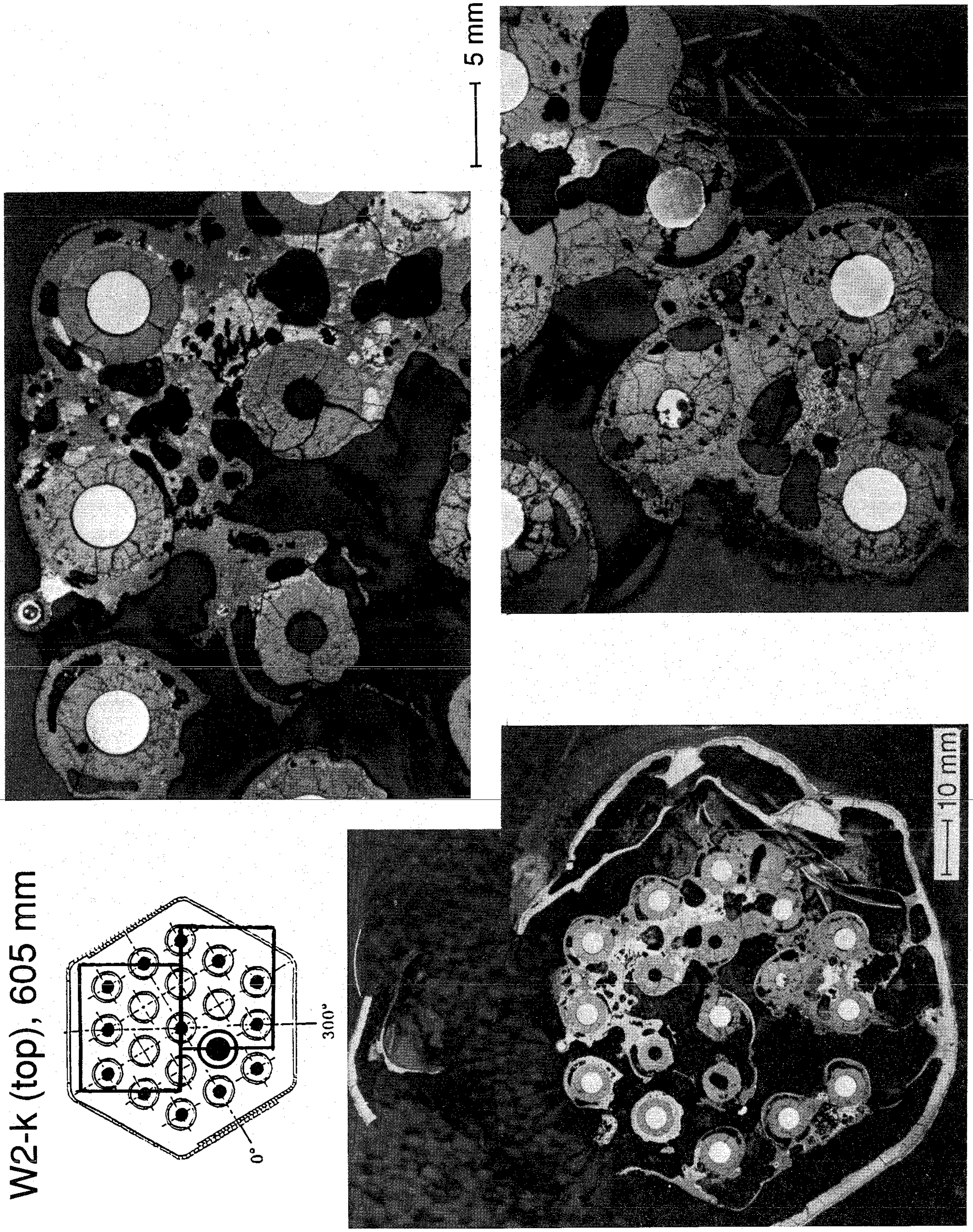

Fig. 145: Cross section CORA-W2-k (top), elevation 605 mm; overview

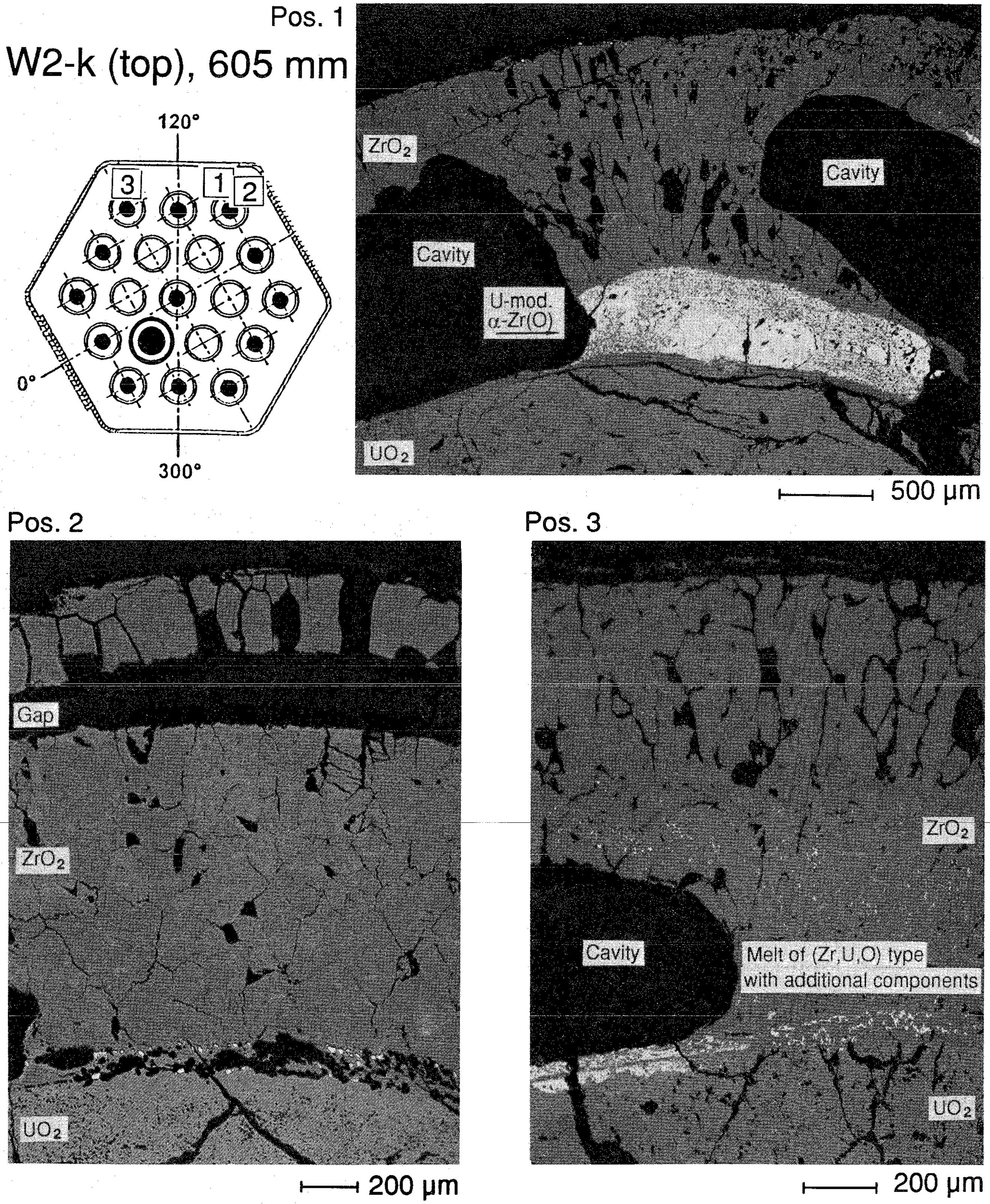

Fig. 146: Cross section CORA-W2-k (top), elevation 605 mm; cladding oxidation

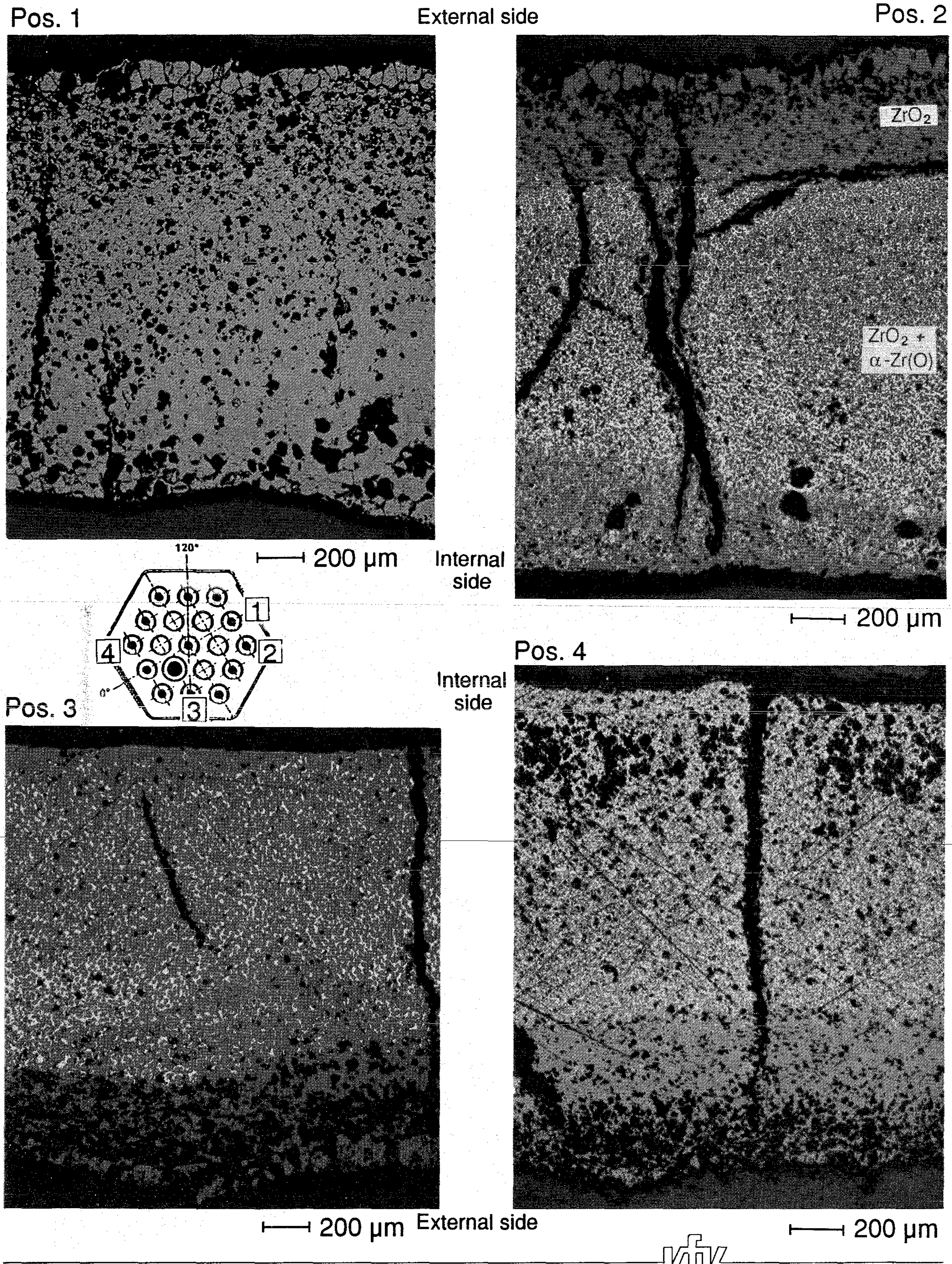

KfK IMF

Fig. 147: Cross section CORA-W2-k (top), elevation 605 mm; shroud oxidation

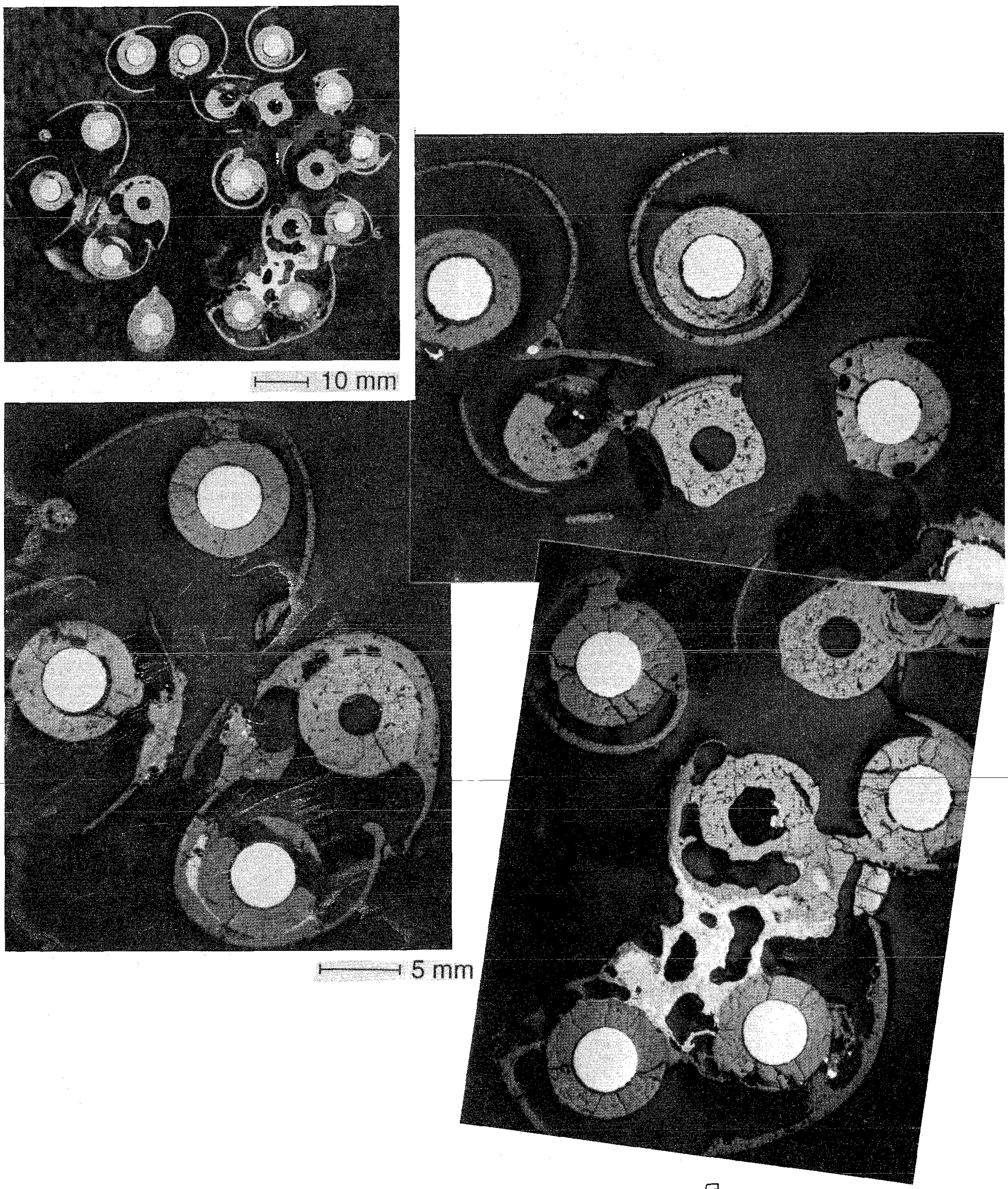

Fig. 148: Cross section CORA-W2-p (top), elevation 910 mm; overview

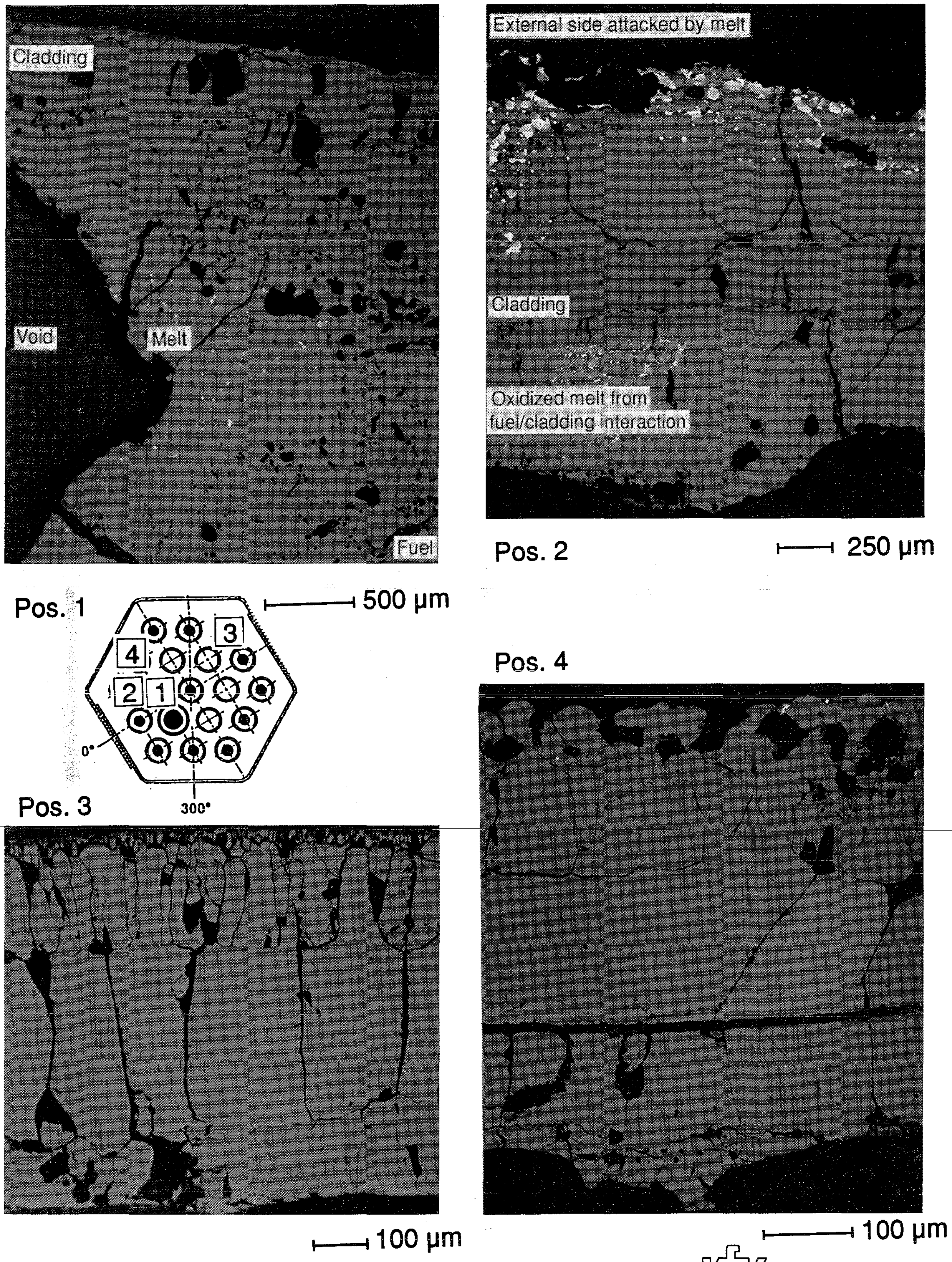

Fig. 149: Cross section CORA-W2-p (top), elevation 910 mm; cladding oxidation

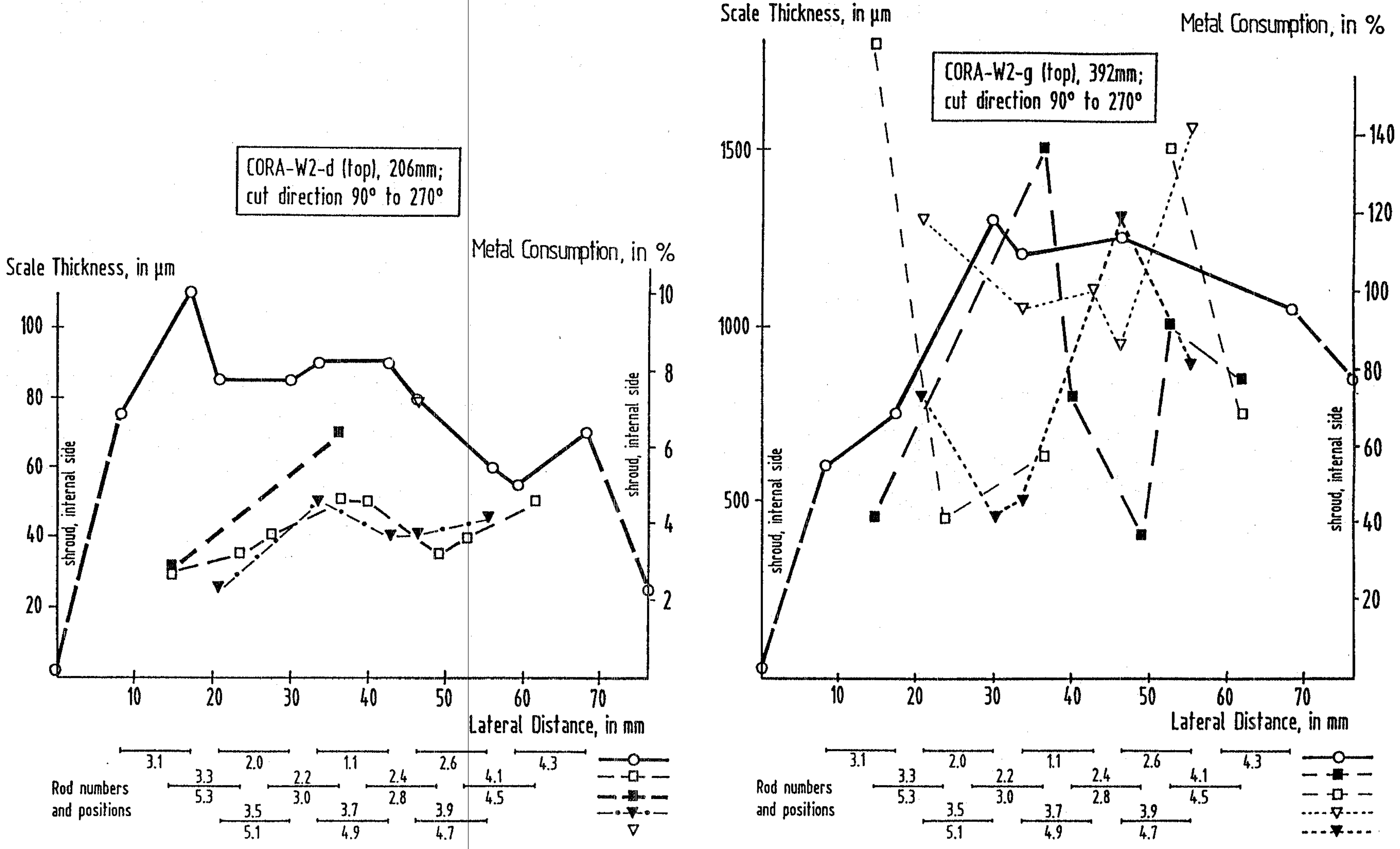

Fig. 150: Cladding oxidation profiles across the bundle CORA-W2 from 90° to 270° at the elevations 206 mm and 392 mm

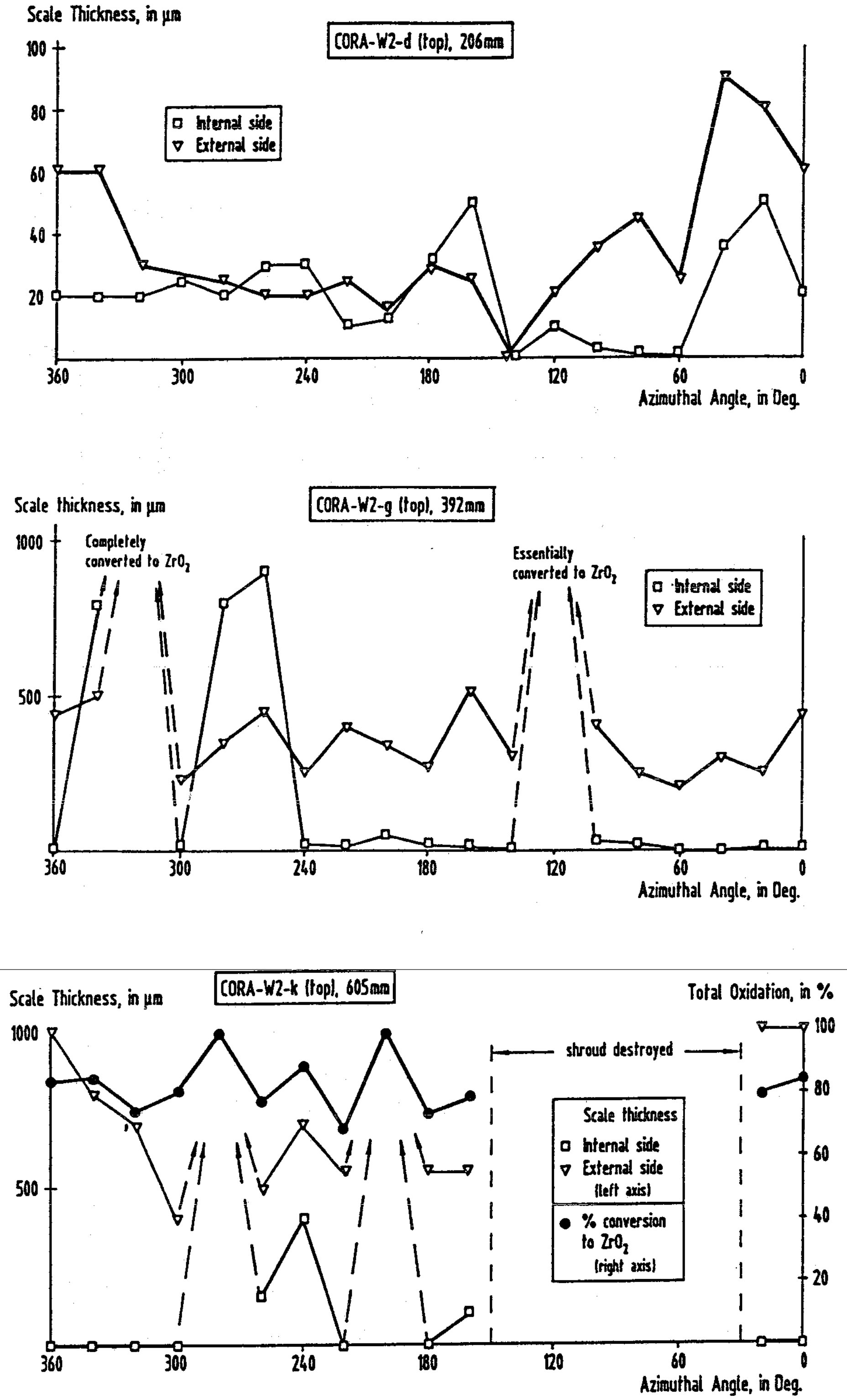

Fig. 151: **Shroud oxidation profiles around the bundle CORA-W2 at the elevations 206 mm, 392 mm and 605 mm**

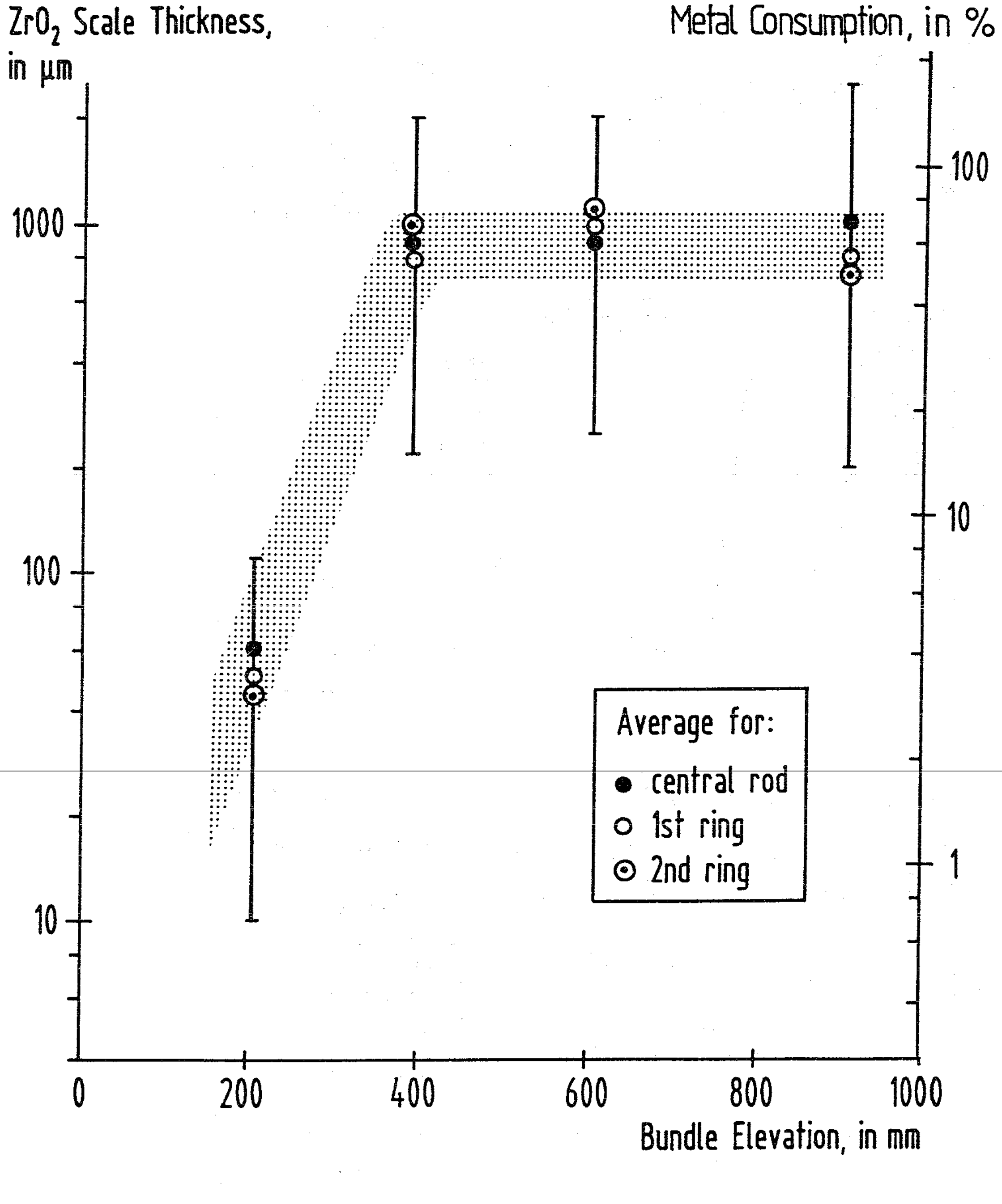

Fig. 152: Axial profile of cladding oxidation along the bundle CORA-W2

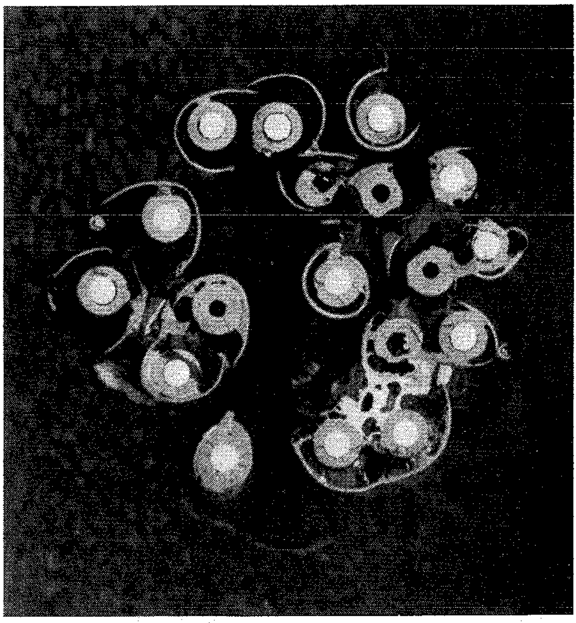

cross section W2-p (top)
910mm

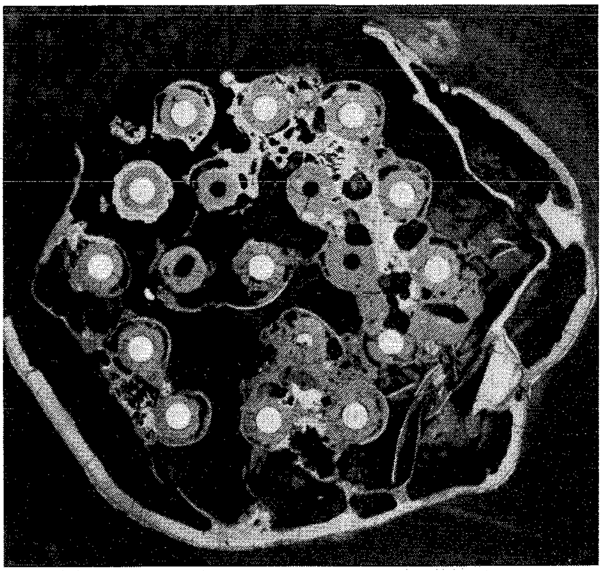

cross section W2-k (top)
605mm

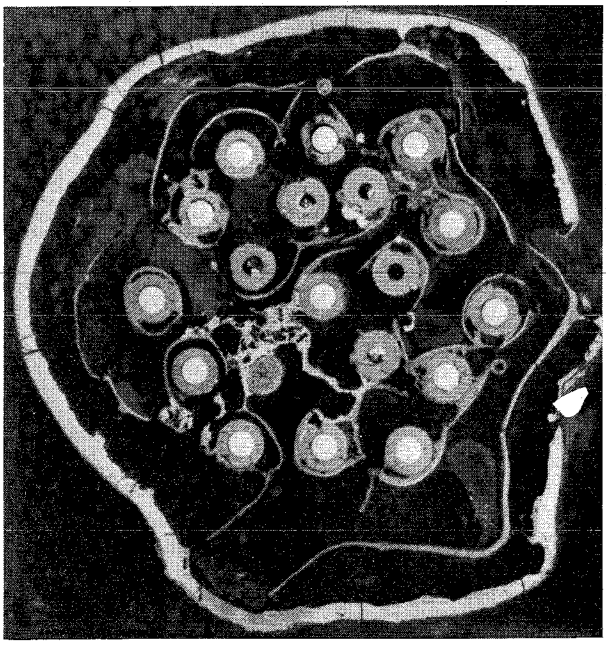

cross section W2-g (top)
392mm

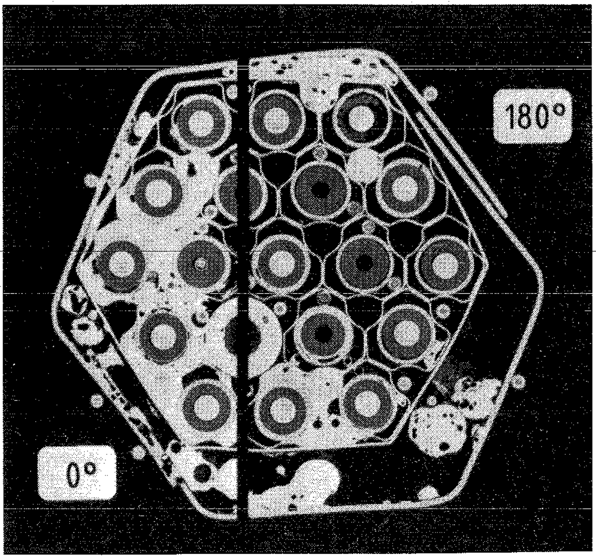

cross section W2-d (top)
206mm

10mm

Fig. 153: Cross sections of the bundle VVER-1000/ CORA-W2 which were examined by SEM/EDX analysis at the Kernforschungszentrum Karlsruhe.

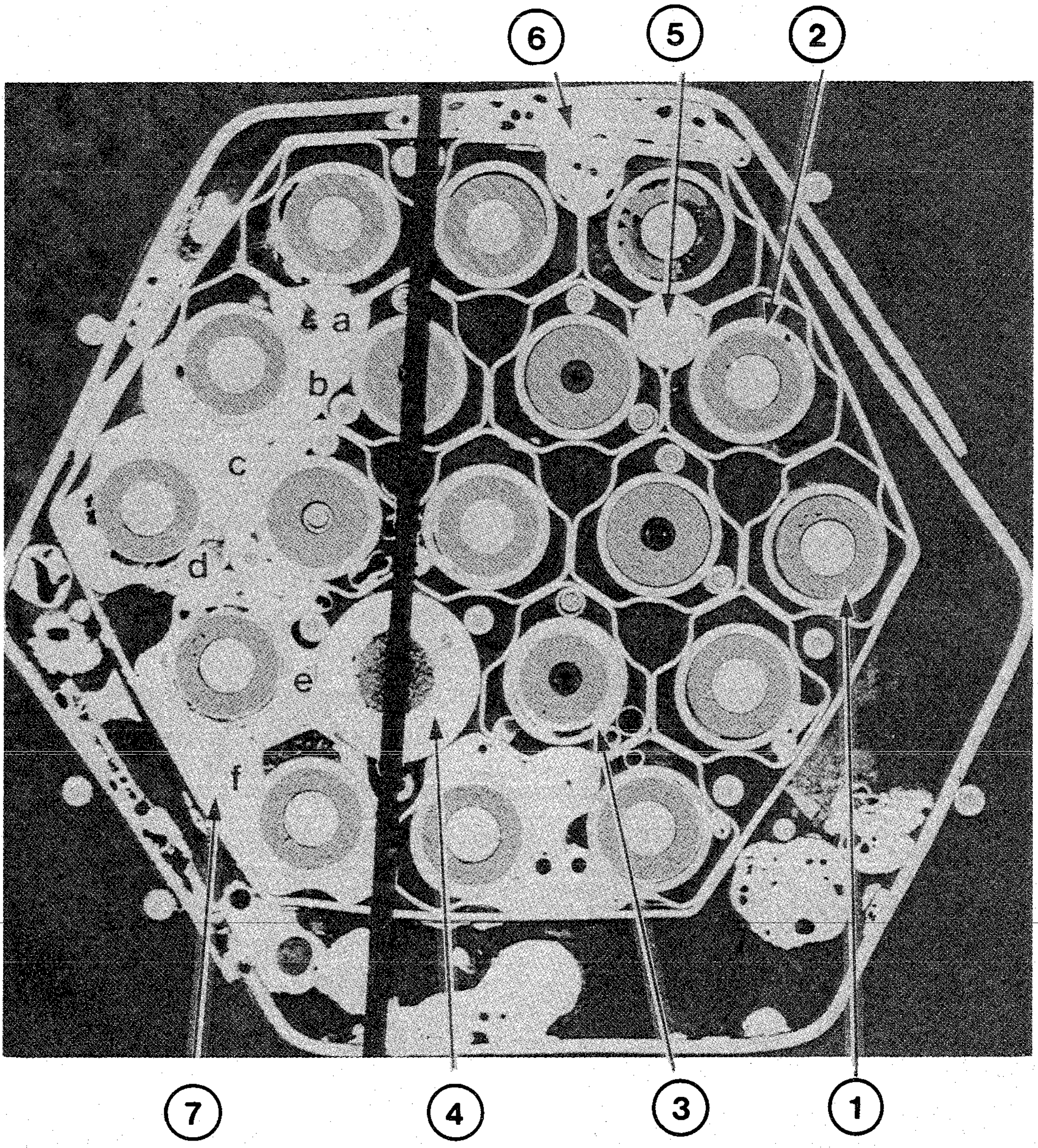

Maßstab 2 : 1

Fig. 154: Fuel rod bundle CORA-W2, cross-section # d (206 mm elevation); Positions of SEM/EDX analysis.

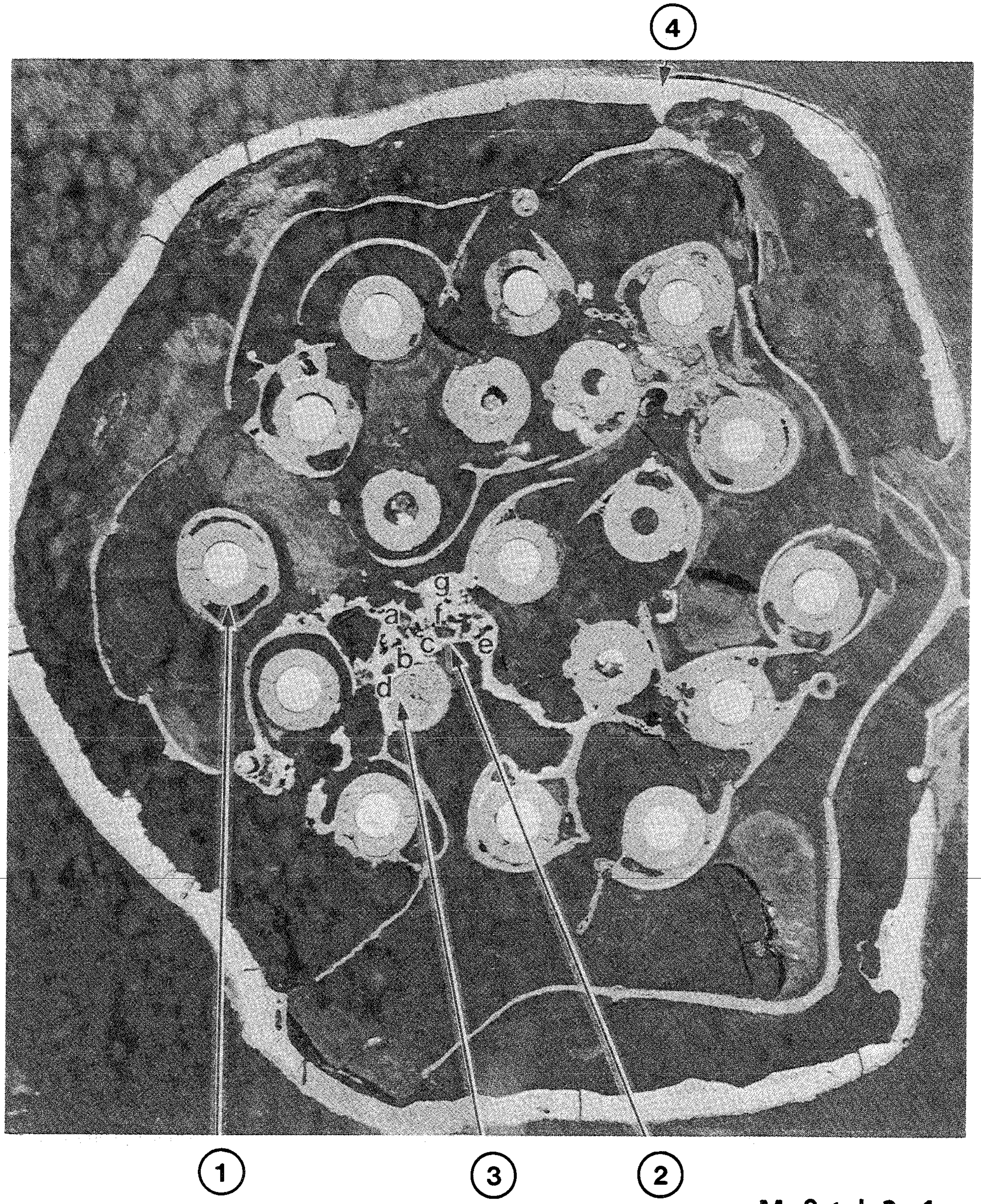

Maßstab 2 : 1

Fig. 155: Fuel rod bundle CORA-W2, cross-section # g (392 mm elevation); Positions of SEM/EDX analysis.

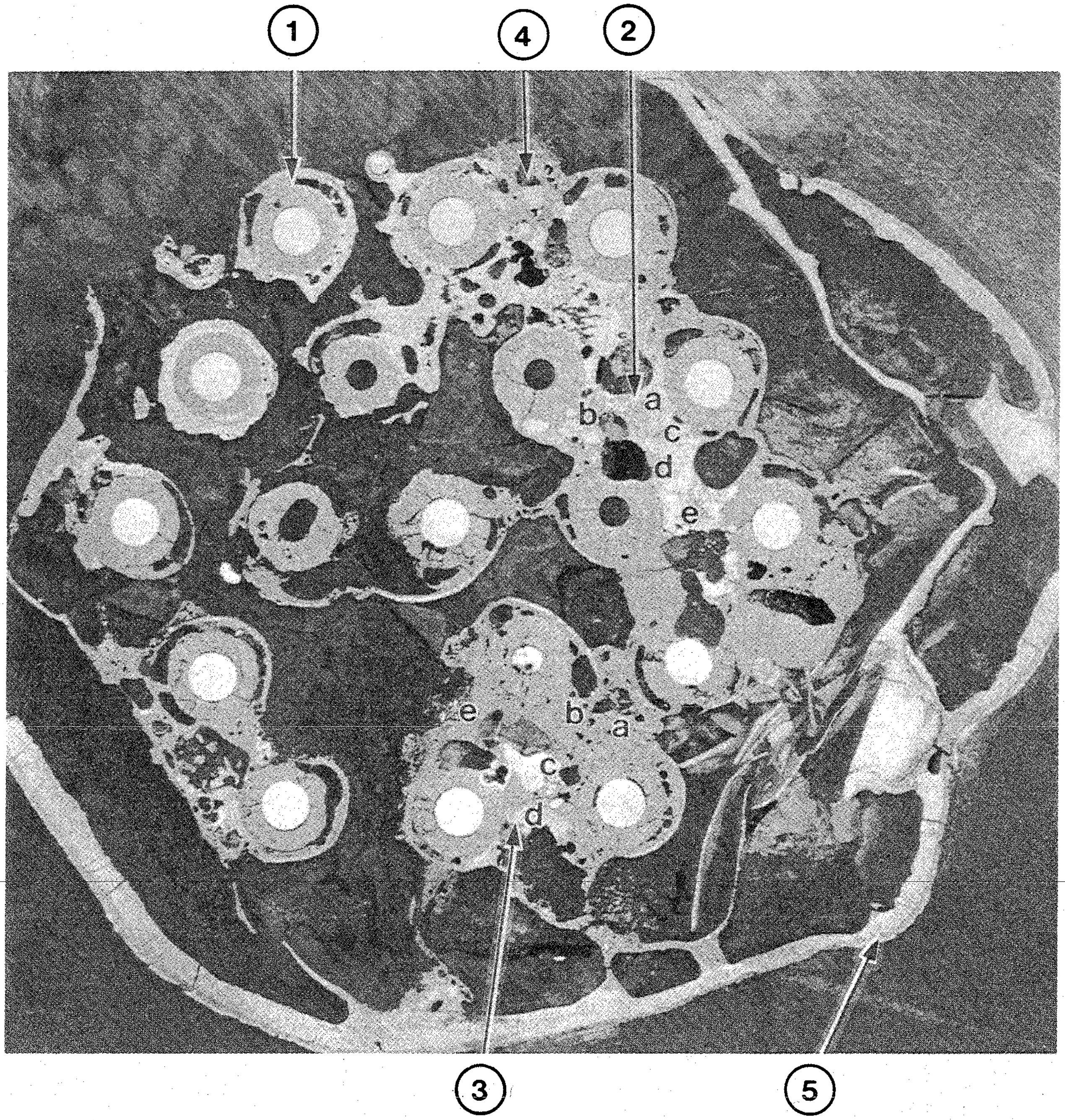

Maßstab 2 : 1

Fig. 156: Fuel rod bundle CORA-W2, cross-section # k (605 mm elevation); Positions of SEM/EDX analysis.

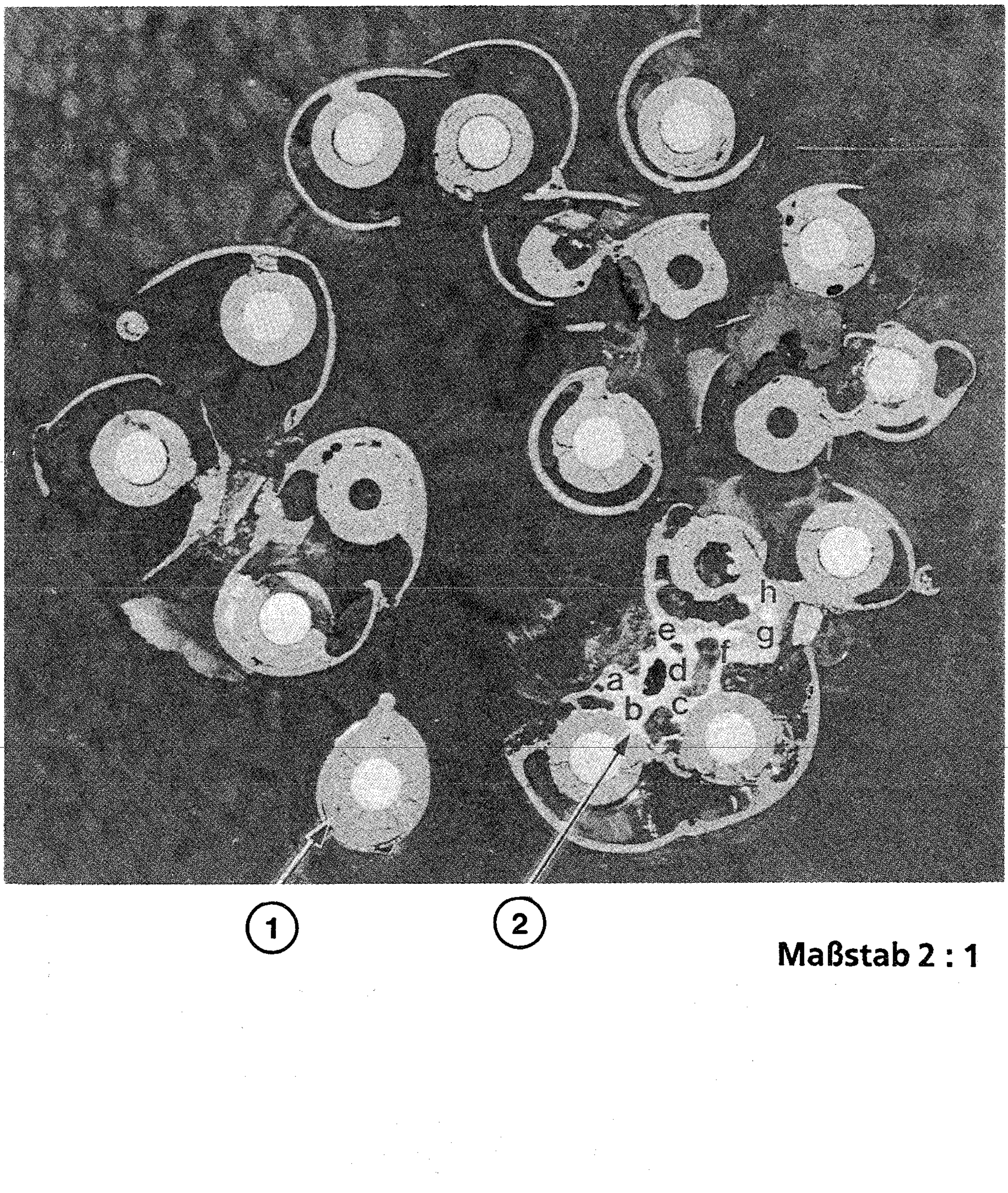

Fig. 157: Fuel rod bundle CORA-W2, cross-section # p (910 mm elevation); Positions of SEM/EDX analysis.

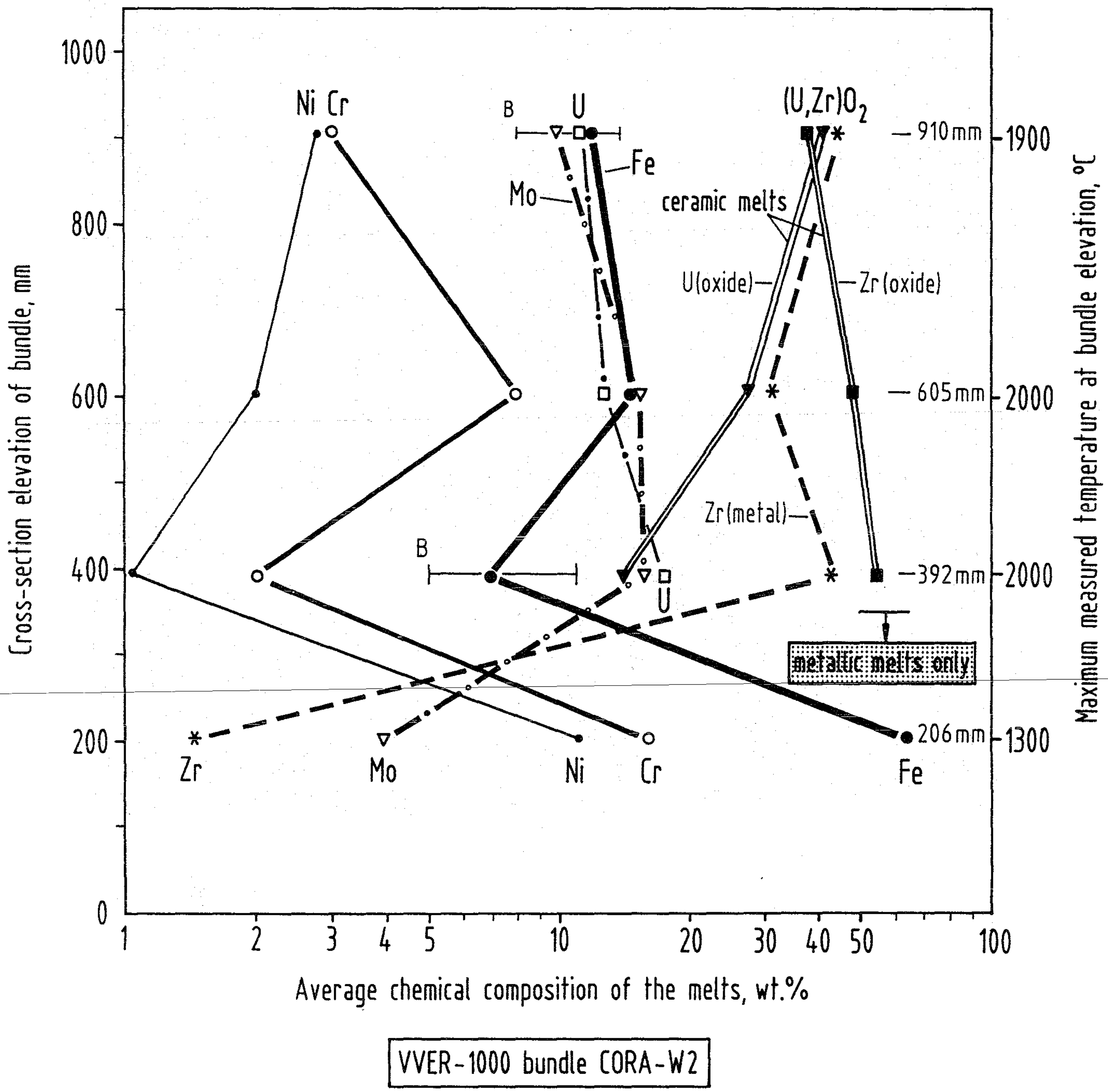

Fig. 158: Chemical composition of examined metallic and ceramic melts as function of bundle elevation (206, 392, 605, 910 mm).

Appendix

Pre-transient Data

Pre-transient data, i.e. data measured before 3000 s (begin of the transient) are provided in the Appendix

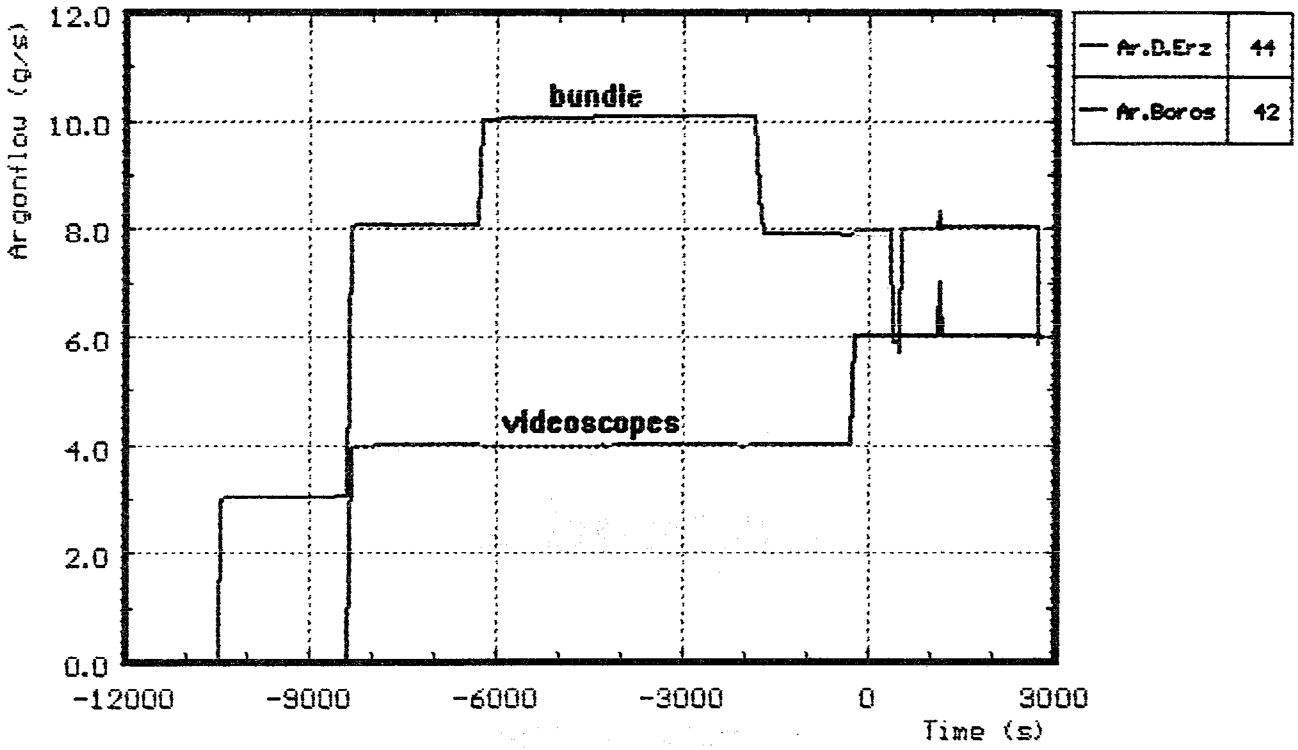

Fig. A1: CORA-W2; Argon input prior to test CORA-W2

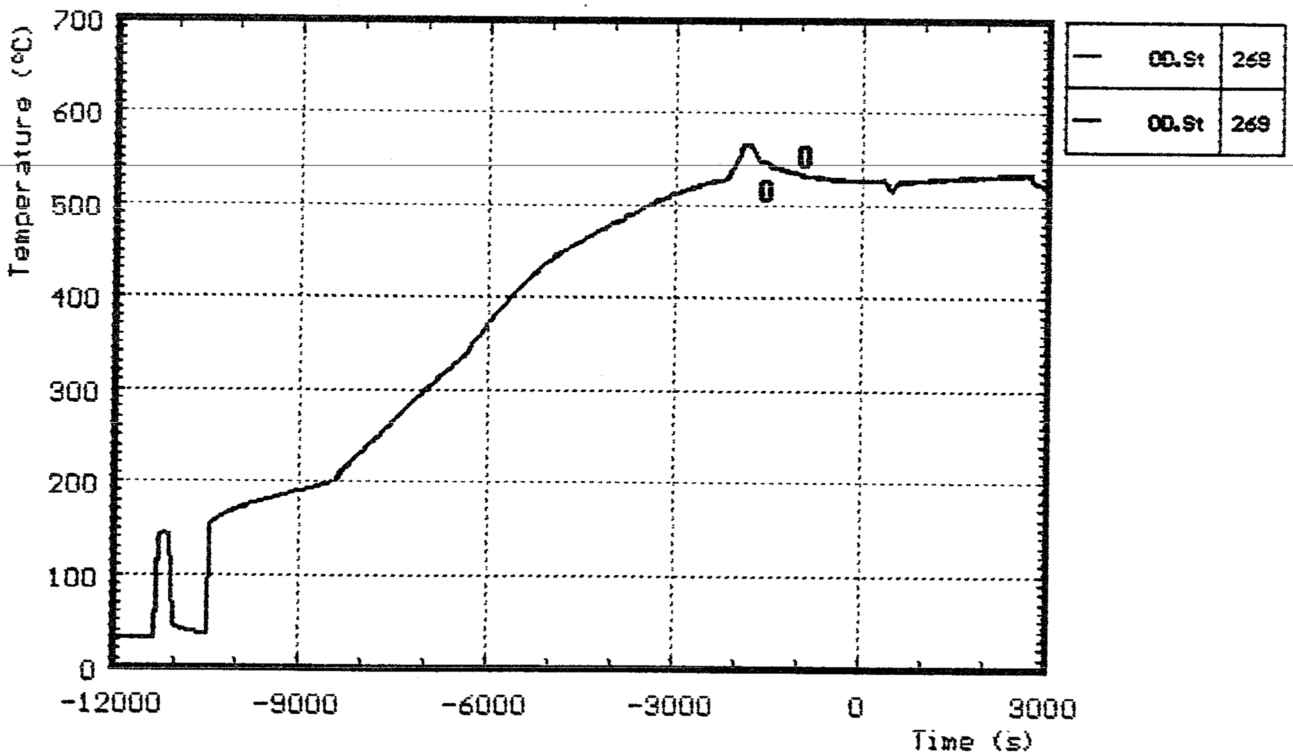

Fig. A2: CORA-W2; Temperature at the entrance of the bundle prior to test

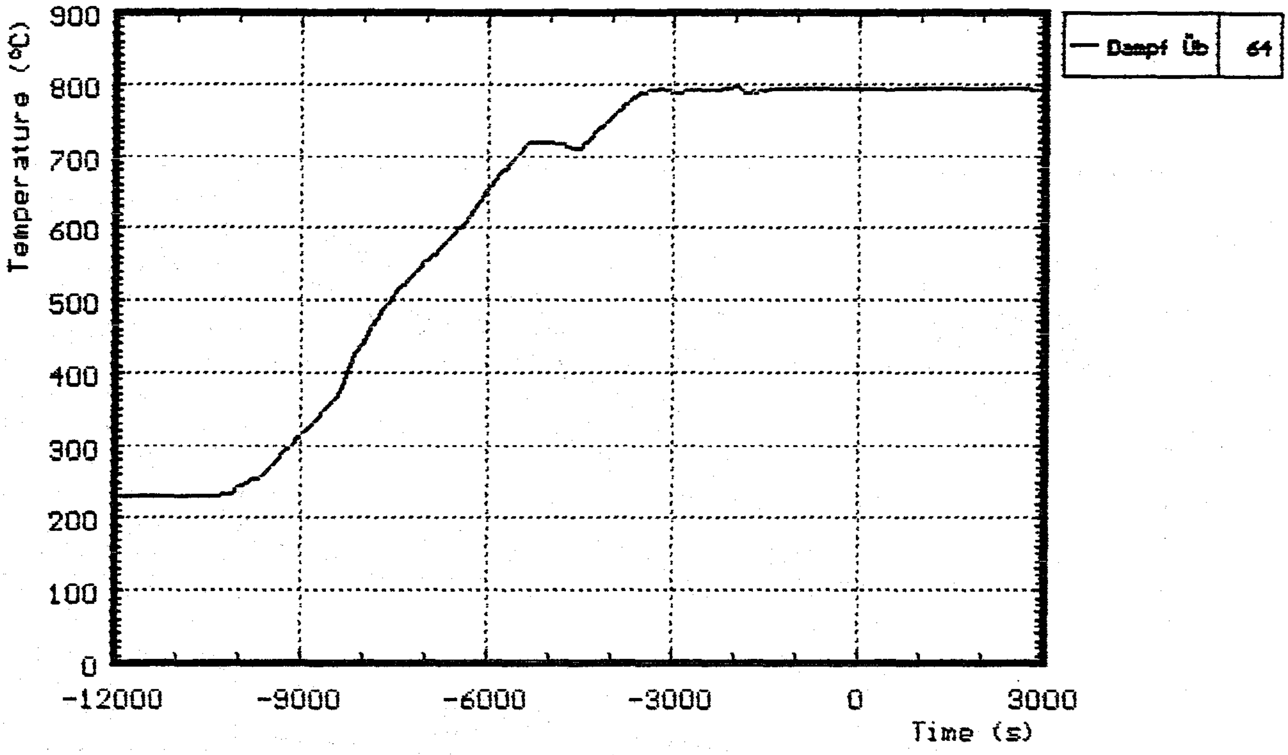

Fig. A3: CORA-W2; Temperature of steam superheater prior to transient

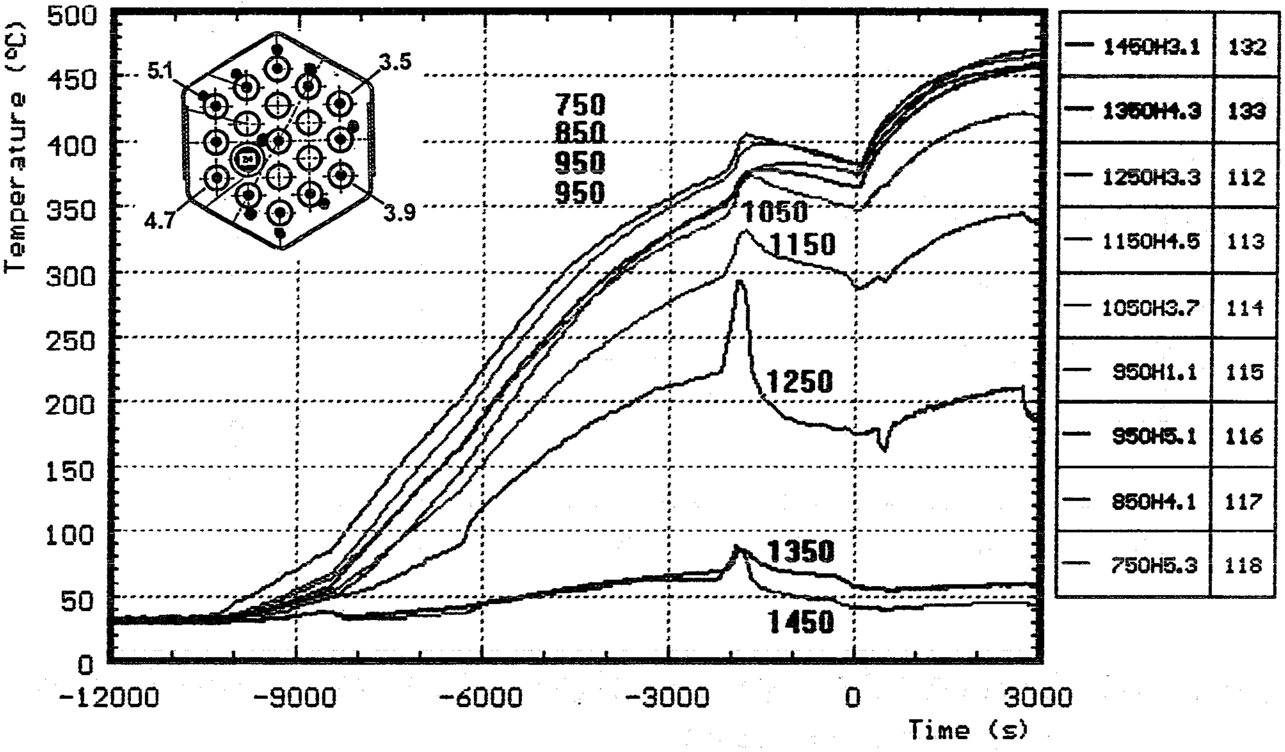

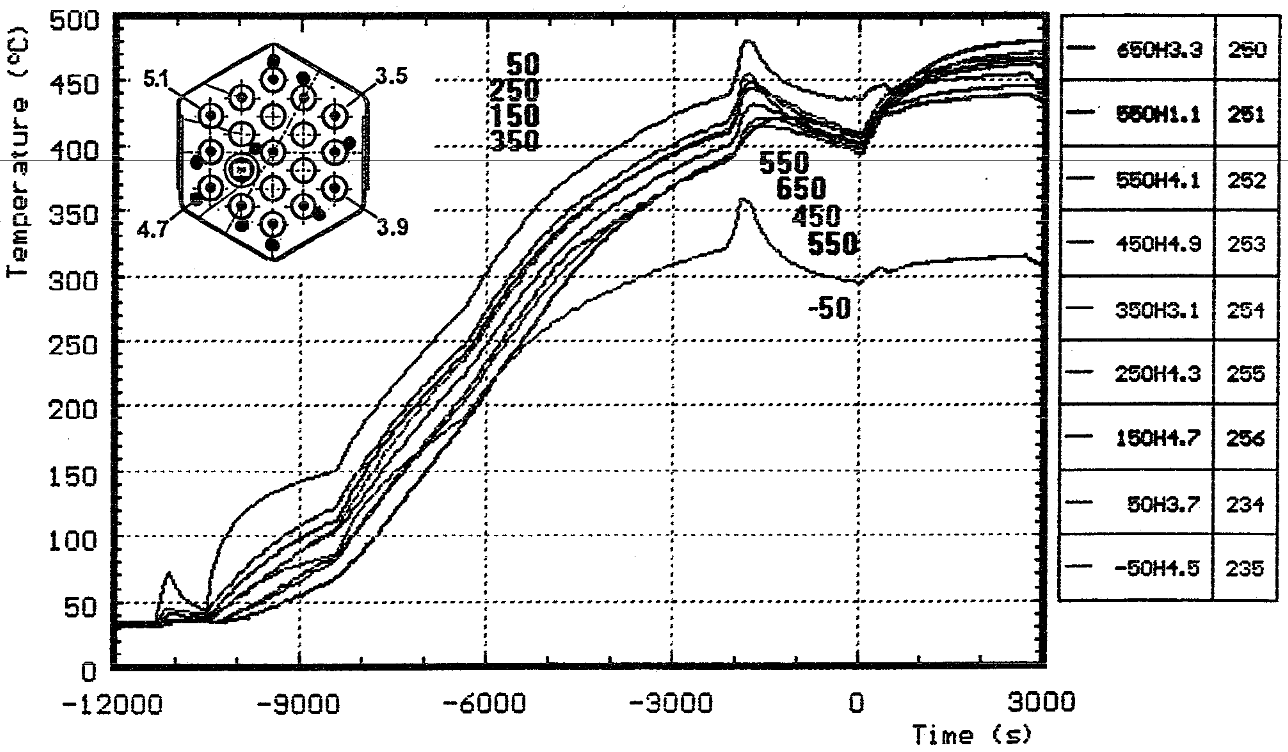

Fig. A4: CORA-W2; Temperatures on heated rods; pre-heat phase

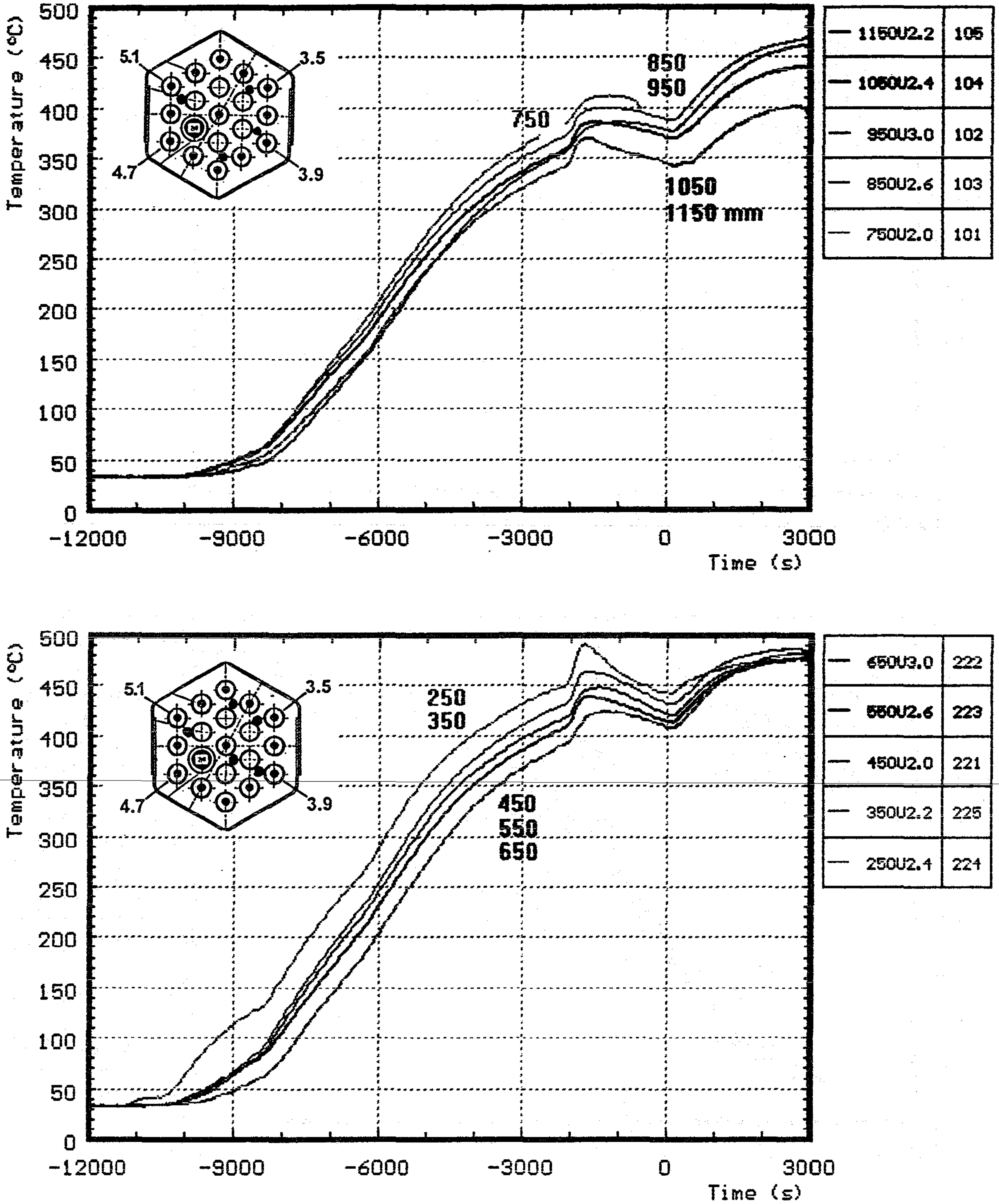

Fig. A5: CORA-W2; Temperatures in unheated rods; pre-heat phase

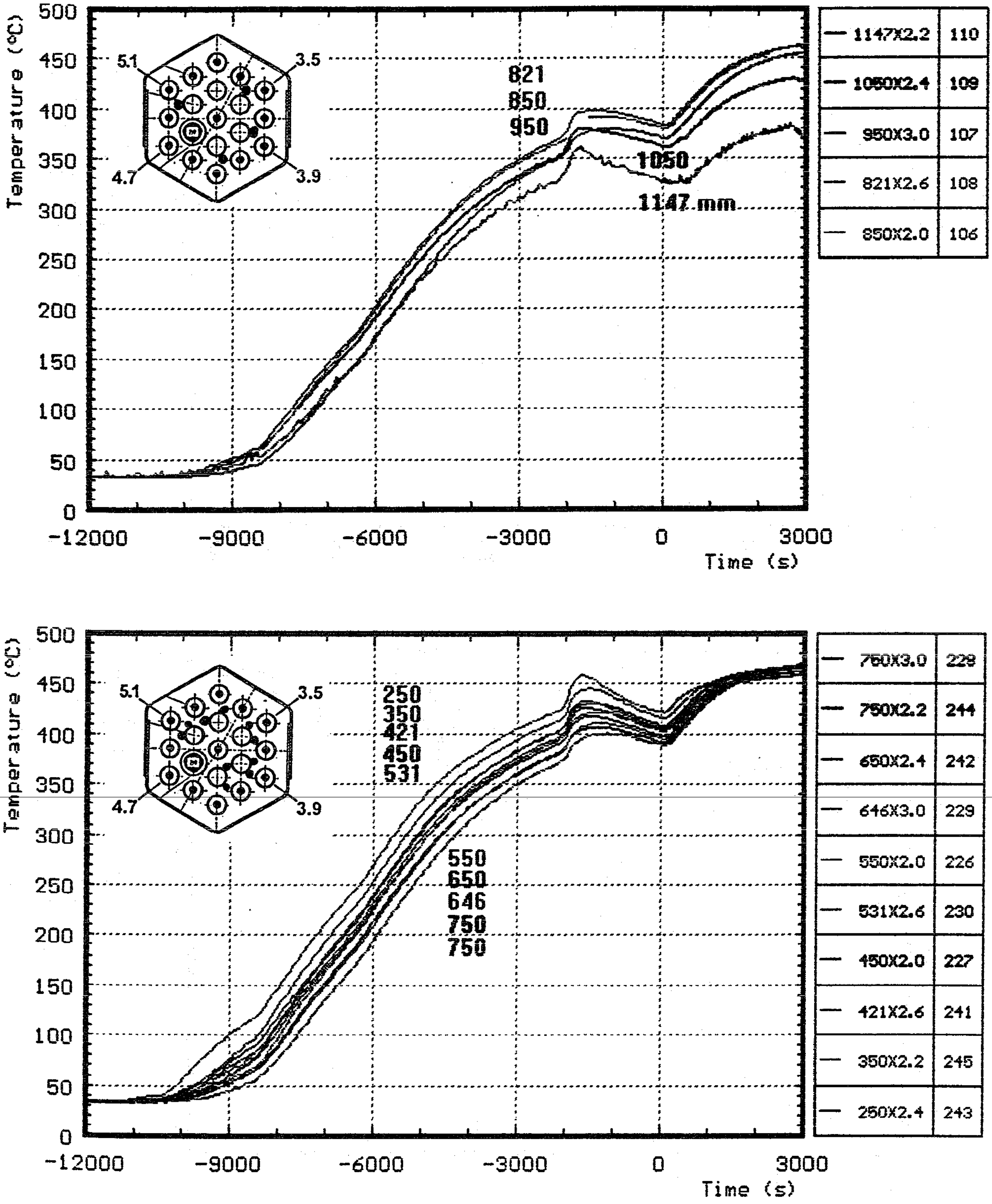

Fig. A6: CORA-W2; Temperatures on unheated rods; pre-heat phase

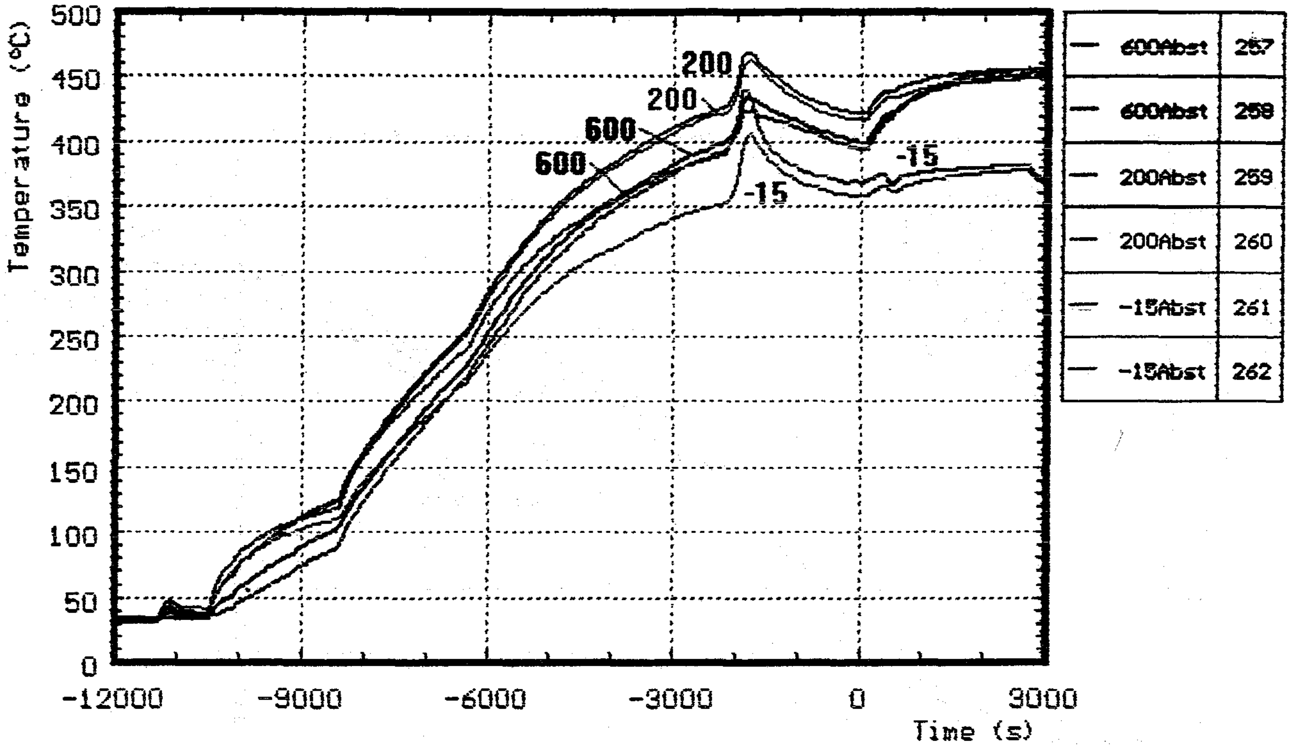

Fig. A7: CORA-W2; Temperatures at the spacer; pre-heat phase

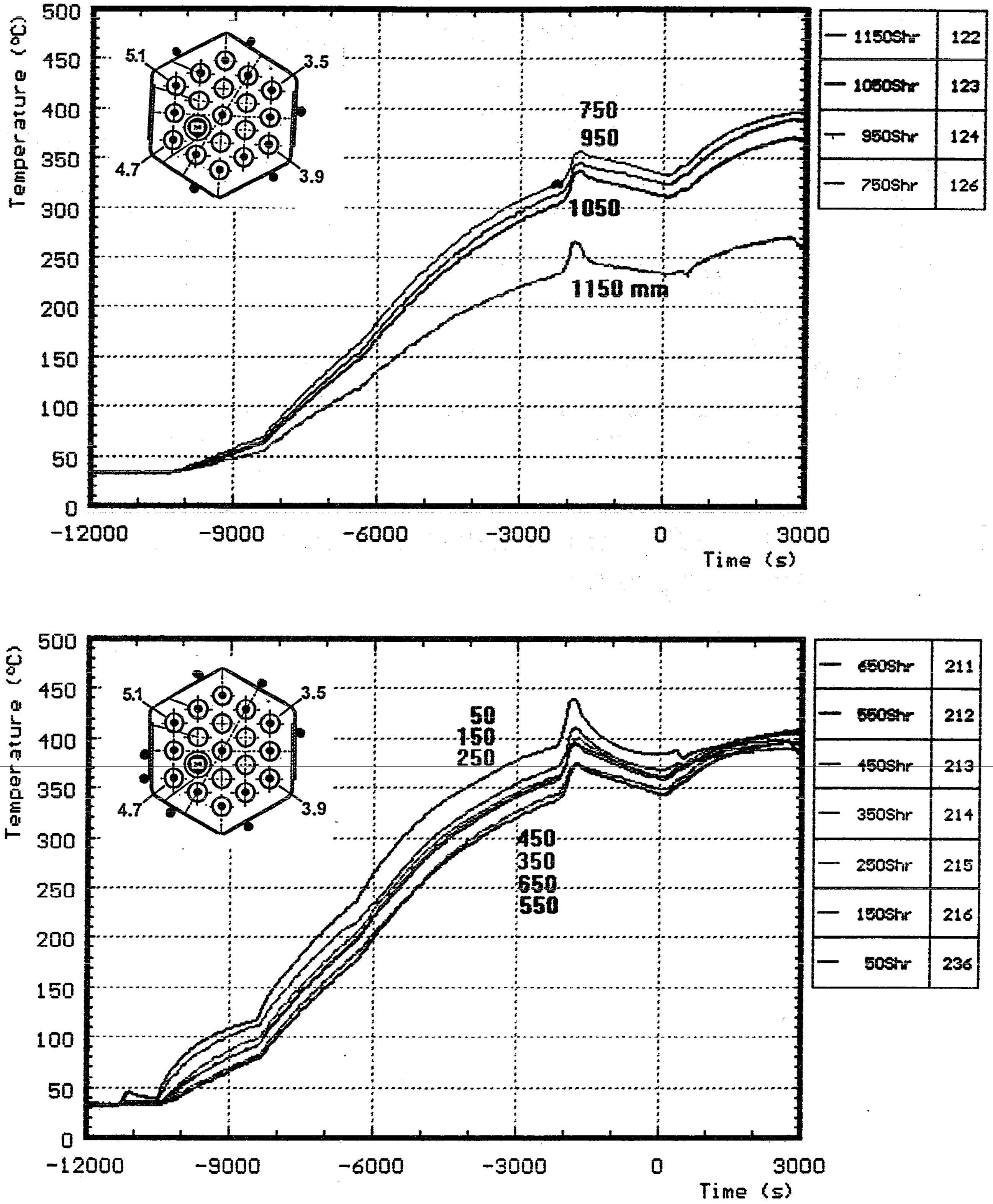

Fig. A8: CORA-W2; Temperatures on outer side of shroud; pre-heat phase

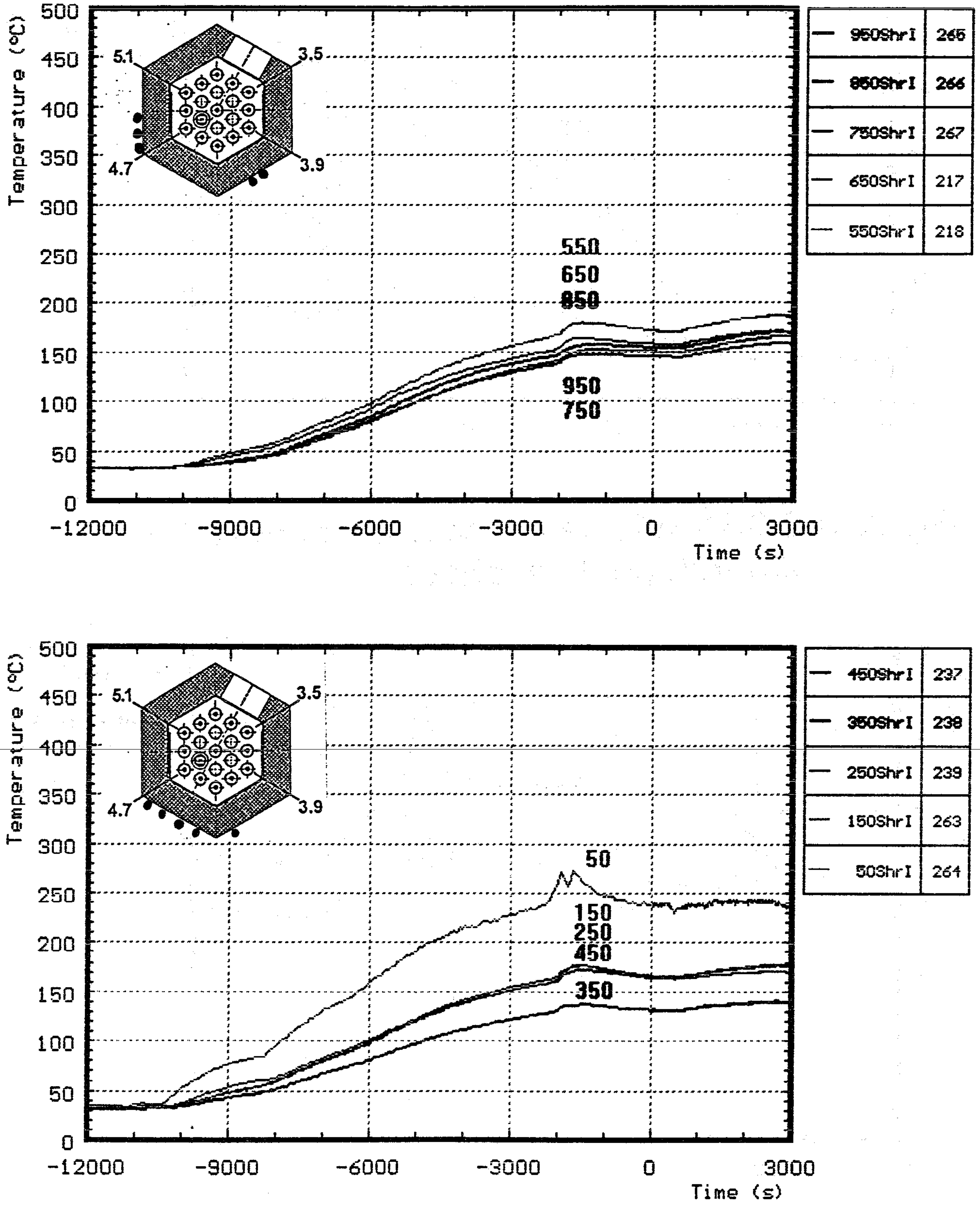

Fig. A9: CORA-W2; Temperatures on shroudinsulation; pre-heat phase

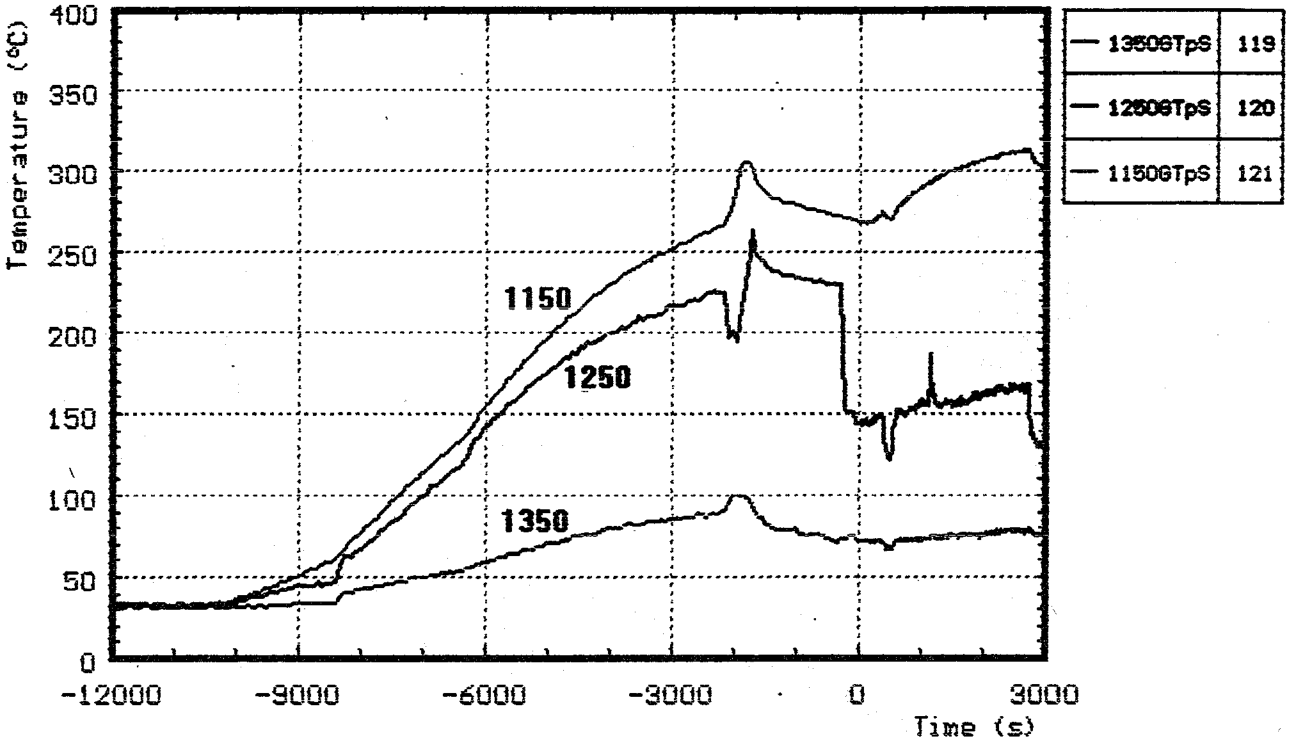

Fig. A10: CORA-W2; Gas temperature above the shroud; pre heat phase

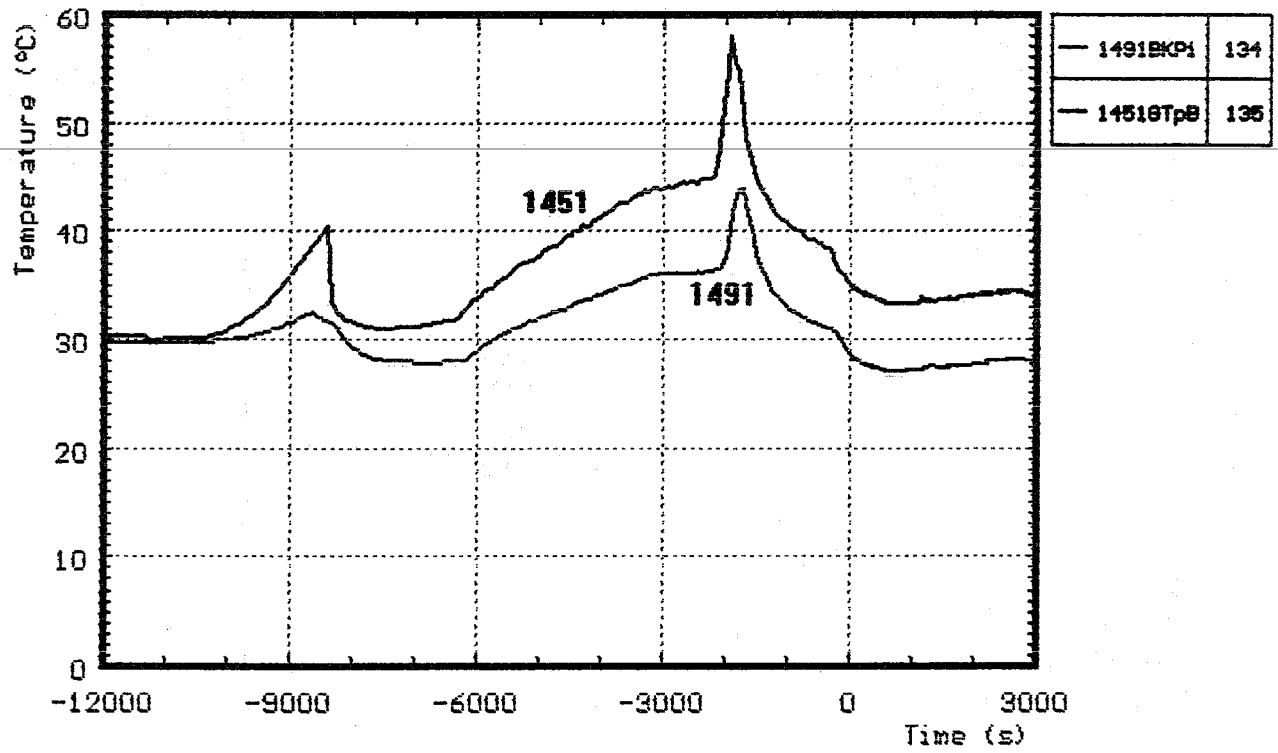

Fig. A11: CORA-W2; Temperature measured in and under the bundle head plate; pre heat phase

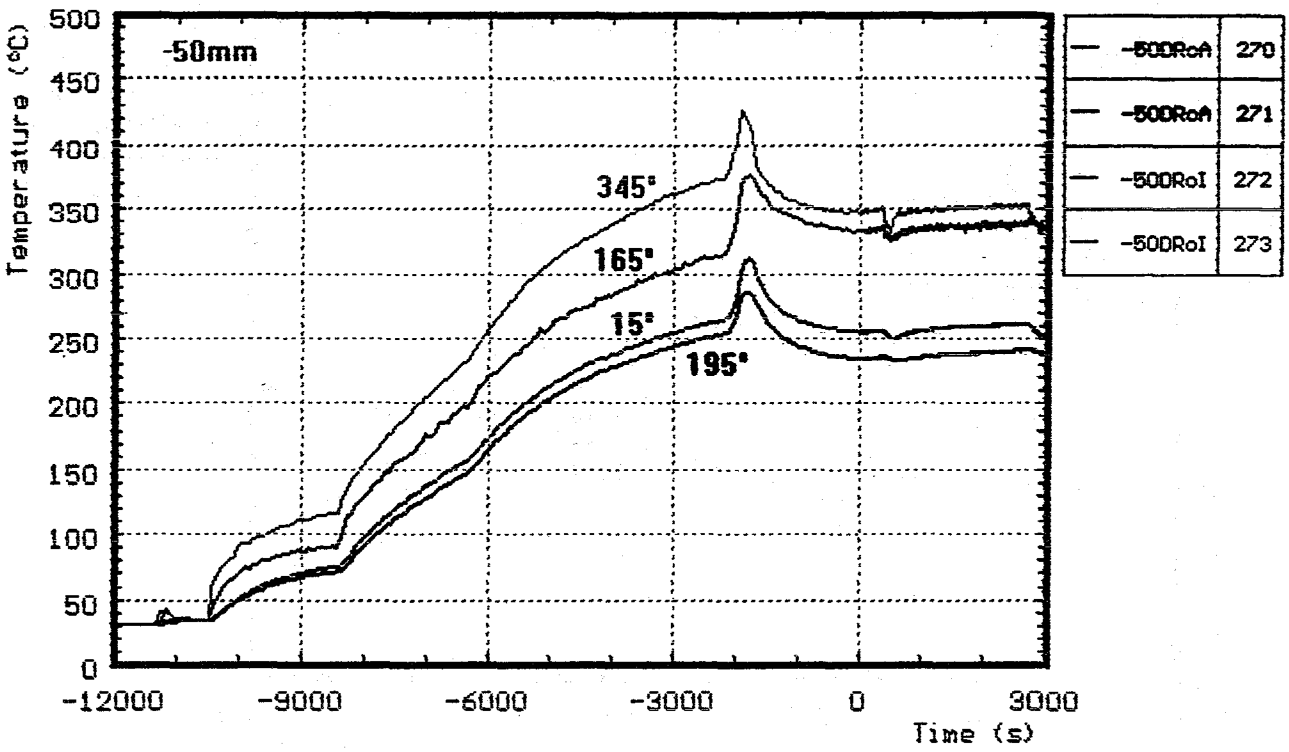

Fig. A12: CORA-W2;Temperatures in the steam tube; pre-heat phase

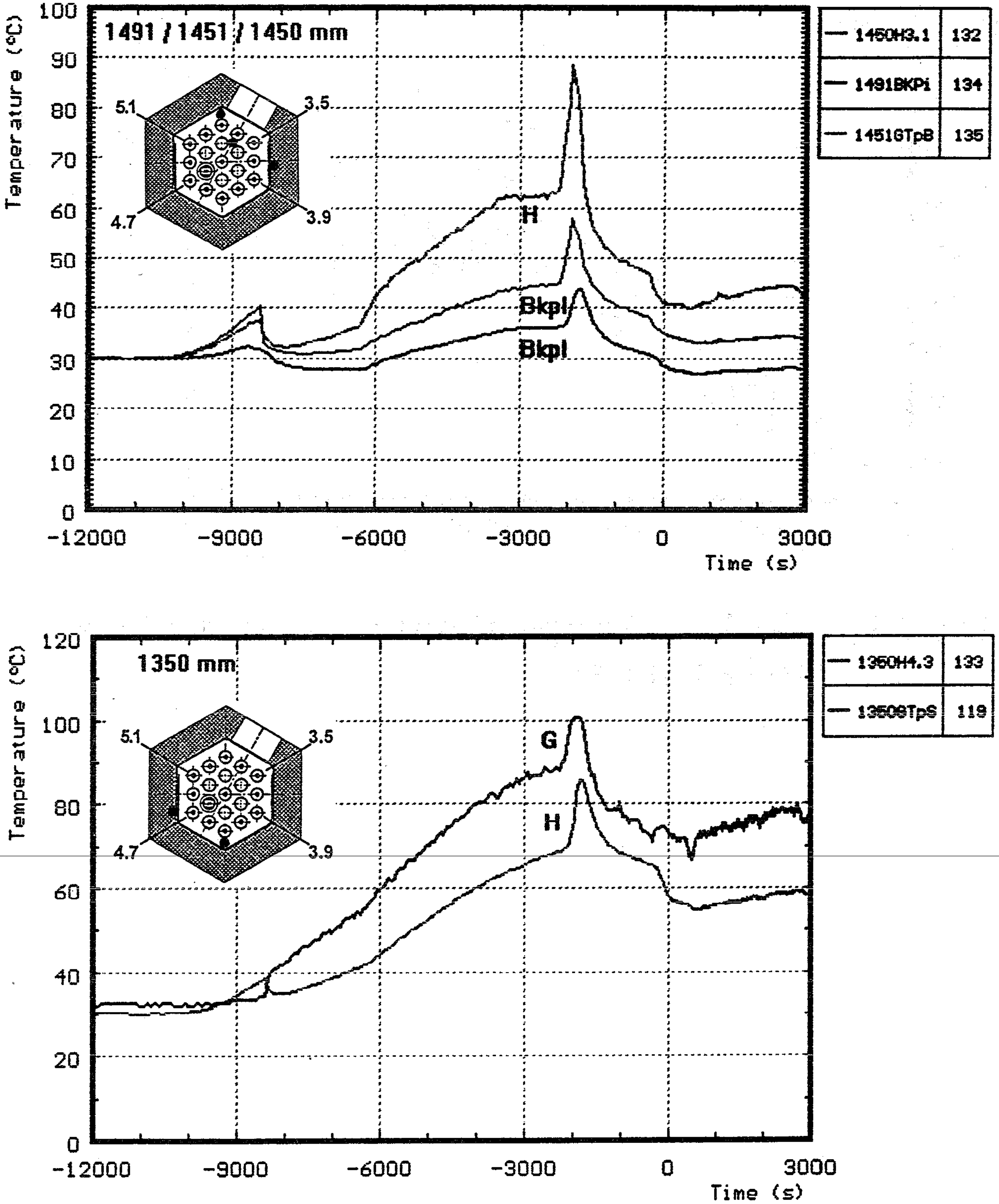

H: heated rods

G: gas temperature Bkpl: bundle heat plate

Fig. A13: CORA-W2; Temperatures at fixed elevations; pre-heat phase (1450, 1350 mm)

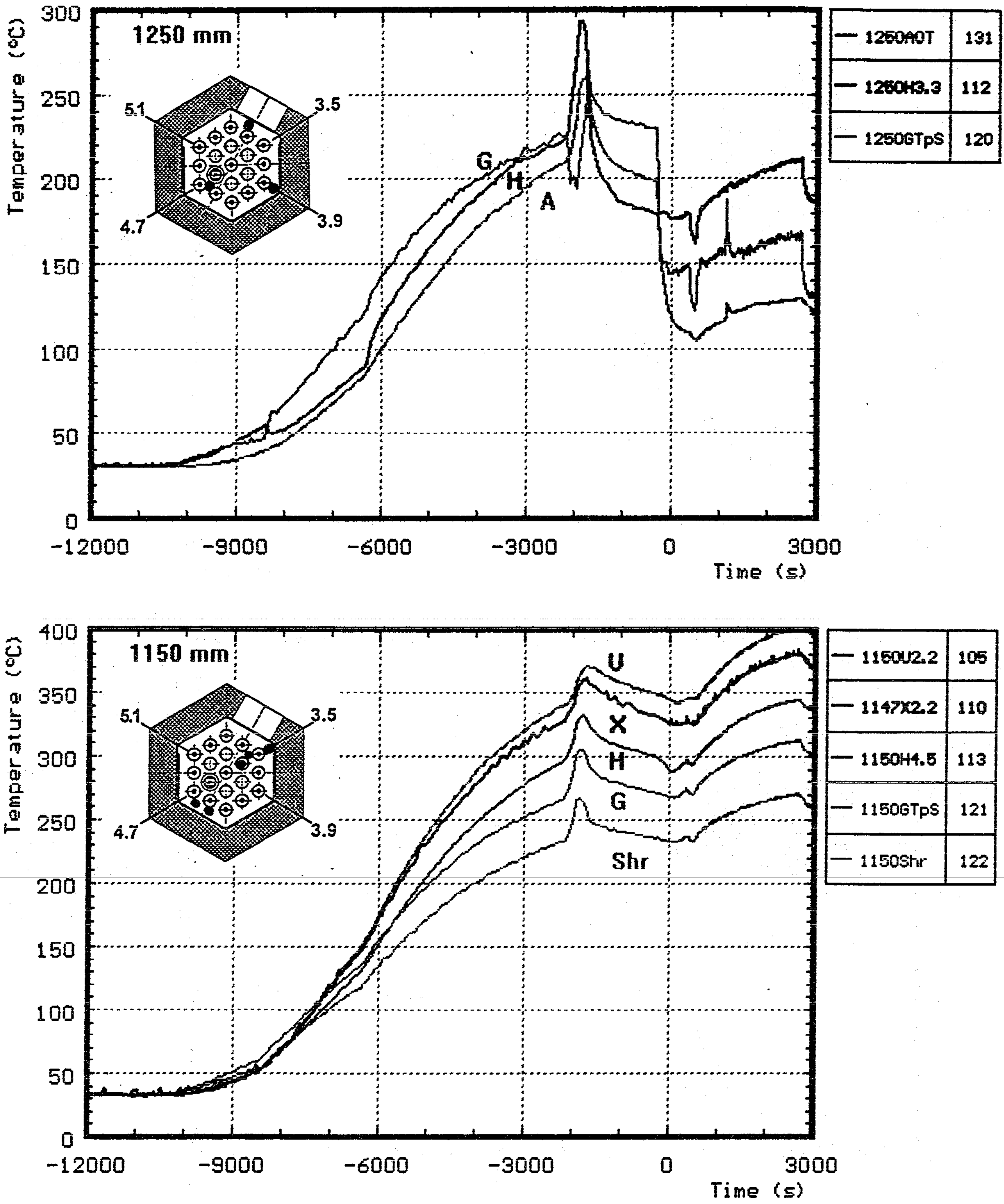

H: heated rods
U: unheated rods
X: on unheated rods

A : on guide tube
G : gas temperature
Shr: on shroud

Fig. A14: CORA-W2; Temperatures at fixed elevations; pre-heat phase (1250, 1150 mm)

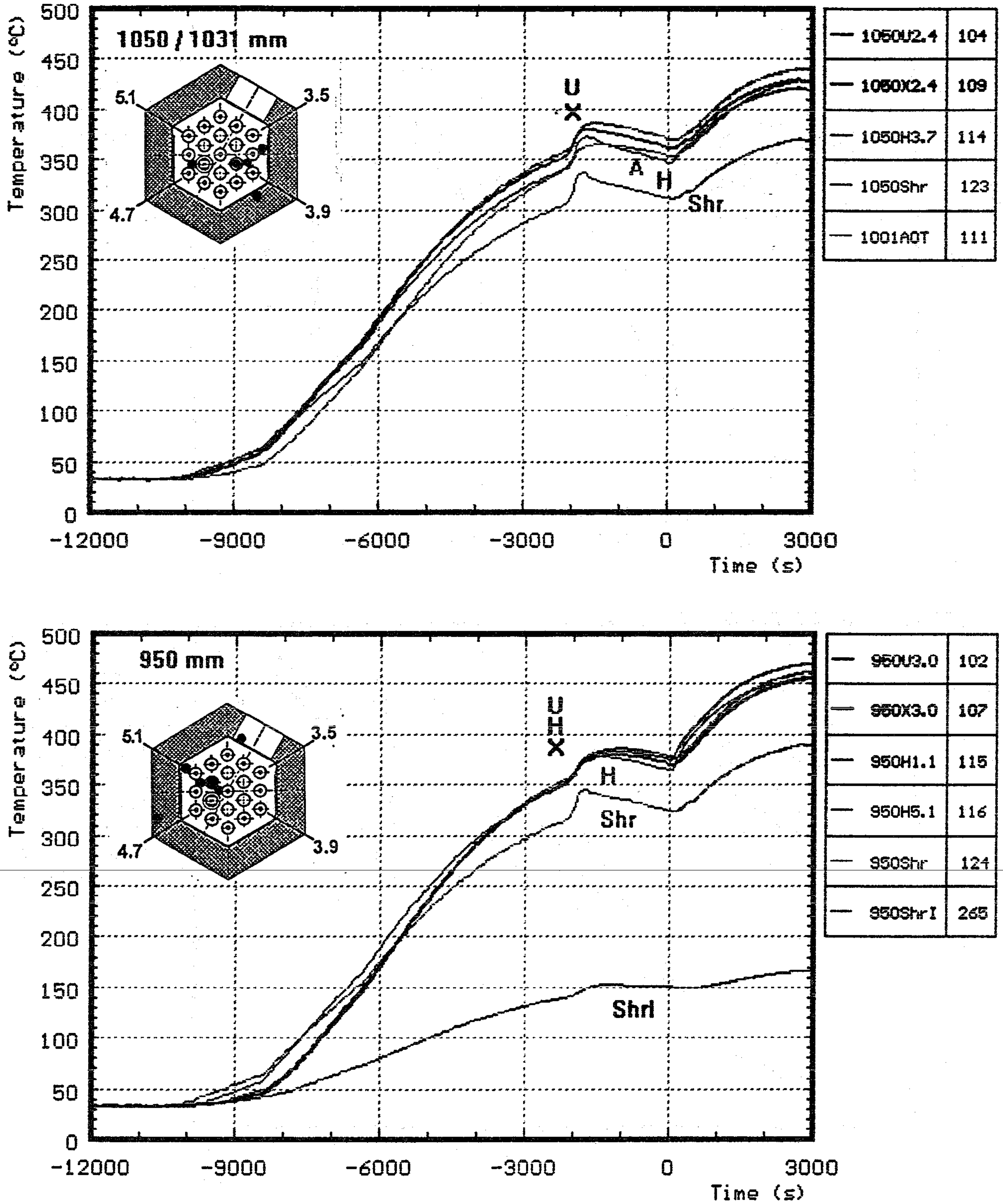

H: heated rods
U: unheated rods
X: on unheated rods

A : on guide tube
ShrI: shroud insulation
Shr : on shroud

Fig. A15: CORA-W2; Temperatures at fixed elevations; pre-heat phase (1050, 950 mm)

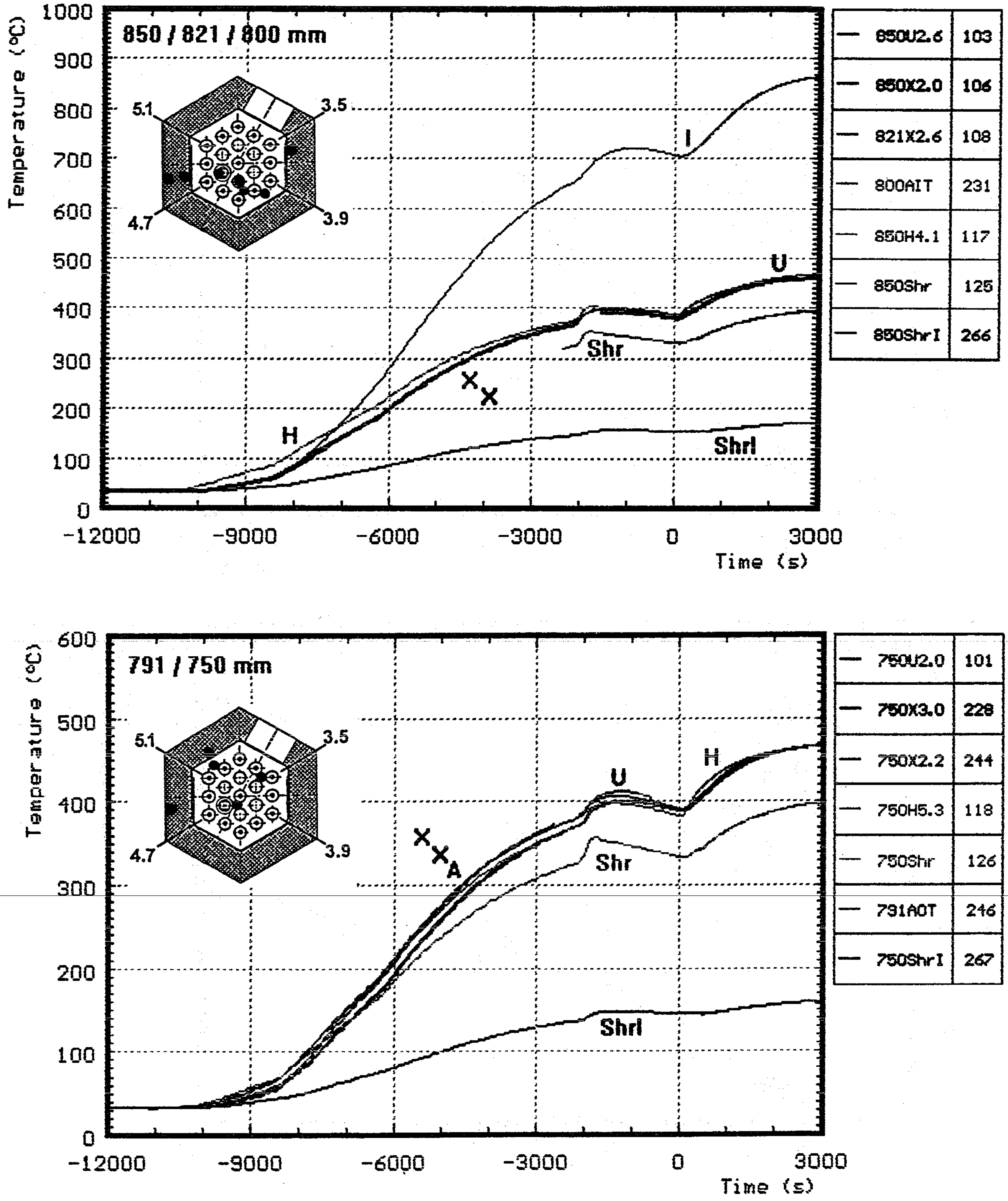

H: heated rods
U: unheated rods
X: on unheated rods
I : on absorber

A : on guide tube
ShrI: shroud insulation
Shr : on shroud

Fig. A16: CORA-W2; Temperatures at fixed elevations; pre-heat phase (850, 750 mm)

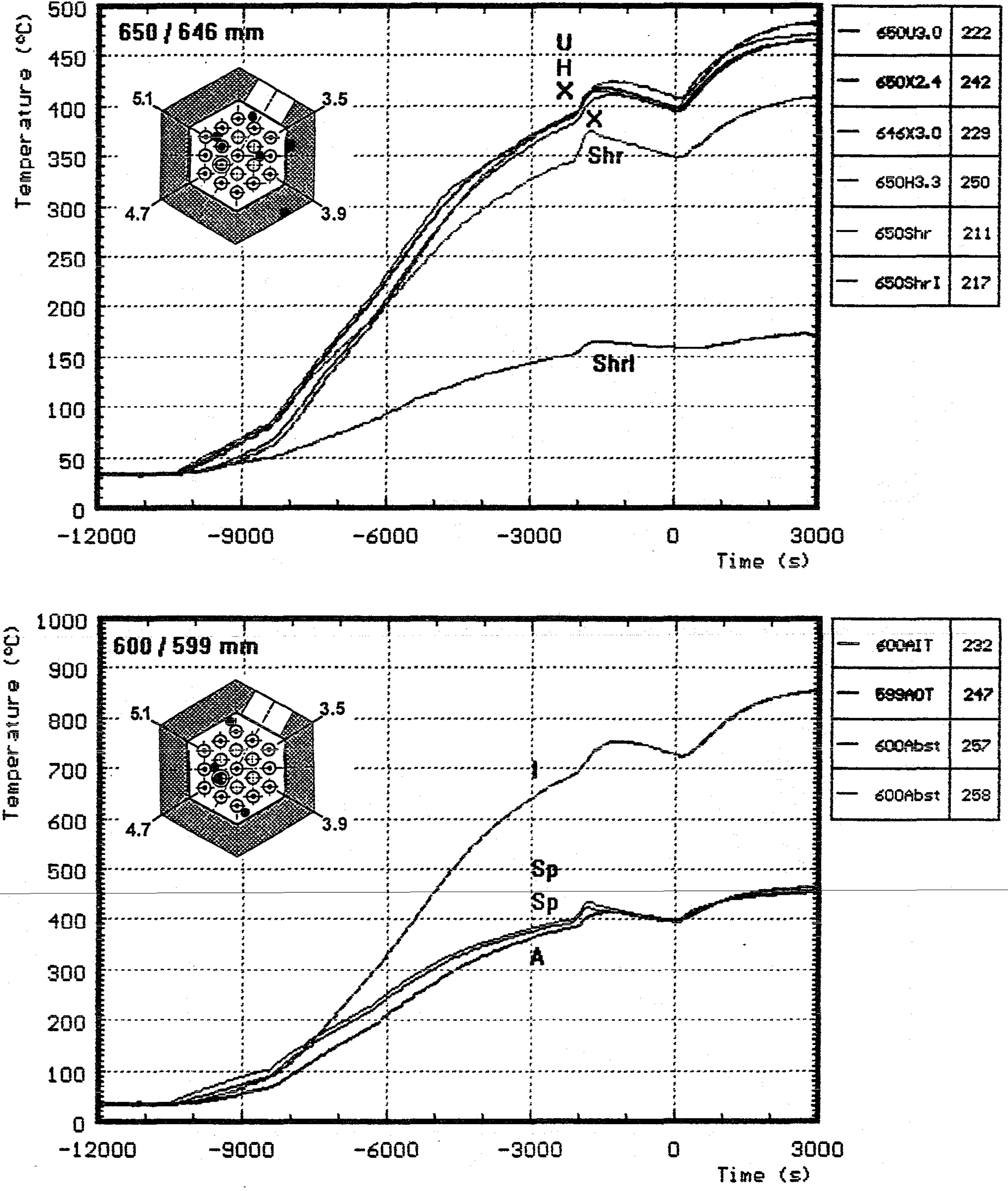

H: heated rods
U: unheated rods
X: on unheated rods
I : on absorber

A : on guide tube
ShrI: shroud insulation
Shr : on shroud
Sp : spacer

Fig. A17: CORA-W2; Temperatures at fixed elevations; pre-heat phase (650, 600 mm)

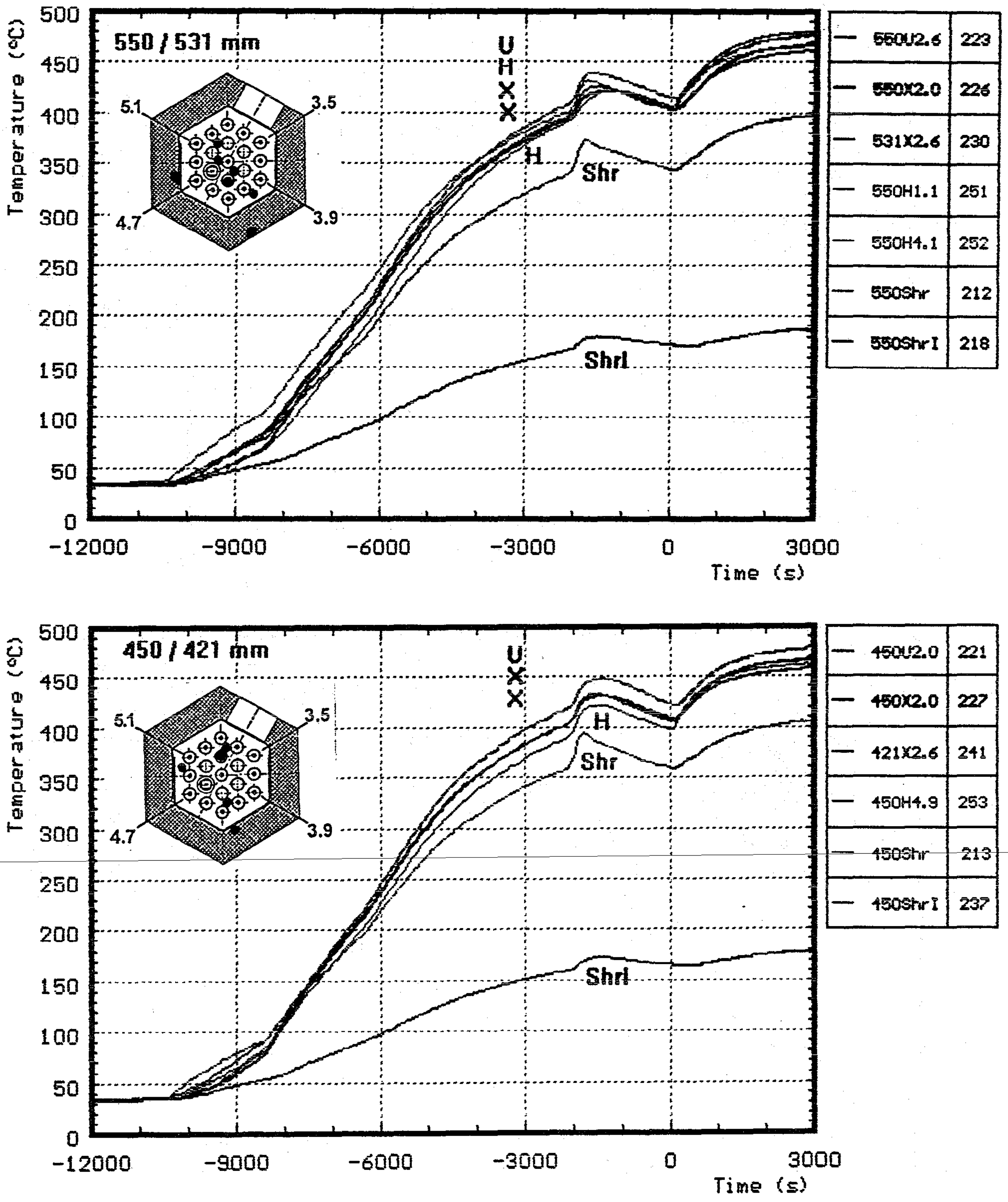

H: heated rods
U: unheated rods
X: on unheated rods

ShrI: shroud insulation
Shr : on shroud

Fig. A18: CORA-W2; Temperatures at fixed elevations; pre-heat phase (550, 450 mm)

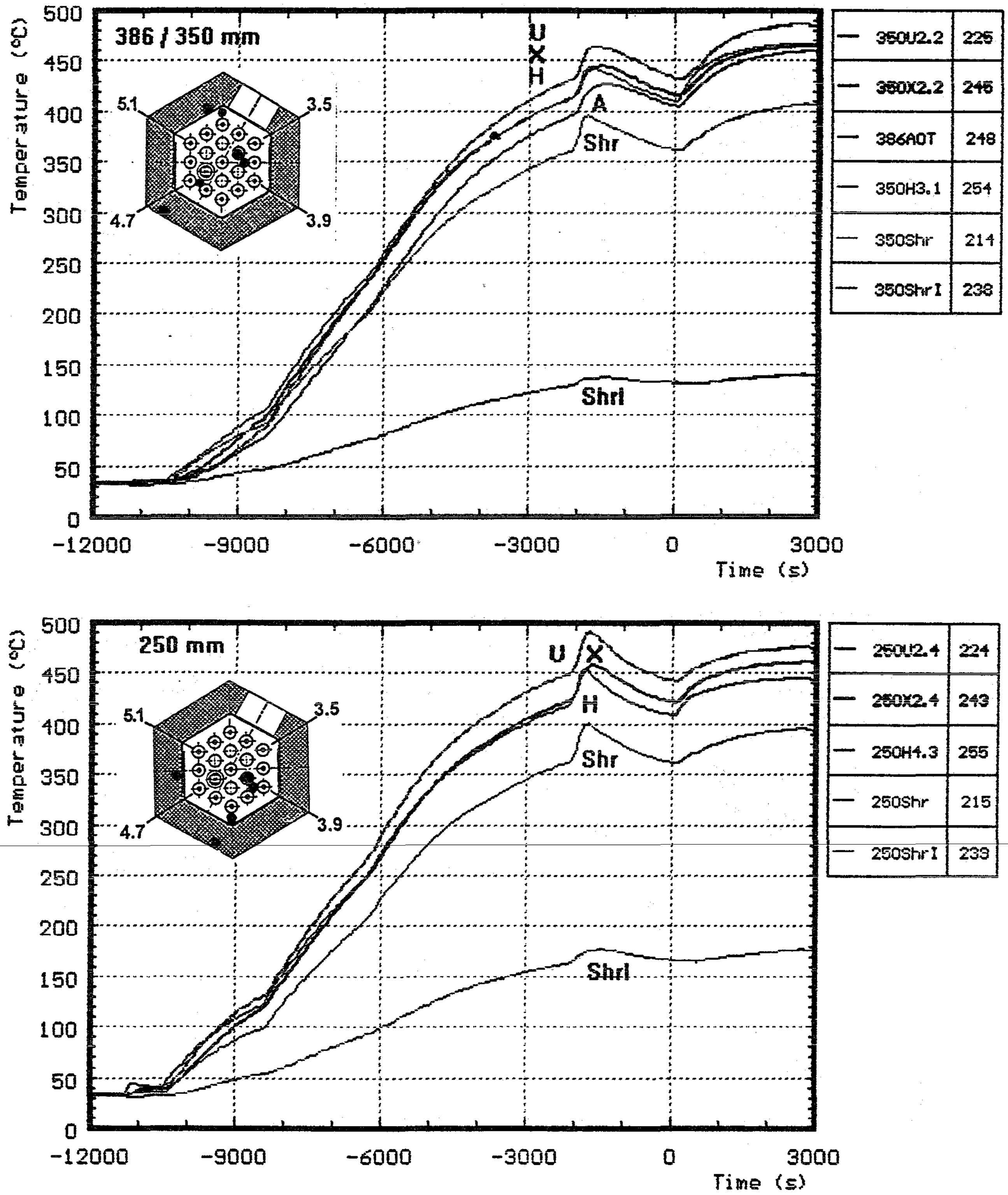

H: heated rods
U: unheated rods
X: on unheated rods

A : on guide tube
ShrI: shroud insulation
Shr : on shroud

Fig. A19: CORA-W2; Temperatures at fixed elevations; pre-heat phase (350, 250 mm)

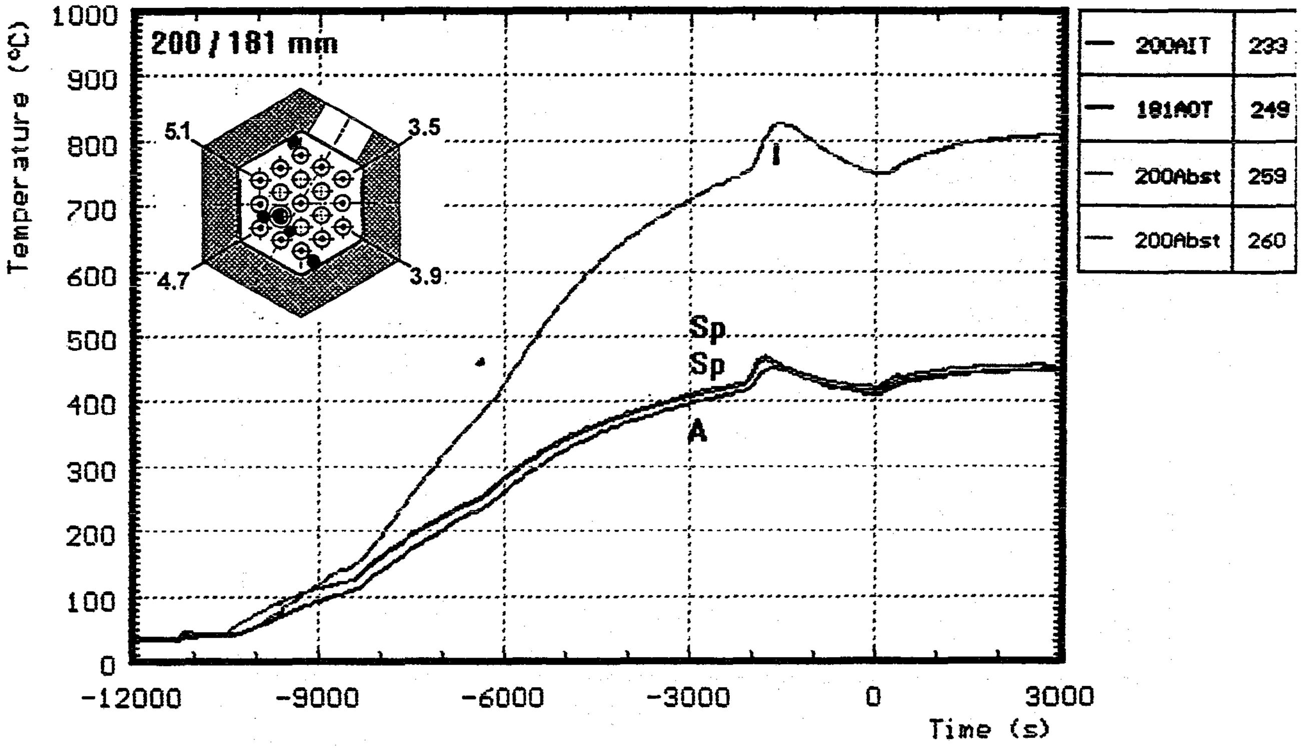

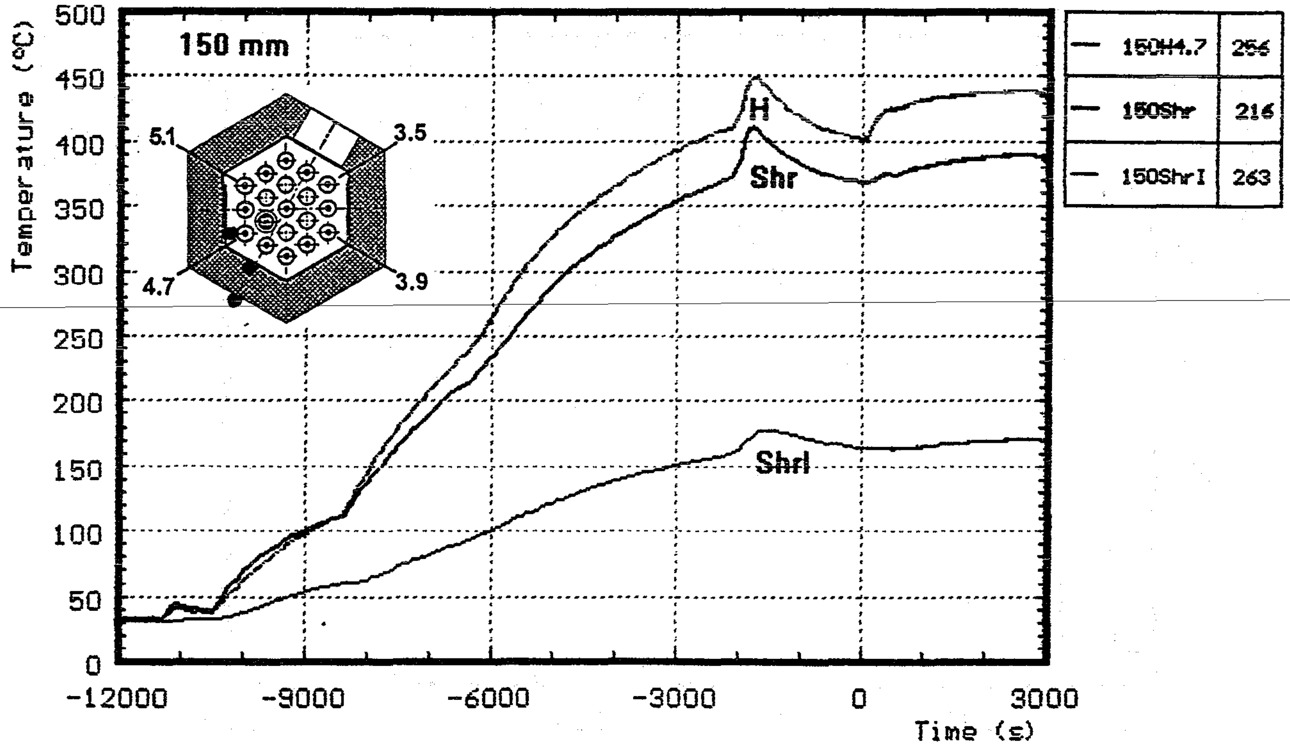

H: heated rods
I : on absorber
A: on guide tube

Sp : spacer
ShrI: shroud insulation
Shr : on shroud

Fig. A20: CORA-W2; Temperatures at fixed elevations; pre-heat phase (200, 150 mm)

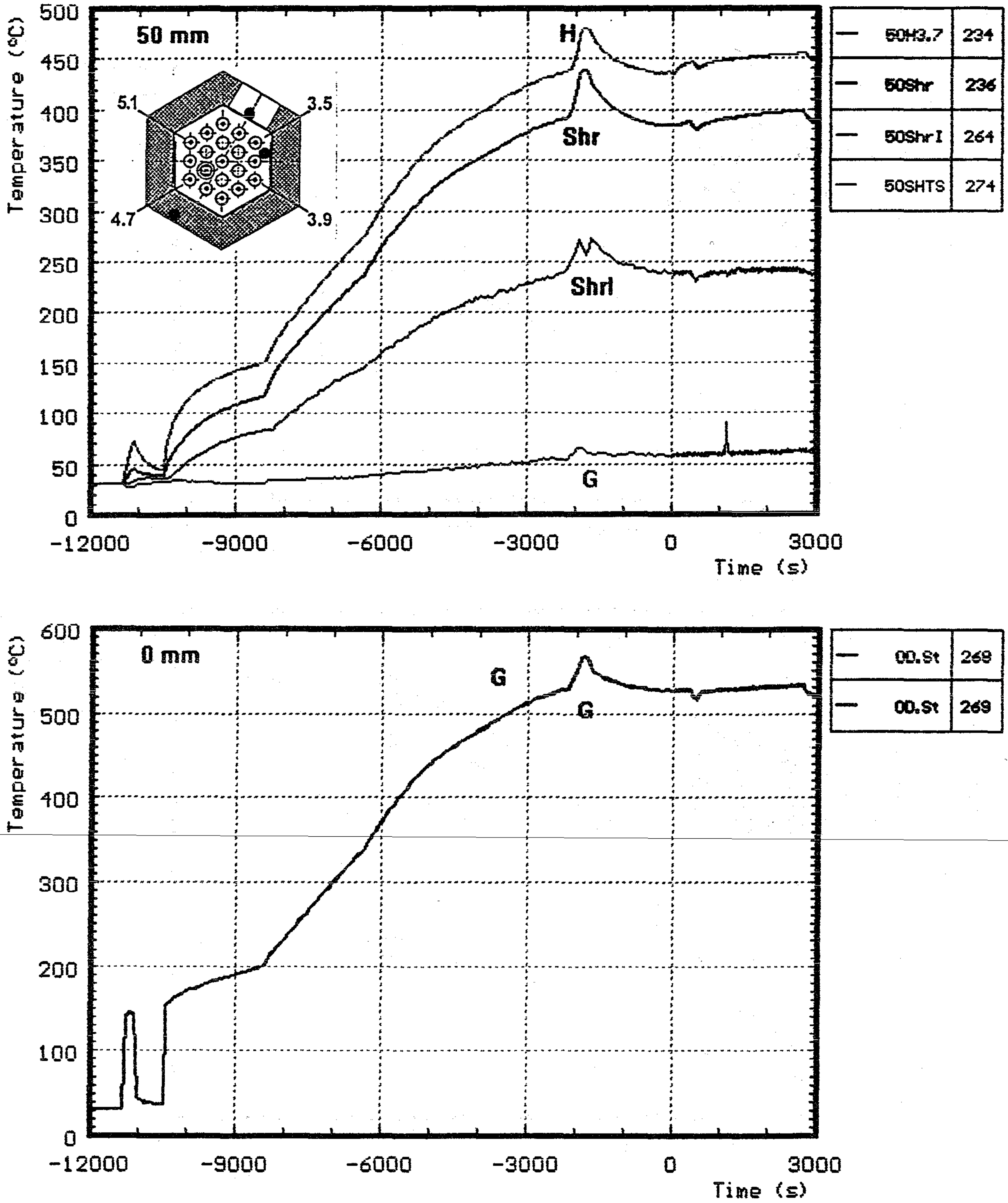

H: heated rods
G: gas temperature

Shr : on shroud
ShrI: shroud insulation

Fig. A21: CORA-W2; Temperatures at fixed elevations; pre-heat phase (50, 0 mm)

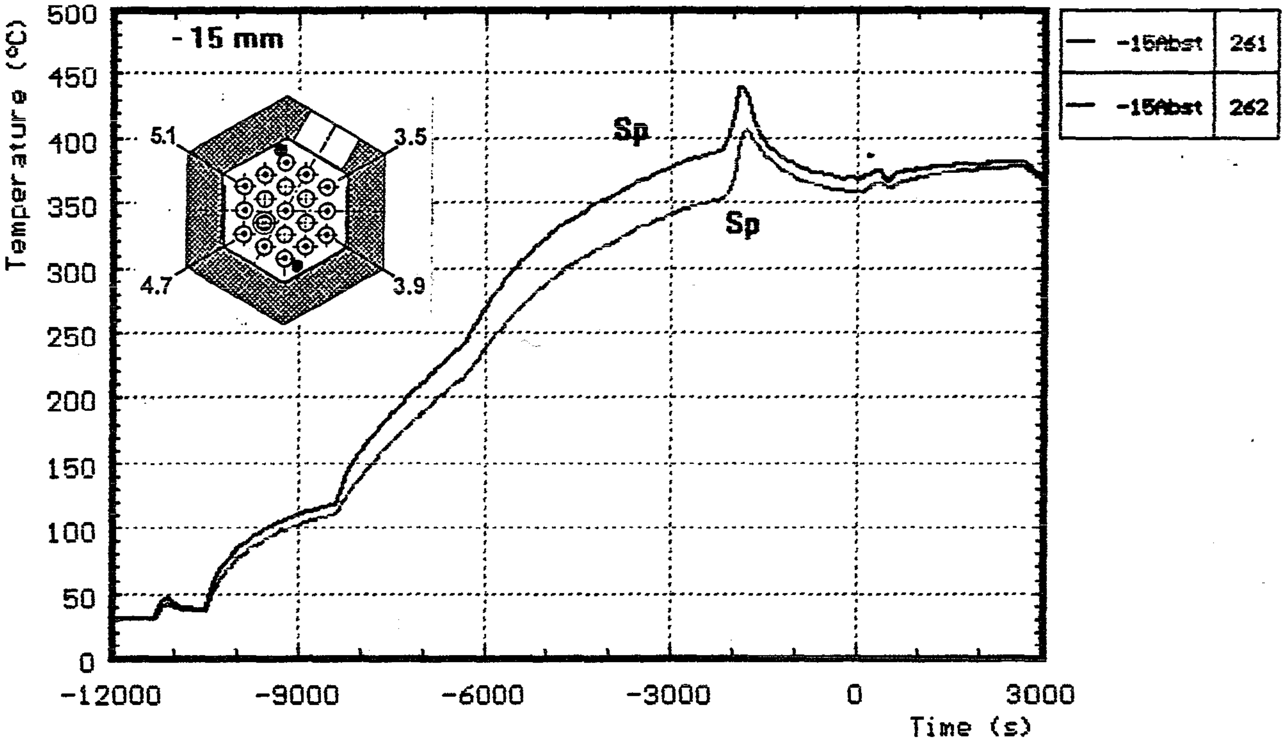

Fig. A22: CORA-W2; Temperatures at fixed elevations; pre-heat phase (-15 mm)

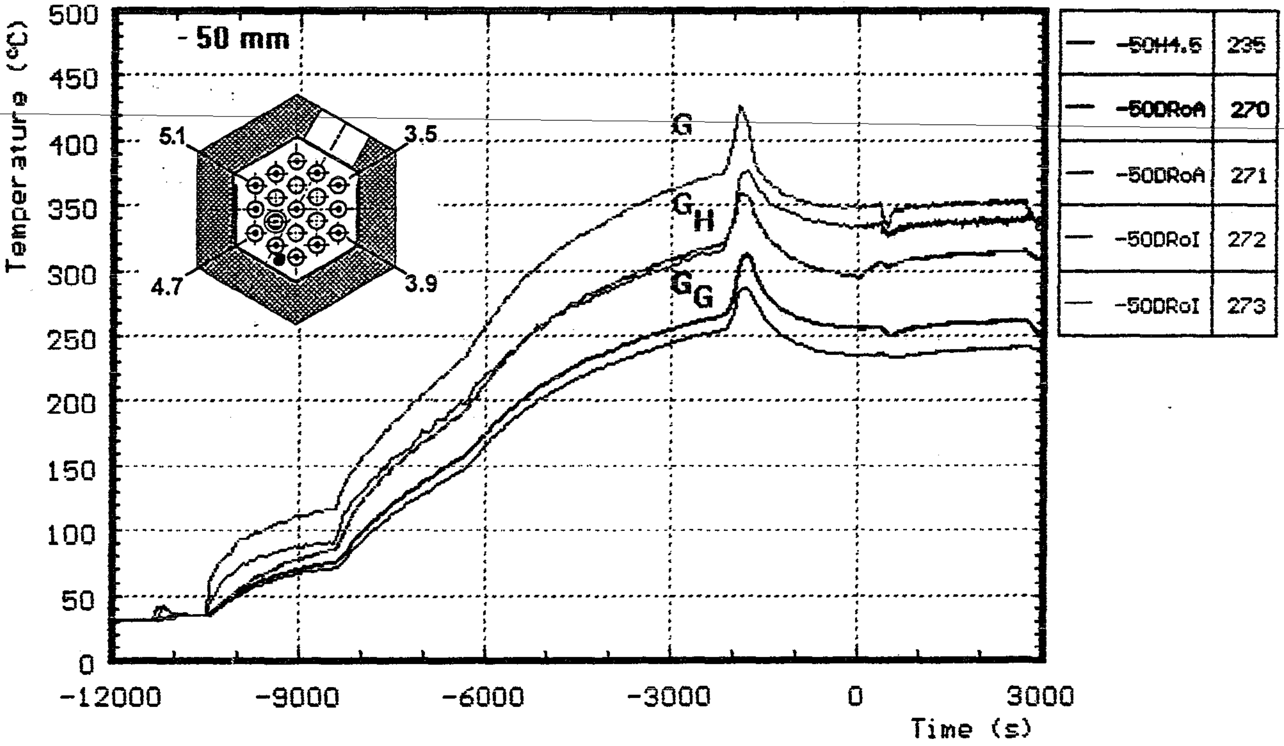

Fig. A23: CORA-W2; Temperatures at fixed elevations; pre-heat phase (-50 mm)